PHOTODISSOCIATION OF ATMOSPHERICALLY IMPORTANT SPECIES

A Thesis Submitted for the Degree of

Doctor of Philosophy

By

Phillip L. Tyley

Trinity College, Oxford.

SCIENCE LIBRARY OXFORD
26 APR 2001

Trinity Term 2000

Contents

Abstract v

Acknowledgements vi

Chapter 1

Introduction 1

1.1 Introduction 1

1.2 Stratospheric Ozone 1

1.2.1 Production of ozone *1*

1.2.2 Removal of ozone *2*

1.2.3 Effects of ozone *3*

1.3 Tropospheric Ozone 4

1.3.1 Sources of Ozone *4*

1.3.2 The effects of ozone in the troposphere *5*

1.4 The ground and low lying energy states of ozone 6

1.5 The photolysis of ozone 10

1.5.1 Absorption of a photon *10*

1.5.2 The UV absorption cross section of ozone *11*

1.5.3 The products from the UV photolysis of ozone *12*

1.6 Quantum yields 14

1.6.1 Early Results *15*

1.6.2 Recent data *17*

1.6.3 Modelling implications *21*

1.7 Dissociation dynamics 24

1.8 Spectroscopy 27

1.9 Current Work 27

Chapter 2

Experimental 32

2.1 Introduction 32

2.2 Molecular Preparation 32

2.3 Laser Systems 34

2.3.1 General 34

2.3.2 Nd:YAG pumped dye laser 34

2.3.3 Excimer pumped dye laser 37

2.3.4 Non-Linear Optics 38

2.3.5 Laser polarisation 39

2.3.6 Optics 41

2.3.7 Laser energy 42

2.3.8 System timing 43

2.4 Bulb bulk gas experiment 44

2.5 Operation of the time-of-flight mass spectrometer 47

2.5.1 Introduction 47

2.5.2 Basic description of the operation of the TOFMS 47

2.5.3 Recent modifications 48

2.5.4 Gas handling 49

2.5.5 Electric Fields and Resolution 51

2.5.6 Ion Detection 52

2.6 Simulation of Time-of-flight Profiles 53

2.6.1 Basic Model 53

2.6.2 Production of fragments with an off axis velocity component 56

2.6.3 Alignment between the fragments and probe laser 59

2.6.4 Core extraction 60

2.7 Time-of-flight profile simulation 61

2.8 Data Acquisition & Analysis 63

2.8.1 Baseline Subtraction 63

Chapter 3

The Relative Quantum Yield of $O(^1D)$ from the Near-UV Photolysis of Ozone 66

3.1 Introduction 66

3.2 Production pathways and previous evidence 67

3.3 Sources of error 67

3.3.1 Random errors 67

3.3.2 Systematic errors 69

3.4 Data collection and analysis 82

3.4.1 Correction factors 82

3.4.2 Quantitative versus qualitative measurements 83

3.4.3 Data collection 85

3.4.4 Errors 87

3.5 Quantum yield results 87

3.6 $O(^1D)$ formation from photolysis wavelengths < 310 nm 95

3.6.1 General discussion 95

3.6.2 Investigation of $O(^1D)$ yield via $O(^3P)$ detection 95

3.7 $O(^1D)$ production at wavelengths ≥ 310 nm 96

3.8 $O(^1D)$ production at wavelengths ≥ 320 nm 98

3.9 $O(^1D)$ quantum yield at a dip in the cross section of ozone 100

3.10 Implications for models of the atmosphere 101

3.10.1 Atmospheric evidence for long wavelength tail 102

3.10.2 Recent comparisons 102

3.11 Conclusions 105

Chapter 4

Time-of-flight Studies on the $O(^1D)$ Atomic Fragment 109

4.1 Introduction to REMPI 109

4.2 REMPI of $O(^1D)$ 111

4.3 Observation of orbital alignment in $O(^1D)$ REMPI 113

4.3.1 Time-of-flight investigation of $^1P_1$ and $^1F_3$ intermediate states 113

4.3.2 Changing alignment factor with photolysis wavelength 120

4.4 Time-of-flight measurements of $O(^1D)$ from the photolysis of ozone (281 nm < λ < 329 nm) 122

4.4.1 Photolysis between 281 nm and 302 nm 123

4.4.2 Photolysis between 306 nm and 322 nm 129

4.4.3 Photolysis between 321 nm and 329 nm 132

4.4.4 Higher Resolution Study of $O(^1D)$ formed over a peak in the absorption cross section of ozone *137*

4.5 Conclusions 140

Chapter 5

Time-of-flight Studies on the $O_2(a^1\Delta_g)$ Molecular Fragment 143

5.1 Introduction 143

5.2 General Information 144

5.2.1 Experimental *145*

5.2.2 Spin-forbidden production of $O_2(a^1\Delta_g)$ *145*

5.2.3 Background subtraction in two-laser experiments *146*

5.2.4 Core extraction *147*

5.2.5 Angular momentum polarisation, v-J correlation *148*

5.3 O_2 energy levels: important aspects 149

5.4 The $O_2(d^1\Pi_g - a^1\Delta_g)$ (2,0) band 150

5.4.1 REMPI Spectrum *150*

5.4.2 Time-of-flight studies *156*

5.5 The $O_2(d^1\Pi_g - a^1\Delta_g)$ (1,0) band 163

5.5.1 REMPI spectrum *163*

5.5.2 Time-of-flight studies *165*

5.5.3 Extension of rules from (2,0) to the (1,0) band *170*

5.6 The $O_2(d^1\Pi_g - a^1\Delta_g)$ (3,0) band 172

5.6.1 Spectrum *172*

5.6.2 Time-of-flight profiles *172*

5.7 Conclusions 174

Abstract

Photodissociation of Atmospherically Important Species

A Thesis Submitted for the Degree of Doctor of Philosophy

Phillip L. Tyley, Trinity College, Oxford.

Trinity Term, 2000.

The photodissociation of ozone by ultraviolet light has a great impact on the photochemistry of the atmosphere. The relative quantum yield for the production of the singlet atomic fragment $O(^1D)$ has been determined in the wavelength region 306 to 327 nm for four temperatures between 227 K and 300 K. The technique of resonance enhanced multi photon ionisation (REMPI) was used to probe directly the $O(^1D)$ photolysis product. These relative measurements have been placed onto an absolute scale by the selection of a calibration point whose value has been agreed by the scientific community. The yields obtained are in good agreement with others reported during the time of the research reported in this thesis and clearly show that three mechanisms contribute to the final quantum yield. Below 310 nm, $O(^1D)$ is produced by a spin-allowed channel, above 320 nm the primary channel is a spin-forbidden one and at intermediate wavelengths photolysis of vibrationally excited ozone contributes to the $O(^1D)$ yield. Elements of the quantum yield data presented in this thesis are being included in a new recommendation for the temperature dependent $O(^1D)$ quantum yield.

Details of the dissociation kinetics, including further evidence confirming the spin-forbidden channel, is presented in time-of-flight studies of the $O(^1D)$ product. Time-of-flight profiles taken between 317 and 321 nm show evidence that, at room temperature, the $O(^1D)$ quantum yield is anti-correlated with the ozone absorption cross section. Excitation of the $O_2(a^1\Delta_g)$ co-fragment has been observed at wavelengths below 296 nm by monitoring the energies of the $O(^1D)$ formed. As the channel for the production of $O_2(a^1\Delta_g, v = 1)$ opens, it is found that energy is preferentially partitioned into rotation of the O_2 fragment rather than into translation. Initial studies on the $O(^1D)$ fragment have shown that the fragment is orbitally aligned and that the choice of REMPI transition can have a significant effect on the time-of-flight profiles and therefore on the measurements that are made from the profiles.

The time-of-flight profiles obtained by probing the $O_2(a^1\Delta_g)$ photofragment have shown that the $O_2(a^1\Delta_g)$ has an angular momentum polarisation that is J dependent, with the even J being strongly polarised and the odd J depolarised. This results in the shape of the time-of-flight profiles being a function of the REMPI laser polarisation; and the study of this behaviour has been used to confirm the assignments in highly perturbed REMPI spectra.

Acknowledgements

Studying for my doctorate has always been one of my ambitions and I must thank Gus for giving me the opportunity to achieve this. Without his backing this thesis would never have been started and I would not have had several years enjoying myself learning many new skills. His insights have explained many conundrums and solved many other problems.

Next my thanks must go to my fellow ozonologists. John Pinot for having showed me how to use the equipment and having written many of the data acquisition programs. To my Part II's, Richard and Tim who kept an old man company and amused even if they did cost me much time and many lost hours of sleep when it came to their thesis deadlines. Finally the Wolf must be mentioned for being a great Post Doc. and for his services in providing beer after a hard day in the lab - it was a great shame he could not have stayed for longer.

To my compatriots in the group go my next set of thanks. A very big thank you must go to Grant for his patient explanations and reading of this thesis. A significant honourable mention for their proof reading efforts also must go to the Irish contingent of Hugh and Ciara - I hope I haven't bothered you too much. To Claire, who managed to escape before she could be forced to join in with the reading, though it has to be said going to America to get married is a bit extreme. Rob with his stories of cars, cars and more cars and hoards of useful laser bits. Thanks also to many others in the group including Rob P, Laura, Vanessa and The Jazz, as well as numerous Part II's, for providing much merriment at tea.

My final and greatest thanks must go to Jan, I cannot think of a way to express my thanks for your constant support. You let me chase after my dreams and I trust that you have not regretted it - I know that I have not. Finally, I hope that I have not ignored you too much recently when we should have been together more, I suppose that payback starts in March.

Chapter 1

Introduction

1.1 Introduction

Other than for the most obvious of reasons, oxygen is crucial to our life on this planet. In the atomic, diatomic and triatomic (ozone) forms oxygen's chemistry greatly influences the state of our atmosphere at all altitudes; with ozone being of particular importance in the stratosphere and troposphere. The impact that ozone has on the atmosphere is all the more impressive given its low concentration (peaking at *ca.* $5x10^{12}$ molecules cm^{-3}, or 10 parts per million by volume, in the stratosphere). This thesis aims to provide further information on the behaviour of ozone when it is photolysed by radiation in the ultraviolet; particularly at those wavelengths found in the lower atmosphere.

1.2 Stratospheric Ozone

The stratosphere's boundaries are determined to a significant extent by the existence of ozone within it. The boundaries are set so that within the stratosphere the temperature gradient with respect to increasing altitude is positive, and the reasons for this will be discussed shortly. The lower boundary, the tropopause, is dependent on latitude and varies between 6 to 8 km at the poles to *ca.* 18 km at the equator. The stratosphere's upper boundary, with the mesosphere, lies at about 50 km. Within these boundaries exists approximately 90% of the atmosphere's ozone, and without it life would be very different from that we experience today.

1.2.1 Production of ozone

Ozone in the stratosphere is a direct result of the interaction of ultraviolet (UV) solar radiation with oxygen molecules in the stratosphere. By the time photons reach the stratosphere, significant filtering of the UV spectrum of the radiation has occurred already.[1,2] Atomic and molecular oxygen and nitrogen are responsible for removing sub 100 nm radiation by an altitude of 100 km; the Schumann-Runge continuum of O_2 removes 100-175 nm radiation by 80 km (in the thermosphere); the Schumann-Runge bands predominantly absorb the radiation between 175-205 nm in the mesosphere; and the Herzberg I system of O_2 absorbs 190-245 nm

radiation in the stratosphere. The last two absorption systems, however, are structured and comparatively weak above 200 nm, the cross section falling by two orders of magnitude between 180 nm and 190 nm. Therefore radiation that can dissociate molecular oxygen into two $O(^3P)$ atoms, the thermodynamic limit for which is 242.5 nm, is still available. It is the reaction of $O(^3P)$ atoms with molecular oxygen that forms ozone *via* the third body recombination:

$$O(^3P) + O_2 + M \rightarrow O_3 + M \qquad \textbf{(1-1)}$$

At this point it should be noted that the absorption spectrum of ozone peaks at 254 nm and that ozone photon absorption usually results in the production of atomic and molecular oxygen. Chapman,[3] in 1929, proposed that the counteracting nature of the production and destruction processes could lead to the formation of a layer in the atmosphere in which the concentration of ozone would be enhanced. The observation of the ozone layer gives credence to this proposition. Whilst the overall concentrations of ozone in the atmosphere are low, they peak in the mid stratosphere (25 to 30 km) at $5x10^{12}$ molecules cm^{-3}, where their corresponding abundance is 6 parts per million by volume. Whilst Chapman was partially correct, it was not long before experimental evidence showed that his calculations were not accurate. The calculations failed to predict correctly the size and altitude of the layer; the major problem being that the model overestimates the ozone column abundance.

1.2.2 Removal of ozone

To improve the model describing the concentration of ozone additional loss mechanisms were needed. These mechanisms were required because the photodissociation of ozone does not lead to a net loss of odd oxygen. The concept of odd oxygen* is important as odd oxygen readily converts between its two forms; with the products of ozone photodissociation eventually reforming ozone *via* reaction (1-1). Since 1950 there have been many modifications to the initial, oxygen only, photochemical sequences to improve the model (see Wayne[1] and Brasseur *et al.*[2] for a detailed discussion). These have included the effects of mesospheric water vapour[4] and catalytic loss cycles involving HO_x, NO_x, ClO_x and BrO_x. These cycles effectively scavenge odd oxygen from the atmosphere and result in the formation of O_2 with a net loss of two in the odd oxygen count.

---

* Odd oxygen is defined as consisting of O and O_3. It is a useful measure as the two species rapidly interconvert.

Above 30km, where there is sufficient atomic oxygen, the cycles take the form (where **X** represents the catalytic species):

$$X + O_3 \rightarrow XO + O_2 \qquad \textbf{(1-2)}$$

$$XO + O \rightarrow X + O_2 \qquad \textbf{(1-3)}$$

$$\text{Net: } O + O_3 \rightarrow 2\,O_2 \qquad \textbf{(1-4)}$$

Below 30 km the concentration of atomic oxygen has decreased to such an extent that the rate of reaction (1-3) is significantly less than that above 30 km. Other catalytic cycles, in which the atomic oxygen in reaction (1-3) is replaced by ozone now become important; the net cycle now being the conversion of two ozone molecules into three oxygen molecules. It is through the effects of these catalytic cycles that man's actions can influence the ozone layer. In particular, the anthropogenic release of certain halogen containing compounds, the chlorofluorocarbons, has been shown, first by Molina and Rowland,[5] to increase the availability of catalytic mediators and thus increase the rate of ozone loss.

1.2.3 Effects of ozone

The ozone layer has two significant properties. The first is the way it filters the solar radiation, very little radiation below 295 nm reaches ground level (a result of Hartley band absorption, $210 < \lambda < 300$ nm) and secondly the tail in the Hartley band, known as the Huggins band ($300 < \lambda < 360$ nm), also causes a significant reduction. The filter action is important as there is strong evidence that UV-B (280-315 nm) is damaging to DNA, potentially causing cancers, cataracts and also affecting plant growth.[1,2,6] The second property of the ozone layer is that, as a result of the absorption of radiation by ozone, the stratosphere heats up and causes a temperature inversion to be formed. The inversion formed prevents the vertical transport of air and reduces the ability of the troposphere and stratosphere to mix and thus stabilises the composition of the stratosphere. A further property is that ozone absorbs radiation in the infrared (IR) at ~9.6 μm; therefore, the ozone acts as a greenhouse gas preventing thermal radiation from leaving the planet's surface. It is estimated that about 3% of the thermal trapping in the atmosphere can be attributed to ozone.[1]

1.3 Tropospheric Ozone

The troposphere contains approximately 85-90% of the atmosphere's mass. The boundary between the troposphere and the stratosphere is known as the tropopause and is located at the altitude at which the rate of temperature change with altitude (dT/dz) changes sign, from negative to positive. The chemistry of the troposphere is still strongly linked to the presence of ozone, as in the stratosphere, but now the influence of ozone is more indirect and centres on the production of oxidising species, particularly OH and NO_3.

1.3.1 Sources of Ozone

Ozone in the troposphere can not be formed *via* the same reaction sequence as in the stratosphere, since molecular oxygen can not be dissociated by the wavelengths of radiation that reach the troposphere. Therefore, the ozone must either come from transport across the tropopause (for example by tropopause folding) or from another source of the atomic oxygen is needed (discussed below). Which of these sources is the most important is a subject under much debate; the debate being complicated by the fact that both processes are subject to significant geographical (on global and local scales) and temporal (short and long term) influences.[1,2,7]

The major source of atomic oxygen, in the troposphere, is from the photolysis of NO_2 by near UV (< 400 nm) radiation. The reaction sequences rely not just on the presence of NO_2 and oxygen, but require also the oxidation of organic compounds to generate the appropriate mechanism. In the free troposphere (the troposphere above the surface – atmosphere boundary, which typically is at 1.5 km over land and 0.5 km over oceans), the primary sequences are based on the oxidation of CO and CH_4. As an example the sequence for methane is:

$$OH + CH_4 \rightarrow CH_3 + H_2O \qquad \textbf{(1-5)}$$

$$CH_3 + O_2 + M \rightarrow CH_3O_2 + M \qquad \textbf{(1-6)}$$

$$CH_3O_2 + NO \rightarrow CH_3O + NO_2 \qquad \textbf{(1-7)}$$

$$CH_3O + O_2 \rightarrow HO_2 + CH_2O \qquad \textbf{(1-8)}$$

$$HO_2 + NO \rightarrow OH + NO_2 \qquad \textbf{(1-9)}$$

$$2(NO_2 + h\nu \rightarrow NO + O) \qquad \textbf{(1-10)}$$

$$2(O + O_2 + M \rightarrow O_3 + M) \qquad \textbf{(1-1)}$$

$$\text{Net: } CH_4 + 4O_2 + h\nu \rightarrow CH_2O + H_2O + 2O_3 \qquad \textbf{(1-11)}$$

The net sequence for CO is:

$$CO + 2O_2 + h\nu \rightarrow CO_2 + O_3 \qquad \textbf{(1-12)}$$

It is important to note that the OH radical plays a very important part in these sequences. The CO sequence also starts with an attack by OH, and the importance of OH and its sources will be discussed further.

A further reaction sequence is also possible, particularly in the boundary layer over continental regions where non-methane hydrocarbons (NMHC), from anthropogenic and biogenic sources, can be oxidised in a similar manner to methane to generate ozone. Whilst even over rural areas the concentrations of NMHC can be significant as a result of biogenic release; it is in industrial regions that the sequence including NMHC can be of great importance, as ozone is a significant component in photochemical smog. The industrial regions are particularly susceptible to this production of ozone as, in addition to the release of the NMHC, NO_x* is readily available and it has been found that the production of NO_x is the rate controlling factor in the reaction sequence.[2]

1.3.2 The effects of ozone in the troposphere

The presence of ozone in the troposphere can be considered a mixed blessing, particularly in the ground boundary region. The main detrimental effects are on biological organisms, ozone has been shown to be capable of causing eye and nose irritation, and respiratory problems for animals, and can also adversely affect vegetation. It is of benefit because of its absorption of UV radiation, but also because of the reactions initiated by the products of ozone photolysis. Whilst gases at higher altitudes have already removed the vast majority of the significantly hazardous UV radiation, there is still sufficient radiation above 300 nm to cause adverse biological effects and any further reduction of the UV-A and UV-B levels will be beneficial. However, the main processes that are of importance in the troposphere are the reactions of ozone's photolysis products. In the daytime ozone can be dissociated to form electronically excited $O(^1D)$ atoms:

---

* NO_x refers to the easily interconverted NO and NO_2 oxides of nitrogen. When concentrations are referred to the concentration of NO_x is the sum of the concentrations of NO and NO_2.

$$O_3 + h\nu \rightarrow O(^1D) + O_2 \qquad \textbf{(1-13)}$$

The majority of the atomic fragments are quenched from $O(^1D)$ to the ground state $O(^3P)$, which can then regenerate ozone *via* reaction (1-1). However, a significant number of $O(^1D)$ atoms react with water in the atmosphere resulting in the production of OH *via*:

$$O(^1D) + H_2O \rightarrow 2\ OH \qquad \textbf{(1-14)}$$

These hydroxyl radicals, which have been referred to as "nature's atmospheric detergent",[8] initiate the oxidation sequence in the atmosphere by reacting for example with carbon monoxide and methane (reaction (1-5)).

1.4 The ground and low lying energy states of ozone

In its chemical ground state ozone belongs to the C_{2v} point group, with a bond angle of 116.8° and bond lengths of 1.278 Å. It is not possible to describe this state in terms of a single electronic configuration, but the dominant (81%) electronic state is:

$$\text{Core} + (5a_1)^2(3b_2)^2(1b_1)^2(6a_1)^2(4b_2)^2(1a_2)^2 \qquad \textbf{(1-15)}$$

The next largest contributor (8%) moves the $(1a_2)^2$ electrons into what was the lowest unoccupied molecular orbital, $2b_1$. Both of these contributors, consisting only of completely filled orbitals, are of $^1A_1$ symmetry. The main contributor is the lowest in energy and is therefore referred to as the X $^1A_1$ state, the other state being the 2 $^1A_1$ state. These, and the other main low lying energy states, are shown in Figure 1-1, the data for which have been drawn from Banichevich *et al.*[9] A major factor that complicates discussion of the energy states and spectroscopy is that, as a result of excitation along the antisymmetric stretch coordinate, the system easily changes from C_{2v} symmetry to C_s, which leads to avoided crossings between states. Details of the electronic spectroscopy of ozone have been reviewed by Bacis *et al.*[10] but a brief overview is included here.

Bacis *et al.*[10] concluded that the structured Wulf absorption band (600 nm to 1100 nm) results, primarily, from transitions from the ground state to the $^3A_2$ and $^3B_1$ levels. Whilst excitation to the $^3A_2$ level is doubly forbidden, as a result of spin conservation and dipole selection rules, Braunstein and Pack[11] found that the transition intensity to the $^3A_2$ level is enhanced by spin-orbit mixing with the $^1B_2$ state. Bacis *et al.* did not wish to draw a firm conclusion on the possibility of the inclusion of the third of the three low lying triplet states, the $^3B_2$, in forming the Wulf band as their model predicted a very low transition moment.

The Chappuis band (400 nm to 650 nm) arises from absorption to the $^1B_1$ and $^1A_2$ states. It would be expected that the $1\,^1A_2 \leftarrow X\,^1A_1$ transition would be forbidden from the electronic dipole selection rules, but it becomes vibronically allowed when the transition includes excitation of the antisymmetric stretch. From Figure 1-1 it can be seen that the $^1B_1$ state is bound and should have a long lifetime.

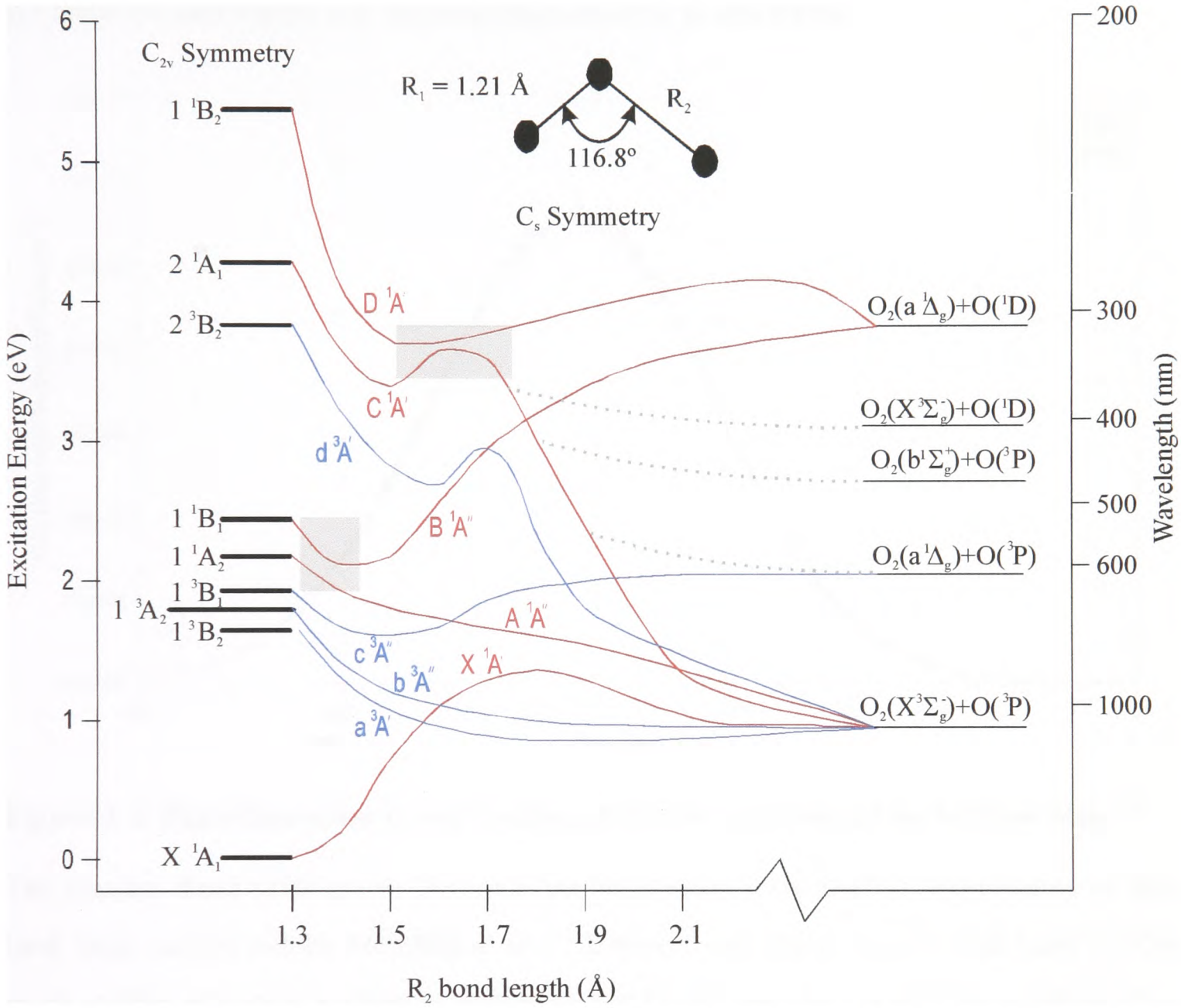

Figure 1-1 The calculated energies of the main low lying electronic states of ozone. The energies have been taken from the closest calculations to the ground state geometry from Banichevich *et al.*[9] Shaded areas denote known crossing points. The dotted lines mark spin-forbidden dissociation pathways that have been observed.

The reason that a long lifetime is not observed is related to the antisymmetric stretch involved in the $^1A_2$ transition. Excitation of the antisymmetric stretch causes the symmetry to change from C_{2v} to C_s, and changes the symmetry of the $^1A_2$ to $\tilde{A}\,^1A''$ and $^1B_1$ to $\tilde{B}\,^1A''$ and the allowed crossing between them becomes an avoided one. The avoided crossing occurs at 120°, over a wide range of bond lengths.[10] The conical section that is formed by this avoided crossing

allows leakage from the upper surface to the lower surface and therefore to the $\tilde{A}\ ^1A''$ state. The $^1A''$ state can be seen from Figure 1-1 to be dissociative and results in the formation of the ground state products ($O(^3P)$ and $O_2(X^3\Sigma_g^-)$). Both states responsible for the Chappuis band therefore dissociate on short timescales.

The ultraviolet absorption features of the Hartley and, particularly, the Huggins bands, shown in Figure 1-2 and Figure 1-3, are of greatest interest in this thesis.

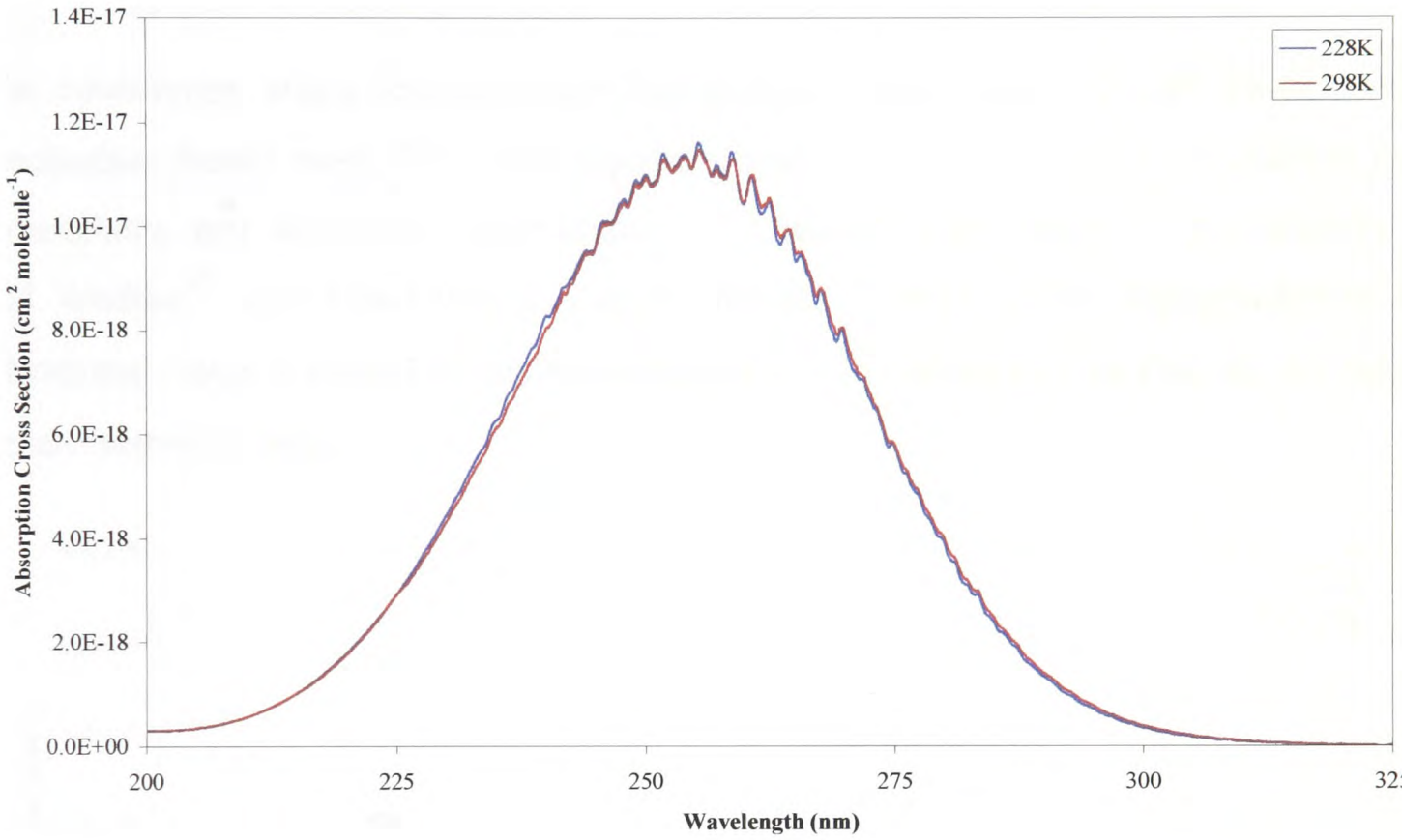

Figure 1-2 The Absorption Cross Section of Ozone as measured by Malicet *et al.* [12]

The Hartley Band (200 nm to 300 nm) has been extensively studied and reviews of this work have been carried out by Steinfeld *et al.*,[13] Wayne[14] and Bacis *et al.*[10] This band is where the cross section of ozone reaches its maximum (at 253.65 nm the NASA[15] recommended value is 1147×10^{-20} cm^2 molecule^{-1}) and the cross section takes the form of a broad peak upon which there is some structure between 240 nm and 270 nm. The Hartley band has been determined by Hay *et al.*[16] and Simons *et al.*[17] and others (see review article by Johnson *et al.*[18]) to correspond to the $^1B_2 \leftarrow X^1A_1$ transition. Whilst Figure 1-1 shows that the $^1B_2$ state correlates with the formation of excited singlet products ($O(^1D)$ and $O_2(a^1\Delta_g)$), it is possible for ground state products to be formed. Once again this results from a crossing becoming avoided as the R_2 bond length is increased, the $2\ ^1A_1$ state becoming $\tilde{C}\ ^1A'$ and the $1\ ^1B_2$ becoming $\tilde{D}\ ^1A'$. Observations of both the excited singlet and the ground state triplet products have been made by many groups (for some examples see singlet,[19,20] triplet[19,21,22,23,24,25]), and although the exact

quantum yields vary with wavelength, they are typically 90% singlet + singlet and 10% triplet + triplet. The observation of the ground state products, and in particular highly vibrationally excited O_2, at around 226 nm has raised the possibility of a new mechanism for the production of ozone. This controversial mechanism results from the observation of an increase in the rate of de-excitation of $O_2(v \geq 26)$ in collision with O_2 compared to rates for lower vibrational levels and the mechanism has been stated as:

$$O_3 + h\nu \rightarrow O_2(X^3\Sigma_g^-, v \geq 26) + O;\ O_2(X^3\Sigma_g^-, v \geq 26) + O_2 \rightarrow O_3 + O \qquad \textbf{(1-16)}$$

The controversy arises between theoretical groups, whose models do not predict that such a mechanism should work,[26,27,28] and experimentalists, who have used the mechanism to explain atmospheric and laboratory observations.[29,30,31] Recent experimental observations by Jongma and Wodtke[32] have found that it is likely that the majority of the depopulation of the high vibrational states is caused by multiquantum ($\Delta v \approx -9$) relaxation, but they do not rule out the ozone formation path.

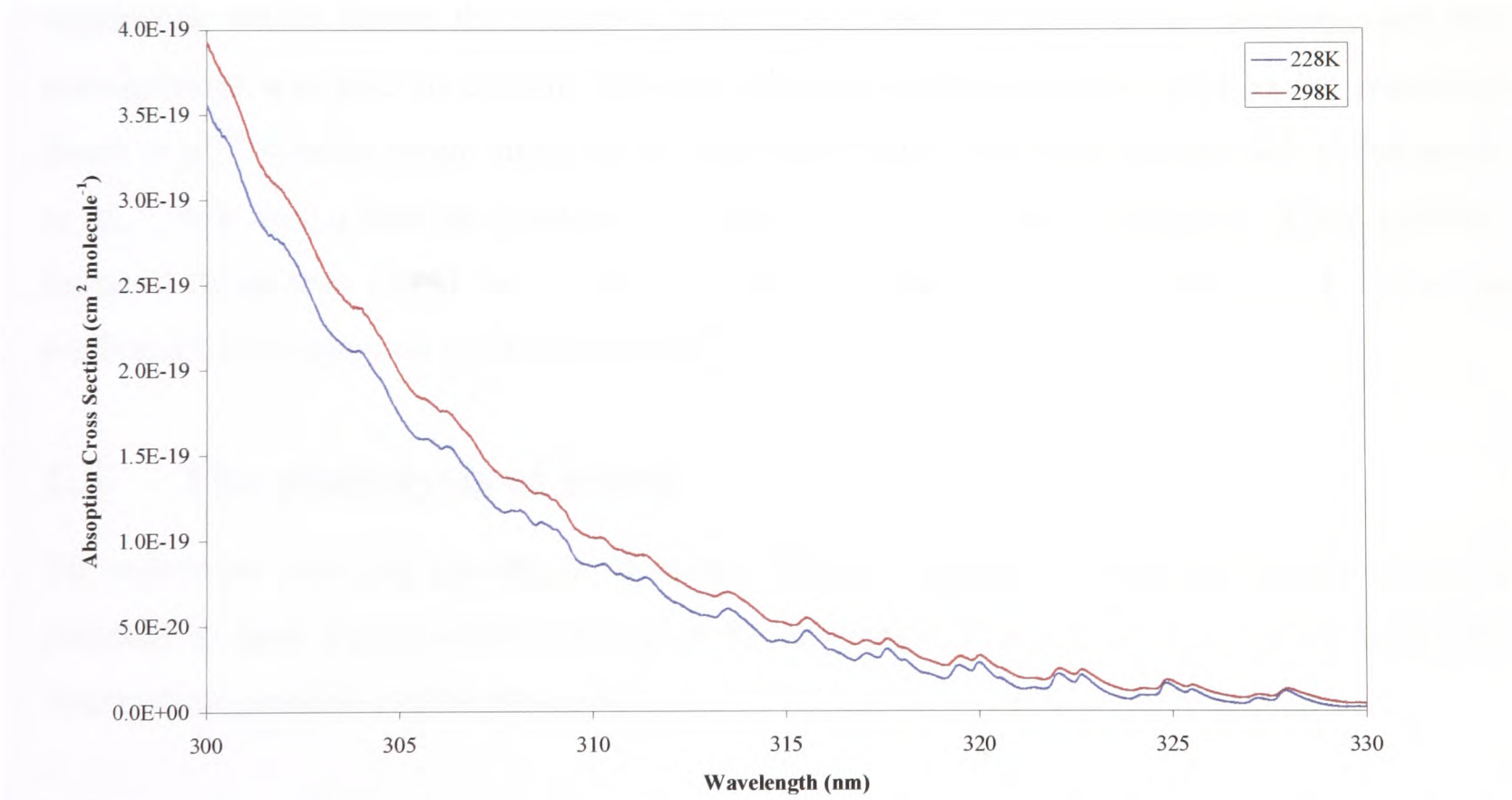

Figure 1-3 Expanded view of the absorption cross section of ozone as measured by Malicet *et al.*[12] in a region of the Huggins band.

The Huggins band (300 nm to 370 nm), partially shown in Figure 1-3, is often viewed as the long wavelength tail of the Hartley band but it is still unclear if the same transition is responsible. Initially it was believed that the transition was to the $1\ ^1B_2$, state with the low intensity of the band being ascribed to poor Frank-Condon overlap between the ground and

upper states. Evidence for this assignment came from both experimental and theoretical sources. Katayama[33] investigated the absorption spectra of a cooled sample and, by considering isotope shift data, he was able to assign the vibrational structure to transitions from the ground vibrational state to vibrationally excited states in the 1 $^1B_2$ electronic state. Using this assignment, Sinha *et al.*[34] investigated the rotational profiles generated in the jet-cooled excitation spectrum of ozone and found that a good fit could be made with the assumption of a 1 $^1B_2$ upper state. Leforestier *et al.*[35] utilised a 3D quantum calculation model with a $^1B_2$ potential energy surface and were able to successfully model the Huggins band's structure.

More recently there has been growing evidence that the transition could be 2 $^1A_1 \leftarrow X^1A_1$. This two electron transition is electronically forbidden but becomes allowed through vibronic coupling with the antisymetric stretch (ν_3), if $\Delta\nu_3$ is odd, and the increase in the intensity of the band is caused by mixing with the 1 $^1B_2$ state responsible for the Hartley band. Evidence for this has come from molecular orbital calculations by Thunemann *et al.*,[36] Hay and Dunning[37] and Banichevich *et al.* [9,38] Assuming the transition to be 2 $^1A_1 \leftarrow X^1A_1$, Joens[39] used symmetry arguments, which forced the condition that $\Delta\nu_3$ is odd, to reassign the spectrum; and this reassignment was able to explain fully the observed spectrum and simplified the results of Sinha *et al.*[34] A more recent study on the rotational profiles has been carried out by Takahashi *et al.*,[40] who found that the rotational constants required in their simulation of the profiles, matched those that would be expected for the secondary minimum of the 2 $^1A_1$ state (as predicted by Banichevich and Peyerimhoff[38]).

1.5 The photolysis of ozone

To understand how the photolysis of ozone affects so much of atmospheric chemistry it is essential to have a good understanding of the absorption process, its cross section and what dissociation products can be produced.

1.5.1 Absorption of a photon

The first stage of photodissociation is the absorption of a photon. No molecule is capable of absorbing photons of all wavelengths and there are conditions that have to be met for the process to take place. The first condition is that there are a pair of energy levels that are separated by the energy of the photon and that the lower state is occupied. The second is that the upper state must be accessible from the lower in terms of the symmetries of the two states.

For an electric dipole transition, the transition probability between the states Ψ_1 and Ψ_2 is given by:

$$P_{12} = |\mu|^2 = \left| \int_\tau \Psi_2^* \hat{\mu} \Psi_1 d\tau \right|^2 \qquad \textbf{(1-17)}$$

where μ is the transition moment and $\hat{\mu}$ is the electric dipole moment operator, both of which are vector quantities. To determine the total probability that a photon will be absorbed P_{12} has to be integrated over all possible initial and final states. It is this integrated quantity that typically is used and is known as the absorption cross section (normal units, cm^2 $molecule^{-1}$). The absorption cross section is not a constant number but varies significantly with the wavelength of the photon that is being considered and may also change depending upon the physical environment (temperature, pressure etc) and the characteristics of the upper electronic state. Part of the dependence of the cross section on the upper state arises if the upper state has a very short lifetime, as a result of emission or predissociation, so that the uncertainty in the energy of the upper state becomes large and results in a wide range of photon energies being absorbed.

Instead of having to use the molecular wavefunctions to calculate the transition probability it is possible to use symmetry arguments to specify conditions when the probability should be zero. These rules depend on the type of transition occurring (rotational, vibrational or electronic) and the system to which they apply. For non-linear molecules, such as ozone, many of the quantum numbers that are used in detailing the selection rules for diatomic molecules are no longer good quantum numbers. For light atoms, the main quantum number that remains good for non-linear molecules is the total spin angular momentum, which has the selection rule that it should not change, i.e. $\Delta S = 0$. In the case of ozone, which is composed of light atoms, spin-orbit coupling, which would permit the selection rule to be broken, should be weak; therefore as ozone has a singlet ground state the main transitions should be to other singlet states, with absorption to triplet states being much weaker in intensity, which is observed.

1.5.2 The UV absorption cross section of ozone

The UV absorption cross section of ozone has been measured by a number of groups including Bass and Paur,[41] Molina and Molina,[42] Malicet *et al.* [12] and Burrows *et al.*[43] Generally there is good agreement between the values obtained. The main discrepancies occur at wavelengths greater than 320 nm; even then they do not exceed 6% until wavelengths over 350 nm are

reached. The Hartley band absorption cross section is temperature dependent, with most groups reporting that the feature increases in wavelength slightly as the temperature increases (in the data of Malicet *et al.* changing the temperature from 228 K to 298 K causes a + 0.1 nm shift). This shift also shows in a slight reduction in the cross section as the temperature is increased for wavelengths below 260 nm whilst the cross section increases with temperature above this wavelength. The cross section in the Huggins band can be seen in Figure 1-3 to be temperature dependent, with the general cross section falling as the temperature is decreased. However, the structure that exists on the general cross section has a different temperature dependence, with the size and position of the peaks changing with temperature. A point worthy of note here is that the UV cross section of ozone changes considerably if the ozone is in a vibrationally excited state. The work of McDade and McGrath[44] and that of Alder-Golden *et al.*[45] showed that the peak in the cross section shifts at least 3500 cm^{-1} to the red for ozone which has been vibrationally excited *via* the ν_3 asymmetric stretch.

1.5.3 The products from the UV photolysis of ozone

For tropospheric ($\lambda > 290$ nm) applications the following dissociation pathways are energetically allowed (for ozone with no internal energy):

$O_3 + h\nu \rightarrow$	$O(^1D) + O_2(a\ ^1\Delta_g)$	$\lambda \leq 310.3$ nm	**Path 1-A**
	$O(^1D) + O_2(X\ ^3\Sigma^-_g)$	$\lambda \leq 410.6$ nm	**Path 1-B**
	$O(^3P) + O_2(b\ ^1\Sigma^+_g)$	$\lambda \leq 462.9$ nm	**Path 1-C**
	$O(^3P) + O_2(a\ ^1\Delta_g)$	$\lambda \leq 611.0$ nm	**Path 1-D**
	$O(^3P) + O_2(X\ ^3\Sigma^-_g)$	$\lambda \leq 1178$ nm	**Path 1-E**

The wavelength shown alongside each pathway is the longest wavelength radiation that can dissociate an ozone molecule with no internal energy *via* that pathway. The dissociation path that is followed after photon absorption, at a specific wavelength, is determined by the nature of the potential energy surface of the excited ozone molecule, which has been discussed in section 1.4. It would be expected that Path 1-A and Path 1-E would be the major pathways followed as they are the only pathways that are allowed by the rules of spin conservation, which generally hold for molecules formed from light atoms. In fact **all** of the pathways listed

have been observed at varying yields depending on the photolysis wavelength. The $O(^1D)$ from the spin-forbidden Path 1-B has been observed directly by Takahashi *et al.*,[46] Denzer *et al.*[47,48] and Ball *et al.*,[49] and indirectly by Talukdar *et al.*,[50] Bauer *et al.*[51] and Armerding *et al.*[52] The $O(^3P)$ from Path 1-C has been reported by O'Keeffe *et al.*,[53] who also observed the $O_2(b\ ^1\Sigma^+_g)$. The $O_2(a^1\Delta_g)$ from Path 1-D has been reported by Ball *et al.*, first as quantum yield measurements[54] and then with time-of-flight studies.[55] Figure 1-4 shows the dissociation paths that can be followed in the Huggins band.

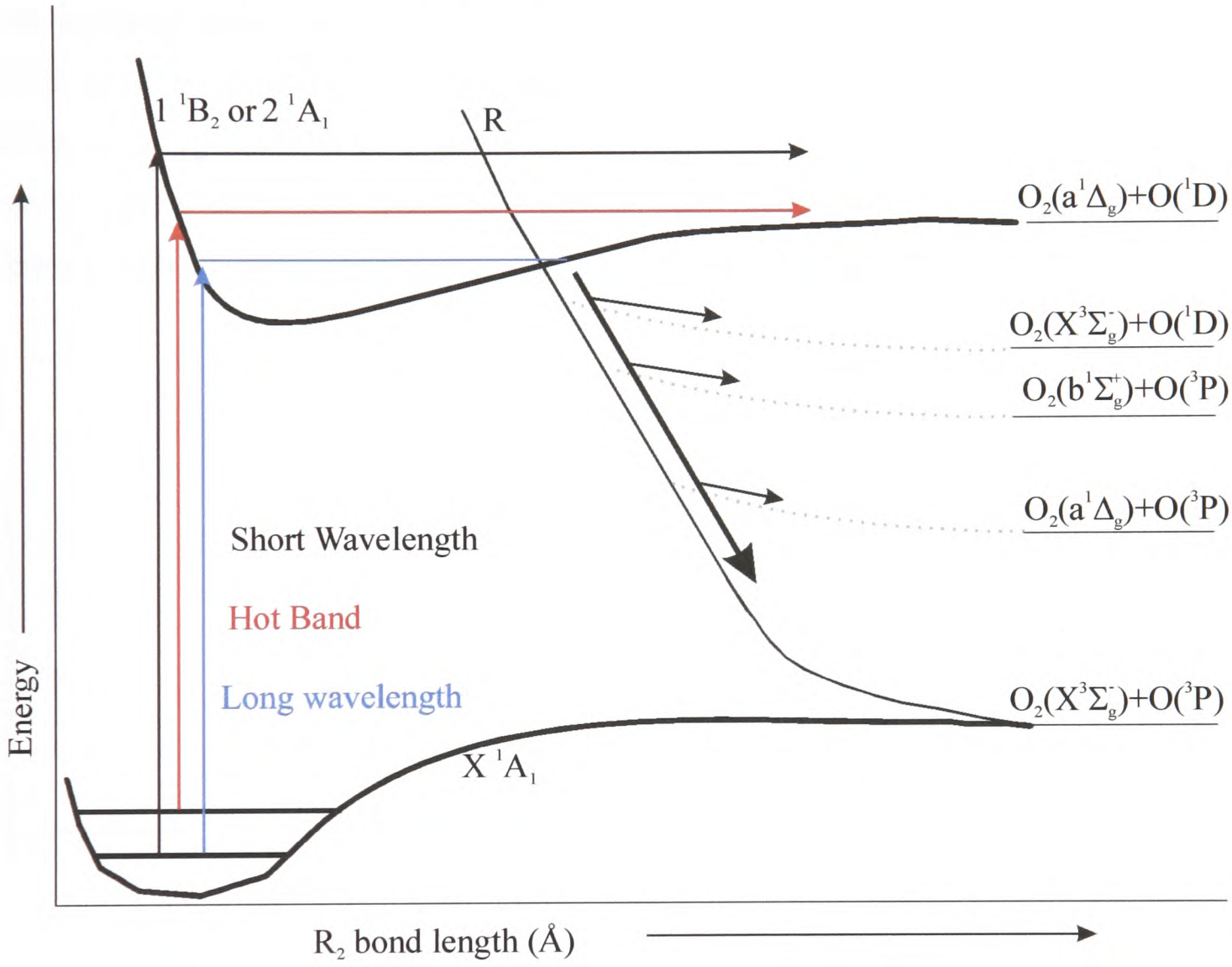

Figure 1-4 Dissociation paths in the Huggins band. Note that the dissociative state R may be different depending on the final state reached. Short wavelengths are below 310 nm, with long wavelengths greater than this.

In addition to the observation of all of the pathways, fragments formed above their thermodynamic limit have been observed. It is possible to access these pathways, which would otherwise be closed, if the ozone is internally excited; the access is illustrated as the hot band absorption in Figure 1-4. The addition of one quantum of the asymmetric stretch (1042 cm^{-1}) in ozone is sufficient to push the wavelength threshold of Path 1-A from 310.3 nm to 320.7 nm.

The change in the threshold has been seen in the temperature dependence of the quantum yield in this wavelength region[50,51,52] (decreasing the temperature reduces the population in the excited state and this causes the overall quantum yield to fall) and in measurements of the velocities of the fragments.[48, 55]

1.6 Quantum yields

The probability that any particular product is formed from an initial set of conditions is known as the quantum yield; and this information is essential if an overall rate of formation for that product is to be evaluated. A given quantum yield may account for only a single reaction pathway or as a sum over a number of them. For $O(^1D)$ in the Huggins band, it is the latter measure that is commonly given as there are three pathways active, all of which behave differently with the initial conditions.

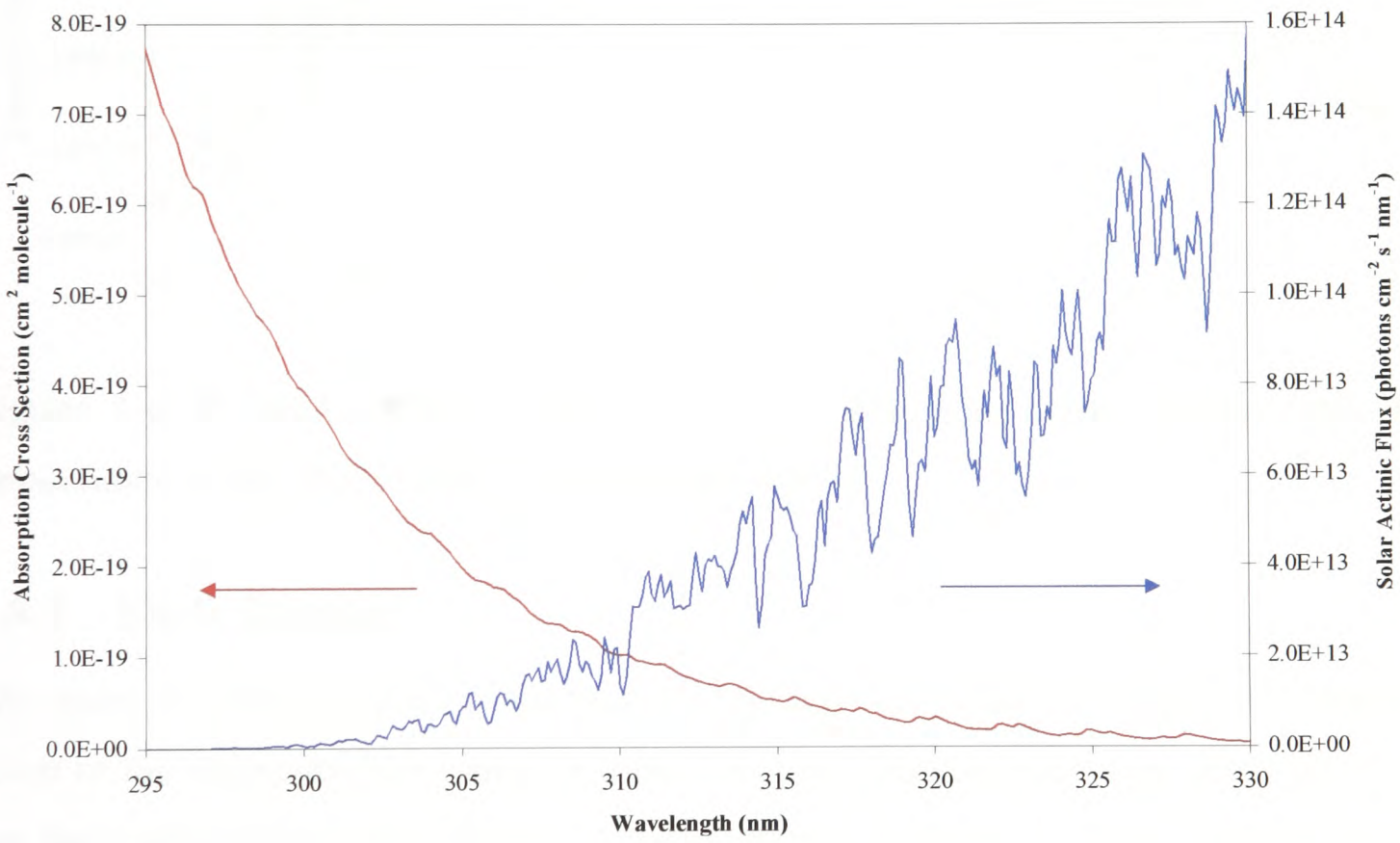

Figure 1-5 Wavelength dependence of the absorption cross section of ozone compared with the changing solar actinic flux. The solar flux was calculated using the STAR model[56] for typical mid summer conditions near Oxford. The absorption cross section is that of Malicet *et al.*[12] at 295 K.

The production of $O(^1D)$ has great significance to the oxidation processes in the atmosphere and, as a result, much effort has been spent in trying to determine an accurate value for its quantum yield. As it is in the Huggins band wavelength region that significant levels of UV radiation penetrate into the troposphere, it is within this wavelength region that much effort has

been expended. The potential of this region to change the production rates can be seen from Figure 1-5 which shows that, whilst the ozone absorption cross section is falling, the actinic flux that penetrates into the troposphere is starting to rise rapidly. The product of these two curves, which can be seen in Figure 1-6, shows the importance of each wavelength in this band.

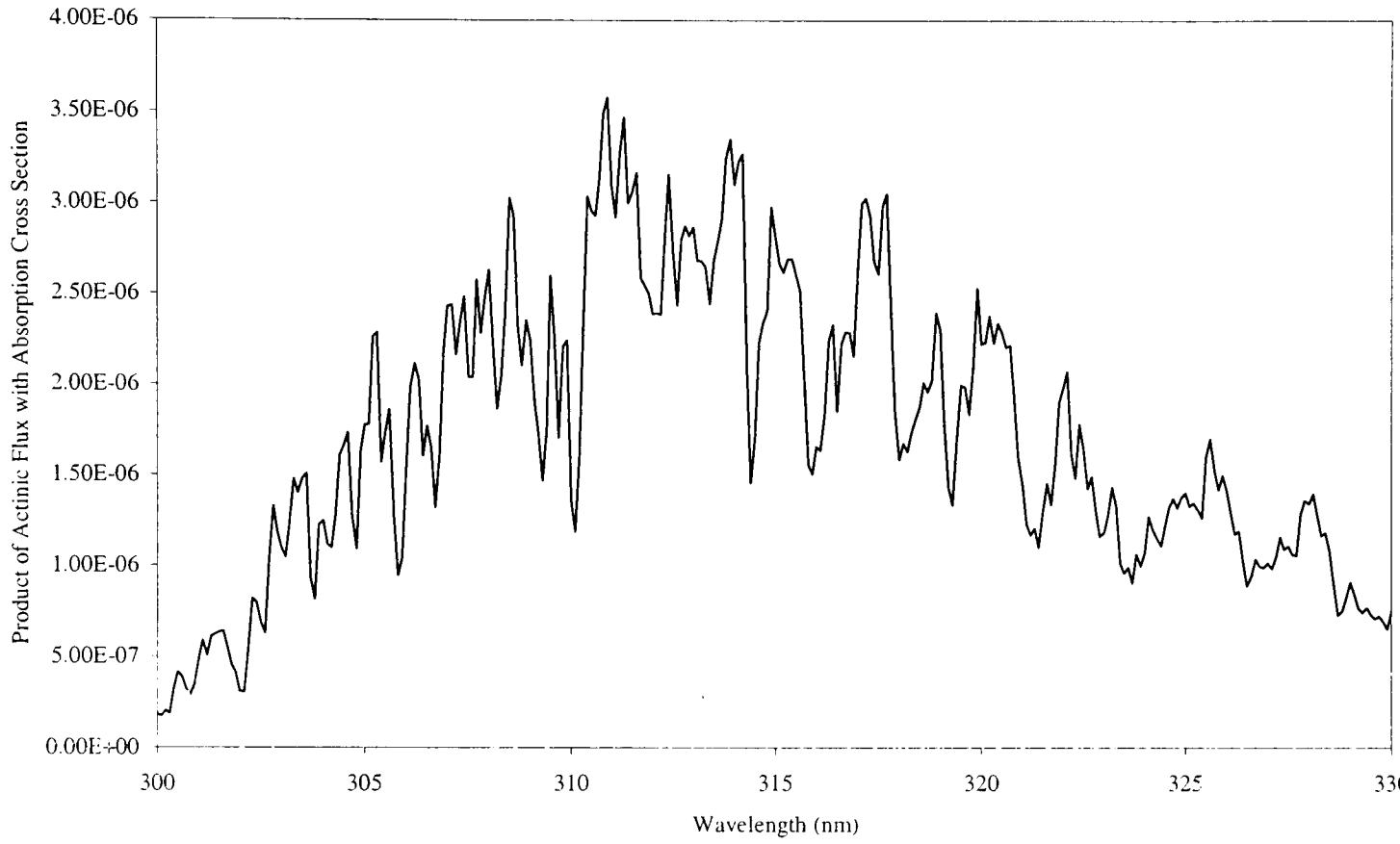

Figure 1-6 Product of the actinic flux and absorption cross section showing the importance of the 310 to 330 nm wavelength region.

1.6.1 Early Results

The quantum yield data prior to the start of this thesis can be seen in Figure 1-7. Initially, as a result of the thermodynamic limit of Path 1-A, few measurements were made above 310 nm but these did indicate that $O(^1D)$ was being produced above its thermodynamic limit.[57,58,59] However, despite this evidence, the yields above the limit were ascribed to experimental errors by Lin and DeMore[59] and the evidence was ignored.

It was probably the work of Moortgat *et al.*[60,61,62] that acted as the impetus to reinvestigate the quantum yield. The impetus was because they observed a definite yield above the thermodynamic limit; and that the yield was temperature dependent, falling as the temperature was reduced. It was unfortunate for Philen *et al.*[63] that their results suffered from a 2 nm calibration error on the measured wavelength; for if this had been recognised their data would have supported those of Moortgat. The data of Moorgat *et al.*[60] also showed that the production

of O(^{1}D) continued to much higher wavelengths than had been expected, up to and in excess of 320 nm; a figure that was shortly afterwards supported by the work of Brock and Watson.[64]

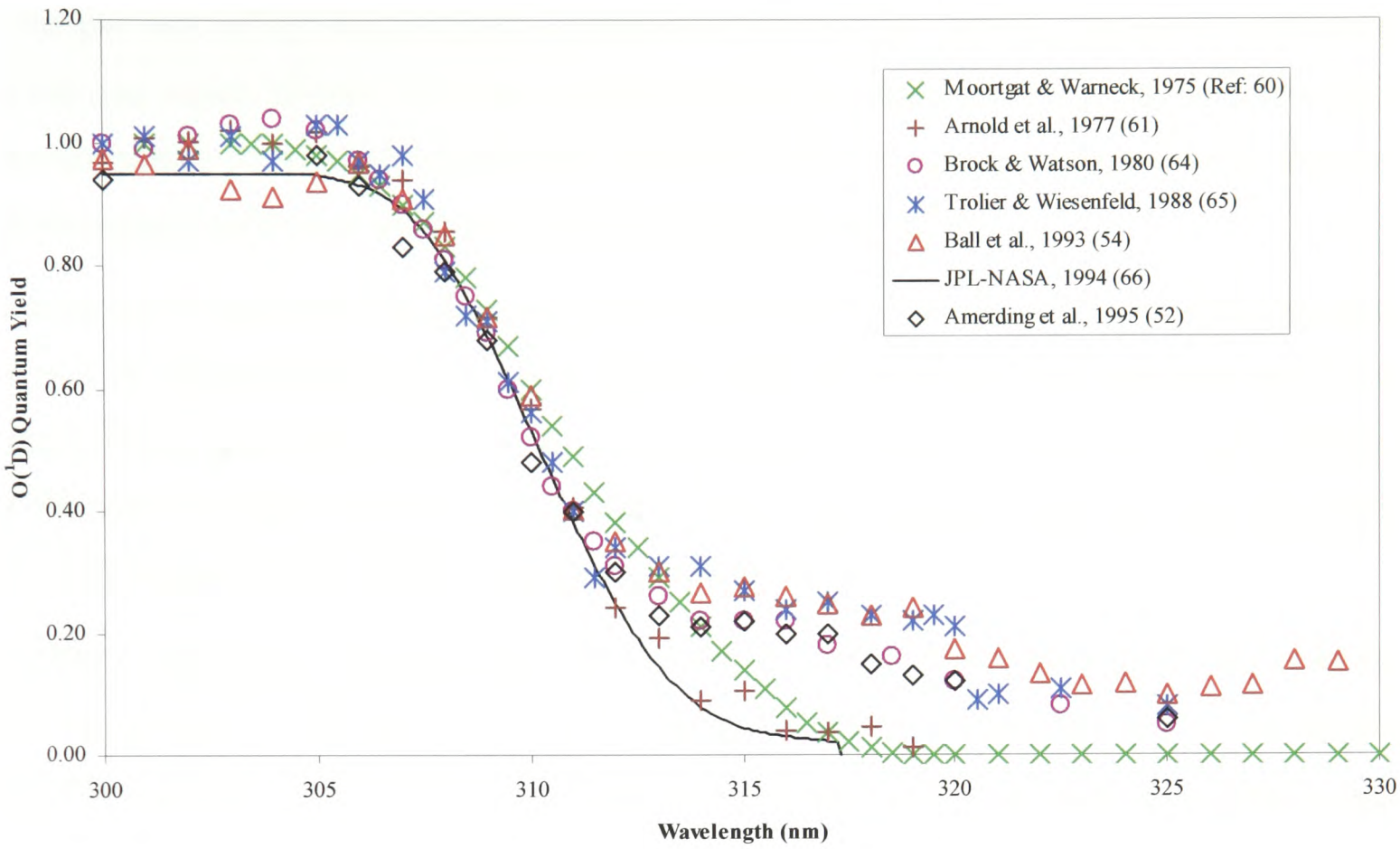

Figure 1-7 Early measurements of the O(^{1}D) quantum yield in the Huggins band.

Two explanations for the formation of O(^{1}D) above 310 nm were proposed. Moortgat attributed the O(^{1}D) production to dissociation of rotationally excited ozone, whilst Brock and Watson raised the possibility of the spin-forbidden Path 1-B. Absorption by vibrationally excited ozone, in the bending mode, was proposed as a further possible explanation for the origin of the O(^{1}D) above the thermodynamic limit by Alder-Golden *et al.*[45] Despite still more evidence that a long wavelength tail existed from Trolier and Wiesenfeld[65] and Ball *et al.*,[54] the recommended values from NASA,[66]which had been updated in 1994, refused to accept that production of O(^{1}D) was possible above 317 nm stating that

"An exception is that the "tail" sometimes seen in the laser experiments at longer wavelengths has been eliminated, on the grounds that it is not reproduced in the monochromator experiments and may be an artefact."

though they did accept that further work was needed to clarify the issue. Michelsen *et al.*[67] then produced a model that utilised the stretching vibrational modes and which fitted the observed data, including the temperature dependence with greater accuracy. This model also accounted for some of the production observed to occur above 320 nm.

Although a temperature dependence was reported by Moortgat *et al.*[60], the first clear indication that there was a major effect at wavelengths around 315 nm to 320 nm came from measurements on the $O_2(a^1\Delta_g)$ fragment by Ball *et al.*[68] Here it was shown that a reduction in the temperature of the ozone caused minimal effect on the $O_2(a^1\Delta_g)$ quantum yield below 305 nm and above 320 nm, but that a marked reduction was seen in the intermediate region. The possibilities of both the vibrationally mediated Path 1-A and the spin-forbidden Path 1-D were discussed, with clear implications for the formation of $O(^1D)$.

The final set of data that was produced prior to the start of the research reported in this thesis was that of Armerding *et al.*,[69] which agreed with the previous data obtained using laser methods. They considered that their data supported the model of Michelsen *et al.* and stated that the spin-forbidden process was unlikely, which was because they had very low yields above 325 nm and did not observe any production at 355 nm.

A problem that many of the early data sets had was the choice of reference point. The reference point was needed as the data was gathered in a quantitative manner but not on an absolute scale. The quantum yield at any wavelength (Φ_λ) was measured relative to the reference point and the quantum yield at the reference point (Φ_{ref}) was then used to transfer the relative measurements onto an absolute scale. Many of the early studies took as their reference point a value of $\Phi_{ref} = 1$ at 302.5 nm. Recent absolute measurements have fixed $\Phi_{308} = 0.78 \pm 0.02$ which if applied to the older data would require the value at 302.5 nm to be between 0.9 and 0.95. It is therefore clear that the older data need to be renormalised to a correct reference value if they are to be used.

1.6.2 Recent data

During the course of this research there have been five further studies on the quantum yield of $O(^1D)$ reported and two changes to the NASA recommendations; these are as shown in Figure 1-8.

Immediately prior to the start of the research reported here, Takahashi *et al.*[70] produced an untabulated quantum yield for $O(^1D)$. The quantum yield was obtained by monitoring the atomic $O(^1D)$ and $O(^3P)$ fragments using vacuum ultraviolet laser induced fluorescence (LIF). If the assumption is made that absorption of a photon always leads to dissociation, then the addition of appropriately weighted $O(^1D)$ and $O(^3P)$ measurements should result in a spectrum that matches the absorption cross section. Having made a suitable match to the cross section, it

is possible to extract the probability of formation for each of the fragments. These data were generated at the highest wavelength resolution yet to be presented, with a step size of 0.02 nm. They clearly showed that $O(^1D)$ was produced up to 326 nm, and that there were three regions separated by distinct falls in the quantum yield. The regions were < 308 nm, 312 nm to 319 nm and above 320 nm with the gaps between the ranges being where the yield fell from the value at the shorter wavelength to that at the higher.

The first tabulated data set, that of Silvente *et al.*[71] determined the quantum yield by reacting the $O(^1D)$ produced in the photolysis step with H_2 to form OH and then measuring this by laser induced fluorescence (LIF). Although they detected $O(^1D)$ up at 336 nm, which further acted to confirm the belief that there was a long wavelength tail and that the spin-forbidden path must be operating, their measurements below 310 nm contained a lot of noise. The authors of this data set have now accepted that there were significant errors in these data.

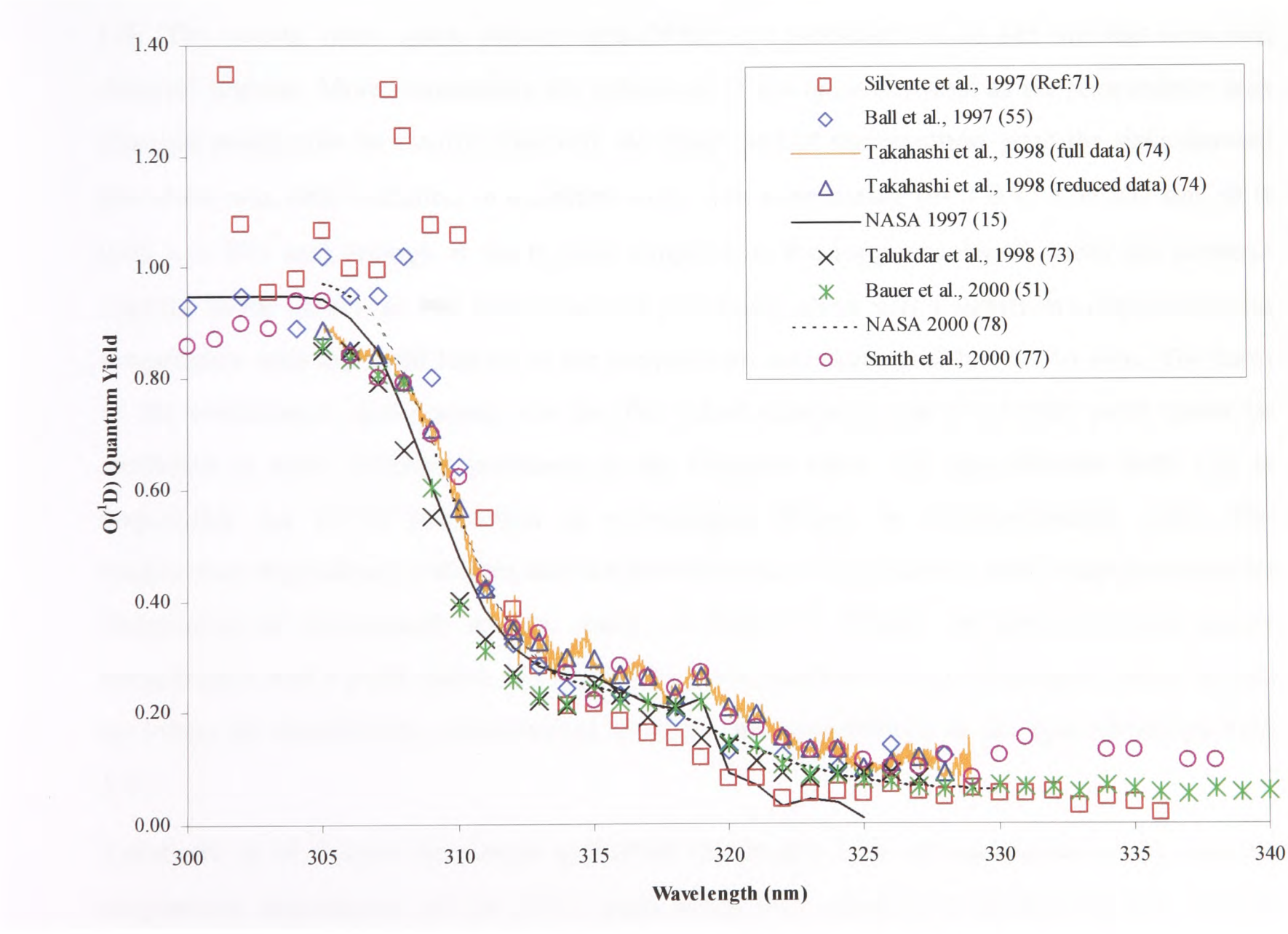

Figure 1-8 Recent measurements and recommendations for the $O(^1D)$ quantum yield.

In the following issue of Chemical Physics Letters, Ball *et al.*[49] presented tabulated data that had been obtained by direct detection of the $O(^1D)$ *via* resonance enhanced multi photon ionisation (REMPI). The data showed the existence of the long wavelength tail but due to the coarse wavelength resolution only the fall between 308 nm and 312 nm can be resolved; the second fall off around 320 nm can not be seen amongst the general decline in the $O(^1D)$ quantum yield. It was this work that formed the basis for the results reported by Pinot[72] and the REMPI detection method that was employed is the same as was used in obtaining the data presented in Chapter 3 of this thesis.

Talukdar *et al.*[73] provided the first set of data that investigated the temperature dependence of the $O(^1D)$ quantum yield using modern techniques. The data were obtained using two methods, an absolute method in which the $O(^1D)$ was quantitatively converted to $O(^3P)$ and then measured by resonance fluorescence (see Talukdar *et al.*[50] for details) and a relative method in which the $O(^1D)$ formed reacted with either H_2 or H_2O to form OH, which was then detected by LIF. The results, once again, showed that $O(^1D)$ was produced above 325 nm and with two drop off regions. More importantly the behaviour of the quantum yield as the temperature was changed could now be clearly observed. At either end of the quantum yield the data showed that there was little variation in quantum yield with temperature ($\Phi \approx 0.95$ $\lambda < 307$ nm, $\Phi \approx 0.08$ $\lambda > 323$ nm), though at the highest temperature the long wavelength yield did increase slightly. In the centre, as had been observed previously, there was a significant dependence on temperature with the yield falling as the temperature was decreased, but not to zero. The form of the temperature dependence was the first clear statement that the $O(^1D)$ yield could be attributed to three different processes in the Huggins band. The spin-allowed Path 1-A is responsible for $O(^1D)$ production at wavelengths below the thermodynamic limit. The temperature dependence indicates that the second region was at least in part being generated by dissociation of vibrationally excited ozone *via* Path 1-A. Finally the non zero yield at low temperatures and a yield above 325 nm (when even ozone with two vibrational quanta should no longer be significantly contributing) indicates the contribution of the spin-forbidden Path 1-B.

Takahashi *et al.*[74] soon afterwards published the results of a comprehensive study into the temperature dependence of the $O(^1D)$ yield using their method of monitoring both atomic fragments. In addition to showing a similar set of results to Talukdar *et al.*,[73] though the actual values tended to be slightly greater, other additional interesting data were presented, mostly as a result of the increased resolution employed. First, was that the yield in the second region,

between 312 nm and 320 nm, appeared to have structure and that this structure anti-correlated with the absorption cross section. The anti-correlation could be seen to result from the vibrational channel, for as the temperature was decreased the scale of the structure decreased. Second, and partly related to the first, was that the production of $O(^1D)$ was found to correlate very strongly with the cross section at long wavelengths, resulting in an approximately constant quantum yield. The enhancement of the signal on features of the cross section was confirmed by high resolution Doppler profiles that were taken on and off peaks in the absorption cross section. The profiles showed that on a peak in the cross section the production of fast $O(^1D)$ fragments (fast, as the extra energy available from dissociation *via* the spin-forbidden path is partitioned into the kinetic energy of the fragments) is greater than off the peaks. The correlation of the total $O(^1D)$ and $O(^3P)$ products to the cross section has implications for the model of the photodissociation process as it suggests that they both originate from the same upper state. The upper state then couples with a dissociative potential which primarily leads to the production of the triplet products, with other spin-forbidden paths occurring as inter system crossings between the repulsive state and the relevant triplet surface.

Bauer *et al.*[51] examined the $O(^1D)$ production up to higher wavelengths than any previous study examining up to 375 nm at 295 K and 340 nm at 273 K. The experiment used the reaction of $O(^1D)$ with either H_2 or CH_4 to form OH which was then probed by LIF. The data are generally in good agreement with others where they overlap, although the first fall off point does appear to occur at slightly shorter wavelengths than the majority of other studies (by *ca.* 1.5 nm). Outside of this range and continuing up to 350 nm they record a constant and temperature independent quantum yield of *ca.* 0.06. Above 350 nm the yield depends on the cross section data that is used. They find that if they use the data of Brion *et al.*[75] the quantum yield appears to increase again, whilst if they use the data of Voigt *et al.*[76] the quantum yield continues at *ca.* 0.06 until 375 nm.

As this thesis was being finalised, Smith *et al.*[77] reported quantum yields between 295 nm and 338 nm at room temperature and at spot wavelengths at a number of temperatures. As opposed to the rest of the recent measurements no lasers were used in the experiments. The photolysis of ozone was achieved by selecting the desired wavelength with a monochromator from a white light source (Xe arc lamp). The $O(^1D)$ produced was detected by chemical ionisation mass spectrometry, the $O(^1D)$ reacting with N_2O and the NO product of this then reacted with O_3^- to form NO_3^- which was detected *via* a quadrupole mass spectrometer. Their results are broadly in line with the other recent measurements, being towards the high end of the previous

range. The main discrepancy is the estimation of the spin-forbidden channel, a yield of *ca.* 0.12 is found compared to the previous estimates of 0.06 to 0.08.

Finally NASA have updated their recommendation for the $O(^1D)$ quantum yield twice. The first update in 1997[15] was based on the model proposed by Michelsen *et al.*[67] Although it modelled the 310 nm to 320 nm region with much better results, this model still failed to account for the component of the long wavelength tail that resulted from the spin-forbidden channel. The existence of the spin-forbidden channel has recently been accepted by the NASA panel and the latest recommendation[78] fits the observations much better than the previous recommendations.

1.6.3 Modelling implications

The main reason that accurate figures for the $O(^1D)$ quantum yield are necessary is that it is a fundamental input to many atmospheric models. Any model attempting to predict the chemical processes in the atmosphere needs to know the rate of production of the main oxidants and these are directly linked to the production of $O(^1D)$ from the photolysis of ozone. To be able to specify this rate of production the model requires data on four major factors relating to: the actinic flux, the physical conditions of the ozone, the absorption cross section and the quantum yield for $O(^1D)$ production.

The actinic flux can either be a measured set of data or determined within the model itself, in which case knowledge of the time, date and location are required. One of the main reasons for these requirements is that the solar zenith angle needs to be calculated, this not only affects the photon density (the area on the Earth's surface that a unit area of exoatmospheric photons impacts on is given by $\sec\theta$ where θ is the angle between the suns rays and the normal to the surface), but also the spectrum of the light that reaches the surface as a result of an increased path length through the atmosphere (which requires an accurate knowledge of the altitude concentration profiles of all species that absorb in the wavelength region of interest). If the actinic flux is being modelled, then this is often one of the most complex elements of the full model. There are a number of models that can be used to determine the actinic flux including the TUV model of the National Centre for Atmospheric Research Boulder Co., STAR of the Meteorological Institute University of Munich (used to generate the figures earlier in this Chapter) and JHU/APL of Juelich. The International Photolysis Frequency Measurement and Model Intercomparison (IPMMI) campaign has aimed to compare the models against a common set of measurements taken using the flux measuring apparatus of several of the groups (IPMMI); the results of the IPMMI study have yet to be published. One set of the major

data used in the actinic models is the set of absorption cross sections of the constituents of the atmosphere. As detailed in Section 1.5.2, the absorption cross section for ozone has been measured by a number of groups and it is a matter of choice which of the data sets is used.

The physical conditions of the ozone are required to determine the concentration of the ozone and specify which data sets are to be used in other factors, e.g. the cross section and quantum yield, which are known to depend on the temperature of the ozone. This is an active area of field research with many methods, in situ and remote, being used to measure conditions and concentrations for many atmospheric species.

Finally, the quantum yield must be known. The effect that using an incorrect quantum yield has on the modelled production of $O(^1D)$ can be very significant, as was described by Ravishankara *et al.*[8] As an example of the error that can result from the use of an incorrect quantum yield, the data in Figure 1-6 were multiplied by the quantum yields as specified by NASA in 1994[66] and 2000[78] to obtain a figure that represents the $O(^1D)$ production at each wavelength. The result of this calculation is shown in Figure 1-9. It is immediately apparent that the modelled $O(^1D)$ production is significantly less when the NASA 1994 data was used compared to the NASA 2000 data, as a result of the long wavelength tail that exists in the NASA 2000 data. If the area under each of the graphs is integrated it turns out that the rate of production as determined by the NASA 1994 data is only 75% of that predicted by NASA 2000.

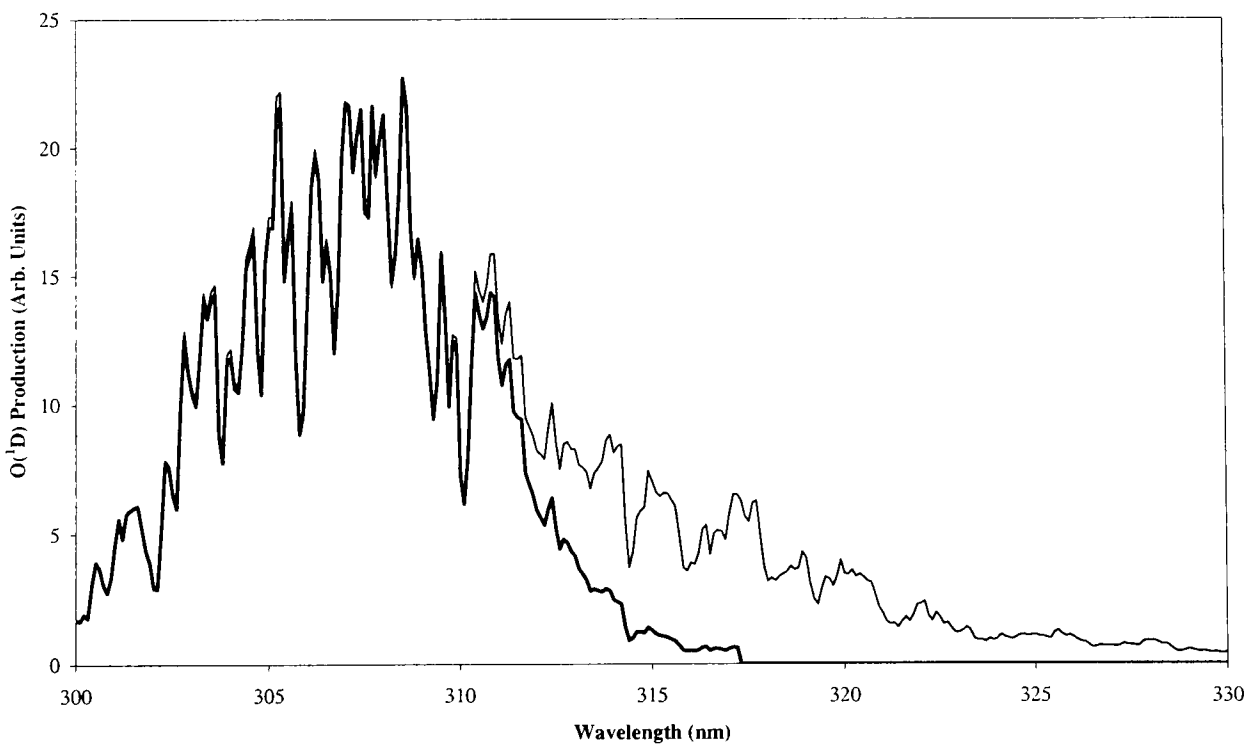

Figure 1-9 Production of $O(^1D)$ by wavelength for Oxford in the mid summer. The bold line uses the quantum yield from NASA 1994 and the thin line from NASA 2000.

If a more extreme solar zenith angle is employed in the calculations the discrepancy becomes more pronounced, as at higher angles the actinic flux is shifted more to the red, thereby increasing the influence of the tail in the quantum yield. Figure 1-10 shows the production curves based on a zenith angle of 70°.

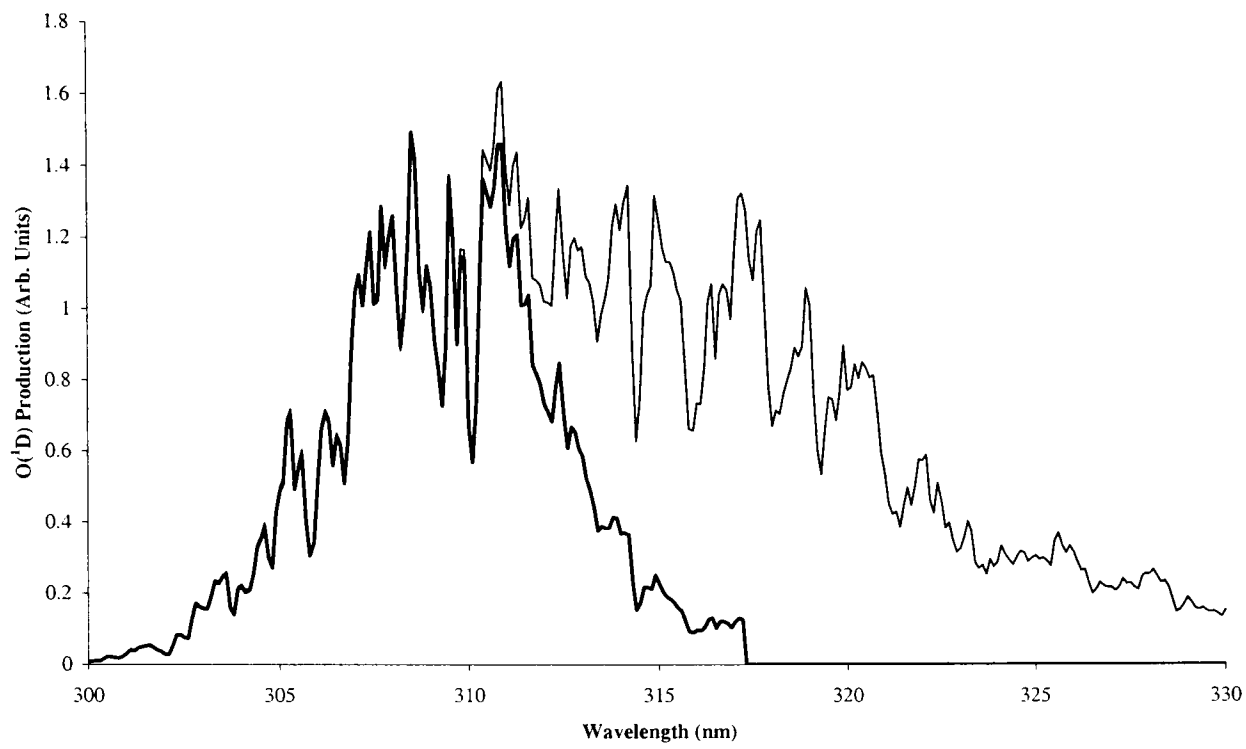

Figure 1-10 Production of O(^{1}D) by wavelength for a solar zenith angle of 70°.

In this case it is clear that the production of O(^{1}D) above 310 nm according to NASA 2000 results in a much greater total production rate; if the integrals are considered the NASA 1994 data is shown to be less than 50% of that predicted by the NASA 2000 quantum yield. Hofzumahaus and Hancock,[79] Talukdar *et al.*[73] and Blindauer *et al.*[80] have carried out more detailed studies and have determined that quantum yields that do not take into account long wavelength production of O(^{1}D), particularly for high solar zenith angles, can underestimate the O(^{1}D) production by up to a factor of five.

The need to improve the accuracy of the O(^{1}D) quantum yield has been shown in comparisons between the photolysis frequencies measured in the atmosphere and those modelled. Müller *et al.*[81] and Shetter *et al.*[82] observed that their measurements on the O(^{1}D) production rate exceeded their predictions using early NASA quantum yields. Both groups found that significant improvements were made when quantum yields that included a long wavelength tail were incorporated into their models; Shetter *et al.*[82] going on to establish a quantum yield by deconvoluting the measured actinic flux and a cross section from his measured production rates.

Finally, the need for a common, and accurate, quantum yield to enable the easy comparison between different models, can be shown by a quick survey of a number of modelling papers published during the last two years. This showed that in the sample taken (15 papers) four different sets of quantum yield data were used; NASA 1994[66] (2), NASA 1997[15] (4), Shetter *et al.*[82] (5) and Talukdar *et al.*[73] (4), and one model whilst claiming to be using a data set that included the spin-forbidden channel was using the model from Michelsen *et al.*[67]. As a result of this need, a group, consisting of the researchers working on the measurement of the $O(^1D)$ quantum yield, has been formed and has determined an agreed quantum yield (which is wavelength and temperature dependent). The agreed statement is due to be published soon.

1.7 Dissociation dynamics

Whilst quantum yield data can provide evidence that a pathway might be active, for example through production above a thermodynamic limit or a strong temperature dependence, it cannot determine which pathway caused the fragment to be formed. The inability to determine the pathway is because most systems used in quantum yield measurements detect only the existence of a particular fragment or reaction product and not its full energetics. Information on the kinetic energy of the fragments can lead to establishment of the path as the threshold energy (D_0(AB-C), where AB and C can be electronically excited) can be determined from the following energy balance (for a parent triatomic with no internal energy):

$$h\nu = D_0(AB\text{-}C) + E_{internal}(AB) + KE_{AB} + KE_C \qquad \textbf{(1-18)}$$

The internal energy of the fragment AB can be rotational or vibrational and can therefore lead to a wide range of values for the kinetic energies. It must be noted that the kinetic energies of the two fragments are not independent as the momentum of the parent molecule must be conserved. If information on the angular distribution of the fragments can be obtained then this can provide insights into the transition that occurred, including the lifetime of the molecule between photon absorption and dissociation. To gain the data needed for either of these analyses, fragments must be probed in a state selective manner; the following methods are some of those commonly used to probe and then detect the specific fragments. Butler and Neumark provide a useful, if slightly out of date*, review of the main methods.[83]

---

* Mostly due to advances in ion imaging techniques over the past four years.

It is possible for an atom or molecule to absorb more than one photon simultaneously though the probability is very small. This process can be enhanced significantly if the total energy of the photons is equal to the energy between two states. This requirement for enhancement causes state selectivity in the atoms or molecules that will absorb. As photon densities need to be high for this process to occur with any real efficiency, the system could absorb further photons, particularly if the energy of this second absorption step causes the system to ionise. This process of exciting a resonant intermediate state, and then ionising from the intermediate, is known as resonance enhanced multi photon ionisation (REMPI) and will be discussed in greater depth in Section 4.1. As the ions and electrons formed in the ionisation process are charged, extraction from the ionisation source and then detection can be comparatively easily achieved. Initially it was only possible to obtain either the speed distribution or the internal energy of the fragments, but since 1985 there have been many advances both in the theory, and instruments, available so that complex information can now be obtained. The two main methods of detection extract the same information, but in different ways.

The method used in this thesis is to monitor the ion signal in time, referred to as REMPI-TOF. After the work of Zare[84] determined that the angular distribution of photofragments could be characterised by a single parameter β, it took many years before the state selectivity required in detection became available. Mons and Dimicoli[85] showed how it was possible to extract significant quantities of information from data taken in this manner and the theory of the process has been extended further by the work of Simpson *et al.*[86] and Rakitzis and Zare.[87] Cl_2 is an example of a molecule whose photodissociation has been extensively studied using this method by a number of authors.[88,86,89,90] Some other molecules that have been examined using this technique include ozone (both O_2[53,55,91] and O[47,48,92] fragments probed), OClO (both ClO and O fragments probed),[93] NO_2 (O probed),[94] CH_2BrCl (Br probed)[95] and CF_2I_2 (I probed).[96]

Closely related to the REMPI-TOF method is the ion imaging technique, originally carried out by Chandler and Houston.[97] This approach has the significant benefit, over the time recording method, of enabling velocity and alignment information to be extracted from a single experiment; whereas the latter method requires at least two experimental geometries to be used. In recent years great improvements in CCD technology coupled with other enhancements such as those of Eppink and Parker[98] and Chang *et al.*[99] have enabled images to be obtained with much improved spatial resolution enabling high quality data to be obtained in comparatively short periods of time. In addition to work on Cl_2[100,101] that has been carried out significant work has been carried out on N_2O,[102,103,104] NO_2[105] and O_3.[106,107,108]

A further alternative detection scheme, employed when multiple fragments are formed, uses the photoelectron-photoion-photoion coincidence model (PEPIPICO) which, unlike the previous methods, detects both the electrons and the ions that are formed. The electrons can be measured in either of the two ways described previously and the ions are usually detected using a position sensitive technique, see Lavollée[109] and Takahashi *et al.*[110] for examples.

A very similar method to REMPI is Rydberg TOF in which the chosen fragment is raised to a very high Rydberg state ($n \approx 100$) and then ionised with a weak electric field. This method is known as mass analysed threshold ionisation (MATI). The resulting ions can then be detected *via* imaging techniques or total signal methods (when spectra are recorded it is not necessary to get the full information from the ions but only the number that were produced).

A different approach that can be employed is laser induced fluorescence (LIF). In this method a photon is absorbed by the fragment to produce an excited level from which it can decay by fluorescence. It is the fluorescence signal that is then detected and used to determine the overall signal. If the bandwidth of the probe laser is narrow, with respect to the Doppler line width, then the probe wavelength can be scanned over the wavelength of the transition. The probe laser can then selectively detect fragments that are moving towards, or away from, the laser as these fragments have the frequency of the LIF transition Doppler shifted. The result is a Doppler profile which can be deconvoluted to give the speed distribution along the laser's propagation axis (whereas experiments using only the time of flight detect the speed distribution parallel to the time-of-flight axis, which is usually perpendicular to the laser's propagation axis). The speed distribution can be used for the same purposes as the time profiles gained *via* TOF mass spectrometry, i.e. kinetics of the dissociation processes and anisotropies. Takahashi *et al.* have used this method extensively on ozone dissociation investigating $O(^1D)$ and $O(^3P)$ speed[46,74,111] and angular[111] distributions; investigating the rotational profile of spectral lines[40] to gain information on the transition and determining PHOFEX spectra (a photofragment excitation spectrum is effectively a spectrum of production for a particular fragment).[74,108] Other examples of uses of LIF can be found in the review by Butler and Neumark.[83] If the LIF probe laser is scanned over the Doppler profile or its bandwidth is larger than that of the Doppler shift then the method can also be used as a measure of the total fragment signal. LIF can be carried out directly on the fragment or on a species that is formed after the fragment has reacted. For ozone it is common to detect OH formed from the reaction of $O(^1D)$ with a hydrogen containing molecule e.g. H_2O, H_2 or CH_4.

1.8 Spectroscopy

In order that a technique such as REMPI can be utilised it is necessary to know where the transitions occur. For atomic species this takes the form of several sharp and well defined lines corresponding to the resonant intermediate state, unless autoionisation acts as a competing process to the absorption of the ionising photons when the lines can broaden. For molecular species the situation tends to be much more complex; the final molecular electronic energy level will have energy shifts from the base electronic energy level resulting from rotational and vibrational excitation; additionally the intermediate state may be able to predissociate. Furthermore, if perturbations exist in the energy levels as a result of coupling between Rydberg and valence energy levels, the spectra can become extremely difficult to assign. Previous attempts[72,112] to assign the REMPI bands of $O_2(a^1\Delta_g)$ between 310 nm and 335 nm have been only partially successful, as a result of the perturbations between various energy levels, and only recently has a detailed assignment of the bands been completed.[113] The approaches taken to try and extract information on the REMPI transition from the kinetics of the probed photofragments are discussed in Chapter 5.

1.9 Current Work

The main aim of the work presented in this thesis was to establish the values for the $O(^1D)$ quantum yield in the Huggins band at multiple temperatures, and to carry this out using a method that directly probed the $O(^1D)$ produced. Also, time-of-flight investigations on the dynamics of the dissociation were to be made to determine the pathways in operation.

The results have shown that $O(^1D)$ is produced *via* a spin-forbidden path when ozone was photolysed above 310 nm and that photolysis of hot band ozone could enhance the rate of production of ozone between 310 nm and 320 nm. Additional measurements on the $O(^1D)$ fragment have shown that the choice of REMPI transition can have a significant impact on any measurements made of the $O(^1D)$ photodissociation parameters. Investigations on the $O_2(a^1\Delta_g)$ fragment have shown evidence for angular momentum polarisation and a detectivity function that depends on the REMPI transition being employed. The latter has been shown to help in the determination of the spectroscopy of the REMPI transition.

References:

1 R.P. Wayne, *Chemistry of Atmospheres*, Oxford University Press, Oxford UK (2000).

2 G.P. Brasseur, J.J. Orlando and G.S. Tyndall, *Atmospheric Chemistry and Global Change*, Oxford University Press, New York USA (1999).

3 S. Chapman, *Mem. Roy. Meteorol. Soc.*, **3** (1930) 103.

4 D.R. Bates and M. Nicolet, *J. Geophys. Res.*, **55** (1950) 301.

5 M.J. Molina and F.S. Rowland, *Nature*, **249** (1974) 810.

6 Many examples can be found in the journal *Photochemistry & Photobiology* of discussions of the effects of UV radiation.

7 J. Lelieveld and F.J. Dentener, *J. Geophys. Res.*,**105** (2000) 3531.

8 A.R. Ravishankara, G. Hancock, M. Kawasaki and Y. Matsumi, *Science*, **280** (1998) 60.

9 A. Banichevich, S.D. Peyerimhoff and F. Grein, *Chem. Phys.*, **178** (1993) 155.

10 R. Bacis, A.J. Bouvier, and J.M. Flaud, *Spectrochimica Acta Part A*, **54** (1998) 17.

11 M. Braunstein and R.T Pack, *J. Chem. Phys.*, **96** (1992) 6378.

12 J. Malicet, D. Daumont, J. Charbonnier, C. Parisse, A. Chakir and J. Brion, *J. Atmos. Chem.*, **21** (1995) 263.

13 J.I. Steinfeld, S.M. Alder-Golden, J.W. Gallagher, *J. Phys. Chem.* , **16** (1987) 911.

14 R.P. Wayne, *Handbook of Environmental Chemistry Vol.2 Part E - Reactions and Processes*, O. Hutzinger (ed.), Springer Verlag, Berlin (1989) 1.

15 W.B. DeMore, S.P. Sander, D.M. Golden, R.F. Hampson, M.J. Kurlo, C.J. Howard, A.R. Ravishankara, C.E. Kolb and M.J. Molina, *Chemical Kinetics and Photochemical Data for Use in Stratospheric Modeling Evaluation Number 12*, JPL 97-4, NASA Jet Propulsion Laboratory Publication (1997).

16 P.J. Hay, R.T Pack, R.B. Walker and E.J. Heller, *J. Phys. Chem.*, **86** (1982) 862.

17 J.W. Simons, R.J. Paur, H.A. Webster and E.J. Bair, J. Chem. Phys., **59** (1973) 1203.

18 B.R. Johnson, C. Kittrell, P.B. Kelly and J.L. Kinsey, *J. Phys. Chem.*, **100** (1996) 7743.

19 R. Ogorzalek Loo, W.J. Marinelli, P.L. Houston, S. Arepalli, J.R. Weisenfeld and R.W. Field, *J. Chem. Phys.*, **91** (1989) 5185.

20 A.G. Suits, R.L. Miller, L.S. Bontuyan and P.L. Houston, *J. Chem. Soc. Faraday Trans.*, **89** (1993) 1443.

21 C.E. Fairchild, E.J. Stone and G.M. Lawrence, *J. Chem. Phys.*, **69** (1978) 3632.

22 S.M. Shamsuddin, Y. Inagaki, Y. Matsumi and M. Kawasaki, *Can. J. Chem.*, **72** (1994) 637.

23 R.J. Wilson, J.A. Mueller and P.L. Houston, *J. Phys. Chem. A*, **101** (1997) 7593.

24 J.A. Syage, *J. Phys. Chem.*, **99** (1995) 16530.

25 J.J. Valentini, *Chem. Phys. Lett.*, **96** (1983) 395.

26 D. Lauvergnat and D.C. Clary, *J. Chem. Phys.*, **108** (1998) 3566.

27 R. Hernandez-Lamoneda, R. Toumi and D.C. Clary, *J. Chem. Phys.*, **102** (1995) 9544.

28 A.J.C. Varandas and W. Wang, *Chem. Phys.*, **2** (1997) 167.

29 R.L. Miller, A.G. Suits, P.L. Houston, R. Toumi, J.A. Mack and A.M. Wodtke, *Science*, **265** (1994) 1831.

30 T.G. Slanger, *Science*, **265** (1994) 1817.

31 C.A. Rogaski, J.M. Price, J.A. Mack and A.M. Wodtke, *Geophys. Res. Lett.*, **20** (1993) 2885.

32 R.T. Jongma and A.M. Wodtke, *J. Chem. Phys.*, **111** (1999) 10957.

33 D.H Katayama, *J. Chem. Phys.*, **71** (1979) 815.

34 A. Sinha, D. Imre, J.H. Goble and J.L. Kinsey, *J. Chem. Phys.*, **84** (1986) 6108.

[35] C. Leforestier, F. LeQuere, K. Yamashita and K. Morokuma, *J. Chem. Phys.*, **101** (1994) 3806.

[36] K.H. Thunemann, S.D. Peyerimhoff and R.J. Buenkar, *J. Mol. Spec.*, **70** (1978) 432.

[37] P.J. Hay and T.H. Dunning, *J. Chem. Phys.*, **67** (1977) 2290.

[38] A. Banichevich and S.D. Peyerimhoff, *Chem. Phys.*, **174** (1993) 93.

[39] J.A. Joens, *J. Chem. Phys.*, **101** (1994) 5431.

[40] K. Takahashi, M. Kishigami, N. Taniguchi, Y. Matsumi and M. Kawasaki, *J. Chem. Phys.*, **106** (1997) 6390.

[41] A.M. Bass and R.J. Paur, *Proc. Quadriennial Ozone Symp.* Chalkidiki Greece, eds. C. Zefros and A. Ghazi. Reidel. Dordrecht, (1984) 606p.

[42] L.T. Molina and M.J. Molina, *J. Geophys. Res.*, **91** (1986) 14501.

[43] J.P. Burrows, A. Richter, A. Dehn, B. Deters, S. Himmelmann, S. Voigt and J. Orphal, *J. Quant. Spectrosc. Radiat. Transfer*, **61** (1999) 509.

[44] I.C. McDade and W.D. McGrath, *Chem. Phys. Lett.*, **73** (1980) 413.

[45] S.M. Adler-Golden, E.L. Schweitzer and J. I. Steinfeld, *J. Chem. Phys.*, **76** (1982) 2201.

[46] K. Takahashi, M. Kishigami, Y. Matsumi, M. Kawasaki and A.J. Orr-Ewing, *J. Chem. Phys.*, **105** (1996) 5290.

[47] W. Denzer, G. Hancock, J.C. Pinot de Moira and P.L. Tyley, *Chem. Phys. Lett.*, **280** (1997) 496.

[48] W. Denzer, G. Hancock, J.C. Pinot de Moira and P.L. Tyley, *Chem. Phys.*, **231** (1998) 109.

[49] S.M. Ball, G. Hancock, S.E. Martin and J.C. Pinot de Moira, *Chem. Phys. Lett.*, **264** (1997) 531.

[50] R.K. Talukdar, M.K. Gilles, F. Battin-Leclerc and A.R. Ravishankara, *Geophys. Res. Lett.*, **24** (1997) 1091.

[51] D. Bauer, L. D'Ottone and A. Hynes, *Phys. Chem. Chem. Phys.*, **2** (2000) 1421.

[52] W. Armerding, F.J. Comes and B. Schülke, *J. Phys. Chem.*, **99** (1995) 3137.

[53] P. O'Keeffe, T. Ridley, K.P. Lawley, R.R.J. Maier and R.J. Donovan, *J. Chem. Phys.*, **110** (1999) 10803.

[54] S.M. Ball, G. Hancock, I.J. Murphy and S.P. Rayner, *Geophys. Res. Lett.*, **20** (1993) 2063.

[55] S.M. Ball, G. Hancock, J.C. Pinot de Moira, C.M. Sadowski and F. Winterbottom, *Chem. Phys. Lett.*, **245** (1995) 1.

[56] A. Ruggaber, R. Dlugi and T. Nakajima, *J. Atmos. Chem.*, **18** (1994) 171.

[57] I.T.N. Jones and R.P. Wayne, *Chem. Phys.*, **51** (1969) 3617.

[58] I.T.N. Jones and R.P. Wayne, *Proc. Royal Soc. Lond.*, **319A** (1970) 273.

[59] C.L. Lin and W.B. DeMore, *J. Photochem.*, **2** (1973/4) 161.

[60] G.K. Moortgat and P. Warneck, *Z. Naturforsch*, **30a** (1975) 835.

[61] I. Arnold, F.J. Comes and G.K. Moortgat, *Chem. Phys.*, **24** (1977) 211.

[62] G.K. Moortgat, E. Kudszus and P. Warneck, *J. Chem. Soc. Faraday Trans. II*, **73** (1977) 1216.

[63] D.L. Philen, R.T. Watson and D.D. Davis, *J. Chem. Phys.*, **67** (1977) 3316.

[64] J.C. Brock and R.T. Watson, *Chem. Phys.*, **46** (1980) 477.

[65] M. Trollier and J.R. Wiesenfeld, *J. Geophys. Res.*, **93** (1988) 7119.

[66] W.B. DeMore, S.P. Sander, D.M. Golden, R.F. Hampson, M.J. Kurlo, C.J. Howard, A.R. Ravishankara, C.E. Kolb and M.J. Molina, *Chemical Kinetics and Photochemical Data for Use in Stratospheric Modeling Evaluation Number 11*, JPL 94-26, NASA Jet Propulsion Laboratory Publication (1994).

[67] H.A. Michelsen, R.J. Salawitch, P.O. Wennberg and J.G. Anderson, *Geophys. Res. Lett.*, **21** (1994) 2227.

[68] S.M. Ball, G. Hancock and F. Winterbottom, *Faraday Discuss*, **100** (1995) 215.

[69] W. Armerding, F.J. Comes and B. Schulke, *J. Phys. Chem.*, **99** (1995) 3137.

[70] K. Takahashi, Y. Matsumi and M. Kawasaki, *J. Phys. Chem.*, **100** (1996) 4084.

[71] E. Silvente, R.C. Richter, M. Zheng, E.S. Saltzman and A.J. Hynes, *Chem. Phys. Lett.*, **264** (1997) 309.

[72] J.C. Pinot de Moira, Laser Studies of Atmospheric Chemistry, D.Phil Thesis, Oxford University, 1998.

[73] R.K. Talukdar, C.A. Longfellow, M.K. Gilles and A.R. Ravishankara, *Geophys. Res. Lett.*, **25** (1998) 143.

[74] K. Takahashi, N. Taniguchi, Y. Matsumi, M. Kawasaki and M.N.R Ashfold, *J. Chem. Phys.*, **108** (1998) 7161.

[75] J. Brion, A. Chakir, J. Charbonnier, C. Parisse and J. Malicet, *J. Atmos. Chem.*, **30** (1998) 291.

[76] S. Voigt, J. Orphal and J.P. Burrows, *Chem. Phys. Lett.*, submitted.

[77] G.D. Smith, L.T. Molina and M.J. Molina, *J. Phys. Chem. A*, **104** (2000) 8916.

[78] W.B. DeMore, R.R. Friedl, S.P. Sander, D.M. Golden, R.F. Hampson, M.J. Kurlo, R.E. Huie, G.K. Moortgat, A.R. Ravishankara, C.E. Kolb and M.J. Molina, *Chemical Kinetics and Photochemical Data for Use in Stratospheric Modeling Evaluation Number 13*, JPL 00-3, NASA Jet Propulsion Laboratory Publication (2000).

[79] A. Hofzumahaus and G. Hancock, Final Report Contract No. ENV4-CT95-0158.

[80] C. Blindauer, V. Rozanov and J.P. Burrows, *J. Atmos. Chem.*, **24** (1996) 1.

[81] M. Müller, A. Kraus and A. Hofzumahaus, *Geophys. Res. Lett.*, **22** (1995) 679.

[82] R. Shetter, C.A. Cantrell, K.O. Lantz, S.J. Flocke, J.J. Orlando, G.S.Tyndall, T.M. Gilpin, C.A.Fischer, S. Madronich, J.G. Calvert and W. Junkermann, *J. Geophys. Res.*, **101**, (1996) 14631.

[83] L.J. Butler and D.M. Neumark, *J. Phys. Chem.*, **100** (1996) 12801.

[84] R.N. Zare, *Mol. Photochem.*, **4** (1972) 1.

[85] M. Mons and I. Dimicoli, *J. Chem. Phys.*, **90** (1989) 4037

[86] W.R. Simpson, A.J. Orr-Ewing, T.P. Rakitzis, S.A. Kandel and R.N. Zare, *J. Chem. Phys.*, **103** (1995) 7299.

[87] T.P. Rakitzis and R.N. Zare, *J. Chem. Phys.*, **110** (1999) 3341.

[88] Y. Matsumi, M. Kawasaki, T. Sato, T. Kinugawa and T. Arikawa, *Chem. Phys. Lett.*, **155** (1989) 487.

[89] Y. Matsumi, K. Tonokura and M. Kawasaki, *J. Chem. Phys.*, **97** (1992) 1065.

[90] T.P. Rakitzis, S.A. Kandel, A.J. Alexander, Z.H. Kim and R.N. Zare, *J. Chem. Phys.*, **110** (1999) 3351.

[91] P. O'Keeffe, T. Ridley, S. Wang, K.P. Lawley and R.J. Donovan, *Chem. Phys. Lett.*, **298** (1998) 368.

[92] R.C. Richter and A.J. Hynes, *J. Phys. Chem.*, **100** (1996) 8061.

[93] C.J. Kreher, R.T. Carter and J.R. Huber, *J. Chem. Phys.*, **110** (1999) 3309.

[94] Chi-Hsun Hsieh, Yi-Shyuan Lee, A. Fuji, Shih-Huang Lee and K. Liu, *Chem. Phys. Lett.*, **277** (1997) 33.

[95] W.S. McGivern, R. Li, P. Zou and S.W. North, *J. Chem. Phys.*, **111** (1999) 5771.

[96] K. Bergmann, R.T. Carter, G.E. Hall and J.R. Huber, *J. Chem. Phys.*, **109** (1998) 474.

[97] D.W. Chandler and P.L. Houston, *J. Chem. Phys.*, **87** (1987) 1445.

[98] A.T.J.B. Eppink and D.H. Parker, *Rev. Sci. Inst.*, **68** (1997) 3477.

[99] Bor-Yu Chang, R.C. Hoetzlein, J.A. Mueller, J.D. Geiser and P.L. Houston, *Rev. Sci. Inst.*, **69** (1998) 1665.

[100] P.C. Samartzis, I Sakellariou, T.Gougousi and T.N. Kitsopoulos, *J. Chem. Phys.*,**107** (1997) 43.

[101] P.C. Samartzis, B.L.G. Bakker, T.P. Rakitzis, D.H. Parker and T.N. Kitsopoulos, **110** (1999) 5201.

[102] D.W. Neyer, A.J.R. Heck, D.W. Chandler, J.M. Tuele and M. Janssen, *J. Phys. Chem.*, **103** (1999) 10388.

[103] M. Ahmed, E.R. Wouters, D.S. Peterka, O.S. Vasyutinskii and A.G. Suits, *Faraday Discuss.*, **113** (1999) 425.

[104] J.M. Tuele, G.C. Groenenboom, D.W. Neyer, D.W. Chandler and M.H.M. Janssen, *Chem. Phys. Lett.*, **320** (2000) 177.

[105] M. Ahmed, D.S. Peterka, A.S. Bracker, O.S. Vasyutinskii and A.G. Suits, *J. Chem. Phys.*, **110** (1999) 4115.

[106] A.G. Suits, R.L. Miller, L.S. Bontuyan and P.L. Houston, *J. Chem. Soc. Faraday Trans.*, **89** (1993) 1443.

[107] J.A. Syage, *J. Chem. Phys.*, **105** (1996) 1007.

[108] N. Taniguchi, K. Takahashi, Y. Matsumi, S.M. Dylewski, J.D. Geiser and P.L. Houston, *J. Chem. Phys.*, **111** (1999) 6350.

[109] M. Lavollee, *Rev. Sci. Inst.*, **70** (1999) 2968.

[110] M. Takahashi, J.P. Cave and J.H.D. Eland, *Rev. Sci. Inst.*, **71** (2000) 1337.

[111] K. Takahashi, N. Taniguchi, Y. Matsumi and M. Kawasaki, *Chem. Phys.*, **231** (1998) 171.

[112] R.D. Johnson III, G.R. Long and J.W. Hudgens, *J. Chem. Phys.*, **87** (1987) 1977.

[113] B.R. Lewis, S.T. Gibson, J.S. Morrill and M.L. Ginter, *J. Chem. Phys.*, **111** (1999) 186.

Chapter 2

Experimental

2.1 Introduction

The experimental apparatus for the experiments described in this thesis was based about two laser systems and two detection systems, which could be used in any necessary combination. A typical experiment utilised the output from one of the laser systems to photolyse ozone and the second laser to probe the desired product *via* REMPI. The ionised fragments generated would then be detected by one of two systems. The first system was a glass bulb in which a pair of charged plates was used to measure the current generated by the ions formed; this system was predominantly used in determining the quantum yields as detailed in Chapter 3. The second detection system was a modified Wiley-McLaren time-of-flight mass spectrometer (TOFMS) which was used when more information on the energetics of the photolysis step was desired. Figure 2-1 gives an overview of the experimental set up.

2.2 Molecular Preparation

Two methods were used to prepare the ozone used; one involved the preparation of a significant quantity of ozone which was stored and used as required and the other produced a small, but continuous, supply of ozone which was used immediately.

The bulk quantities of ozone were produced by the following procedure. Dried molecular oxygen was passed through a 600 mA high voltage discharge in an Argentox ozonizer which converted ~2% of the oxygen to ozone. The oxygen / ozone mixture was passed through a 200 K trap, to remove any oxides of nitrogen, and then into a second 200 K trap which contained silica gel that adsorbed the ozone and a small quantity of oxygen; the remaining gas was vented from the system. The traps were held at 200 K by surrounding them with a trichloroethylene / dry-ice slush bath. After approximately one and a half hours, when sufficient ozone had been trapped, the oxygen flow was stopped, the first trap isolated and the oxygen on the second trap pumped off. After half an hour of this pumping the ozone was then allowed to desorb into a previously evacuated collection bulb by removing the slush bath, allowing the silica gel to warm up.

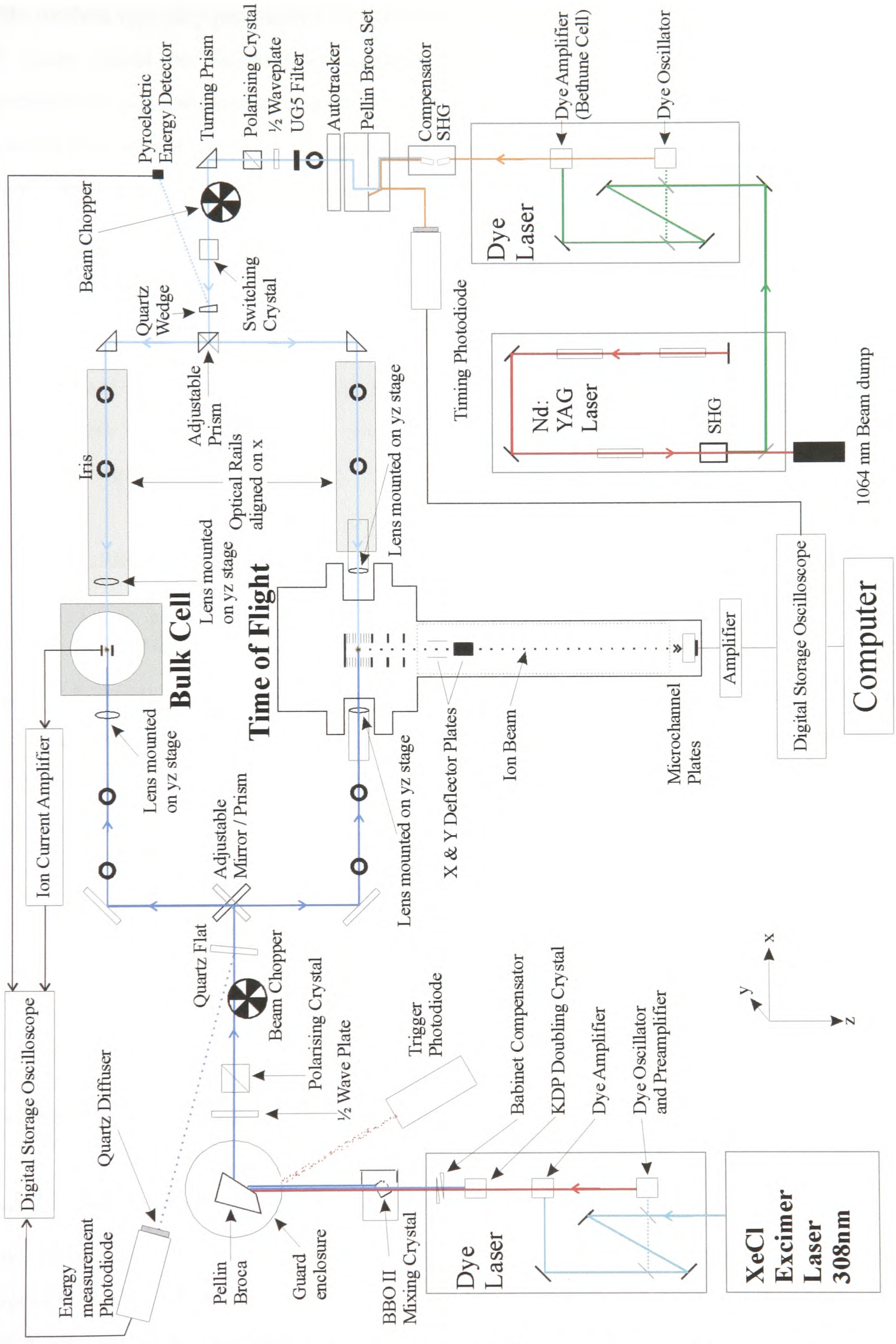

Figure 2-1 Typical experimental layout for an O(^{1}D) REMPI experiment. The adjustable mirror and prism are used to set the detection system employed.

This method typically produced 120 Torr of a 50:50 mix of ozone and oxygen; the percentage of ozone could be checked by measuring the absorption of 254 nm light in an UV spectrometer. Ozone produced in this way was stored in a glass bulb that was mounted in a wooden box, which had been designed to minimise the risks from explosion. The stored ozone would decompose to molecular oxygen with a half-life of approximately one month.

The continuous flow method generated ozone in a similar manner, a flow of oxygen was passed over an electrical discharge in a small cell. However, in this case the 2% ozone mixture was not trapped but directly passed into the experimental apparatus.

In both cases the ozone was supplied to the experimental apparatus through a system of Nylon and stainless steel tubing. Contact with any surface that could catalyse the decomposition of the ozone, e.g. copper, was avoided.

2.3 Laser Systems

2.3.1 General

Table 2-1 lists the primary important characteristics of the two pump laser systems used and a more detailed explanation of the laser systems are given in the following paragraphs. The REMPI schemes employed in the selective detection of fragments formed by photolysis are discussed in depth in Chapter 4, for $O(^1D)$, and Chapter 5, for $O_2(a^1\Delta_g)$.

Pump System	Max. Output (mJ pulse^{-1})	Output Wavelength (nm)	Repetition Rate (Hz)	Temporal Width (ns)	Bandwidth (cm^{-1})
Spectra Physics	1300, 850	1064, 532	10	8	1
Lambda Physik	105	308	10	10	0.8

Table 2-1 General specifications of the pump laser systems

2.3.2 Nd:YAG pumped dye laser

The more powerful of the two laser systems was a Nd:YAG pumped tuneable dye laser (Spectra Physics GCR 230-10 that pumped a Laser Analytical Systems (LAS) LDL2051). A Nd:YAG laser is an example of a laser in which the active medium is in the solid state. The basic operating principles of this laser are that the active medium is illuminated by a carefully chosen flashlamp, whose output has been matched to the absorption bands of the active

medium, in this case the triply ionised neodymium which has been doped into the yttrium aluminium garnet substrate. The excited population rapidly drops down to the $^4F_{3/2}$ state of neodymium in which they have a comparatively long lifetime (230μs). From this level they can radiatively decay to a lower level, the main photon wavelengths being 1338 nm, 1319 nm, 1064 nm or 946 nm. The most probable of these is the transition to $^4I_{11/2}$ state emitting at 1064 nm and this wavelength is selected for output *via* the use of wavelength specific optics. It is possible to operate a laser of this kind in a continuous manner as the $^4I_{11/2}$ state relaxes quickly to the ground $^4I_{9/2}$ state ensuring that the lower state in the laser transition does not experience any population build up. The Nd:YAG used was a Q-switched pulsed system capable of generating 1.3 J pulse^{-1} of its 1064 nm fundamental at 10 Hz. The 532 nm radiation needed to pump the dye laser was generated by frequency doubling the 1064 nm radiation in a potassium dideuterium phosphate (KD*P) to give up to 880 mJ pulse^{-1} of 532 nm radiation; the pulse length was recorded as being 8 ns full width half maximum (FWHM). It should be noted that the maximum output energy of the system was very rarely used and the system was most typically run at about half of its maximum output.

The active medium in the dye laser which enables conversion of the pump beam energy to lasing action at the desired wavelength is the dye whose properties are modified by the solvent used to dissolve it. When irradiated the dye fluoresces at a number of wavelengths as the lower state is part of a continuum resulting from the vibrational modes of the dye and strong molecular interactions between the dye and the solvent. Wavelength selection takes place with the addition of a grating within the laser cavity; the grating ensures that only wavelengths, within the fluorescence band, which are resonant with the cavity are able to lase. There are many dyes available, the choice of which in any particular application depends on the pump radiation and the output wavelength desired. Dyes are available to work from *ca.* 310 nm to over 1000 nm. Further modification of the wavelength range of a particular dye can be achieved with the choice of solvent and the exact concentrations of the dye. Dye lasers are often not very efficient as a result of a number of processes competing with radiative decay from the upper to lower lasing states and the peak efficiency is often under 10%, though some dyes can have efficiencies of greater than 20% in ideal conditions. In order to achieve the maximum output from the laser system a Bethune cell was used as the amplifying cuvette; a Bethune cell is designed to enable the high flow rates needed to prevent dye deterioration when the dye is being irradiated by high energy pump laser pulses.

In the majority of the experiments reported here DCM* / methanol was the dye / solvent mix used, which could be tuned from 608 nm to 660 nm in the fundamental and had a peak efficiency of 21% at 635 nm. Table 2-2 states the dyes employed and the wavelength ranges they were used over. In order to achieve the desired wavelength range the fundamental radiation from the dye was frequency doubled by a potassium dihydrogen phosphate (KDP) crystal. The operation of the frequency doubler is described in Section 2.3.4.

Wavelength (nm)	Dye Used
270-280	Rhodamine 590†
280-300	Rhodamine 610‡
290-310	Kiton Red§
304-330	DCM

Table 2-2 Laser dyes used in the Nd:YAG pumped laser system

The optimal angle of operation for the doubling crystal is dependent on the wavelength of the fundamental in use and therefore the output beam's direction is also wavelength dependent; any change in beam direction is highly undesirable when two beams need to be overlapped. To minimise the beam movement, the doubling unit contained a compensating crystal, that had the same dimensions and refractive index as the doubling crystal, which was rotated at the same time as the doubling crystal, but in the opposite sense. The LAS dye laser was often used in a wavelength scanning mode and to ensure that the doubling efficiency was maximised an autotracking unit was used which, once calibrated in the wavelength region being used, would rotate the doubling crystal to the necessary optimal angle as the wavelength was changed.

As the fundamental and doubled radiation leave the doubling crystal along the same optical path the fundamental was removed by a four crystal Pellin-Broca prism set. A final UG5 filter was used to prevent any remaining stray fundamental radiation from contaminating the beam but the filter also halved the final UV beam energy, to typically 1-2 mJ $pulse^{-1}$. This energy could be further reduced, if needed, by utilising the optics that controlled the laser's final polarisation and these are discussed in Section 2.3.5.

---

* 4-Dicyanmethylene-2-methyl-6-(p-dimethylaminostyryl)-*4H* -pyran

† Benzoic Acid, 2-[6-(ethylamino)-3-(ethylimino)-2,7-dimethyl-3H-xanthen-9-yl]-ethyl ester, monohydrochloride

‡ 2-[6-(Diethylamino)-3-(diethylimino)-3H-xanthen-9-yl] benzoic acid

§ Ethanaminium, N-[6-diethylamino)-9-(2,4-disulfophenyl)-3H-xanthen-3-ylidene]-N-ethylhydroxid, inner salt, sodium salt.

2.3.3 Excimer pumped dye laser

The second laser system was an excimer pumped dye laser. The pump laser in this case was a Lambda Physik EMG 101MSC operating with XeCl that typically produced 100 mJ pulse^{-1} of 308 nm radiation when operated at 20 kV and 10 Hz. The excimer laser pumped a Lambda Physik dye laser (FL2002). The pump laser operates by firing a high voltage discharge in the lasing cavity which is filled with a mixture of xenon, hydrogen chloride and neon. The discharge results in the formation of an excited xenon chloride exciplex that rapidly decays to the ground state with the emission of a photon. Unlike the excited state, the ground state is not bound and immediately dissociates, ensuring that the population of the lower state can not build up and the necessary population inversion is maintained.

When this system was used as the REMPI probe for $O(^1D)$, *via* the following scheme:

$$O^+(^2D_{5/2,3/2}) \leftarrow O(^1F_3) \leftarrow\leftarrow O(^1D_2)$$

which required 203.81 nm to excite the $O^1F \leftarrow\leftarrow O^1D$ intermediate transition, the following arrangement was utilised. The dye in the FL2002 was Kiton Red (Sulforhodamine B) in spectroscopic grade methanol; this dye could be tuned to a fundamental wavelength of 611.43 nm with an efficiency of up to 15%. The fundamental was then doubled in a KDP crystal which operated with a 10% efficiency. The doubled and remaining fundamental light were then polarisation matched in a Babinet compensator, before being frequency mixed in a β-barium borate type II (BBO II) crystal to generate 203.81 nm radiation. The same arrangement was used for REMPI of $O(^1D)$ *via* the $^1P_1$ intermediate at 205.47 nm.

For the experiments when this laser acted as the photolysis source, and the LAS system generated the $O_2(a^1\Delta_g)$ REMPI probe, a variety of dyes were used and the fundamental doubled with the use of an appropriate crystal. Table 2-3 gives a full list of the dyes and corresponding frequency doubling crystals used in the excimer pumped system.

Wavelength (nm)	Dye	Non-linear Optic Crystal
203.81	Kiton red	KDP for SHG and BBO II for mixing
270-280	Coumarin 153*	KDP - Lambda Physik FL31
~300	Kiton Red	KDP - Lambda Physik FL30

Table 2-3 Laser dyes used in the excimer pumped system.

* 2,3,5,6-1H,4H-Tetrahydro-8-trifluormethylquinolizino-[9,9a,1-gh] coumarin

The desired output radiation was separated from the remaining fundamental (and for the O(^{1}D) experiments the remaining doubled) radiation by a single crystal Pellin-Broca prism and passed to the beam steering optics. Only a single crystal was needed to separate the various wavelengths of radiation; this was because no change in the wavelength of the desired output was required during an experiment, and between experiments at different wavelengths, the beam could be realigned if necessary.

2.3.4 Non-Linear Optics

It is beyond the scope of this thesis to provide a comprehensive guide to the operation of non-linear optical materials but a basic description will be given here. When light passes through a medium with non-linear susceptibility it induces a polarisation, P, which can be described by the following expansion in terms of the driving electric field, E:

$$P = \varepsilon_0[\chi^{(1)}.E + \chi^{(2)}.E^2 + \chi^{(1)}.E^3 \ldots.] \qquad \textbf{(2-1)}$$

where $\chi^{(k)}$ is the kth order susceptibility for the material.[1] If more than one photon is present in the medium then the total electric field is a combination of the fields of the two photons. In this case the E^2 term, when expanded, includes terms which are not functions of one photon frequency only. Therefore, if two photons of frequency ω_1 and ω_2 are present at the same time, the E^2 term will include waves that have $\omega_1 + \omega_2$ and $\omega_1 - \omega_2$ as their frequencies, a process that is known as sum frequency generation (SFG). In the special case of second harmonic generation (SHG), where ω_1 and ω_2 are the same, this leads to radiation of frequency $2\omega_2$ being generated. With the addition of more photons it is possible to generate even higher frequencies. As examples the generation of 532 nm radiation *via* SHG using the 1064 nm radiation generated by a Nd:YAG laser is commonly carried out and it is possible to generate the 5th harmonic at 213 nm. The generation of the new waves occurs throughout the medium and therefore for good conversion efficiency the new waves must be formed in such a way that they interfere constructively. Constructive interference occurs when the phase matching condition, i.e. the phase vectors of the input and output beams are matched ($\Delta k = 0$), is met. The phase matching condition is achieved by ensuring that the refractive indices for the waves are the same; this matching is normally obtained by rotating the crystal's optical axis in relation to the beam's direction of propagation. For a dispersive medium rotation of the crystal's optical axis changes the refractive index of the extraordinary wave, which enables the phase vectors to be adjusted and brought into the necessary alignment. As the optical properties of the crystal are

temperature dependent, it was necessary to maintain the crystals at a constant temperature, otherwise the matching angle would have to be reoptimised regularly. Therefore, all of the crystals employed were mounted on temperature stabilised platforms and the lasers were allowed to fire for a short while before the final optimisation took place as the laser beams generated localised heating within the crystals.

The process of SHG has the capability, in a suitable material such as BBO, to generate radiation down to 205 nm but no materials have been found that will produce radiation below this wavelength with any efficiency. As 203.81 nm was required for $O(^1D)$ detection, sum frequency generation was used, in which the dye fundamental is mixed with SHG radiation that has been formed in another crystal to result in effectively frequency tripled radiation.

As a point of interest non-linear materials can carry out the opposite process, i.e. generating two photons of lower energy from a single input. This process is used, for example in the Optical Parametric Oscillator (OPO), to generate tuneable radiation without the need for a dye laser. BBO has been found to be able to generate useful radiation from the UV to IR, the precise range depending on the pumping wavelength. It has yet to be seen if systems based on these principles will eventually take over from dye laser systems.

2.3.5 Laser polarisation

Whilst the polarisation of the lasers was not critical during the bulk quantum yield experiments it is of major importance when the TOFMS was being used. In the majority of experiments when wavelengths above 300 nm were employed, a Glan Taylor calcite polarising crystal was used to set the desired polarisation and a set of half wave plates was used to rotate the polarisation of the beam before this crystal. When the half wave plates were set to an angle that did not maximise the output from the polariser (e.g. when the incoming beam polarisation lay at an angle θ to the chosen polarisation axis) the polariser acted as an attenuator as it would only pass $\cos(\theta)$ of the incoming electric field. Operation of the polariser as an attenuator was useful for two significant reasons. First, it meant that the pump source power did not have to be changed to obtain the required power, which was undesirable as changing the power of the pump laser was found to significantly alter the timing between the two lasers firing; and second, that the beam profile was not altered significantly by this method as could occur if an iris was used.

When it was desired to change the polarisation during an experimental run (so as to reduce errors possible between experimental runs) an alternative method was used. This method employed a KD*P crystal, mounted so that a voltage could be applied along its length. Application of a voltage changes the refractive index of the crystal and causes the phase of the light to be retarded. Therefore, as the applied voltage was increased the polarisation of the beam would change from linear to elliptical to circular to elliptical and then to linear again, but now at 90° to the initial polarisation. The voltage required to perform this 90° rotation depended on the wavelength and the precise alignment of the system, but typically was between 3.5 kV and 4.5 kV. The voltage supply unit could be binary controlled by the data acquisition computer to enable the switching between the two polarisations within a single run. This crystal required very careful alignment to ensure that the polarisation was rotated the correct amount and when set up correctly the beam was, with the voltage on or off, better than 95% pure.

Standard polarising components did not work at 203.81 nm as calcite absorbs > 90% of the radiation at this wavelength. Three methods were used to polarise this radiation. The first method was to use a Quartz Rochon polariser; the second used tilt tuned half wave plates and the last an α BBO polarising crystal. The quartz Rochon polariser was used when low power was required; it was found that, because quartz is an optically active material and therefore the incoming linearly polarised light had its polarisation effectively scrambled by the quartz before the polarisation took place, the power was approximately halved. The Rochon polariser operated by deviating one polarisation by 0.5° and this unwanted radiation could be blocked further down the beam path by an iris. Because of the power loss experienced when using the Rochon polariser, a second method was employed on occasion; this alternative was to use a set of quartz half wave plates and then tilt them with respect to the direction of beam propagation. Tilting the ½-wave plates enabled them to operate outside of their normal wavelength operating region. The polarisation was set by placing a quartz plate at the Brewster angle to the desired polarisation and the half wave plates then tilted so as to minimise the reflection from the plate. Finally an α BBO polarising crystal was purchased, this operated in the same way as a Glan Taylor prism but, as a result of the optical properties of the α BBO, it had a working range of 200 nm to 270 nm, which could be extended by tilt tuning of the crystal. It was found that this crystal did decrease the available power by nearly as much as the Rochon polariser, but the α BBO was used in preference as it did not alter the beam profile, which the Rochon polariser could if not very carefully aligned.

2.3.6 Optics

Other than for the 203.81 nm beam, the primary steering method for the laser beams was to use prisms which had broadband anti reflection coatings (centred at 300 nm). Beam steering for the 203.81 nm beam was achieved by utilising mirrors which had been coated for maximum reflection at 204 nm when set at 45° to the beam. All steering optics were fitted to stable optical mounts. All optical components were firmly attached to optical benches *via* post holders that attached either directly to the bench, to kinematic mounts or to controlled motion platforms. The use of kinematic mounts enabled the removal and reinsertion of components with minimal change to the beam steering, particularly for the optics which were used to change the detector system.

For both detection systems beam focusing, and final beam steering, was achieved through the use of quartz lenses, 20 mm in diameter and with a typical focal length of 22 cm. Those used for the 203.81 nm radiation had been anti reflection coated for 204 nm to minimise the reflection losses. All lenses were mounted on y-z translation stages to enable the beams to be steered into the interaction region and to ensure that a good overlap of the beams was achieved. Most of the stages were mechanically operated but a pair of electronically driven stages were introduced during the course of the work reported in this thesis to control the y-z position of the REMPI lens for the TOFMS with greater accuracy than was possible manually.

In the case of one-laser experiments, or for the REMPI beam of two-laser experiments, the x, y and z positions of the lenses were set to maximise the signal received by the appropriate detector. Normally in the two-laser experiments the interaction point was defined by the optics which controlled the beam from the excimer pumped laser. The basis for this choice was that the beam from the excimer pumped laser typically was used as the REMPI probe beam. The y-z translation stages on the LAS side were mounted on optical rails which enabled controlled movement in the x axis; the purpose of x axis movement was to control the position of the focal point of the beam. The ideal location of the focal point varied between experiments and was decided upon by considering the following factors. First, there are the two counter productive factors based on the location of the focal points. The closer the focal point of the photolysis beam is to the interaction region the larger the signal that can be recorded; however, it is possible to have too high a laser intensity which can result in the saturation of the molecular sample. Second, when operated at high photon densities, it is possible for a laser to generate a multiphoton signal. Whilst this multiphoton signal is the origin of the signal observed for a one-laser experiment, for a two-laser experiment any multiphoton signal

originating from a single laser can be an undesirable signal that would have to be removed in the data analysis stage. When possible the focus of the photolysis lens was positioned outside of the volume that could be detected, e.g. for a two-laser experiment in the bulk cell the focus of the photolysis beam was positioned so that it was at least 1 cm from the ion detection plates, where it was found that few, if any, ions produced would be collected at the plates.

To make the alignment of the laser beams easier once an accurate alignment of the lasers had been obtained, irises were placed so that initial beam alignment could be made according to reference points outside of the detection systems. The use of irises was found to be necessary as it was almost impossible to align the system purely by scanning the focus points of the laser beams.

2.3.7 Laser energy

As the output energy of the lasers varied from shot to shot it was necessary to correct the measured signals for the energy variation. In order to obtain a sample of the main beam a quartz plate was placed in the path of the main beam and the energy of the reflected beam, *ca.* 5% of the main beam, was measured. This plate was placed at a very fine angle to the main beam in order to minimise any change in the reflection percentage that could be caused when changing the polarisation of the beam. The plate used on the beam originating from the excimer pumped dye laser had parallel faces but it was found that a wedge shaped profile was required for the beam from the Nd:YAG pumped dye laser. The wedge requirement was because when a plate with parallel faces was used there was a significant change in the reflection percentage depending on the wavelength of the beam. The changes, which occurred as oscillations of period 0.016 nm, were found to be as a result of an etalon effect caused by mixing of the reflections from the front and rear surfaces of the flat. Some small variation was found to exist still in the percentage of the beam reflected when the wedge was employed, but the variation was determined to be significantly less than the overall error in the energy measurement. This residual error was also found to be random between experiments; a result of minor movements of the beam prior to the wedge meaning that the oscillation was not fixed to the wavelength.

A pyroelectric energy meter (Gentec ED-100A) was used to measure the energy reflected from the wedge. Gentec energy meters have a coating which means that their efficiency is roughly independent of wavelength, from the UV to the IR. To determine the actual energy in the main beam, and how it was related to the reflected reading, another pyroelectric head (Gentec ED-

200L without its diffuser) was used. The pyroelectric head in the main beam measured the beam energy after the plate and enabled a good relationship between the energies of the reflected and transmitted beams to be determined. An accurate, quantitative, value for the main beam energy was of particular importance when trying to determine the degree of saturation in the interaction region. As a result of the beam from the Lambda Physik laser normally being a factor of at least ten lower in energy than the beam from the LAS dye laser, the detector used had to be more sensitive than the pyroelectric detectors used for the measurements of the LAS laser's beam. A UV sensitive photodiode (Lambda Physik FL302UV) was the energy measuring device. The energy response of this photodiode was confirmed as linear with respect to the main beam by measuring the main beam energy with a pyroelectric detector similar to that used to measure the reflection of the LAS beam.

The outputs of the detectors were recorded on a digital oscilloscope, the Gentec outputs having been amplified by Gentec EDX-1 amplifiers.

2.3.8 System timing

A pulse generator that had been built in-house controlled the overall timing of the experiment. The primary trigger was set to run at 10 Hz and this signal acted as the master from which all other timing was derived. When the time-of-flight detector was in use the pulsed valve was triggered first and after 1.4 ms, the time required for the gas to reach the interaction region, the laser sequence was initiated. The first step of the laser sequence was to trigger the flash lamps of the YAG; after 184 μs the excimer was triggered and after a further 1.69 μs the Q switch on the YAG was fired and a pulse was sent to the chopping wheel controller to synchronize the wheel's rotation. The chopping wheel was used to selectively block the laser beams to enable signals for background subtraction to be measured. The timing could be adjusted in 1 ns steps to ensure the desired delay between laser pulses was achieved, typically in the 5-10 ns range with a deviation of ±5 ns.

The acquisition system was triggered by a photodiode (Hamamatsu S1722-02, 1 ns rise time, spectral range 190-1060 nm) which monitored stray fundamental light from the REMPI laser. The external trigger input of the LeCroy 9350A digital storage oscilloscope was used to monitor this signal and the trigger could be passed onto further oscilloscopes in a daisy chain manner. A second photodiode, of the same make as noted previously, was used to monitor the output of the photolysis laser to enable the time delay between the two lasers to be measured, and the delay could be accurately determined to within 1 ns. This method of triggering was

used to minimise the effect of random jitter between the pulse generator signals and the REMPI laser firing.

2.4 Bulb bulk gas experiment

When only ion counting was required in terms of detection, such as for the quantum yield measurements, a bulk cell was used which, *via* a pair of parallel plates, measured the current resulting from the ions formed. This apparatus is shown in Figure 2-2 and Figure 2-3. The cell was formed from a Pyrex sphere with two ports for the input and exhaust of gases, two larger apertures that held the window assemblies and a final port into which the detection plate assembly was inserted.

The gas sample within the bulb was either static, with the gas being regularly changed to ensure that the experimental conditions did not change significantly over time, or flowing through the cell, the gas being drawn through the cell by a two stage rotary pump (Edwards E2M). A static sample was used when the gas under investigation had to be prepared in small quantities, typically a few hundred Torr, and stored before use; the flow system was used when either large quantities of gas were available or the gas could be prepared in a flow arrangement. Typical pressures were 2 Torr for a static fill and 8 Torr for a flowing gas. The temperature of the gas was monitored by a thermocouple that was placed inside a fine stainless steel tube that penetrated into the sphere *via* the gas outlet port. The pressure in the cell was measured by a capacitance manometer (MKS Instruments 10 Torr Baratron) fitted to the inlet arm of the gas handling glassware. The temperature in the cell was controlled by a constantly circulating air current which could be heated or cooled as necessary; the airflow is shown in Figure 2-2. Heating took place in the external tower where adhesive heating mats had been applied to the exterior of the heat exchanger. Cooling of the cell was not an easily controlled factor and the desired temperatures were reached in the following ways. To hold the temperature of the cell at 273 K the centre section of the heat exchanger was filled with dry ice; to reduce it further to 243 K dry ice was also placed inside a tray at the top of the shielded enclosure; and to obtain 227 K the dry ice in the heat exchanger had liquid nitrogen added to it. To maintain the cooling, regular checks were made on the levels of the coolants and they were refilled as necessary. Typically the temperature would be stabilised to ± 1 K for periods of *ca.* twenty minutes and ± 2 K over half an hour without intervention on the levels of the coolants.

The counter propagating photolysis and probe laser beams entered the bulb through windows on opposite sides of the cell. When the gas was at room temperature the windows were sealed

with 38 mm diameter fused silica plates. For low temperatures this arrangement could not be used as condensation would form on the window. Therefore, an arrangement consisting of an evacuated cell with a pair of fused silica windows at either end was used to thermally isolate the outer window. The REMPI probe beam was focused between a pair of nickel plates which were located about the centre of the bulb and were separated from one another by 20 mm. A detailed view of the bulb can be seen in Figure 2-3. The nickel plates had a potential difference set between them, typically 100 V, which accelerated any ions formed so they travelled towards the plates. These accelerated ions could collide with molecules in the bulk gas causing further ionisation, effectively amplifying the ion signal. The current formed by the ions was further amplified and converted into a voltage by a purpose built unit before being sent to an oscilloscope for data acquisition. The ion current measured using this method has previously been shown to be linear with the initial number of ions formed by the REMPI pulse up to a pressure of 10 Torr.[2]

The ion detecting plates could act as very efficient aerials for stray electromagnetic radiation and therefore steps to prevent interference were necessary. The main measure was to place the bulb in a large copper enclosure, which acted as a Faraday cage to prevent the ingress of stray radiation. Secondly, the thermocouple wire was run inside stainless steel tubing until it left the enclosure and this tubing was earthed to the enclosure. Finally, all other possible sources of radiation, e.g. the air circulation fan and the heating mats, were external to the enclosure. One of the main reasons for the construction of the separate cooling tower was to house possible sources of electromagnetic interference.

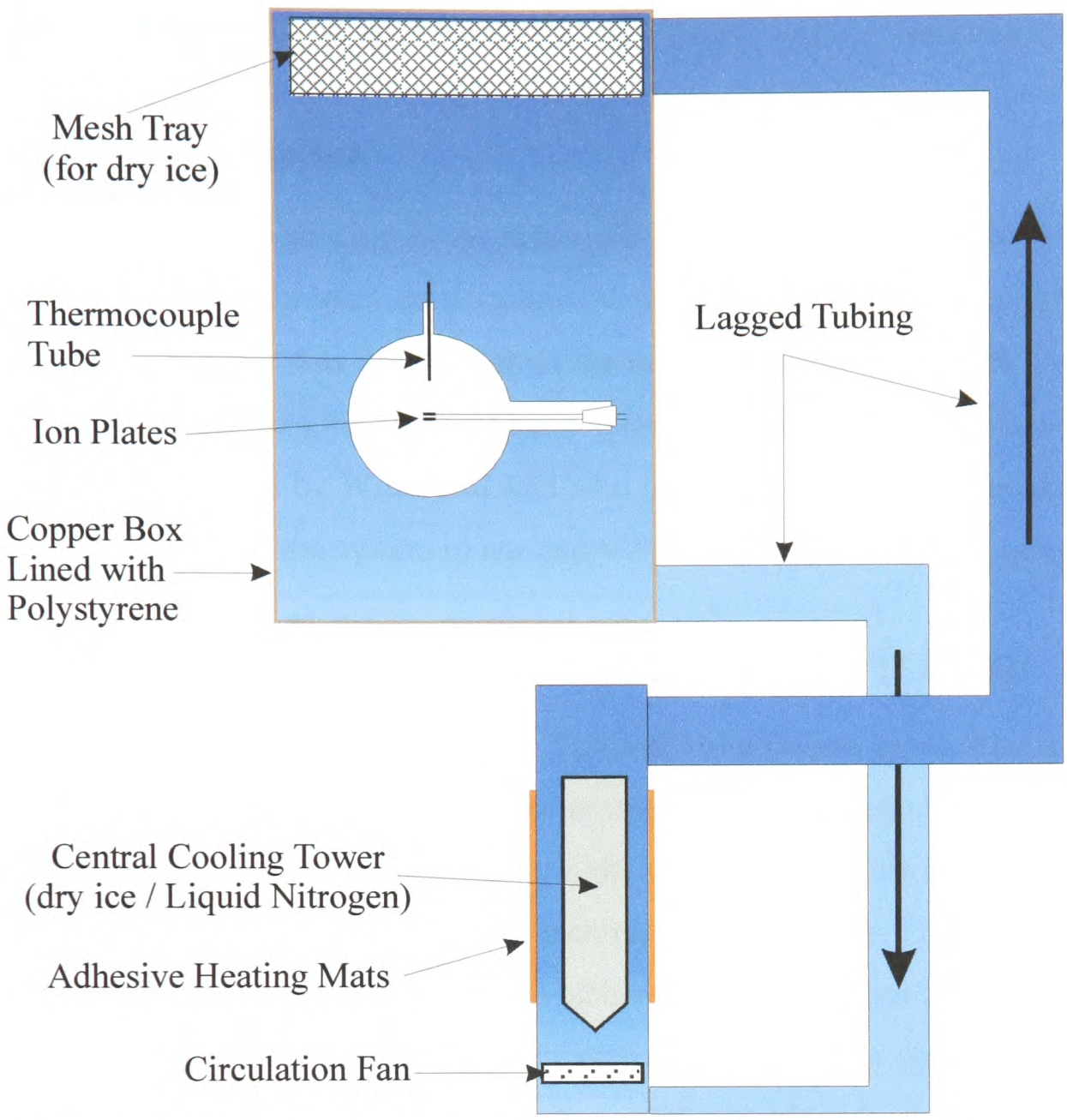

Figure 2-2 Overview of the cooling system employed for the bulb.

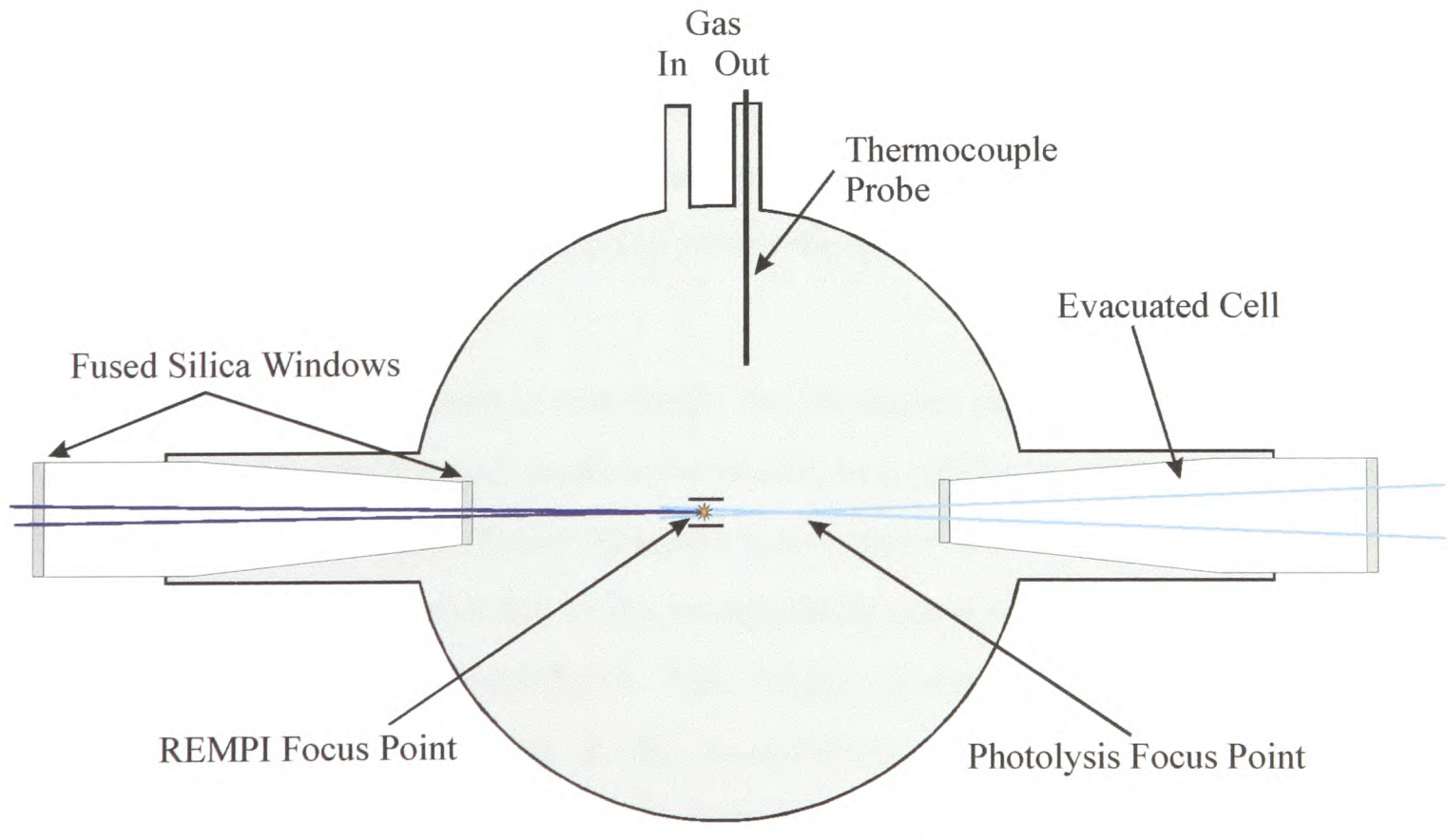

Figure 2-3 Detailed view of a two-laser experiment in the bulb.

2.5 Operation of the time-of-flight mass spectrometer

2.5.1 Introduction

When information relating to the dissociation dynamics was required, be it speed distributions, translational anisotropies or selection of a particular dissociation pathway, a time-of-flight mass spectrometer was used to gather the necessary information. The basic design and method of operation for the time-of-flight mass spectrometer used in the research reported in this thesis was first proposed by Wiley and McLaren in 1955.[3] A number of modifications to this design had been made on the system in use and will be detailed later in this section.

2.5.2 Basic description of the operation of the TOFMS

Gas enters the main chamber of the TOFMS *via* a pulsed valve. The photolysis laser is set to fire once the main section of the gas jet reaches the interaction region. The REMPI pulse then forms ions in the first of three stages in the spectrometer. This stage is bounded along the time-of-flight axis by two metal plates, the extractor and repeller. The ions formed in this region are subjected to a small electrical field which accelerates the ions along the time-of-flight axis and through a wire mesh in the extractor plate. The mesh was stretched over the aperture in the extractor plate to minimise any distortions that are caused by the aperture in the extractor plate. As the ions pass into the second region they are further accelerated by a stronger electric field, reaching their final velocity as they pass through a further wire mesh into the third stage, the drift tube. In the drift tube the ions continue with the velocity with which they entered the field free region until they are detected at the end of the drift tube. An overview of the design of the time-of-flight mass spectrometer used to obtain the time-of-flight results reported in this thesis is shown in Figure 2-4.

For the experiments described in this thesis, the resolution relating to the initial kinetic energy distribution of the ions formed needs to be maximised, whilst maintaining a good signal level. The voltages employed in a Wiley-McLaren spectrometer with two acceleration regions can be set to reduce the time spread due to the spatial distribution and control the time spread due to the initial kinetic energy distribution. The effects of the initial spatial distribution can be reduced by setting the potential in the acceleration region to achieve the space focusing condition, which will be discussed further in Section 2.6.1. As the REMPI process requires high laser fluences, the REMPI laser beam is focused within the source region to a diameter of 90 μm FWHM, and therefore any signal variation due to the initial spatial distribution should

be small and easily overcome if space focusing conditions are used. The potential in the source region can control the resolution relating to the initial kinetic energy distribution. If the voltage is set high then the time spread caused by the initial kinetic energy distribution is reduced and a high mass resolution is obtained; however, if it is important to resolve the initial kinetic energy distribution, as was required for this research, the voltage should be set to a low value. A significant modification to the basic design was made to the source region of the spectrometer to reduce the field distortions caused by the body of the pulsed valve. This modification was to introduce a number of shielding electrodes, linked together by a resistor chain, between the extractor and repeller plates.

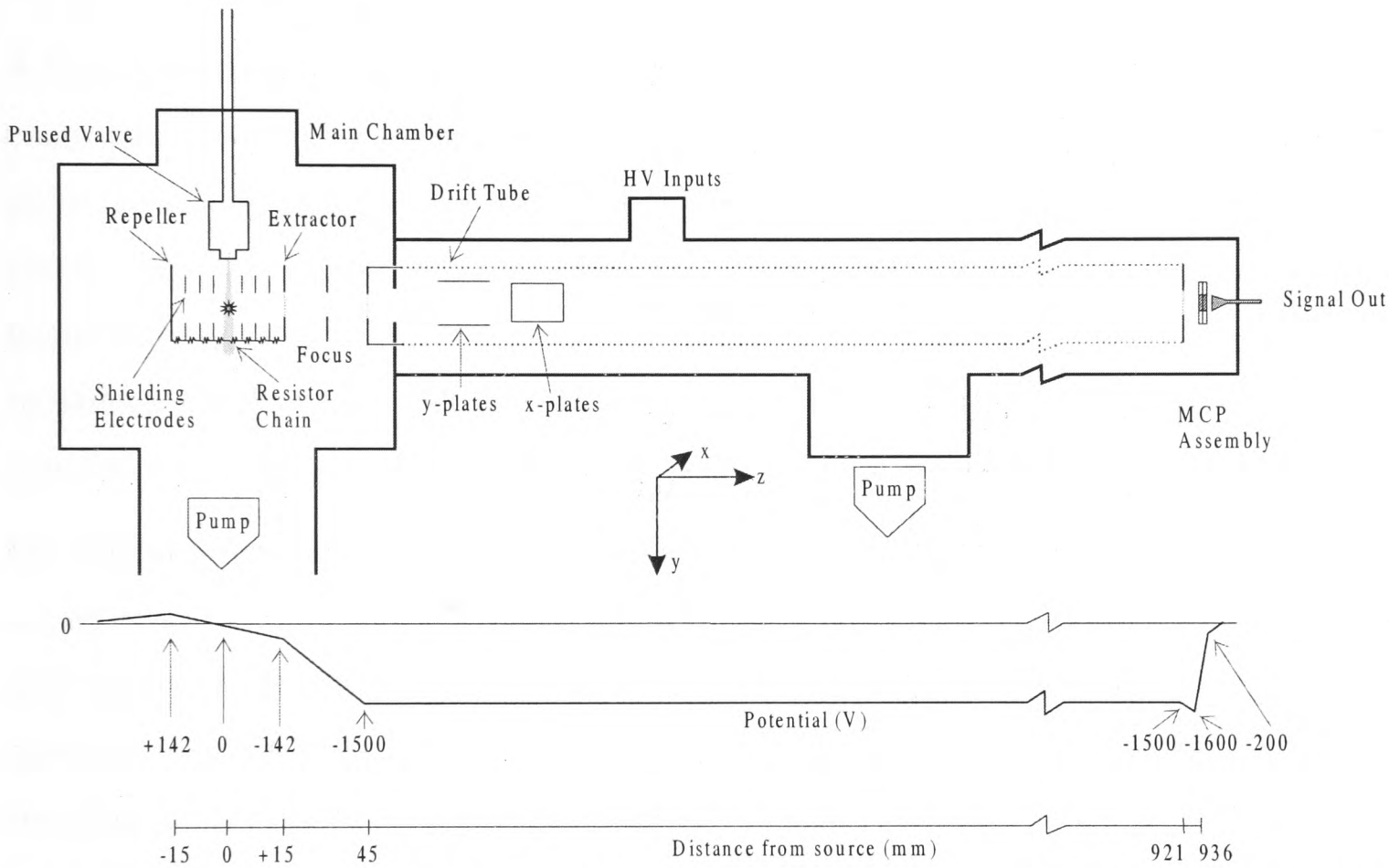

Figure 2-4 Schematic of the modified Wiley-McLaren time-of-flight mass spectrometer. Typical potentials employed are shown.

2.5.3 Recent modifications

During the course of the research reported in this thesis some further modifications were made to the electronics controlling the time-of-flight tube's operation, though not all were employed generating the results described within this thesis. The most important was the ability to increase the acceleration voltage. A greater acceleration voltage can be desirable as it will reduce the overall time of flight of the ions and therefore ensure that fewer ions miss the detector as a result of off axis velocity components. The maximum voltage on the drift tube

was limited to be no more than 100 V greater than the front micro channel plate's voltage. The voltage restriction was imposed as otherwise it was found that secondary ions, formed at the mesh at the end of the drift tube would be accelerated to the detector, and significantly distort the signal away from that which would be formed by the ions from the REMPI process. To increase the acceleration voltage without raising the drift tube voltage it was necessary to either float the micro channel plate detectors away from the electrical ground of the time-of-flight tube or raise the centre point between the extractor and repeller plates to a positive voltage. The former was not possible without a major redesign of the detector assembly both electrically and mechanically; the latter, however, was possible with a minor redesign of the high voltage supply unit.

A less significant but necessary modification was to modify the *y* axis steering plates' voltage control to allow an additional voltage to be applied to them on application of a control TTL pulse. This additional voltage was set to a value that meant that any ions passing between the plates whilst the voltage was on would miss the detector. The ability to prevent selected ions from reaching the detector was a useful addition as undesired large signals, that could saturate or damage the detector, could be prevented from reaching the detector whilst the desired signal could pass through and experience only the necessary y axis steering correction voltage.

Finally the focus voltage was altered to be no longer totally independent of the extractor and acceleration voltages but adjustable about a small range half way between the extractor and drift tube voltage (50% ± 10%). An earlier modification, to enable the focus voltage to be independently set, was found to be ineffective, as although it was meant to improve the focusing of the ion beam, it in fact severely distorted the fields making accurate modelling impossible.

2.5.4 Gas handling

The gas under investigation, normally ozone, was introduced to the main chamber of the time-of-flight spectrometer *via* a pulsed valve (General Electric, nozzle diameter 500 μm) which was controlled by a home built driver. The driver initiated gas entry to the system by sending a 120 V pulse to the valve to open it. The voltage then rapidly dropped back to the holding voltage, 40 V, which was then held until the desired quantity of gas had been introduced. The quantity of gas admitted was dependent on the backing pressure and the desired signal level and was also subject to a limit which corresponded to a maximum pressure at the detector of 2×10^{-6} Torr to prevent damage to the MCP plates. The backing pressure was regulated by using

a stainless steel needle valve on the inlet to the pulsed valve and was measured with a capacitance manometer (Datametrics Baratron 1-1000 Torr). Typically a backing pressure of 50 Torr and a pulse width of 270 μs was sufficient to generate a good signal, whilst not overloading the MCP detector. The nozzle was placed so that the probe region of the laser was within the supersonic expansion of the molecular beam. The propagation direction of the jet was perpendicular to both the time-of-flight axis (Z axis) and the axis along which the counter-propagating laser beams were fired (X axis). As the pressure in the time-of-flight tube was limited, the backing pressure behind the jet had to be kept low. A low backing pressure meant that the cooling of the beam in the supersonic expansion was not particularly efficient. Pinot[4] reported the following temperatures for the gas jet; translational 9 K; rotational 215 K; vibrational 300 K - no cooling. Future plans for the spectrometer include the introduction of a skimmer, which would permit higher backing pressures without exceeding the time-of-flight tube pressure limits.

The main chamber was continuously pumped by a 1000 ls^{-1} turbo-molecular pump (Leybold Turbovac 1000C) situated at the bottom of the main chamber, which was fore pumped by a rotary vacuum pump (Leybold D40B). During experiments a purge of argon was fed into the turbo-molecular pump to prevent any corrosive reagent gases from reaching the pump ball bearings. The drift tube was differentially pumped by a smaller, 145 ls^{-1}, turbo-molecular pump (Leybold Turbovac 150V) which was fore-pumped by another rotary pump (Leybold D40B).

Ion gauges (Alcatel JBA 11P) were used to measure the pressure in both the main chamber and the drift tube. Their use was preferable to Penning ionisation gauges because of the strong magnetic fields that the latter produce. The fields were undesirable as they would cause severe distortion in the ion trajectories. However, as the ion gauges produce significant numbers of ions themselves, the ion gauge on the drift tube was turned off during data collection because of the large background signal that it produced. It was not necessary for the ion gauge on the main chamber to be turned off as doing so made little difference to the background signal recorded. Typical pressures in the system were 8.8×10^{-8} Torr for the main chamber and 1.3×10^{-7} Torr for the drift tube with the pulsed valve off; when the valve operated under typical conditions the pressures were, 6×10^{-6} Torr in the main chamber and $< 2 \times 10^{-6}$ Torr in the drift tube.

2.5.5 Electric Fields and Resolution

With the drift tube operating at –1500 V an O_2^+ ion would take *ca.* 11.0 μs to complete its journey from the source region to the detector. The time resolution of the spectrometer was approximately 1-2 ns, which means that the resolution was about 0.01% of the overall time of flight. Given this very fine degree of resolution any small changes in the experimental conditions could significantly affect the time-of-flight profile recorded.

The most likely contributory factor to these errors are the electric fields within the machine. The fields must be stable over time, in all time scales, and must be well characterised if the ion trajectories are to be successfully modelled. The field at any point must be stable during the time that ions are close to that point; if not the ions that are otherwise identical will experience differing fields and therefore have different times of flight. The electric fields must be stable between pulses during an experiment if the averaging procedure is to be valid; and finally, the fields must be accurate over the long term if the calibration tests which determined the modelling parameters are to be generally valid. Whilst it is possible for the modelling procedure to allow for fields which are not perfectly parallel or perpendicular to the time-of-flight axis, it does make the process significantly more difficult; therefore, it is highly desirable to ensure that the fields are as close to pure parallel / perpendicular as possible.

It is in the source region that the first problems occur. Despite the shielding electrodes that surround this region the pulsed valve, which is necessarily held at ground potential, can cause distortions in the extraction fields. Simulations made using the ion trajectory simulation program SIMION have shown that the residual effect of the pulsed valve is to cause at most a difference in the total time of flight of 3 ns between ions formed at different distances from the pulsed valve, along the experimental *y* axis, but with otherwise identical parameters.[4]

To accurately align the source assembly perpendicular to the time-of-flight axis, a helium-neon laser was shone onto the repeller plate at the back of the assembly. The orientation of the plate was then adjusted so that the beam was reflected back along the time-of-flight axis. The rest of the source and acceleration assemblies were held to this orientation by means of carefully machined spacers, thereby ensuring that the fields were parallel to the time-of-flight axis.

Field distortions, which would act as ion lenses, between regions of different electric field strength were minimised with the use of wire mesh grids to cover the apertures separating the regions. Gold meshes (95% transmitting) were used between the source and acceleration and between the acceleration and drift regions. A stainless steel (82% transmitting) mesh was used

on the aperture between the drift tube and the MCP detection region. The meshes were carefully stretched over the apertures to ensure that they themselves were not responsible for any field distortions.

The focus plate, which had been added as part of an old set of modifications made to the spectrometer, was always held at a voltage that was approximately midway between the extractor and drift voltages. The restriction on the voltage applied to the focus plate was because it had been found that if the focus plate was used to focus the ions it introduced more problems than it solved.

Final correction of the ions direction of travel, to ensure that they hit the MCPs, was carried out by two sets of deflection plates. Each set consisted of two plates 100 mm long, 35 mm wide and held parallel 20 mm apart from each other. Application of a potential, normally less than 10 V, between the plates caused a field perpendicular to the time-of-flight axis to be formed. The field between the plates accelerated the ions in the desired direction causing a deviation at the MCP detector. The two sets were positioned so that they enabled corrections to be made on the experimental x and y axes. However, in addition to the desired shift, a perturbation in the drift tube's field occurred at the each end of the plates. The effect of the perturbation was evaluated, again using SIMION, and found to cause variations in the region of 2 ns for ions that passed at different heights between the plates. These distortions could be removed if the steering voltages were only applied when the ions were between the plates.

2.5.6 Ion Detection

On completing their journey *via* the field free drift tube, the ions pass through a final mesh which separates the drift tube from the micro channel plate (MCP) detector. This detector consisted of a pair of micro channel plates (Galileo 1397-1816, 18 mm active diameter) placed one on top of the other. When the ions impact the front surface of the detector the ion signal is converted to an electron signal and this signal would be amplified by a factor that depended on the potential difference between the front face of the first plate and the rear of the second plate. The rear of the second plate was held at –200 V from a collecting pin which was at 0 V and to achieve the desired signal levels the front face was set to –1.6kV; the resulting 1.4 kV potential difference between the plates gave an enhancement of *ca.* 2×10^5 electrons per ion impact.

The electron signal was connected *via* a short cable to a further amplification stage (Mini Circuits ZPUL-30P) and the output from the amplifier passed to a digital storage oscilloscope

(DSO) (LeCroy 9350A, 500 MHz, 10^9 samples s^{-1}, 2 channels) for the final stage of the detection process.

2.6 Simulation of Time-of-flight Profiles

Section 2.5 provided information on the operation of the TOFMS and this section will provide a more theoretical approach to explain the appearance of a time-of-flight profile.

2.6.1 Basic Model

In a Wiley-McLaren TOFMS there are three main sections of interest when describing the motion of an ion. These are the region in which the ions are generated, the region where the ions are accelerated and finally a region in which is there is no electric field where the ions travel to the detector. It was the inclusion of separate source and acceleration regions that meant the Wiley-McLaren design was an improvement on previous designs as the spectrometer was easier to adjust and greater resolution could be achieved.

Ions of different mass within the spectrometer can be differentiated from each other by their flight times as their kinetic energies are mass dependent. An ion with initial kinetic energy U_0 when placed in an electric field will be accelerated and will gain kinetic energy equal to qdE_{Region}, where q is the charge on the ion, d is the distance travelled and E_{region} the electric field within the region. It should be noted that the increase in kinetic energy is independent of the ion's mass. The final kinetic energy of an ion having passed through the spectrometer will be the sum of its initial kinetic energy and the energy gains from each region it has passed through. Therefore, the final speed of the ion, v, can be given by:

$$v = \sqrt{\frac{2\left(U_0 + \sum_{region} qd_{region}E_{region}\right)}{m}} \qquad \textbf{(2-2)}$$

As the energy terms in (2-2) are independent of mass, the final speed will vary with mass. This results in ions with different masses taking different times to travel a set distance. If a time gate is then placed at a set distance it is possible to detect ions of a specified mass.

If it is assumed that the initial kinetic energy of the ion will be much less than the energy imparted to it by motion in the electric field, that the electric fields are uniform and directed

towards the detector and that the ion velocities are non relativistic, then the total time for the ions flight would be given by:

$$t_0 = \left(\sqrt{2m}\right)\left(\frac{d_s}{\sqrt{qd_sE_s}} + \frac{d_a}{\sqrt{qd_sE_s} + \sqrt{qd_sE_s + qd_aE_a}} + \frac{d_d}{2\sqrt{qd_sE_s + qd_aE_a}} \right) \qquad \textbf{(2-3)}$$

where the subscripts *s*, *a* and *d* signify the source, acceleration and drift regions respectively.

For a given mass in any experiment nearly all of the parameters in this equation are constant but crucially one is not. As the ions are not formed at a point source the value of d_s will vary depending exactly where the ion is formed within the probe beam. The location of ion formation is of particular concern because it is in the source region that the ions are travelling at their slowest, and therefore the time taken to cover this extra distance will be at its greatest. Initial inspection of (2-3) shows that the first term depends on the square root of d_s. It is possible to overcome this problem by carrying out a procedure that is referred to as space focusing. The procedure aims to remove the dependence on the initial location of the ion by a careful selection of the source and acceleration region voltages. Space focusing can be best explained by example, an ion formed slightly further from the extractor than the centre of the beam will gain more kinetic energy than the ions formed at the centre ($U_{gain} \propto d$). The higher kinetic energy means that the ion will enter the acceleration region with greater speed. Once the ions have traversed the acceleration region they continue down the drift tube, with the ions formed further from the extractor travelling faster than the central ions. Conversely ions that were formed closer to the extractor will be travelling slower than the central ions. With careful selection of the voltages in the source and acceleration regions, the difference in flight time as a result of the starting position is countered by the ion's increased speed during the rest of its journey. Therefore, the space focusing procedure will result in ions formed at different points arriving at the same time. The voltages required to obtain the space focusing condition can be determined numerically and it was found that for the spectrometer in use the condition was obtained when the extractor plate was set to 0.094 times the drift tube voltage.

One of the main pieces of information that is available from the TOFMS is the kinetic energy distribution of the fragments formed in the photolysis step. The initial kinetic energy of the parent photofragment is, to within a very small margin, the same as that of the ion formed. The very small change in kinetic energy is because it is the electron that carries away the vast majority of the kinetic energy released as a result of momentum conservation, e.g. for a hydrogen atom, when ionised, the proton carries only 1/1835 of the kinetic energy. If the

conditions have been set so that the initial position of the ion does not affect the time it takes to travel to the detector, the initial kinetic energy of the ion can be accounted for in a simple manner. This method works by calculating the time that it would take the field within the source region to bring the ion, which is initially moving away from the detector to rest. This case is ion (a) in Figure 2-5.

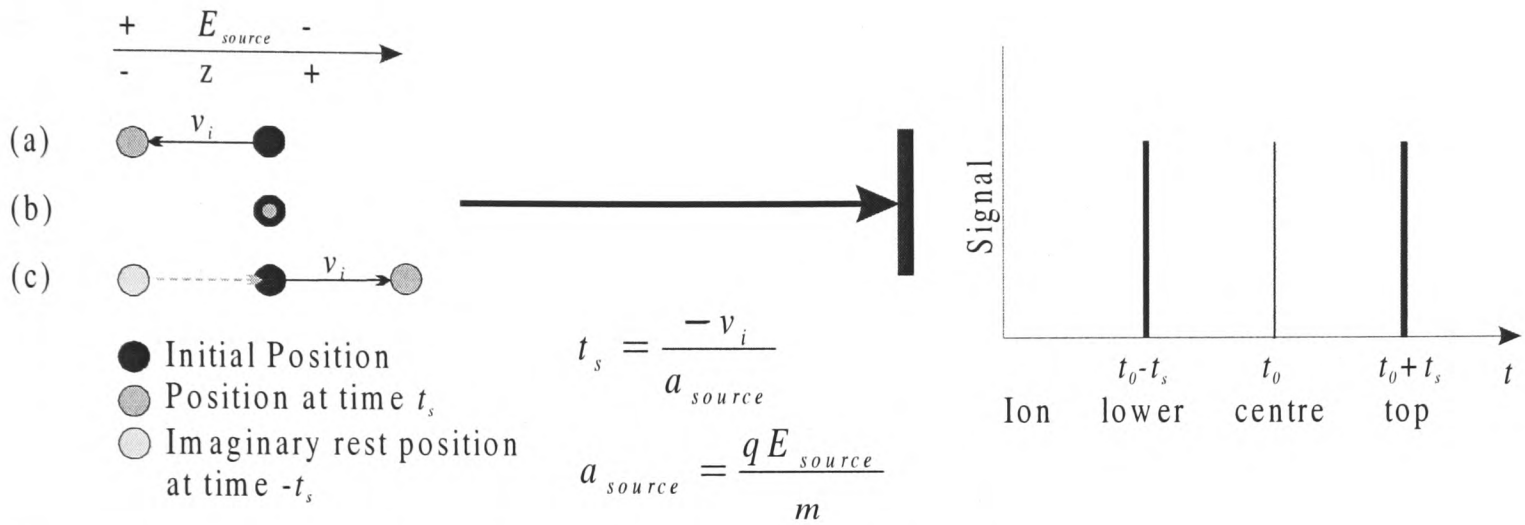

Figure 2-5 Initial motion of an ion in the source region.

Having calculated the time taken to bring the ion to rest, it remains to calculate the time that the ion takes for the remainder of its journey. However, if the space focusing conditions are being met then the position of the stopped ion does not affect the time of flight further. Therefore, the initial kinetic energy can be determined from a function relating to the difference in the time of arrival between ions formed with initial kinetic energy and ions formed from stationary parents. The time required to bring an ion, mass m, to rest, from an initial energy U_0, is given by:

$$t_s = \frac{\sqrt{2mU_0}}{qE_{source}} \qquad \textbf{(2-4)}$$

assuming that the ion's velocity is directed only along the time-of-flight axis away from the detector. If the ion was in fact travelling towards the detector, as for the ion (c) in Figure 2-5, the stopping time becomes negative which will mean that the ion will arrive before the initially stationary ions. As the distribution of velocities has to be symmetric about $v_i = 0$, the ions will arrive at the detector at times symmetric about t_0 as is illustrated on the right hand side of Figure 2-5. The deviation from the centre point will be directly proportional to the initial v_z component of the ions' velocity.

Unfortunately the modelling of a true time-of-flight profile is not quite as simple as has been described. In reality there are a number of factors that act to make the profiles significantly

more complex. First, there is the instrumental response that changes the clean arrival spike into a slightly blurred peak, which becomes a problem when the initial velocity distribution is not from a monoenergetic source, as the profile is now a convolution of the velocity distribution and the instrumental response. Secondly, the detector is only sensitive to the v_z component of the ion's velocity; any off-axis (off the time-of-flight axis) component of velocity results in the ion being assigned a lower speed than it was actually travelling with. Off-axis velocity components can further complicate the model as a finite bandwidth probe laser and the Doppler shift of the probe transition caused by ions travelling off the TOF axis but along the laser propagation axis. A laser with an infinitely broad bandwidth could ionise fragments irrespective of their off-axis components. If the bandwidth is infinitely narrow, then a specific off axis component would be monitored; whereas a finite bandwidth results in a further convolution being imposed onto the ion signal. Thirdly, the TOFMS is of finite size; therefore, an ion with a significant off-axis velocity component could miss the detector. Finally it is possible that the probe laser will not interact with all of the photolysis fragments equally, particularly in relation to possible alignment effects between the polarisation of the laser and fragments.

The first of these problems can be overcome by determining the TOFMS instrumental response and then either deconvoluting this from the observed signal or including it in a forward simulation. However, the other problems are not as simple to remove and will now be discussed in greater depth.

2.6.2 Production of fragments with an off axis velocity component

Whilst the model presented in Section 2.6.1 was based on ions being produced with their kinetic energy being distributed only along the TOF axis, this situation is highly unlikely to occur in an experiment. In fact the actual distribution, $D(\mathbf{v},\theta)$, of fragment recoil velocities, $\mathbf{v}$, will be aligned to the electric vector of the photolysis radiation, $\boldsymbol{\varepsilon}_p$, through the relationship:

$$D(v,\theta) = \frac{1}{4\pi}\left(1 + \beta[\mathbf{v}]P_2[\cos\theta]\right) \qquad \textbf{(2-5)}$$

where θ is the angle between the fragments velocity and the electric vector, $\beta[\mathbf{v}]$ is the speed dependent anisotropy factor (and has limits of $-1 \leq \beta \leq 2$) and P_2 is the second degree Legendre polynomial given by:

$$P_2[x] = \frac{3x^2 - 1}{2} \qquad \textbf{(2-6)}$$

Examples of the distributions obtained for different values of β are given in Figure 2-6. It should be noted that for the special case of $\beta = 0$, $D(\mathbf{v}, \theta)$ becomes independent of θ and is therefore isotropic. $D(\mathbf{v}, \theta)$ can also be independent of β if the value of P_2 is zero, which occurs when θ takes the value of 54.74°, a figure known as the magic angle.

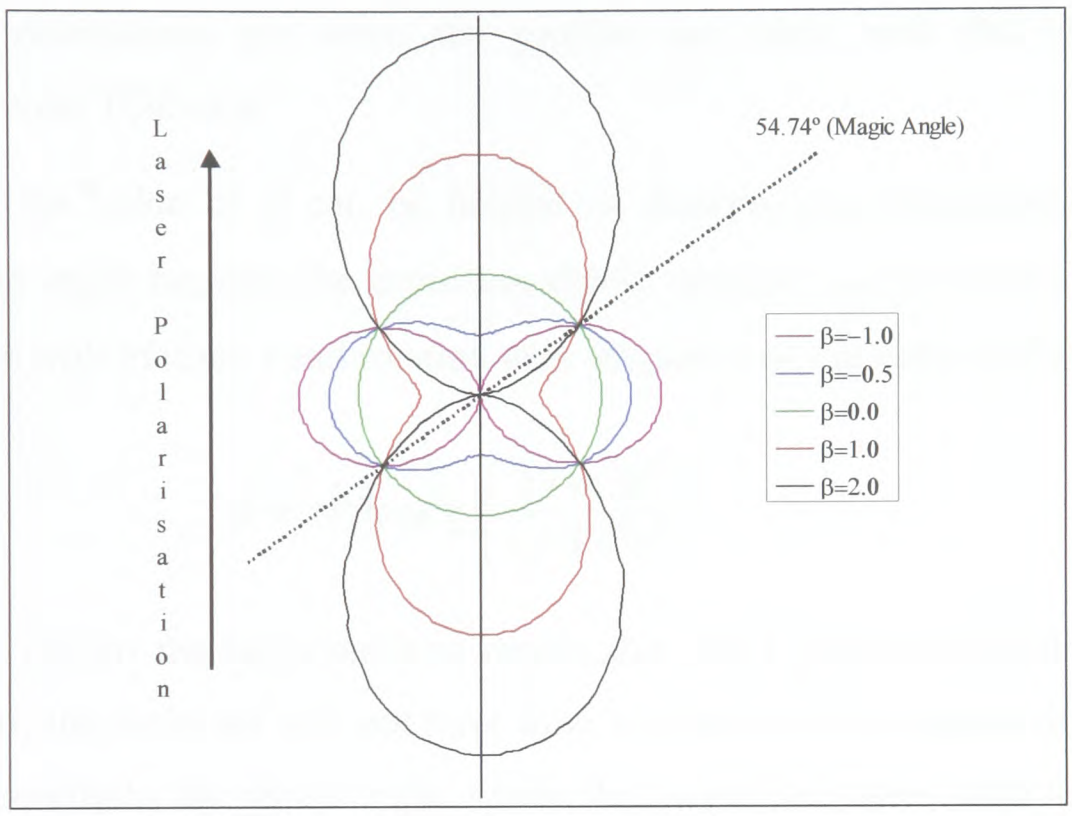

Figure 2-6 The effect of β on the angular distribution of fragment velocities. The radius at a given angle gives the probability of a fragment being emitted in that direction.

Furthermore, it should be noted that whilst Figure 2-6 describes the probability of recoil, it does not give a representation of the probability of an ion travelling at θ to the laser polarisation. To obtain the probability the angular distribution has to take into account a weighting that results from the need to sum over all values of ϕ, the angle about the z axis. The summation results in the probability that the fragment will be ejected at an angle θ being given by:

$$P(\mathbf{v}, \theta) = \frac{\sin\theta}{2}(1 + \beta[\mathbf{v}]P_2[\cos\theta])d\theta \qquad \textbf{(2-7)}$$

When β is positive the fragments are formed preferentially along the same axis as ε_p, and if negative the fragments preferentially travel perpendicularly to ε_p. As the angle between the TOF axis and the laser's polarisation can be adjusted, the projection of the fragments' velocities

onto the TOF axis, and therefore the detector, can be changed. If the limiting cases of β = -1 and β = 2 are considered the effects on the TOF profile are as follows. For β = -1 if the laser is polarised along the time-of-flight axis then a broad single peak would be seen, whereas if the laser was perpendicular two peaks would be observed; the situation is reversed for the case of β = 2 (i.e. parallel two peaks, perpendicular one peak).

Therefore, information relating to the angular distribution of the fragments can be obtained if profiles are taken at more then one angle between the TOF axis and the laser's polarisation. The most suitable orientations are when the profiles are taken with the laser parallel and perpendicular to the TOF axis.

Knowledge of the value of β can be helpful in determining characteristics of the parent molecule. If the angle between the transition dipole moment and the recoil vector is χ for a parent molecule with lifetime τ and rotating with frequency ω, the value of β is given by:

$$\beta = 2P_2[\cos\chi]\left(\frac{1+\omega^2\tau^2}{1+4\omega^2\tau^2}\right) \qquad \textbf{(2-8)}$$

This formula confirms the fairly intuitive results that, for a given rotational frequency, if the lifetime is short, the molecule will not have time to rotate and the angular distribution will be determined primarily by the recoil angle, whilst the longer the parent survives the more likely the fragment will be released in a random direction as a result of the molecules rotation. A value of β close to zero therefore indicates either that the fragment's recoil is at the magic angle to the transition dipole (thereby collapsing P_2) or that the parent's lifetime is significant compared to its rotational period. Conversely, to obtain a large value of β the parent's lifetime must be small compared to the rotational period and the recoil should be parallel to the transition moment.

To obtain data on the speed distribution the best solution is to fix the angle θ to the magic angle, at which the angular dependence collapses and the TOF profile becomes that of a "top hat". The effect of setting the polarisation to the magic angle can be seen in Figure 2-7. The figure also shows that for ions formed with several possible speeds, it should be comparatively easy to extract the speed distribution. For each of the layers the outer edge denotes the speed of that layer and, as long as the detection efficiency is not speed dependent, the area of the layer will give the relative population of fragments at a given speed.

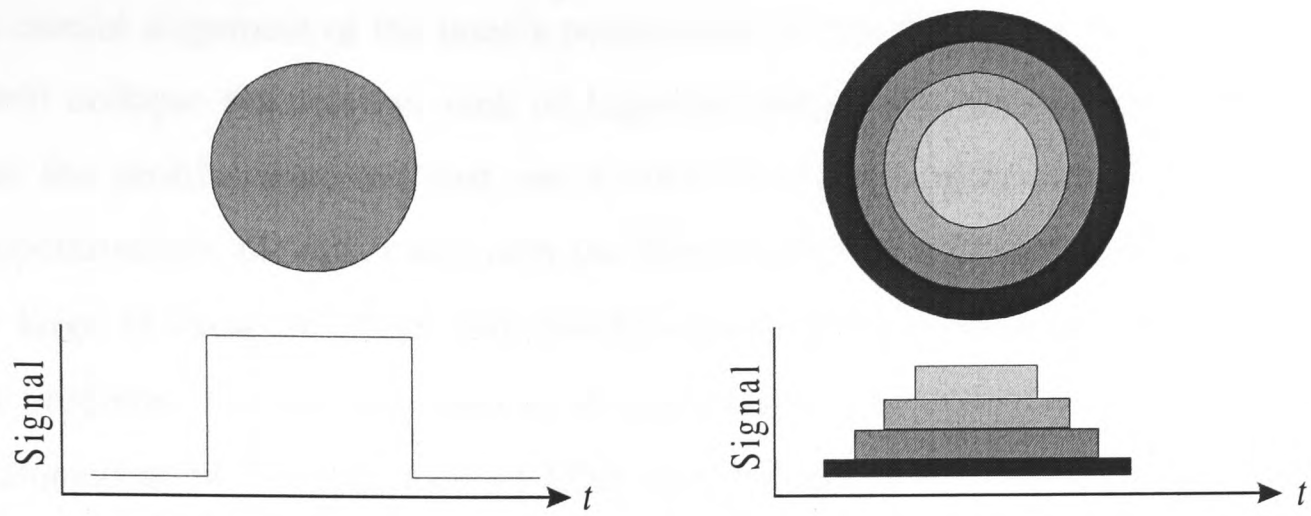

Figure 2-7 Expected time-of-flight profiles for photolysis at the magic angle. The left figures denotes the appearance of a monoenergetic ion source. The figure on the right shows how a distribution of speeds might appear.

2.6.3 Alignment between the fragments and probe laser

The efficiency of the production of ions depends on the alignment between the photofragment's transition moment for the REMPI scheme and the probe laser's polarisation. Should the distribution of this transition moment be anisotropic then the detection efficiency can be polarisation dependent. If there is a strong laboratory alignment of the transition moments, the time-of-flight profile can change significantly depending on the polarisation of the probe laser.

An example of angular momentum alignment can be observed form the dissociation of the molecule ABC into A + BC as shown in Figure 2-8. Assuming ABC has a bent configuration then, if the AB bond is broken impulsively, a torque will be imposed on the BC fragment such that it rotates in the plane of ABC. **J** is perpendicular to this rotation and therefore to the direction of motion. This alignment can be blurred by initial rotation of the parent molecule. For atomic fragments it is the alignment of the atom's total angular momentum rather than the rotational angular momentum. For $O(^1D)$ with its zero-spin component the total angular momentum is the same as the electron's angular momentum.

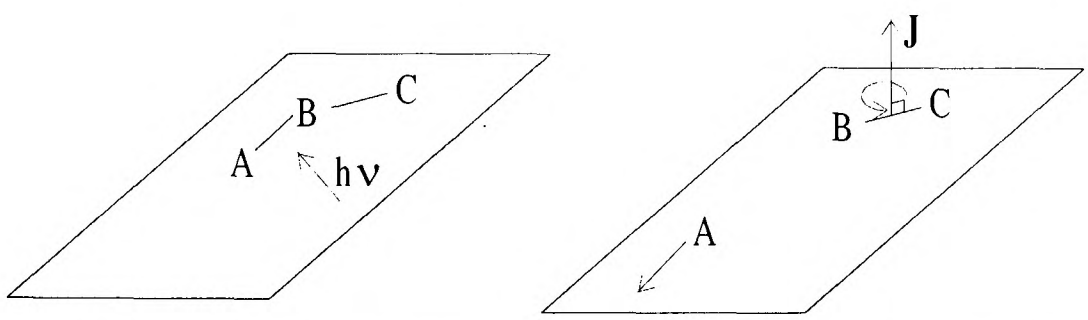

Figure 2-8 Example of v-J alignment, assuming no out of plane rotation.

Once again careful alignment of the laser's polarisation so that it lies at a suitable angle to the TOF axis will collapse the relevant rank of Legendre polynomial and remove any alignment effects from the profiles recorded that are a result of this component rank of the angular momentum polarisation. In many cases only the dipole component of the angular momentum is sufficiently large to cause an effect and therefore using linearly polarised radiation at 54.7° reduces any problems. For the vast majority of experiments recorded in this thesis, the REMPI beam was aligned at 54.7° to the time-of-flight axis collapsing the rank 2 component, which should be the dominant rank. Should higher rank components of the angular momentum have influence on the detectivity, then the use of the magic angle is not sufficient to ensure that the true speed distributions are being recorded. Evidence of alignment effects for both the atomic and molecular fragments from ozone dissociation, found by changing the polarisation of the REMPI beam, are discussed in Chapters 4 and 5.

2.6.4 Core extraction

The failure of all of the ions produced to impact on the detector can significantly change the profile that is recorded. The most common cause of an ion to miss the detector is that it has velocity components off the TOF axis which are sufficiently large that the ions' deviation from the centre line causes them to miss the detector (or in even more extreme cases hit the side of the drift tube or obstructions such as the voltage forming plates). The degree of deviation could be the result of a high off axis velocity or a long flight time, so that even ions with small off axis components will miss, or result from a small detection area. The effect that ions missing the detector has on a time-of-flight profile is known as core extraction and can be accidental, as a result of the instrument's characteristics, or deliberate, by placing an iris before the detector or by choice of voltages, in origin. The effect that core extraction can have on the time-of-flight profile can be seen in Figure 2-9.

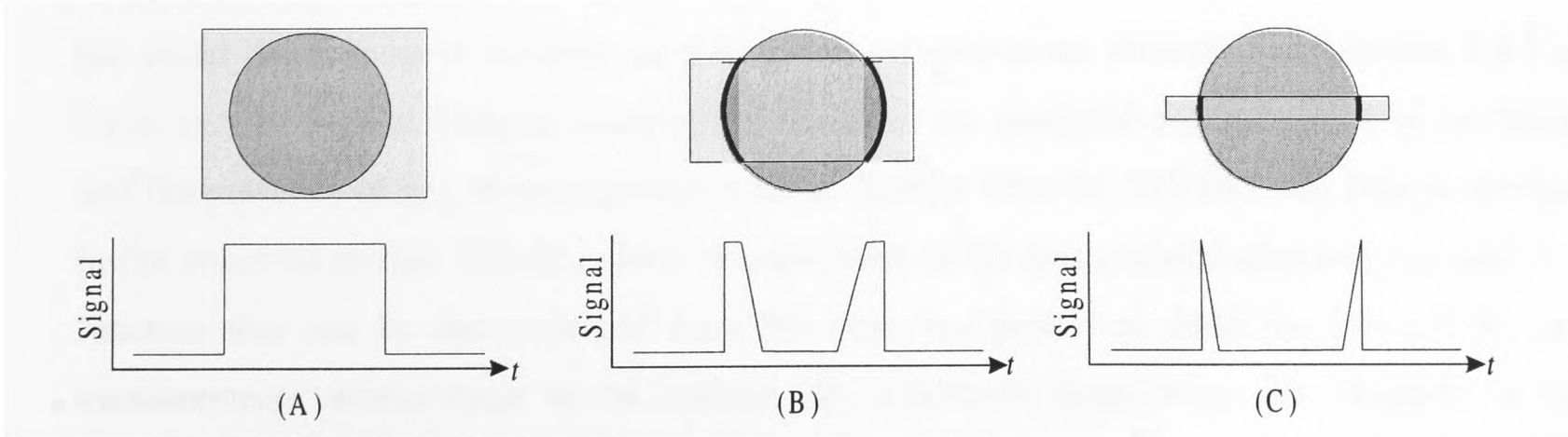

Figure 2-9 The effects of core extraction on a time of flight profile.

The starting point for a profile taken at the magic angle is case (A), where no core extraction is taking place and the full "top hat" signal is observed. As the degree of core extraction is increased, case (B), so that ions with a significant off axis component are no longer detected the signal starts to have a gap in the centre. The core extraction effect reaches the extreme example of (C), for true core extracting conditions when only fragments with a small off axis component are detected resulting in two sharp peaks that correspond to the maximum value of v_z and for the isotropic starting distribution the maximum speed of the fragment.

Core extraction can be a problem, mainly because of the reduction in the number of ions that are detected, but also because the detection efficiency has become velocity dependent, in that high speed fragments are more likely to have a significant off axis component. Furthermore, if the degree of core extraction is intermediate, and the speed distribution of the photofragments is unknown, information can be difficult to extract. For example in case (B), is the true signal monoenergetic and partially core extracted or is the system fully core extracting but with the fragments having a distribution of speeds. However, core extraction can play a very useful role in TOF mass spectrometry. The benefit arises from the ability to fit the value of v_z more accurately, as it is the true velocity along z that is measured rather than a projection of the velocity onto the z axis, which in turn will enable an improved value of β to be determined.

2.7 Time-of-flight profile simulation

There are two possible ways to extract information about the speed distribution from the TOF profiles that are obtained. The first is to apply equations (2-3) and (2-4) and extract the information directly from the data. The second is to compare the profile with a prediction of what the profile should look like.

Unfortunately the first approach is rarely applicable without obtaining a vast quantity of data to characterise the instrumental response to the production of ions. The inability to deconvolute the speed distribution is because, as well as the complications discussed in Sections 2.6.2 to 2.6.4, factors such as Doppler selection of the ions, the temporal characteristics of the lasers and the presence of any imhomogeneities in the fields within the TOFMS will lead to changes in the observed profile. Whilst careful measurement of the instrumental response can lead to a function that can be deconvoluted from the observed profile to yield the true profile, the measurements would have to be carried out whenever there were any changes in the experimental conditions and the effort required to carry out these measurements usually prevents the use of this approach.

Forward simulation is the most common method used to predict the shape of the TOF profiles. This approach models the expected production, motion and detection stages for individual ions and the TOF profile built up by "firing" a large number of these ions (typically a million plus) down the system. The program employed to analyse the TOF profiles within this thesis has been described in some depth by Pinot[4] but the salient features will be now be described.

The laser beams were modelled as having Gaussian profiles (spatially and temporally) and the initial parameters allowed for offsets between the lasers' centre points, including a factor to allow for timing jitter. If only one laser was in use the offsets were set to zero. The initial velocity of the parent molecule to be photolysed was calculated for motion resulting from the supersonic expansion from the pulsed valve. The probability that an ion would be formed travelling at an angle θ to the photolysis axis was calculated according to equation (2-7) and this probability was used as the weighting factor when the ion was added to the time bin at the end of its flight. Various factors that could affect the efficiency of the REMPI process were taken into account, such as the power dependence of the REMPI process, "fly out" of fragments from the REMPI probe region and Doppler shift of the REMPI transition for fragments that had significant off axis components of velocity. The change in REMPI efficiency resulting from alignment between the REMPI polarisation and the transition dipole moment as a result of angular momentum polarisation was not modelled.

The flight of each ion was modelled using equations (2-3) and (2-4). In addition to the ion's motion along the TOF axis, its motion perpendicular to the axis was modelled. By including all velocity components in the model the effects of core extraction were able to be modelled, with ions that arrived at the detector plane but outside of the detector radius not being included in the final profile; any ions that impacted the physical structure of the TOFMS were also discounted. As the electric fields within the TOFMS were not perfectly uniform, it was found necessary to introduce a transverse blurring function to improve the fit between the simulated and experimentally obtained profiles. At the end of the ion's flight the ion, weighted by its probability, was added to a time bin, the full set of which formed the basic time-of-flight profile. To complete the simulation the response of the MCP detector was convoluted with the basic time profile. The response function was determined by recording the average of 600 profiles formed by single ions hitting the detector.

The parameters required for the simulation were determined in a series of experiments on NO and Cl_2 and are reported by Pinot.[4]

2.8 Data Acquisition & Analysis

Data that had to be recorded electronically were measured by either one of two digital storage oscilloscopes (DSOs), these were a LeCroy 9350A, 500 MHz, 10^9 samples s^{-1}, 2 channels; and a LeCroy 9304 175 MHz, 10^8 samples s^{-1}, 4 channels; or an analogue to digital (A to D) converter (Amplicon PC27). The DSOs were used to record data that changed on a shot to shot basis; the DSO used for a measurement depended on the nature of the signal being measured. Fast signals, such as the MCP response and the output from the UV photodiodes, were typically measured on the 9350A oscilloscope, whilst the slower signals, such as the signal from the bulb ion amplifier or the pyroelectric energy detectors, were recorded on the 9304 oscilloscope. The A to D converter was used to measure signals that varied slowly over time, such as the temperature and pressure in the cell. The data were then passed to a computer *via* a GPIB interface, any desired parameters determined and the data then stored on the hard disk using purpose written software. The data stored would then be analysed further after the experiment.

2.8.1 Baseline Subtraction

To generate the desired signal it was necessary to work with high laser fluences. The use of high fluences had the undesired side effect that it was possible for signal to be generated *via* processes that were not those under investigation, e.g. non-resonant multiphoton ionisation or the REMPI pulse forming $O(^1D)$ which it could then detect. The experimental apparatus was set up to minimise the possibility of these undesired signals. When it was not possible to remove them completely, then these signals would have to be subtracted from the measured signal to obtain the true signal value. To obtain the necessary corrections, signals resulting from only the undesired processes were recorded as well as those that resulted from the full experiment. When possible the corrections needed were obtained within a single experimental run through the use of mechanical beam choppers which would operate in a binary fashion, in order to minimise any effects of changing conditions between runs. Therefore, the signal recorded would depend on the shot type, the shot type being determined by which lasers were on. When only one laser produced unwanted signal a sequence which had both lasers on and then only the laser producing the error signal was used. When it was possible that both lasers could produce undesired signals a four way sequence was used, which corresponded to both lasers on, the REMPI laser only on, the photolysis laser only on and neither laser on. When it was not possible to record the necessary corrections during an experimental run, the corrections

were obtained from a dedicated experiment carried out shortly before or after the main experiment.

What should have been the correct signal, S_2, can be calculated from the measured signals by the following methods.

For cases when both lasers produced unwanted signal and both lasers were therefore chopped,

$$S_2 = S_{rp} - S_r - S_p + S_0 \qquad \textbf{(2-9)}$$

For cases when only one of the lasers was chopped (z denoting the laser that was not chopped),

$$S_2 = S_{rp} - S_z \qquad \textbf{(2-10)}$$

where S_x denotes the signal obtained from shot type x and the shot types are "*rp*" both lasers on, "*r*" and "*p*" are when the REMPI and photolysis beams were unblocked respectively and S_0 the background signal when both lasers were blocked. The measurement "S_x" could be a simple measurement on the waveform displayed on the DSO, for example the amplitude of a Gentec power meter's response, or could be a complex measurement such as a full time-of-flight profile.

It was possible to measure the data required for the bulb based experiments on a shot to shot basis and the equation (2-9) or (2-10), as appropriate, applied for each shot. As it was not possible to subtract the actual single-laser signals for each two-laser shot the following method was used to determine an appropriate single-laser value. For each two-laser shot the desired laser power was compared against the powers recorded for the one-laser signals within 100 shots of the shot being calculated, the one-laser signal whose power most closely matched that of the two-laser shot was then used in the subtraction process. An alternative method was tested, wherein the mean signal of all recent shots of a similar energy (defined as being within 10% of the desired target value) was subtracted, but was found to improve insufficiently the accuracy of the results given the extra processing time required. The subtraction method employed resulted in the value of S_2 being known, which could then be further analysed as required discussed in Chapter 3 Section 4, for the case of quantum yields.

Because of limitations on the rate that time-of-flight profiles could be collected and stored by the computer, it was not sensible to record the waveforms generated by the time-of-flight spectrometer on a shot to shot basis. Therefore, the waveforms were averaged in real time by the oscilloscope and transferred to the computer at the end of the acquisition. Depending on the

experiment in progress the averaging was either carried out for each shot type during a run or several runs were made, one for each shot type. The relevant subtraction process was then carried out to derive the true two-laser signal.

References:

1 W. Demtroder, *Laser Spectroscopy 2nd Edition*, Springer-Verlag, Berlin 1996

2 S.M. Ball, *Studies of Laser Photolysis*, D.Phil thesis, Oxford University, 1995.

3 W.C. Wiley and I.H. McLaren, *Review of Scientific Instruments*, **26** (1955) 1150.

4 J.C. Pinot de Moira, *Laser Studies of Atmospheric Chemistry*, D.Phil. thesis, Oxford University, 1998.

Chapter 3

The Relative Quantum Yield of O(^{1}D) from the Near-UV Photolysis of Ozone

3.1 Introduction

The production of O(^{1}D) from the photolysis of ozone has many consequences for the Earth's atmosphere. Above 20 km altitude, and in the ozone layer in particular, the main absorption feature of ozone, the Hartley band, is responsible for filtering out the vast majority of harmful UV radiation between 230 and 290 nm.[1,2] In this spectral region photon absorption produces O(^{1}D) as the main atomic photofragment.[3,4] At lower altitudes the absorption of sunlight by ozone between 295 and 320 nm continues to remove harmful UV radiation and in the troposphere the production of O(^{1}D) is of particular importance because of its role in initiating a large proportion of atmospheric chemistry through the reaction of O(^{1}D) with water or methane to form OH radicals.

This Chapter presents the work that was carried out to determine the relative quantum yield of O(^{1}D) in the wavelength region corresponding to the thermodynamic limits to its production, between 306 and *ca.* 330 nm, at a number of temperatures, 227 K, 247 K, 273 K and 300 K. Of particular note is the fact that the O(^{1}D) produced from the photolysis of ozone was directly probed rather than its production being inferred from the detection of products generated by the reaction of O(^{1}D) with other compounds. The method for this, as discussed in Chapter 2, uses two lasers, the first to photolyse the ozone at the wavelength of interest and the second laser to probe the O(^{1}D) fragments directly *via* REMPI.

After a brief review of the possible pathways by which O(^{1}D) can be formed, a discussion on the potential sources of error in the experiments is presented, this is followed by the results of the experiments and a discussion comparing these results with those from other studies. Finally, the importance of the results is shown with emphasis on how the changing of the O(^{1}D) yield impacts on atmospheric models.

3.2 Production pathways and previous evidence

Theoretically at wavelengths above 300 nm O(^{1}D) can be produced *via* two pathways, one of which conserves the electron spin quantum number and one which does not. Additionally the spin-allowed pathways can have their thermodynamic limit modified if the parent ozone is vibrationally excited. The pathways and their wavelength limits are given by (3-1) to (3-3).

Spin-allowed $O_3\ (\nu_3 = 0) + h\nu \rightarrow O_2(a^1\Delta_g) + O(^1D) \quad \lambda \leq 310.3$ nm **(3-1)**[5]

Spin-allowed + Vibration $O_3\ (\nu_3 = 1) + h\nu \rightarrow O_2(a^1\Delta_g) + O(^1D) \quad \lambda \leq 320.7$ nm **(3-2)**[6]

Spin-forbidden $O_3 + h\nu \rightarrow O_2(X^3\Sigma^-_g) + O(^1D) \quad \lambda \leq 410.6$ nm **(3-3)**[5]

Pathway (3-1) has been identified as the main dissociation pathway for ozone being photolysed by radiation in the main absorption feature of ozone, the Hartley Band. Despite early evidence of O(^{1}D) production above the thermodynamic limit of the spin-allowed pathway, as described in Chapter 1, it has taken a long time for the evidence to be accepted. This acceptance has come in two stages; first, that vibrationally excited ozone can result in the production of O(^{1}D) *via* the spin-allowed pathway (3-2);[7,8,9] and second, that only during the course of the research presented in this thesis has sufficient compelling evidence for its production *via* the spin-forbidden pathway (3-3) been published[6,10,11] for it to be accepted as occurring.

3.3 Sources of error

In order for accurate values of the quantum yields to be obtained at a known precision a number of factors must be taken into account. Sources of error could lead to random, or systematic, errors in the value determined for the quantum yield. Whilst random errors cause uncertainty about the true value, their effect can be reduced by increasing the number of repetitions of the experiment. Systematic errors are much more problematic as they cannot be reduced in the same way.

3.3.1 Random errors

The errors quoted in the quantum yield results given later are the standard deviations (1σ) obtained from a number of experiments. Typically at least ten repetitions of an experimental run were carried out, within which at least 30 repetitions for each necessary measurement were made. The following are some of the most common sources of error.

3.3.1.1 Changing experimental conditions

To prevent any changes in the experimental conditions resulting in systematic errors, individual experiments were conducted in as short in time as practical, typically three minutes for single wavelength measurements and seven minutes when the wavelength was scanned. Keeping the experiments to a short run time was to prevent factors such as: decreasing ozone concentration, drifts in the value of the laser powers (caused by heating effects or dye efficiencies), drifts in the time between the lasers firing (due to changing conditions in the excimer thyratron or after changing the Nd:YAG laser output) and changing cell temperature, from becoming systematic problems.

3.3.1.2 Variation in laser power

The output of the lasers was not constant. The dye laser made by LAS, acting as the photolysis laser, was the more consistent, with its output typically remaining within 3% of the mean, whilst the REMPI laser output (having undergone two non-linear processes) could change significantly. For a typical run 90% of the shots showed energies which obeyed a normal distribution with a standard deviation of 10% of the mean with the rest being between 50% and 75% of the mean. However, this source of error can be allowed for (subject to the factors listed in Section 3.3.2.2) as long as the relationship between the laser energy and signal generated is known. The potential error can be allowed for because, assuming the laser energy does not change much from its mean value, the curves showing the variation of signal with photolysis and REMPI laser energy in Section 3.3.2.2 can be approximated by linear and quadratic functions respectively. A small source of error will remain however as the measurement of the laser energy was correct to $\pm$ 5% and this error can not be accounted for in the renormalisation.

3.3.1.3 Beam overlap

Beam overlap is both a random and systematic error source. The random element comes from the inability to ensure that the two lasers overlap in the same manner for all experiments. The beams could move as a result of changing wavelength, autotracker operation, backlash on the micrometers controlling the lens positions and heating effects within optics. Most of the possible causes of beam movement can be minimised with suitable operational procedures, e.g. small changes in wavelength, optimising the autotracker position regularly, being aware of possible micrometer backlash, allowing the equipment to run for some time before taking measurements to allow temperatures to stabilise and maximising the signal on a regular basis.

3.3.1.4 Laser Timing

For reasons discussed more fully in Section 3.3.2.3, any variation in the delay between the two lasers can result in a change in the measured signal. Most of the timing equipment was sufficiently stable for the variation in the delay not to be a problem; however, as a result of an ageing thyratron in the excimer laser, the time that the excimer fired in relation to its input trigger was subject to a variable jitter, typically ± 10 ns. To ensure that excessive variation in the signal did not occur the timing delay was closely monitored and the variable delay generator set to maintain a mean delay of 5 ns. If the delay was more than 20 ns then the data point was treated as invalid.

3.3.2 Systematic errors

Systematic errors are the bane of the experimentalist as they can be difficult to evaluate and, unlike random errors, they can not be reduced by increasing the number of repetitions. Those of relevance to this work will now be discussed.

3.3.2.1 Ozone quality

During the course of these experiments two different methods of filling the experimental cell with ozone were used. The first, used for the lowest temperature, was to have continuous production and flow of approximately 2% ozone in oxygen through the cell, with the inlet and outlet valves being set for the desired cell pressure. Whilst this method prevents stagnation of the sample gas, the exact percentage of ozone within the cell was variable and could not be monitored, using the experimental apparatus employed, during the course of the experiment. However, these fluctuations were found to be variable with time and thus generated random errors. The second and most commonly used method was to introduce the desired quantity of the ozone / oxygen mix into the cell and work with the mixture until degradation of the signal was observed. This degradation was due to a slow reduction in the ozone percentage, primarily due to photolysis. The degradation, as a result of the conversion of O_3 to O_2, also resulted in a slow increase in the cell pressure, a problem if the ion amplification process is pressure dependent. Keeping the experimental times short, and working with calibration points within the runs, ensures that any changes in the signal level caused by changes in the gas composition should not be systematic in nature.

3.3.2.2 Laser fluence

The REMPI process is not very efficient as a result of the multiple photons required to ionise the species under investigation. Thus to generate a large signal it is desirable to use high photon densities and these densities were achieved by focusing the laser beams. However, these high photon densities can have significant undesirable effects. As it was assumed that the length of the laser pulses did not change significantly shot to shot then the measurable parameter of interest in determining the laser fluence becomes the energy of the pulse.

As the REMPI laser itself forms O(^{1}D) from the photolysis of ozone, the O(^{1}D) signal from the REMPI laser alone has a higher order energy dependence than the signal from the two-laser process. The relationship between REMPI energy and O(^{1}D) ion signal for the cases of REMPI-only and two-laser experiments is shown in Figure 3-1.

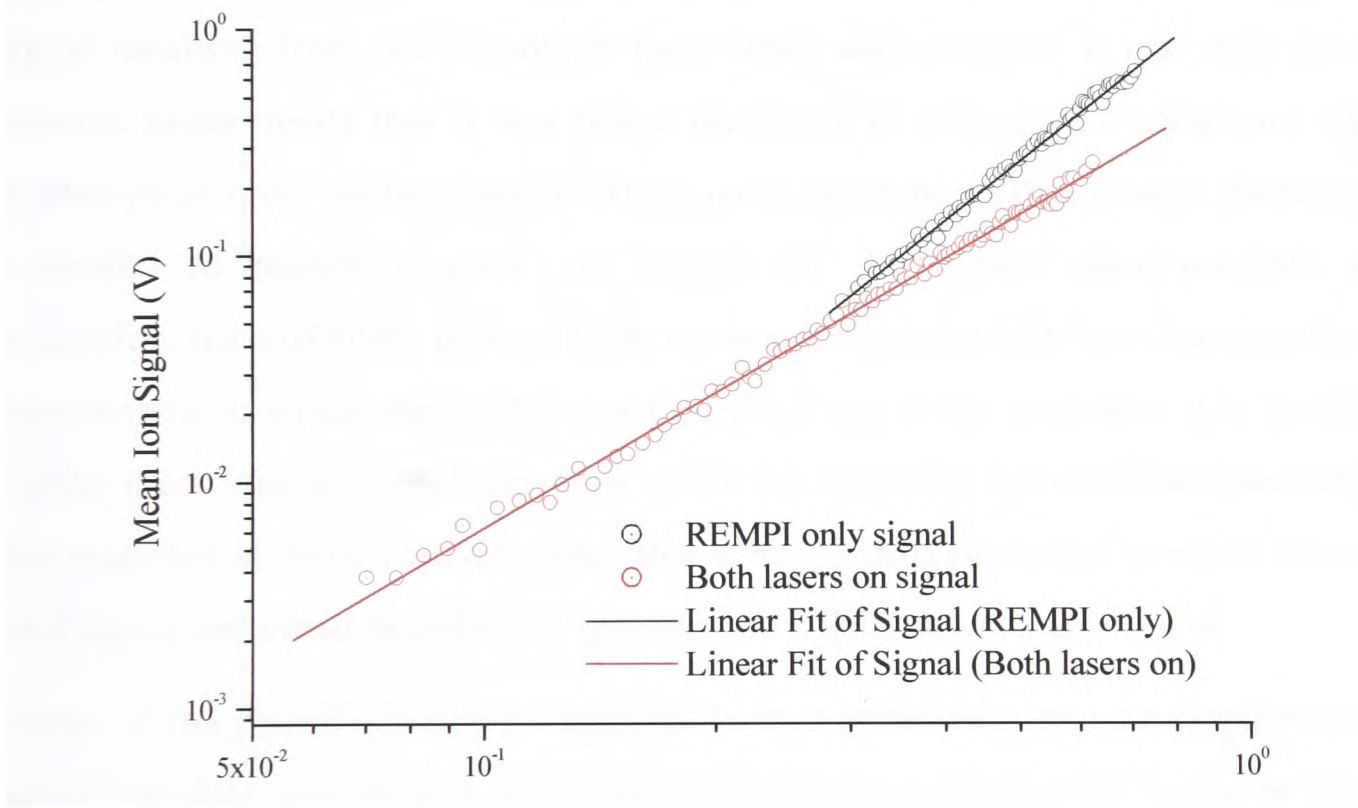

Figure 3-1 Determination of the REMPI energy dependence for the ion signal. Note the gain of the ion amplifier was changed between the two experiments.

From the linear fits made on the data shown in Figure 3-1, it has been determined that the ion signal in the REMPI-only experiment, was proportional to the REMPI energy measurement to the power of 2.7 ± 0.3. When both lasers were on (photolysis wavelength 308 nm at low energy) the dependence was 1.98 ± 0.2. Therefore, as the REMPI energy is increased, the one-laser signal grows faster than the total two-laser signal and so contributes a larger proportion to the measured signal. The use of a high REMPI laser fluence to obtain a large signal will make the background subtraction process increasingly difficult and inaccurate. Therefore, the REMPI

energy was set so that in a two-laser signal (photolysis wavelength 312 nm, chosen as it is after the sharp fall in the quantum yield) the REMPI laser's contribution was no more than 10%. As the photolysis wavelength was increased the REMPI-only contribution became proportionally larger but it was kept below 50% of the entire signal.

There are two concerns when high photolysis energies are employed. The first is that the ion signal due to $O(^1D)$ could be contaminated with ions formed by other processes and the second is that saturation of the photolysis process could occur. The first arises as, in addition to general non resonant multiphoton processes, there are a number of molecular oxygen REMPI transitions in the wavelength region to be covered. The main potential REMPI contaminants are the $O_2(a^1\Delta_g)$ REMPI transitions around 311 nm and 320 nm. The probability of REMPI contamination was minimised by setting the position of the photolysis lens such that even when the photolysis wavelength was set to a known $O_2(a^1\Delta_g)$ REMPI transition, 321.784 nm, the signal resulting from the photolysis laser alone was minimal. It was only for the lowest temperature experiments that it was found necessary to subtract a background signal as the lower absorption cross section and $O(^1D)$ quantum yield meant that greater photolysis energies were needed to record a good ion signal. To investigate other possible sources of contamination, time-of-flight profiles were recorded, covering both the O and the O_2 masses, at the wavelengths at which the $O(^1D)$ quantum yield was to be measured. The profiles showed that whilst there was some enhancement of the O_2^+ detected between one-laser and two-laser profiles recorded at certain wavelengths, this enhancement amounted to much less than 1% of the total signal and could therefore be ignored as a significant source of error.

Saturation of the photolysis step is undesirable as it invalidates two assumptions made in the analysis of the data, namely that the signal is linearly dependent on the energy of the photolysis laser pulse and that the local ozone concentration is not significantly changed by dissociation caused by the photolysis laser. Taking the latter, more minor, problem first, if the ozone concentration were to be significantly depleted as a result of the photolysis step, then any REMPI-only signal that needs to be subtracted becomes more difficult to determine. This is because REMPI-only ion signals are measured at full ozone concentration and these values would be overestimates of the true REMPI-only contribution in a two-laser experiment. However, this is less of a problem than the non-linear effects as an incorrect estimate of the REMPI-only signal is most likely to affect experiments at long wavelengths, as the two-laser : REMPI-only signal ratio is at its lowest here; but because of the falling cross section measurements at long wavelengths are those least likely to suffer from a saturation problem.

It is possible to see saturation of the photolysis step as it shows up as a non-linear function in how the signal relates to the laser energy, such as is shown in Figure 3-2. The non-linearity would take the form of a smaller signal being measured at high energies than would be expected if a linear relationship was being followed. An example of the non-linearity can be seen in Figure 3-2 for 308 nm as the signal above 1.5 mJ is below the line suggested by the data below 0.5 mJ. In principle it is possible to correct for linearity errors by measuring the signal generated over a wide range of laser energies and determining a correction factor based upon these data. However, in practice determining the correction is not feasible, particularly as it would have to be repeated at every wavelength at which measurements were being made to ensure the appropriate correction was being made.

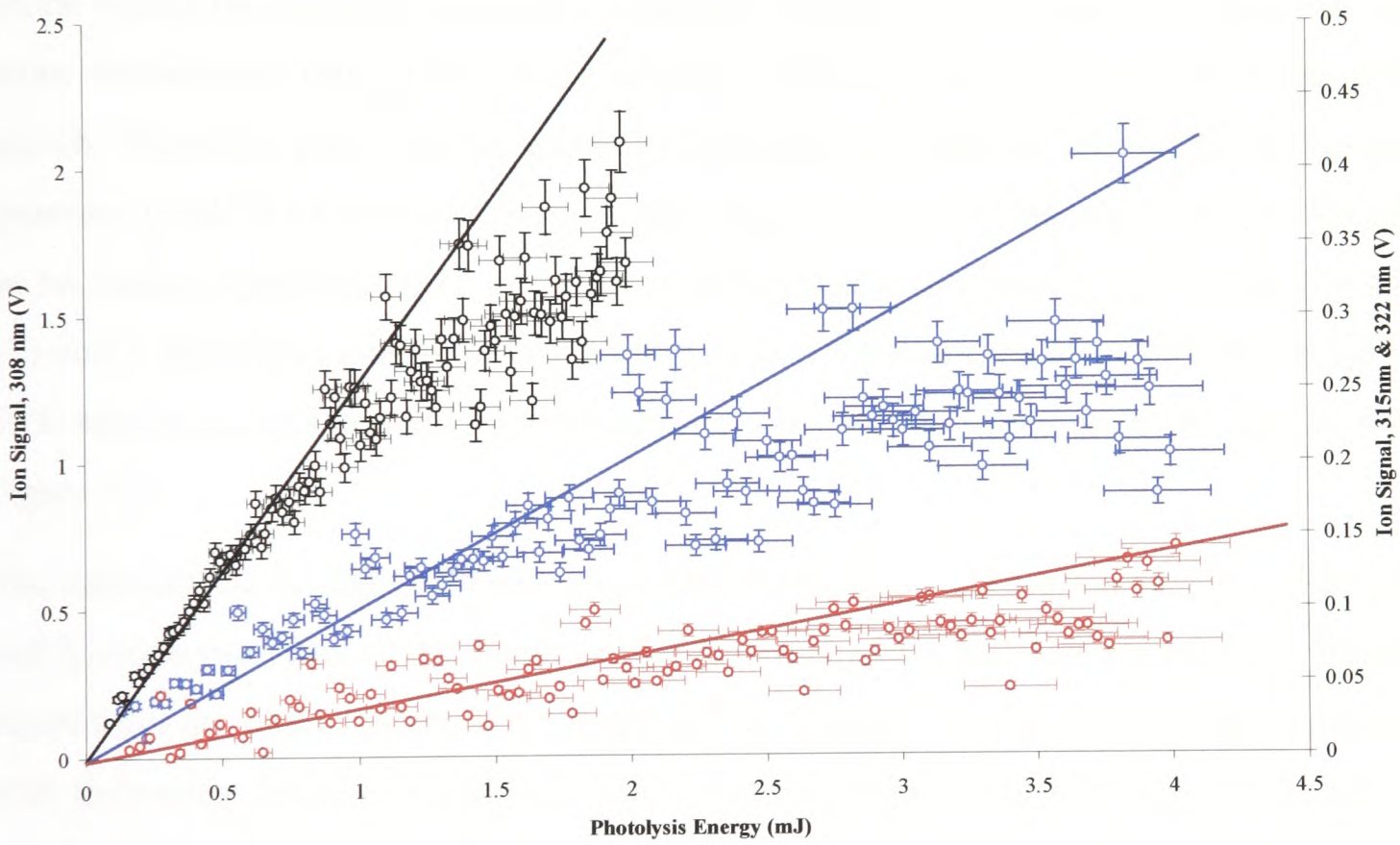

Figure 3-2 Comparison of how the generated O(^{1}D) ion signal varies with photolysis power at various wavelengths (Black = 308 nm, Blue = 315 nm, Red = 322 nm).

As an order of magnitude calculation it is possible to estimate the degree of saturation by taking the product of the beam fluence (photons cm^{-2}) and the absorption cross section (cm^2 molecule^{-1}). The result of the calculation gives a rough figure of the percentage of ozone that is dissociated. Under normal operating conditions this figure was less than 10% at 308 nm and 322 nm. There is a possible problem, however, at wavelengths between 310 nm and 320 nm. The problem is because whilst the measure is less than 10% for ground state ozone, it reaches 50% for ozone which is vibrationally excited, because this excited ozone has a much larger cross section. McDade and McGrath[12] found that the peak in the absorption spectrum shifted

4000 cm^{-1} to the red for vibrationally excited ozone and Adler-Golden *et al.*[7] determined the red shift to be 3500 cm^{-1}. Michelsen *et al.*[9] determined vibrational cross sections by examining the temperature dependence of the cross section finding a significant increase for vibrationally excited ozone. In the region of interest, McDade and McGrath show a shift of *ca.* 2000 cm^{-1}, which at 315 nm corresponds to a σ_v: σ_0 ratio of *ca.* 17:1; the ratio from Adler-Golden is *ca.* 25:1 at this wavelength, and that from Michelsen *et al. ca.* 30:1. Also, Zittel and Little[13] reported an O(^{1}D) yield at 314.5 nm up to 70 times greater when ozone was irradiated with a CO_2 laser tuned to the ν_3 vibration of ozone prior to photolysis. They attributed the increased production of O(^{1}D) to a mixture of an enhanced quantum yield (ϕ_v : ϕ_0 = 6 ± 2:1) and an enhanced absorption cross section (σ_v: $\sigma_0 \geq 8.4$). Saturation of 50% of the vibrationally excited ozone would be expected to cause a noticeable degree of non-linearity despite the fact that at room temperature only 0.6% of the ozone is excited with one quantum in the asymmetric stretch. Therefore, care must be taken to ensure that this effect is allowed for in the final O(^{1}D) quantum yield. If we consider normal operating conditions in the region where this effect will be becoming significant (312 nm), then a vibrationally enhanced cross section (by a factor of 12) and a photolysis energy of 0.5 mJ in a cross sectional area of $8x10^{-4}$ cm^{-2} would imply a 60% saturation, and certainly would indicate a marked deviation from linearity in the data of Figure 3-2.

The calculations of degree of saturation described previously used a very simplistic approach and a crude estimate of the beam profile and it may be that a more complex model would account for the observations. It is theoretically possible to model how the signal should change with increasing fluence, modelling each ion generating process with appropriate functions for their spatial and temporal characteristics (examples of models can be found in the work of Ball[14] and Pinot[15]). In practice it was found that it was too difficult to determine suitable functions that accurately modelled the interaction of the photolysis and REMPI lasers with the ozone.

Therefore, a more pragmatic solution was sought in which experiments were carried out at room temperature to determine the extent to which any saturation was affecting the quantum yields measured. The solution took two forms; for the first, measurements such as those in Figure 3-2 were made; and for the second, the quantum yield at 312 nm was measured relative to that at 308 nm (using the same method of determining the quantum yield that was used in the 227 K experiments). In the first method, whilst it is possible to see in Figure 3-2 the effect of saturation at high laser energies, these energies are well above those at which quantum yield

data were taken. The results of the second approach to determine if there is significant saturation of the vibrational channel are shown in Figure 3-3. Saturation of the signal at 312 nm should show up as a falling of the relative quantum yield and, whilst a slight downward trend could be being observed, there is no significant change in the relative quantum yield over the wavelengths investigated, within the error limits of the measurements.

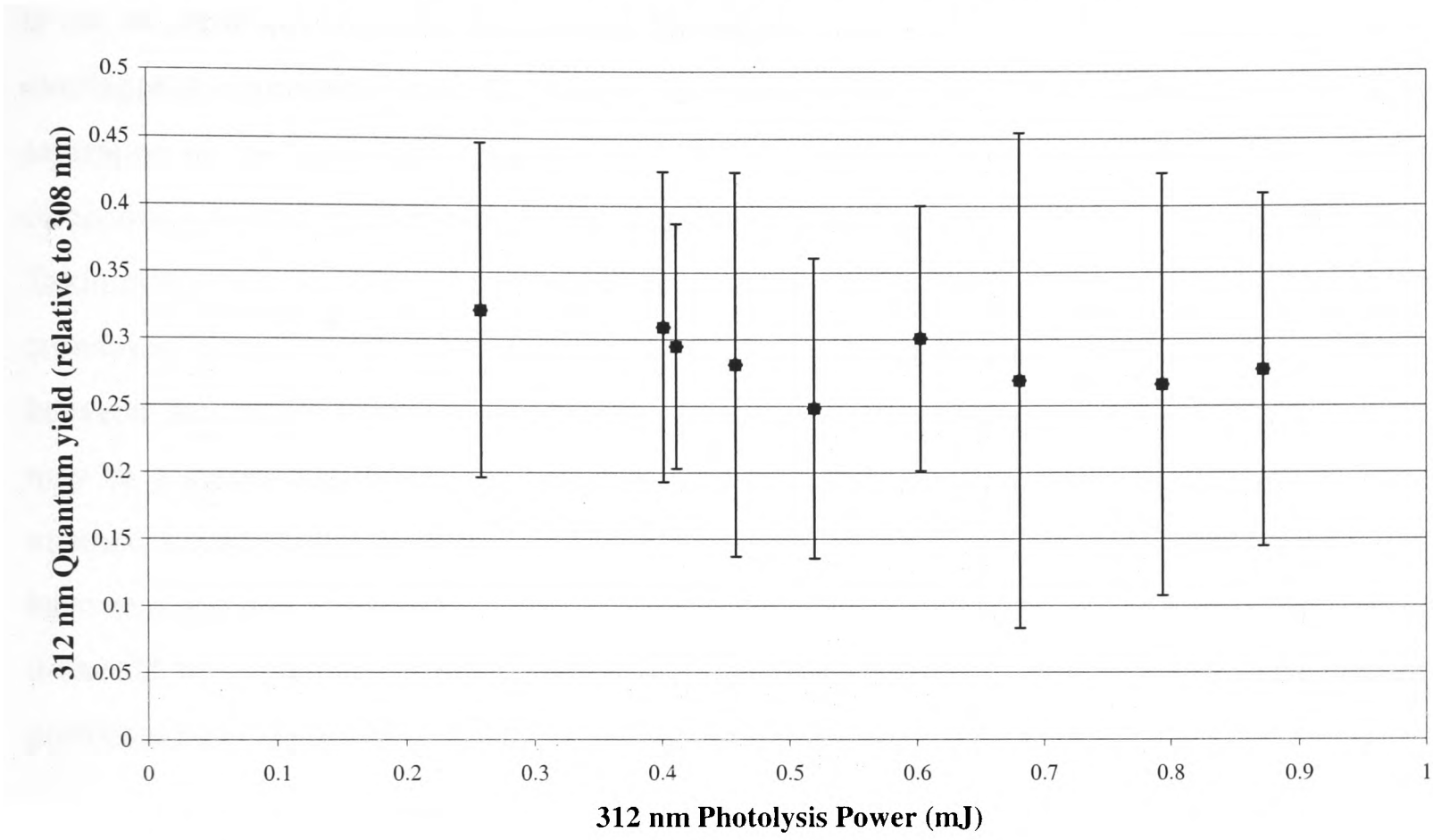

Figure 3-3 Plot of the relative quantum yield between λ = 308 nm and λ = 312 nm as the photolysis power is increased. The photolysis energy at 308 nm was constant and set so that the signal was not saturated.

The data of Figure 3-2 were used to determine the maximum photolysis energies below which saturation would not cause deviation from linearity, namely 0.6 mJ at 308 nm, 1.5 mJ at 315 nm and 2.5 mJ at 322 nm. At wavelengths between these fixed values, maximum energies were interpolated by taking into account the relative absorption cross sections. In practice the laser was run at typically 0.5, 1.2 and 2 mJ at the set wavelengths respectively.

To confirm that this approach was valid a comparison between the quantum yields reported here and those of Takahashi *et al.*[16] was made. The comparison was made with the data of Takahashi *et al.* as their detection method was a direct measure of the O(^{1}D) and O(^{3}P) products; thereby removing difficulties that could have been experienced if comparison were made against data from indirect detection methods. Takahashi *et al.* tested the linearity of their signal against photolysis power and did not observe any saturation at any of the wavelengths

tested. Their lack of saturation is not unexpected as the LIF technique that they employed is more sensitive than the REMPI method employed here* and as a result did not require the photolysis laser to be focused†. The comparison showed that for wavelengths between 310 nm and 320 nm the quantum yields reported here are on average 0.04 lower than those reported by Takahashi *et al.* Once errors on the Takahashi *et al.* data are taken into account this difference is not as great as it initially seems with the upper error bars of the data reported here almost overlapping completely with the lower error bars on the data from Takahashi *et al.* Should saturation of the vibrational channel have been a problem in the data reported here, then the corrections needed would increase the quantum yield reported to more in-line with the data of Takahashi *et al.* However, if further comparisons are made to other groups' measurements, this correction would move the data away from their overall average. The increased difference between the results from the direct and indirect probing techniques, would suggest that there may be a systematic difference between measuring the quantum yields in a direct or indirect manner, a discrepancy that will be discussed briefly in Section 3.7. Overall the conclusion has been reached that the quantum yields measured are a fair reflection of the true values, but that it should be noted that they are likely to be towards the lower limits if undetected saturation problems have occurred.

3.3.2.3 Laser timing

For a number of reasons the concentration of $O(^1D)$ falls rapidly once it has been produced by photolysis. To minimise the time available for the loss processes, and any process that could lead to the production of additional $O(^1D)$ as a result of any reactions of photofragments, the time between the production and detection of the $O(^1D)$ should be kept short, and with minimal variation, to avoid systematic errors. Figure 3-4 shows how the ion signal varied with delay between the laser pulses along with a model based on the main expected loss processes, which are the reaction between the $O(^1D)$ and the remaining ozone (rate constant at 298 K, 2.4×10^{-10} cm^3 $molecule^{-1}$ s^{-1} [4]) and its quenching by molecular oxygen (rate constant at 298 K, 4×10^{-11} cm^3 $molecule^{-1}$ s^{-1} [4]).

---

* Whilst the detection of ions formed from REMPI can be achieved with greater efficiency that detecting the photons emitted in LIF, the LIF process has a greater probability of occurring. High REMPI photon densities increase the signal when only a small number of species are available to be detected but these densities could not be employed in these experiments as a result of the large background signal that they would generate.

† The photolysis beam for Takahashi *et al.* was ≈ 4 mm diameter as opposed to ≈ 0.16 mm in the REMPI experiment and was of similar energy. Therefore, the degree of saturation would be over 600 times less than experienced in the REMPI based experiments.

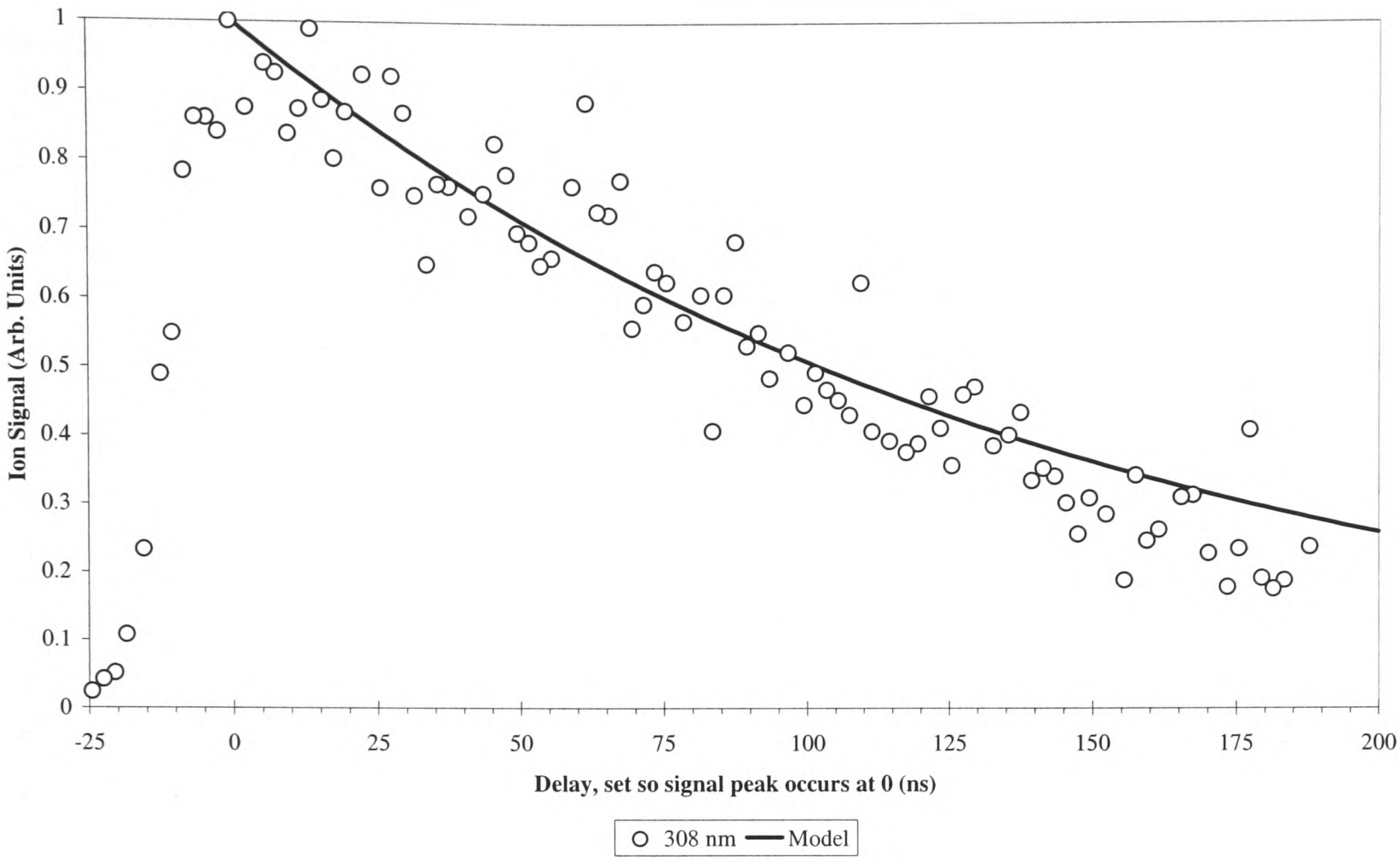

Figure 3-4 Decay of the O(^{1}D) ion signal with time. The timebase has been set so that the signal maximum, which should be when both lasers fire simultaneously, occurs at t = 0 ns.

A loss process, which could make up the small difference between the data and model, is that O(^{1}D) could leave the probe region in the time between the two lasers firing. For all of these loss processes it should also be noted that translationally excited O(^{1}D) could behave in a different way from translationally cold O(^{1}D), causing a greater loss of fast O(^{1}D) than slow O(^{1}D), which could result in an detection efficiency that is O(^{1}D) speed dependent. One factor that the O(^{1}D) speed distribution depends upon is the dissociating wavelength, as the energy of the photon dictates the dissociation pathways available and the energy available to be portioned amongst the fragments formed. Examination of the time dependence of the signal was therefore carried out at wavelengths typical of each pathway. O(^{1}D) formed from the vibrationless spin-allowed channel close to the thermodynamic limit will have very low speeds, that from the vibrationally mediated channel can have up to a further 695 cm^{-1} of kinetic energy which corresponds to a speed of *ca.* 1000 m s^{-1}, whilst the O(^{1}D) from the spin-forbidden process can be travelling at speeds of up to 2800 m s^{-1} (depending on the internal energy of the O_2 co-fragment).

Given that the fast fragments should travel a greater distance between the photolysis and REMPI lasers firing, it is possible that they would have a greater chance of either reacting or

diffusing out of the probed region. In the typical time between the lasers firing, a fast $O(^1D)$ should suffer two collisions during a room temperature experiment, whilst the slow $O(^1D)$ would have less than one. Additionally the higher kinetic energy of the fast $O(^1D)$ should aid it to climb and possibly overcome reaction barriers. For the possible additional loss process of diffusion given that the probe laser's beam size is much smaller than the pump laser's (~90 μm compared to ~250 μm) it is not expected that there should be a significant loss of ions from the region to be probed. The potential loss of ions was checked by a simple Monte Carlo simulation which modelled the beam profiles and the motion of the ions. The initial ion positions were modelled by a Gaussian distribution and their motions by an isotropic random distribution of velocities, the maximum speed of which was 2800 m s^{-1}. The simulation showed that there was an increase in the effective beam width over the initial Gaussian distribution, but there should be no significant loss of ions. For both of these possible loss factors a comparison of the rate of signal loss for slow (generated at 308 nm) and fast (generated at 316.5 nm and 320.5 nm) $O(^1D)$ should give a clear indication if one of these processes is of concern.

As can be seen from Figure 3-5 the two loss rates appear to be fairly similar though at the longer wavelengths there does appear to be a small peak at short delays. Whilst the large experimental errors in these data, ± 20%, could account for the differences, it may be that there is a real effect being measured. If there is a real effect and it is caused by a difference in the reaction rates for slow and fast $O(^1D)$ a simple model has shown that the rate constants must be about two orders of magnitude higher than the standard published values which were used to generate the model used in Figure 3-4. Given the magnitude of the errors on these data it is concluded that, if the timing is set to a delay of 5 ns, there is no clear significant systematic error attributable to the faster $O(^1D)$. If there is any effect resulting from high speed $O(^1D)$ it should result in the measurements made being an underestimate of the true quantum yield.

The final possible problem relating to the delay between the two lasers firing would be if the REMPI process were to photolyse the molecular products of the initial photolysis step forming $O(^1D)$ which the REMPI pulse would then detect. The problem is that $O(^1D)$ produced in this fashion could not be differentiated from $O(^1D)$ produced in the initial step using the basic ion detection system used in the gathering of the quantum yield data. The production of $O(^1D)$ from the molecular product can be discounted as a problem for the following reasons.

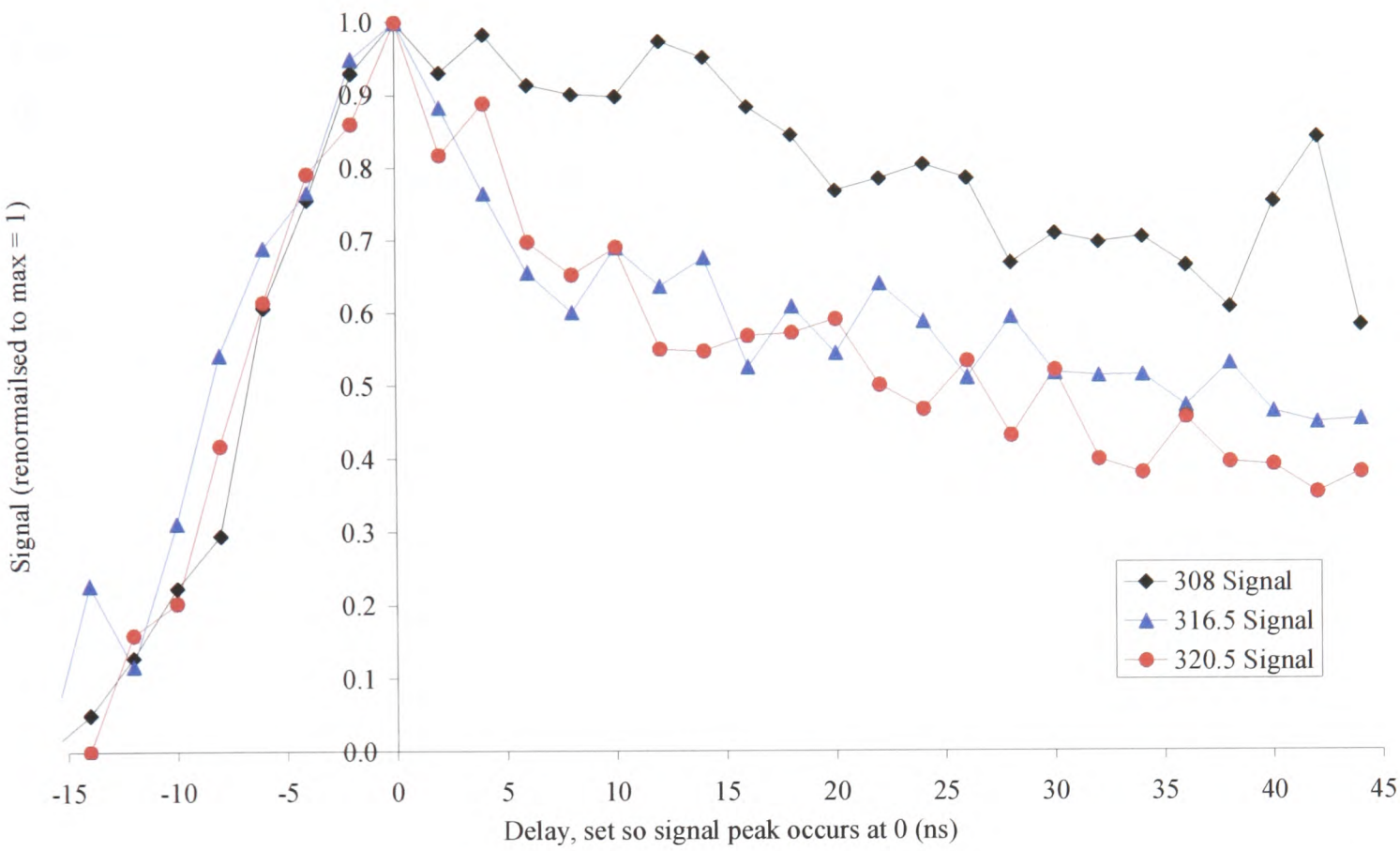

Figure 3-5 Variation in Signal with timing delay for several wavelengths. Negative time relates to the REMPI laser firing before the photolysis laser.

First, the molecular products are expected to react much more slowly than the highly excited O(^{1}D) and the production of O(^{1}D) from them is not observed in the time dependence of the two-laser signals in Figure 3-4 and Figure 3-5, which it is not. Second, the squared energy dependence of the ion signal on REMPI energy would not hold if the REMPI laser was also responsible for part of the photolysis step; a dependence closer to cubic would be expected. Finally, no additional channels are observed when similar experiments are carried out in the TOF system.

3.3.2.4 Doppler selection of fragments

An O(^{1}D) atom which is travelling with an appreciable velocity component along the laser propagation axis will have the REMPI transition Doppler shifted. The shift could affect the efficiency of the detection system if the Doppler shift is significant compared to the bandwidth of the probe laser. Furthermore, as a result of the different pathways available as the photolysis wavelength is changed, the kinetic energy of the ions and therefore their Doppler shift will be a function of the photolysis wavelength.

This problem has been observed by Takahashi *et al.*,[16] the only other group that directly measured the O(^{1}D) product. In their first work on this problem they did not investigate any

Doppler width influence on the signal as, at the time, the $O(^1D)$ was assumed to come from the vibrationally excited channel (3-2) which should not produce $O(^1D)$ at significant speeds.[17] In their later work[16], reported when more evidence of the spin-forbidden channel (3-3) had been reported, they determined that they would not have the same detection efficiency for the slow and fast channels by measuring Doppler profiles of the $O(^1D)$ produced across their wavelength range (305-329 nm). They found that above 310 nm the linewidth increased smoothly as the wavelength increased and therefore a correction factor would be required to allow for the change in detection efficiency (determined as 1.25 × signal recorded at 328 nm when measured relative to 305 nm at 295 K). Interestingly there was not much difference between the quantum yield results reported in the two publications, one with and one without such a correction. Bearing in mind this possible problem it was necessary to determine if the current experimental set up also required such a conversion factor.

The first step was to determine the bandwidth of the transition and this was done using conditions that should have ensured that the $O(^1D)$ was translationally relaxed before it was probed (80 Torr He, ~10 Torr O_2, 0.2 Torr O_3 20 ns between lasers, photolysis wavelength 306 nm). The transition bandwidth was found to be 0.7 cm^{-1} FWHM by scanning the detection laser across the transition and monitoring the ion current generated. The Doppler width due to the thermal motion should be 0.15 cm^{-1}, leaving an instrumental bandwidth of 0.68 cm^{-1}. To determine the Doppler bandwidth at typical wavelengths for each pathway, the REMPI laser was scanned across the transition whilst the sample was being photolysed and the resulting ion signal recorded. Normal quantum yield experimental conditions were used for these experiments.

Figure 3-6 shows the results of measurements made of the detected ion signal for each of the different process regions, with the profiles renormalised to their maximum values. It can be seen that the width of the profiles increases as the wavelength is increased. The form of these profiles should be the convolution of the instrumental bandwidth with the speed distribution which has been projected onto the direction of laser propagation. The overall speed distribution at a given wavelength should be a function of which processes are active (as these control the energy and angular distribution of the $O(^1D)$ fragments) and their relative strengths.

Unfortunately the velocity distribution is difficult to determine accurately for $O(^1D)$ as a result of the many possible states of its molecular co-fragment and uncertainties in the anisotropy parameter, β, for the different channels. It is believed that β is positive for all channels but decreases as the wavelength is increased, also velocity dependent β values have been

observed.[18] However, by measuring the Doppler profile we automatically measure the axial component of the fragment's velocity and so, once the instrumental bandwidth of 0.68 cm^{-1} has been deconvoluted from these profiles, the wavelength dependent bandwidths can be determined. These were found to be amenable to fitting by Gaussian functions and the results were 0.45 cm^{-1} at 308 nm, 0.68 cm^{-1} at 315 nm and 0.90 cm^{-1} at 322 nm. To determine the extent of the possible loss of fragments an analysis of the Gaussian curves was carried out. The analysis showed that if the detection limit of the instrumental bandwidth was set such that it missed 2.3% (2σ width) of the ions, then for the fastest fragments the loss would be 6.7%, thereby resulting in an underestimation of the fast fragments of 4.4%. It is likely that this is an upper limit to the underestimate as the ion signal to which the Gaussian was fitted for the fast fragments was not particularly symmetric as a result of low ion signals. If the negative wavenumber section of the 322 nm profile is used then the width falls to 0.8 cm^{-1} and the underestimation to 2%. These errors are considered negligible and we note that our effective REMPI bandwidth is greater than that of Takahashi *et al.*[16]

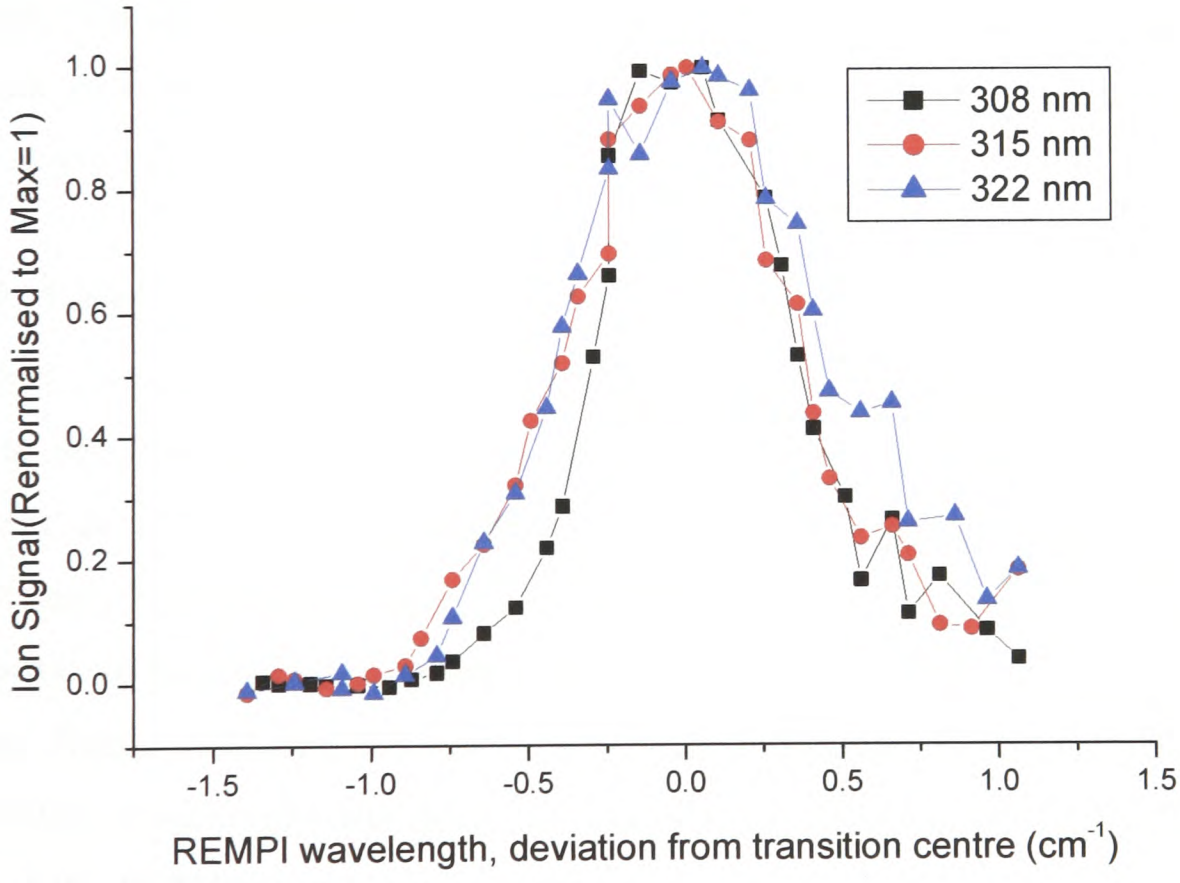

Figure 3-6 Examination of variation of ion signal detected as the REMPI laser is detuned from the centre of the transition.

3.3.2.5 Beam overlap

The major problem relating to beam overlap is the likely systematic error that can be generated when maximising the signal at different wavelengths, particularly for the determination of reference points. The problem with maximising the signal is that it is much more easily achieved at low wavelengths, where the signal is large, than at long wavelengths, where the signal is small; if all factors remained the same the signal at 308 nm could be up to 30 times higher than that at 320 nm. Therefore, the signal to noise ratio is much better for the low wavelength measurements and hence the low wavelength beam geometry can be more accurately positioned. As errors can only lead to an underestimate of the true signal and they will be greater at longer wavelengths then it is possible that the long wavelength reference points will be underestimates of their true values and therefore affect all points based upon these erroneous reference points. The fall in signal, reducing the ease of system alignment, can be minimised somewhat by increasing the photolysis power to counteract the falling cross section, until the fluence limits, as detailed in Section 3.3.2.2, are reached, but the falling $O(^1D)$ quantum yield can not be corrected for in this way. Therefore, great care was taken to try to minimise this problem, which was aided through the use of programs that enabled short time averaged signals to be monitored, thereby reducing the difficulty in aligning the lasers caused by the shot to shot variation in signal.

3.3.2.6 Laser polarisation

An effect that needed to be investigated was whether the efficiency in detecting the $O(^1D)$ could be affected by the polarisation of the lasers used. The main concern is that if different processes are involved in the dissociation of the ozone then the alignment of the photolysis products and the photolysis laser could change with wavelength and the REMPI process may be sensitive to this change in product alignment. Two sets of tests were carried out to confirm that any change in alignment was not a significant problem. First, the relative quantum yield between two wavelengths was measured when the photolysis laser's polarisation was the same as that of the REMPI laser and also orthogonal to it.[15] These tests was carried out for the ratios 310 nm : 305 nm and also 322 nm : 312 nm and the results showed that, within error limits, there was no change; therefore, it was assumed that if there is any effect then it must affect both wavelengths equally. Second, the alignment of the photolysis laser was fixed and the REMPI laser's polarisation rotated; these experiments were performed in the time-of-flight spectrometer, and are reported in Section 4.3.2. At most of the photolysis wavelengths tested,

changing the REMPI polarisation was found to have only a very small effect on the time-of-flight profile observed; therefore, it was assumed that there would be little difference in the signal measured in the cell. However, there may be a fine structure element to this, as the work reported by Denzer *et al.*[11] showed that on a peak in the ozone absorption cross section, where the spin-forbidden component of the signal increases, there is a small change for the fast O(^{1}D) detected.

3.4 Data collection and analysis

3.4.1 Correction factors

The data gathered were processed in the following manner. First, as has been described in Section 2.8, the true two-laser signal, S_2, was determined by subtracting from the measured two-laser signal a quantity which had been determined as the likely sum of the single-laser contributions (always a figure relating to the ions produced by the REMPI laser alone and if necessary a further quantity relating to the photolysis laser's contribution). Secondly, as it is not possible to maintain perfectly constant laser energy output, the true two-laser signal needs to be normalised against the measured REMPI and photolysis laser energies to give the normalised signal. The normalisation took the form of dividing S_2 by the product of the photolysis energy (E_{photo}) and the square of the REMPI energy (E_{REMPI}); the basis of the squared factor having been shown in Section 3.3.2.2. Thirdly, for each wavelength within an experiment a mean was then calculated by averaging the power normalised signals over all valid laser shots. Signals were classed as invalid if any measurement had failed to be recorded properly, e.g. if a suitable one-laser signal could not be determined or if the normalised signal was significantly in excess of the calculated mean (more than 3 standard deviations). Finally, the mean signals need to be corrected for any wavelength dependent factors. The most obvious of these factors is a correction required for the cross section of ozone $\sigma_{\lambda,T}$, as for any wavelength the number of ozone molecules photolysed, for a given laser energy, is directly related to the cross section. The cross section data used were supplied by Prof. Jean Brion from Malicet *et al.*[19] Further possible corrections relate to the linearity of the laser energy measured and the actual energy being used to photolyse the sample. The two main possible problems, non-linearity of the fraction of the beam sampled and attenuation of the beam within the bulb prior to the interaction region, were found to cause errors of 1-2% if ignored and therefore for

the sake of simplicity the percentage error was carried through rather than calculating the effects for every experiment. The effective calculation made was:

$$x_y(\lambda,T)=\frac{1}{\sigma_{\lambda,T}}.\frac{1}{n}.\sum_{i=1}^{n}\frac{S_{2,i}}{E^2_{REMPI,i}.E_{photo,i}} \qquad \textbf{(3-4)}$$

where x_y is the basic quantum yield for experiment y and the sum is over the n valid shots. At this stage x_y is a relative measurement and must be placed onto an absolute scale by some means.

3.4.2 Quantitative *versus* qualitative measurements

Whilst x_y is directly related to the absolute O(^{1}D) quantum yield the constant of proportionality that links it to the absolute value depends on many factors which are not easily determined. These factors include the beams' shapes and overlap (to give the number of ions in the collection region), the exact nature of the ion amplification process within the gas (to determine the ion current generated) and the efficiency of the ion current to voltage conversion process. Out of the many studies that have looked at the O(^{1}D) quantum yield problem the majority did not try to measure an absolute value but determined a relative value. Of the recent studies some of the data from Talukdar *et al.*[22] was determined by an absolute method (the data presented were a mixture of absolute measurements made by resonance fluorescence and relative measurements by detection of OH formed by O(^{1}D) reaction). Takahashi *et al.*[16] determined values by direct measurements of the O(^{1}D) and O(^{3}P) formed and placed the quantum yields on an absolute scale by forcing a weighted sum of the signals to follow the absorption cross section. The most common approach[22,23,24,28] was to employ a method that estimated the absolute quantum yield $\phi_{relative}[\lambda]$ by relating the signal at the desired wavelength, $x[\lambda]$, to that measured at a reference wavelength, $x[\lambda_{ref}]$, at which the quantum yield is known, $\phi[\lambda_{ref}]$:

$$\phi_{relative}[\lambda]=\frac{x[\lambda]}{x[\lambda_{ref}]}\phi[\lambda_{ref}] \qquad \textbf{(3-5)}$$

This was the method chosen in this work and each value of x_y from equation (3-4) was corrected using this calculation. Equation (3-5) was often used in a recursive manner, i.e. the yield at the reference wavelength that was being used was itself a relative quantum yield which had been calculated in relation to another reference point. This recursion was found to be

necessary as the rapidly falling cross section and the general reduction in quantum yield over the full wavelength range being examined, meant that different experimental conditions were required to ensure a good signal to noise ratio in the various wavelength sub ranges. The final reference point was always the absolute quantum yield at 308 nm at the appropriate temperature. This point was chosen because of the number of studies that have been carried out at this wavelength to determine the absolute $O(^1D)$ yield. A method that had been used in the past,[23] normalising to an average value of the quantum yield between 300 nm and 305 nm, was not employed as the correct values for the quantum yield in this region are not known with sufficient accuracy. Table 3-1 gives the absolute values that have been previously reported for the $O(^1D)$ yield at room temperature.

Source	$\phi[O(^1D)]$	Quoted Error	Method Used
Greenblatt & Wiesenfeld[20]	0.79	±0.02	Resonance Fluorescence
Talukdar *et al.*[21]	0.78	±0.06	Resonance Fluorescence
Talukdar *et al.*[22]	0.78	±0.02	Resonance Fluorescence / LIF
Takahashi *et al.*[16]	0.79	±0.11	LIF

Table 3-1 Absolute Quantum yield of $O(^1D)$ produced by photolysis of ozone at 308 nm.

The method utilised by Greenblatt and Wiesenfeld[20] and Talukdar *et al.*[21,22] monitored the resonance fluorescence of $O(^3P)$ after photodissociation of ozone. The signal obtained enabled both the initial production of $O(^3P)$ and the $O(^3P)$ generated by the reaction / quenching of the $O(^1D)$ with ozone[20,21,22] or N_2[21,22] to be monitored. The ratio of $O(^1D)$ to $O(^3P)$ could therefore be deduced after appropriate analysis of the fluorescence signals. The LIF detection methods employed by Takahashi *et al.*[16] and Talukdar *et al.*[21,22] have already been discussed in the introduction. It was decided that the values for the primary reference points used for the work presented here, Table 3-2, should be those of Talukdar *et al.*[22] as the temperatures reported more closely matched the temperatures used and had smaller errors. The value at 247 K was generated from his model. It is acknowledged that these figures do include relative measurements which could lead to inaccuracy but general peer review has accepted them.

Temperature (K)	Talukdar *et al.* Temperature (K)	ϕ[O(^{1}D)]	Quoted Error
227	223	0.74	±0.02
247	247 - calculated	0.75	±0.02
273	273	0.77	±0.02
298	298	0.78	±0.02

Table 3-2 Reference absolute quantum yields at 308 nm used in this work (from Talukdar *et al.*[22]).

The wavelengths of the secondary reference points were chosen to minimise the errors introduced by the point (for example; having to add the error on the reference point to that of all the points using that point and possible change in the beam overlap) whilst maximising the signal to noise ratio (for example; changing the photolysis power; adjusting the amplification factor on the ion amplifier and setting suitable scales on the oscilloscopes).

Once all of the measurements x_y had been converted onto an absolute scale, the mean of all of the corrected values at each wavelength was calculated and these means are the quantum yields reported in Section 3.5.

3.4.3 Data collection

Two methods were employed during the course of gathering the data for this thesis. The ranges, intermediate reference points and data intervals are given in Table 3-3.

Temperature (K)	Ranges	Reference Points	Interval (nm)
227	306-313, 312-320, 320-330	308, 312, 320	1
247 & 273	306-310, 308-312, 311-315, 314-318, 317-321	308, 310, 313, 316, 319	0.5
298	306-311, 310-315, 314-319, 318-323, 322-327	308, 312.5, 316.5, 320.5, 324.5	0.5

Table 3-3 Ranges and calibration points used.

For the lowest temperature, 227 K, the method employed was to examine each sub range a number of times and on different days. Within each sub range the data points were measured several times, at least seven and typically twelve; the wavelength of the data point having been chosen at random from the list of those to be examined. A value for the appropriate reference point was measured immediately before each data point and it was to this point that the data

point was normalised. This method had the advantage of minimising any error due to changes in experimental conditions and reducing systematic errors due to the ordering of the data points, but the repeated measurement of the reference points meant that overall the method was slow. The reference points were also evaluated in the same manner and the beam overlap problem as discussed in Section 3.3.2.5 is now of concern and cannot be allowed for.

For the other temperatures it was decided that there should be a trade off between the number of reference points that were to be taken and the number of data points taken. To achieve the trade off, each range was covered by scanning the photolysis laser across the wavelength range, making at least 40 two-laser shots at each wavelength. To prevent an increase in the error measurement, caused by the reduction in the number of shots at each wavelength, the number of measurements taken at each wavelength was increased to a minimum of twenty. To reduce the possibility of systematic error, resulting from the non random selection of wavelengths, scans were carried out in pairs, with an increasing wavelength scan being immediately followed by a decreasing wavelength run. The wavelength ranges used were checked to ensure that there was no obvious change in signal due to any beam movement by confirming that the lens position for maximum signal of the centre of the scan was also the optimal point for either end of the scan range. To determine how to join the various ranges together two methods were employed. The first relied on the overlapping of the scan ranges, as the yields for each overlapped point must be the same irrespective of the scan range employed and so by calculating a ratio for each of the wavelengths in the overlap a correction factor between each range could be determined. This method will lead to error propagation as any error on one overlap set will be passed on to all ranges that come after it. It is also possible that a significant bias could be introduced to the results if the measured yield changes from its true value at either end of the scan; for example as a result of beam movement. The other method was to determine the absolute quantum yield for each of the centre points of the ranges, in a similar manner to that employed during the lowest temperature experiments, and then relate the other wavelengths in the scan to this point. This method maintains the same possible sources of error as already stated for the lowest temperature method. It was found that the first method typically generated values that were higher than the second, but both methods lay within each others' error bars. As the overlap method was found to produce a minor positive shift and the reference point method a slight negative shift a simple average of the two methods was used to determine the final value.

3.4.4 Errors

The errors quoted for each quantum yield are one standard deviation from the mean. Included in the final confidence limits are uncertainties passed on from the reference quantum yields and the cross section of ozone. Where errors from different sources, e.g. the error due to shot to shot variation and the error from the cross section of ozone, were combined they were added through the use of the standard errors method. It should be noted here that the majority of the systematic errors discussed in Section 3.3.2, if they have not been fully allowed for, are expected to result in an underestimate of the quantum yield at the longer wavelengths.

3.5 Quantum yield results

The quantum yields of O(^{1}D) from the photolysis of ozone at various temperatures and wavelengths as determined by the work in this thesis are given in Table 3-4. The various temperatures are shown comparatively in Figure 3-7, Figure 3-8 and Figure 3-9 compare the results from this thesis with those which were reported during or just before the course of this thesis (those of Ball *et al.*,[23] Takahashi *et al.*,[16] Talukdar *et al.*,[22] Armerding *et al.*[24] and Bauer *et al.*[28]) and the NASA recommendations of 1994,[25] 1997[4] and 2000.[26]

At 227 K the form of the O(^{1}D) yield is not dissimilar to that which has been reported by other groups or the latest NASA recommendation, but differs significantly from that of the 1994 and 1997 NASA recommendations. A rough plateau where $\phi = 0.9$ exists for measurements made below 307 nm, and between 307 nm and 313 nm the yield falls rapidly to a level of approximately $\phi = 0.1$. The fall off in the NASA 2000 figures agrees more closely with the reported work than the earlier recommendations but the upper limit remains slightly high. After 313 nm, and up to 320 nm, the yield remains roughly (within errors) constant at the lower level agreeing well with other reported data and the latest NASA values. The measured yield is slightly higher than the 1997 data, the discrepancy increasing as the wavelength increases, and significantly greater than the 1994 data which is zero above 314 nm. Above 320 nm the yield appears to grow again and there may be some variation, with the value of ϕ oscillating between 0.1 and 0.15; however, the error margins are significant at these wavelengths and it is quite possible that the oscillations are not real.

Wavelength (nm)	227 K	±	247 K	±	273 K	±	300 K	±
305.0	0.91	0.09						
305.5	0.85	0.09						
306.0	0.89	0.11	0.82	0.08	0.73	0.08	0.88	0.10
306.5			0.84	0.09	0.76	0.08	0.86	0.09
307.0	0.87	0.08	0.84	0.09	0.76	0.08	0.82	0.09
307.5	0.83	0.07	0.82	0.08	0.79	0.08	0.82	0.09
308.0	0.74	0.01	0.73	0.10	0.76	0.11	0.78	0.08
308.5	0.68	0.05	0.72	0.10	0.73	0.10	0.72	0.08
309.0	0.62	0.05	0.63	0.09	0.68	0.10	0.67	0.07
309.5			0.58	0.08	0.59	0.08	0.64	0.07
310.0	0.44	0.04	0.47	0.07	0.50	0.07	0.56	0.08
310.5			0.40	0.04	0.43	0.05	0.47	0.07
311.0	0.28	0.05	0.35	0.05	0.36	0.05	0.43	0.06
311.5			0.28	0.04	0.30	0.04	0.38	0.05
312.0	0.18	0.03	0.26	0.04	0.27	0.04	0.34	0.04
312.5			0.23	0.03	0.26	0.03	0.31	0.04
313.0	0.15	0.01	0.21	0.02	0.25	0.03	0.29	0.04
313.5			0.18	0.02	0.23	0.03	0.26	0.03
314.0	0.11	0.02	0.19	0.03	0.23	0.04	0.26	0.04
314.5			0.17	0.03	0.24	0.04	0.25	0.04
315.0	0.10	0.01	0.17	0.03	0.22	0.04	0.24	0.04
315.5			0.16	0.02	0.18	0.03	0.23	0.03
316.0	0.12	0.01	0.17	0.02	0.19	0.03	0.23	0.03
316.5			0.16	0.02	0.20	0.03	0.22	0.03
317.0	0.09	0.01	0.16	0.03	0.19	0.03	0.23	0.03
317.5			0.15	0.03	0.17	0.03	0.21	0.03
318.0	0.10	0.01	0.15	0.03	0.18	0.03	0.20	0.04
318.5			0.15	0.02	0.20	0.03	0.22	0.04
319.0	0.11	0.01	0.15	0.02	0.21	0.03	0.24	0.04
319.5			0.14	0.02	0.18	0.03	0.20	0.03
320.0	0.11	0.02	0.13	0.02	0.15	0.02	0.18	0.03
320.5			0.11	0.02	0.16	0.02	0.19	0.03
321.0	0.12	0.03	0.12	0.02	0.17	0.03	0.19	0.03
321.5							0.17	0.03

Wavelength (nm)	227 K	±	247 K	±	273 K	±	300 K	±
322.0	0.14	0.02					0.15	0.03
322.5							0.13	0.03
323.0	0.10	0.02					0.13	0.03
323.5							0.14	0.03
324.0	0.15	0.04					0.14	0.03
324.5							0.14	0.03
325.0	0.13	0.04					0.13	0.02
325.5							0.13	0.03
326.0	0.11	0.03					0.15	0.03
326.5							0.15	0.03
327.0	0.10	0.05					0.16	0.03
328.0	0.08	0.03						
329.0	0.13	0.09						
330.0	0.04	0.05						

Table 3-4 The quantum yield of O(^{1}D) from the photolysis of ozone at specified temperatures and wavelengths.

Whilst the current NASA recommended values are lower than those reported in this thesis, as are most of the other reported data, both of the earlier recommendations can be clearly seen to differ from the reported data. The NASA 1997 data, which allowed for photolysis of ozone in the $\nu_3 = 2$ state, do predict a very small yield above 320 nm (< 2.5%) falling to zero at 325 nm, whilst all of the reported data show a yield of *ca.* 0.08. As noted before, the NASA 1994 data are zero above 314 nm and there can be no doubt that these data are a major error that has been corrected. At 227 K it is expected that the vibrational population of the ν_3 mode would be approximately 20% of that at 300 K and therefore the vibrationally enhanced, spin-allowed channel would not contribute significantly to the overall quantum yield. Therefore, the yield beyond the low temperature wavelength limit of 309.45 ± 0.03 nm for the spin-allowed pathway[27] (3-1) has been attributed to the spin-forbidden channel (3-3) by a number of groups during the course of the research presented in this thesis.

At 300 K the form of the O(^{1}D) yield matches well with what other groups have reported but differs slightly from that given by the current NASA recommendation and differs significantly from the previous recommendations of 1994 and 1997. The location of the fall off in the O(^{1}D) yield, caused by the main spin-allowed pathway becoming inaccessible, is generally agreed

between the various sets of reported data and the latest recommendation, though the data of Bauer *et al.*[28] do have a much steeper gradient for the fall off. The work reported here also supports much of the reported data in that the upper limit for the quantum yield is 0.9 rather than 0.95 previously recommended.[4] Between 312 nm and 320 nm the general trend is for the yield to fall from *ca.* 0.3 to 0.15, the only deviation from this being the oldest NASA recommendation which continues to fall until 317 nm where it reaches zero. In a number of the studies, including that reported here, there appears to be some structure in the yield with a couple of maxima in this range, though the deviation does lie within the experimental errors. These maxima appear to anti correlate with the cross section of ozone and a further investigation into the anti-correlation is reported in Section 3.9. The latest form of the NASA recommendation, in trying to make a comprehensive model, has lost the structure that was evident in the 1997 evaluation which modelled each wavelength individually. The error resulting from a failure to model this structure is not expected to be large, but it does indicate a possible failing of the latest model. Above 320 nm the quantum yield continues to fall, but at a reduced rate, and the consensus is that it appears to reach a lower limit of *ca.* 0.1 at 324 nm after which it remains at a roughly constant value.

The results in this work would suggest a slightly higher value for this limit of *ca.* 0.14 but the values agree within error limits. Agreement between recent data and the NASA 2000 recommendation is reasonable although the data suggest that the lower limit is too low in the model. As the NASA 1997 recommendation is based only on vibrational enhancement, the model fails above 320 nm as its yield falls off to zero by 326 nm. A correction of 0.08 to its values above 320 nm, for a spin-forbidden component, would bring it roughly into line with the reported data. Again the 1994 recommendation from NASA is clearly wrong above 320 nm as it fails to give any O(^{1}D) production here which is in clear disagreement with the observations.

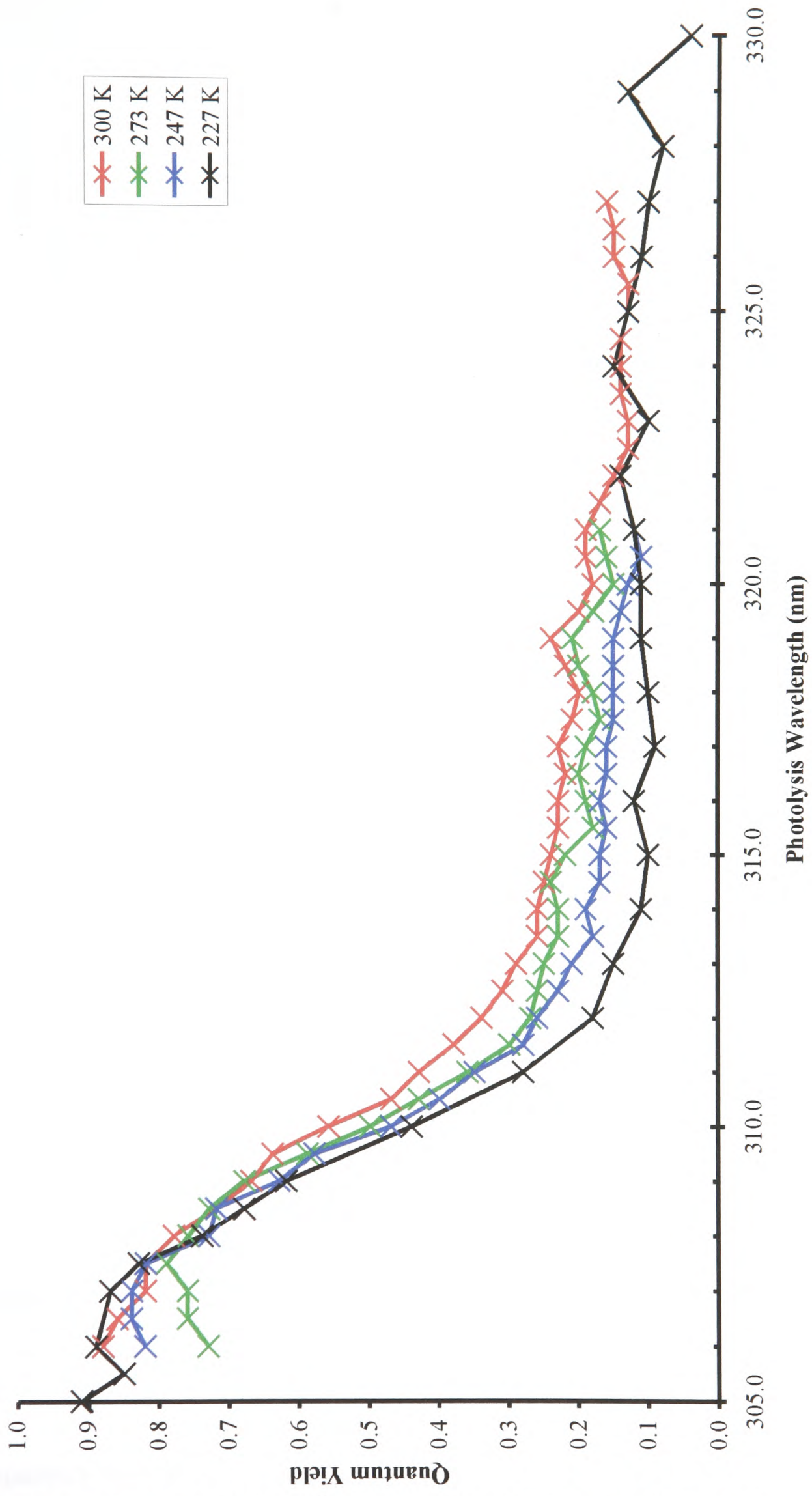

Figure 3-7 The quantum yield of O(^{1}D) from the photolysis of ozone at specified temperatures and wavelengths as determined in this thesis.

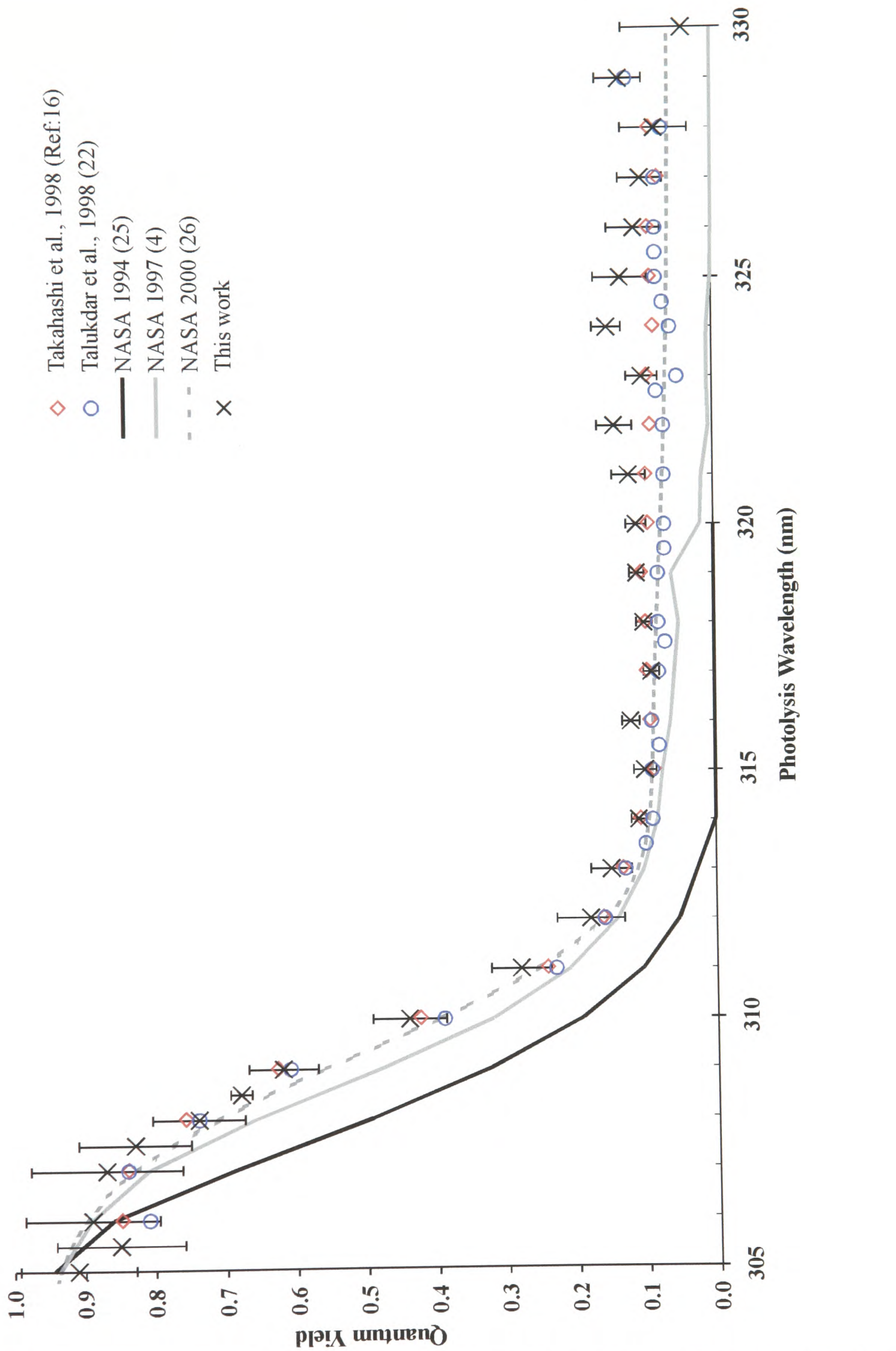

Figure 3-8 Comparison of ≈ 227 K quantum yield data from recent studies and the NASA recommendations of 1994, 1997 and 2000.

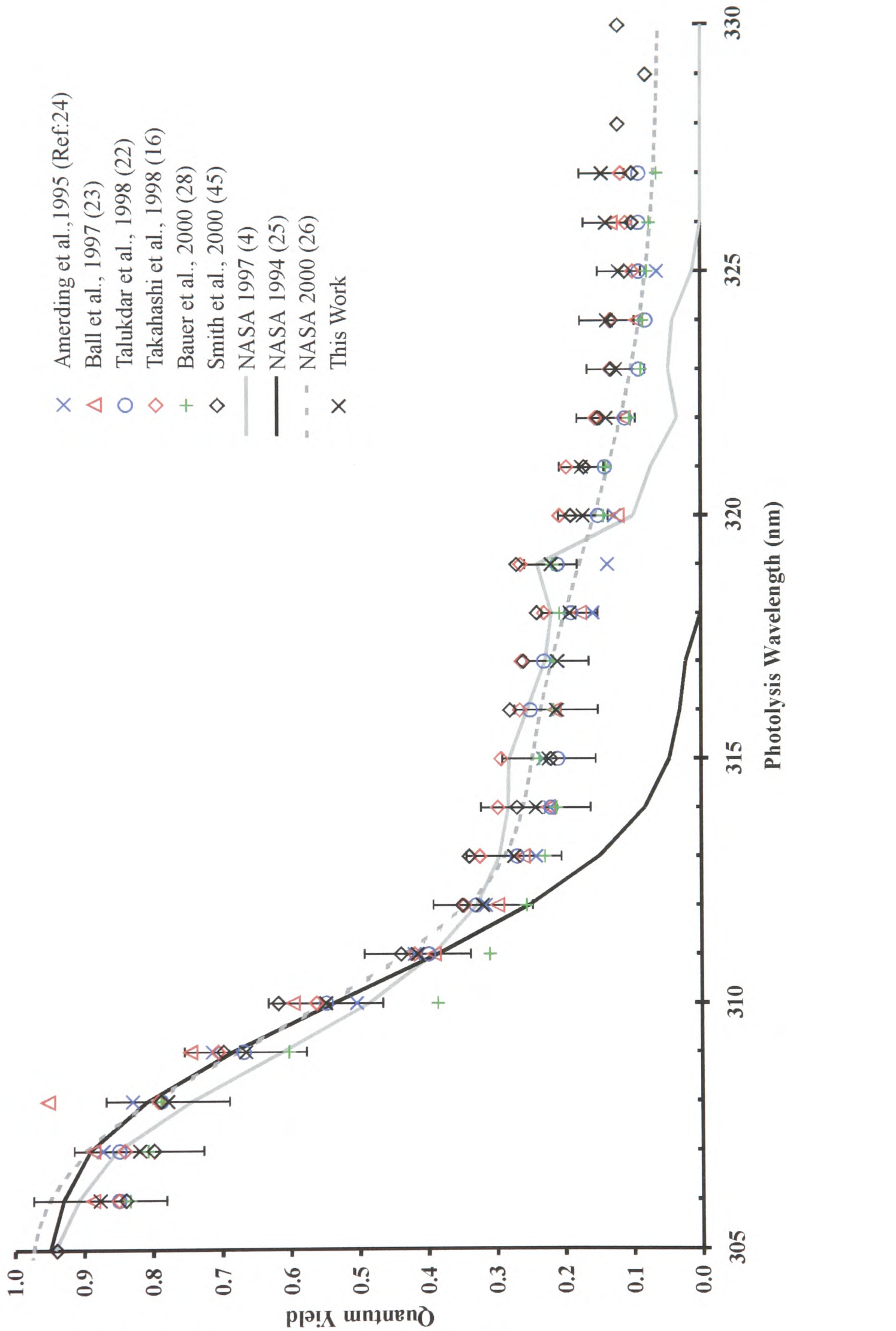

Figure 3-9 Comparison of ≈ 300 K quantum yield data from recent studies and the NASA recommendations of 1994, 1997 and 2000.

The quantum yields for the intermediate temperatures of 247 K and 273 K fall between the yield for the two temperatures described previously. The yield between 310 nm and 320 nm falls as the temperature is reduced, which can be explained by the reduction in the population of vibrationally excited ozone. There does appear to be a problem at the low wavelength end of the data taken, with the measured $\phi(O(^1D))$ being less than expected; the problem is particularly acute for the 273 K data which peaks at 307.5 nm with $\phi(O(^1D)) = 0.78$, whilst the 247 K data may peak at 306 nm with $\phi(O(^1D)) = 0.84$. The cause of the problem at low wavelength is unknown but it should be noted that in the work of Ball *et al.*[23] which normalised the $\phi(O(^1D))$ by taking the average value of the 300 nm to 305 nm data and setting the average to be 0.95, the NASA recommendation at the time, the value of $\phi(O(^1D))$ peaked at 305 nm and 308 nm at a value of 1.02. If the Ball *et al.* data is renormalised so that the value at 308 nm matches the calibration value used in this thesis, a good match is obtained between that and the 273 K data presented here. It may be possible to infer from the match, as the same basic method was used, that there is a source of error that has not been found and that it is some function of the experimental set up.

A significant point that should be made here is that for most of the possible systematic error sources discussed earlier, the effect of the error is to cause the values reported here to be underestimates of the actual quantum yields. Should the values reported here be increased slightly the majority would fall more into line with the data from Takahashi *et al.*,[16] and away from the data reported by groups using indirect measurement techniques. Whilst the indirect methods employ subtly different techniques, they all measure the LIF of OH. Should the relative population of the OH state being probed, to all other states, be related to the speed distribution of the $O(^1D)$ formed, and this not be corrected for, a significant source of error could have been missed. The indirect measurement groups claim that suitable precautions have been taken, for example using different reagent gases to form the OH, precise details of their tests generally have not been presented. Only in the work of Talukdar *et al.*[21] have some comparisons been reported and then for only one wavelength / temperature combination can a good comparison be made. At 308 nm and 298 K the resonance fluorescence method estimated the quantum yield to be 0.78±0.06; the LIF of OD, from D_2O, taken at 300 K agrees well at 0.77±0.05 but the LIF of OH, from H_2O, taken at 298 K only just matches at 0.72±0.06. As at 308 nm the speed distribution of the $O(^1D)$ formed should be low, the potential discrepancy between OH based results and the actual yield is of concern, which becomes greater at longer photolysis wavelengths where the speed distribution changes (the population of different

vibrational states of OH could change as a result). Therefore, whilst the indirect methods claim to be accurate, it is felt that the quantum yields generated from direct measurement of the O(^{1}D) should be considered as closer to the actual quantum yield of O(^{1}D).

3.6 O(^{1}D) formation from photolysis wavelengths < 310 nm

3.6.1 General discussion

As discussed in the introduction, production of O(^{1}D) in the Hartley band results from the absorption to the 1 $^1B_2$ upper state of ozone. For a long time it was assumed that the $^1B_2$ state would dissociate solely *via* pathway (3-1) when photolysed by wavelengths below 306 nm. As a result of a number of absolute measurements of the O(^{1}D) yield between 248 nm and 274 nm and at 305 nm the limiting value for the quantum yield is now 0.9-0.95, with the production of O(^{3}P) with $O_2(X^3\Sigma_g^-)$ accounting for the remainder of the dissociation products. Section 3.6.2 discusses a study that was carried out in which the O(^{3}P) yield was monitored. Whilst the general form of the yield, rising as the wavelength is decreased to a limit of between *ca.* 0.90 and 0.95 at 306 nm, is agreed,[16,22,23,24,28] it is uncertain whether there is structure on the yield or not. In particular many of the studies appear to show a peak in the yield around 306 nm to 307 nm, the magnitude of which is a change of *ca.* 5% in the yield. It should be noted that the magnitude of the change is within the errors of most experiments. The peak has been seen in this work; however, its location appears to vary with temperature but not in any clear way. It is possible that the peak is caused by the onset of the vibrational and / or spin-forbidden channels. Confirmation of the cause of the peak would require more detailed studies between 300 nm and 310 nm at a range of temperatures. However, if this structure is real its influence on atmospheric models is expected to be low as the solar actinic flux is low at these wavelengths.

3.6.2 Investigation of O(^{1}D) yield *via* O(^{3}P) detection

A study was carried out to investigate the upper limit for the O(^{1}D) quantum yield between 303 nm and 310 nm. The study was done using the same general technique used for the room temperature O(^{1}D) quantum yield measurements, but instead of monitoring the production of O(^{1}D), the alternative atomic fragment, O(^{3}P), was probed. REMPI of some of the O(^{3}P) fragments was achieved by a 2+1 REMPI process ionising O($^3P_2$) at 225.65 nm. Only one of the three possible *J* states was investigated as tests carried out by Takahashi *et al.*[16] determined that there was no obvious *J* dependence on the spectra they recorded. Figure 3-10 compares the

measured O(¹D) quantum yield with the inferred O(¹D) quantum yield calculated using the relationship:

$$\phi_y = 1 - (1 - \phi_{308}).\frac{S_\lambda}{S_{308}} \qquad \textbf{(3-6)}$$

where S_λ is the O(³P₂) signal at λ nm and ϕ_y is the O(¹D) quantum yield at *y* nm ($\phi_{308} = 0.78$).

It can be clearly seen in Figure 3-10 that there is a good agreement for the O(¹D) quantum yield

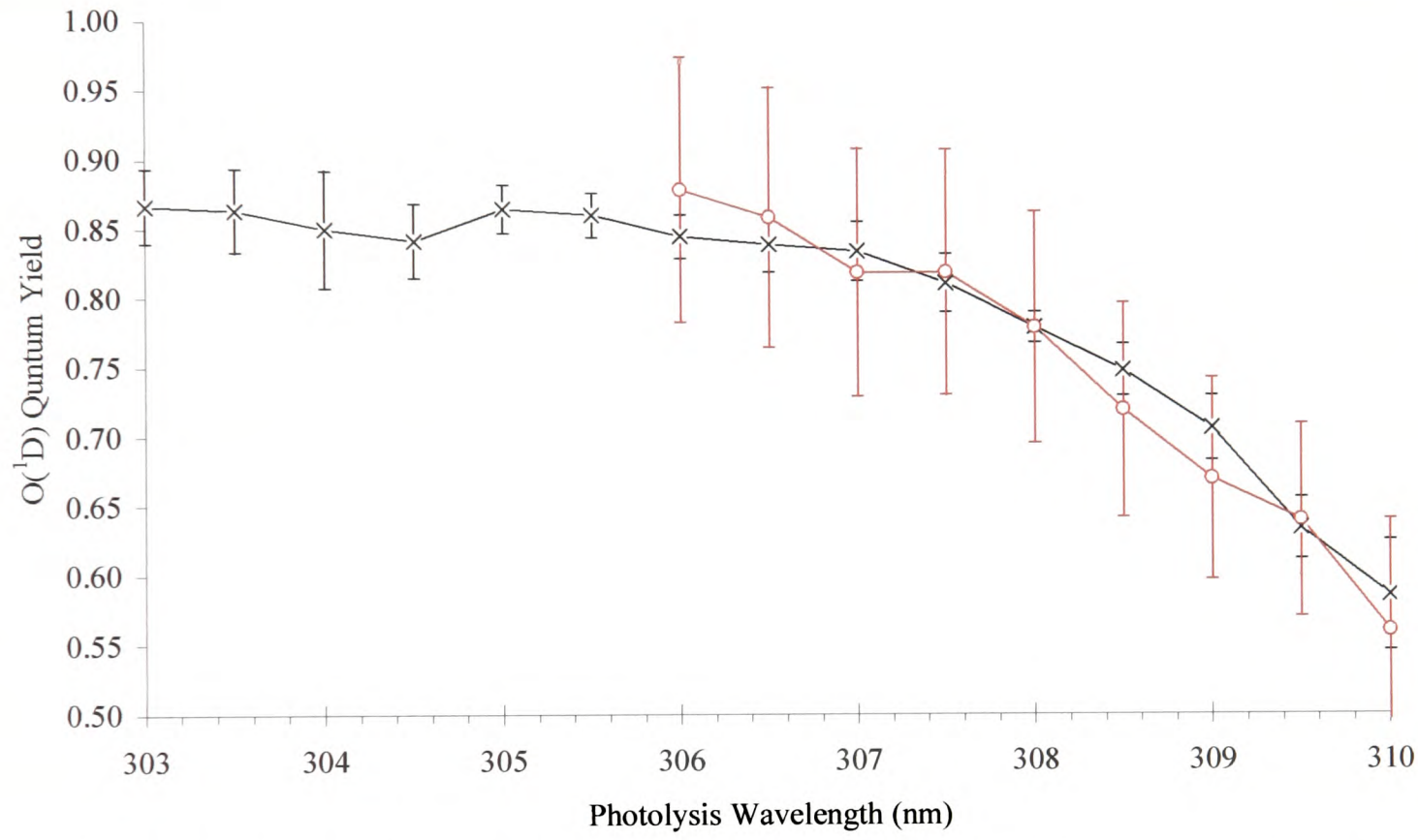

Figure 3-10 Comparison between the O(¹D) yield determined by measurements on the O(¹D) fragment (red) and O(³P) fragment (black).

between the measurements made on the different atomic fragments. The detection of O(³P) at wavelengths < 305 nm clearly demonstrates that the original value of one for the quantum yield here must be incorrect; and from the measurements made it would appear that the correct upper limit is closer to 0.9 than 0.95.

3.7 O(¹D) production at wavelengths ≥ 310 nm

First evidence of the possible production of O(¹D) at wavelengths greater than 310 nm came in the 1960s[29,30] but it was not until during the course of the research reported here that some form of consensus was achieved. At first the observed production of O(¹D) in this region was put down to the experimental bandwidth of the light source[31] and later to rotational energy in

ozone.[32] Work in the 1980s by Adler-Golden *et al.*[7] and Trolier and Wiesenfeld[8] identified the possibility that vibrational energy in the ozone could be the source of the additional energy required to enable the production of O(^{1}D) *via* the spin-allowed channel at wavelengths greater than 310 nm. One potential problem with the inclusion of vibrational energy of the parent ozone into the energy available for dissociation, is that there is only a very small percentage of vibrationally excited ozone with only *ca.* 0.6% of ozone having $\nu_3 > 0$. However, the work of Zittel and Little[13] showed that if the ν_3 vibrational mode is excited ozone will produce *ca.* 70 times more O(^{1}D) when photodissociated at 314.5 nm than ground state ozone. The enhancement in the production of O(^{1}D) is in part due to an increased absorption cross section,[7] which is significantly increased when the ozone is vibrationally excited (wavelength dependent but typically by a factor greater than 10), but the increased cross section alone does not account for all of the increase in the O(^{1}D) yield. Therefore, it appears that the O(^{1}D) quantum yield also increases, with Zittel and Little suggesting a ratio of 6:1 for the vibrational : ground state quantum yield. It was not until the mid 1990s that the influence of vibrational excitation was finally accepted after Michelsen *et al.*[9] presented a model based on several of the data sets available. The NASA recommendation in 1997 was based on this model and marks the formal acceptance of the vibrationally excited channel. Most of the evidence for this channel has come from studies into the temperature dependence of the O(^{1}D) quantum yield, though at this point none of the studies carried out direct measurements of O(^{1}D) but relied on indirect methods in which the O(^{1}D) formed reacts with another compound and then one of the reaction products detected. Since the production of the model by Michelsen *et al.* many more studies have reported production of O(^{1}D) within the hot-band region. The work reported here and that of Takahashi *et al.*[16] are the only direct measurements of the O(^{1}D) quantum yield taken at several temperatures over this hot-band region. These both show a clear fall in the O(^{1}D) yield in this band as the temperature is reduced and, within errors, match the indirect measurements; however, as discussed at the end of Section 3.5, the direct measurements are at the upper end of the error limits given by the indirect measurements. In addition, kinetic energy studies by Denzer *et al.*[11] and Ball *et al.*[33] on the O(^{1}D) and $O_2(a^1\Delta_g)$ fragments that would be produced by such a vibrationally enhanced process, show features that can be attributed to it. For both O(^{1}D) and $O_2(a^1\Delta_g)$ fragments, as the wavelength passes the thermodynamic limit of 310 nm for spin-allowed dissociation, additional kinetic energy has been observed, which corresponds to the energy expected from the partitioning of one quantum of the asymmetric, ν_3, stretch.

In all of the recent studies on the temperature dependence a significant point is that the quantum yield does not fall to zero at the lowest temperatures and the trend is that as the temperature is decreased a non zero lower limit for O(^{1}D) production is approached. Studies of the dynamics of the process have explained this non zero limit *via* the spin-forbidden pathway, which is discussed further in Section 3.8. It is one of the biggest failings in the model of Michelsen *et al.* that, as the temperature is decreased, the O(^{1}D) quantum yield is expected to fall to zero. The inclusion of a non zero limit is expected to cause significant changes to atmospheric models and these changes are discussed further in Section 3.10.

3.8 O(^{1}D) production at wavelengths ≥ 320 nm

The probability that all of the O(^{1}D) observed at wavelengths longer than 320 nm is caused by vibrationally excited ozone is very small, as the $\nu_3 = 1$ channel should close at 320.7 nm and the percentage of ozone in the $\nu_3 = 2$ state at 300 K would be only 3.6×10^{-4}% of the total ozone concentration. However, the cross section for $\nu_3 = 2$ is greater than that of both the ground state and the $\nu_3 = 1$ state and, as the changing cross section for the different vibrational states is not taken into account when calculating the quantum yield, even a small percentage of ozone in the $\nu_3 = 2$ state could impact on the values determined. Temperature variation of the yield would again be the most telling sign that a contribution from vibrational energy of the parental ozone molecule is the source of the energy needed to produce O(^{1}D) from the spin-allowed channel. The value of the O(^{1}D) yield above 320 nm reported here does fall as the temperature is decreased but it is not possible to determine if it is falling at a similar rate to the $\nu_3 = 1$ component, particularly once errors are taken into account. The data of Takahashi *et al.*[16] and Talukdar *et al.*[22] do show such a trend, with the data of Talukdar *et al.* at 320 nm falling from *ca.* 0.2 at 298 K to 0.07 at 223 K, but it is not clear if the rate of fall is enhanced over that found at *ca.* 310 nm which would be expected. The existence of a doubly excited channel operating could be observed in measurements of the speed distribution of the O(^{1}D) produced. When pathway (3-2) becomes active a clear increase in the speed of the O(^{1}D) has been observed, both by Denzer *et al.*[11] and also as reported in Section 4.4.2. A similar observation of an increase in the speed of the O(^{1}D) should occur also at long wavelengths where the $\nu_3 = 1$ channel has closed but the $\nu_3 = 2$ is open. This observation has been made. Therefore, it is highly likely that the temperature dependent component of the quantum yield above 320.7 nm results from the dissociation of ozone with more than one quantum of vibrational energy. If the temperature dependent component is subtracted from the overall quantum yield there is a

significant residual component which appears to be approximately wavelength independent, on the wavelength scale employed. The residual component cannot be explained by vibrationally excited ozone being dissociated and therefore some other process must produce $O(^1D)$.

The spin-forbidden pathway is the main additional process, which was proposed as long ago as 1980 by Brock and Watson,[34] and direct evidence that it exists has been reported by Takahashi *et al.*[6,16,17,35] and Denzer *et al.*[10,11] Takahashi *et al.* used LIF on the $O(^1D)$ fragment formed in the photolysis of ozone to generate Doppler profiles of the $O(^1D)$ fragments. The widths of these profiles give information on the speed distribution of the $O(^1D)$ fragments, and it was found that the components of the speed distribution matched that which could be expected for $O(^1D)$ produced *via* the spin-forbidden pathway (3-3). Further, by detailed analysis of the shape of the Doppler profiles Takahashi *et al.*[16] made estimates of the relative branching ratio between the spin-allowed and spin-forbidden pathways at various wavelengths. These analysis was carried out for samples at 295 K at wavelengths where the switch between the hot-band and spin-forbidden pathways occurs, and for three wavelengths when the sample temperature was 227 K. The latter measurements showed a very sharp fall in the spin-allowed : spin-forbidden ratio between 318.80 nm and 322.71 nm, indicating an almost complete closing of the spin-allowed channel, although it was not particularly strong even at 318.80 nm. At 295 K however, the ratio falls at a much reduced rate, with more than 10% of the signal still being caused by spin-allowed dissociation at 327.99 nm.

Using the time-of-flight system described in this thesis, Denzer *et al.*[11] also showed that, for wavelengths above 320 nm, the maximum speed of the $O(^1D)$ detected was consistent with it having been produced *via* the spin-forbidden pathway. Unlike Takahashi *et al.*, Denzer *et al.* found that, whilst a significant component of the signal was at low energy, it was not possible to extract a spin-allowed : spin-forbidden ratio, as the signal suffered from partial core extraction. Denzer *et al.* also discussed the possibility that the slow $O(^1D)$ fragments being observed were due to a bimodal distribution in the internal energy of the $O_2(X^3\Sigma^-_g)$ co-fragment, which was produced *via* the spin-forbidden pathway, rather than from the spin-allowed pathway; and it was felt that on the available evidence the spin-allowed production was the more likely. This conclusion was based mostly on evidence from another pathway, that producing $O_2(a^1\Delta_g)$ from a different spin-forbidden route (Path 1-D), but also as a result of the degree of change in the fast / slow $O(^1D)$ ratio with wavelength which is significant.

The variation in the fast / slow $O(^1D)$ ratio with wavelength was investigated by both Takahashi *et al.*[16] and Denzer *et al.*[11] Both found that the main relationship was that the

production of fast O(^{1}D) is significantly enhanced when the wavelength corresponds to vibronic absorption peaks in the ozone cross section. This relationship is further discussed in Section 4.4.4. The spin-forbidden quantum yield is not expected to be dependent on the wavelength as the increase in yield is countered by the increase in cross section and these factors would cancel out in the normalisation process.

3.9 O(^{1}D) quantum yield at a dip in the cross section of ozone

From the data shown in Figure 3-7 it appears that there may be some form of structure in the O(^{1}D) quantum yield, particularly in the region where vibrational excitation of the parent ozone molecule is important. As structure could be clearly seen in the results of Takahashi *et al.*[16] but not of Ball *et al.*[36] it was decided to investigate the possibility of structure further.

The investigation took the form of taking a series of improved wavelength resolution quantum yield scans over a short wavelength range about one of the features in the cross section of ozone, between 317 nm and 321 nm. The results of this work are shown in Figure 3-11 and whilst the error bars are significant there is a clear trend that would suggest that the O(^{1}D) yield anti-correlates with the ozone cross section. It is interesting to note that there are possible signs of this anti-correlation in the $O_2(a^1\Delta_g)$ data reported by Ball *et al.*[36]

The anti-correlation can be explained by assuming that the peaks in the structure in the ozone cross section are strongly related to the peaks on the photofragment excitation spectrum of Takahashi *et al.*[6] on which it is known that the production of spin-forbidden O(^{1}D) is enhanced.[16] However, on these peaks there is no enhancement of the vibrationally mediated process. Thus, while the total signal observed increases, it increases less than the change in the cross section and so when the signal is corrected for the cross section a dip occurs. Above 320 nm, and at low temperatures, no dip is expected as now the signal is primarily due to the spin-forbidden process, which matches its change in signal with that of the change in cross section. Unfortunately there is only one set of data that has the wavelength precision needed to confirm or deny any correlation between the O(^{1}D) yield and cross section, that of Takahashi *et al.*[16] The data reported by Takahashi *et al.* appears to have some structure on the yield taken at 227 K, but it is much smaller in magnitude than observed on the 298 K data, and has now switched from being an anti-correlation to a correlation. Given the magnitude of the errors for the data it is difficult to conclude that there definitely is / is not a correlation.

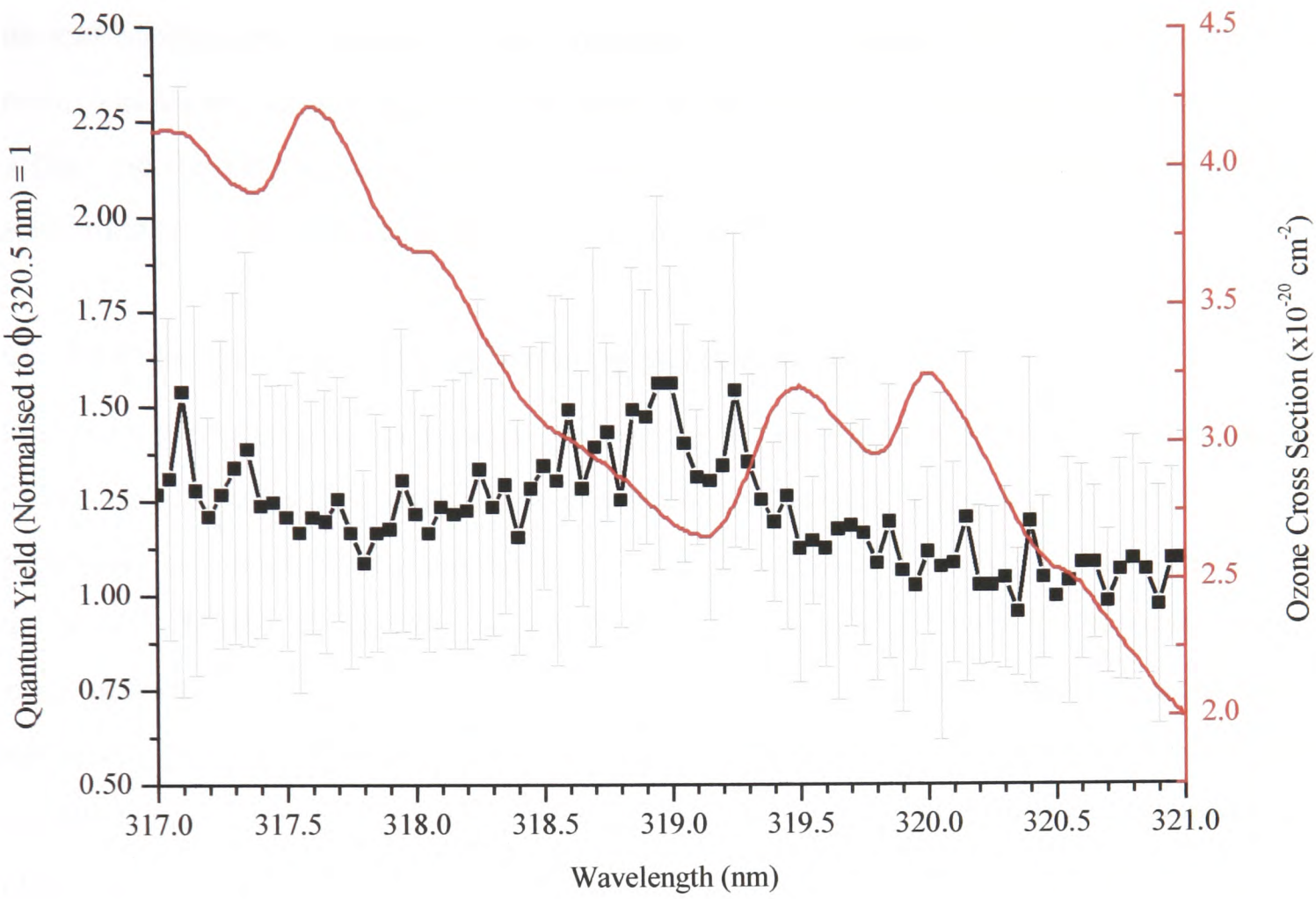

Figure 3-11 Comparison between high resolution quantum yield and ozone cross section.

3.10 Implications for models of the atmosphere

If accurate models of the chemistry of the troposphere are to be made, a good representation of the oxidising capacity of the troposphere must be included and, as stated in Section 1.6.3, determining the oxidising capacity requires knowledge of the rate of production of O(^{1}D). To determine $J[O_3 \rightarrow O(^1D)]$, the rate coefficient for the production of O(^{1}D) from ozone, the following function must be evaluated:

$$J[O_3 \rightarrow O(^1D)] = \iint F[\lambda,h,]\sigma[\lambda,T(h)]\phi[\lambda,T(h)]d\lambda.dh \qquad \textbf{(3-7)}$$

where: F[λ,*h*] is the solar flux reaching altitude *h* at wavelength λ; σ[λ,*T*] is the cross section of ozone at wavelength λ and temperature *T*, which is itself a function of altitude and ϕ[λ,*T*] which is the quantum yield for the production of O(^{1}D) at wavelength λ and temperature *T*.

Of these, the solar flux at a given altitude can be calculated, as absorption at higher altitudes is a function of chemical species, wavelength and temperature. The cross section has been

measured by a number of groups including Molina and Molina,[37] Daumont *et al.*,[19] Bass and Paur[38] and Burrows *et al.*[39] to good agreement (for example agreement between the data of Molina and Molina and Daumont *et al.* it is better than ~2% under 324 nm and *ca.* 5% above 324 nm). Therefore, of the factors that need to be known to generate the rate of O(^{1}D) production and the subsequent chemistry, one of the largest sources of potential error would be the use of incorrect values for the O(^{1}D) quantum yield.[40]

3.10.1 Atmospheric evidence for long wavelength tail

In addition to the laboratory measurements that have been discussed in the previous sections there have been several field campaigns that have investigated the production of O(^{1}D) from the photolysis of ozone in the atmosphere. Early studies were those of Müller *et al.*[41] and Shetter *et al.*[42] Müller *et al.* determined the rate of production of O(^{1}D) *via* two methods, chemical actinometry (CA) and spectroradiometry (SR). The first method measured the production of O(^{1}D) in a controlled cell environment, whilst the second method determined the actinic flux which then enables the production of O(^{1}D) to be modelled if a quantum yield $\phi[\lambda,T]$ is assumed. Müller *et al.* found that if they used the data of NASA 1994[25] they were unable to achieve a CA : SR ratio that was independent of the slant column of ozone. Once Müller *et al.* switched to the data of Brock and Watson,[34] the desired independence was observed. The main difference between the two sets of data is that the Brock and Watson data includes a significant long wavelength tail with O(^{1}D) being detected up to 325 nm. Shetter *et al.*[42] produced similar evidence, this time making a comparison between their measured values and models based on the data of NASA 1994, Michelsen *et al.*[9] and their own quantum yield values (formed from a critical review of the data available at the time) as the slant column of ozone was increased. Again, the NASA data clearly had a dependence on the slant column which could not be explained, whilst the other data sets did not. Both Müller *et al.*[41] and Shetter *et al.*[42] as well as Blindauer *et al.*,[43] who compared models of the NASA 1994 data to that based on Ball *et al.*,[36] found that changing the yield from the NASA 1994 data to some that included the long wavelength tail could significantly increase the production of O(^{1}D) in the atmosphere, reinforcing the need to determine the quantum yield accurately.

3.10.2 Recent comparisons

Talukdar *et al.*[22] and Hofzumahaus and Hancock[44] have reported the effects of changing the O(^{1}D) yield from the previously specified values (NASA 1994[25] and NASA 1997[4]), both using

the O(^{1}D) data from Talukdar.[22] Hofzumahaus concentrated on the effects that would be observed at low solar zenith angles, *ca.* 20°, by altitude. If a constant temperature of 298 K was assumed, then the J[O(^{1}D)] value based upon the O(^{1}D) quantum yield recommended by NASA in 1994 consistently underestimated the values based upon the values recommended by NASA in 1997 and Talukdar *et al.* by *ca.* 20%. When the true temperature profile was used greater differences were observed. First, the NASA 1997 and Talukdar *et al.* based values no longer agreed (a result of the lack of a spin-forbidden contribution at low temperatures in the NASA 1997 model), and second, the altitude profile changed; as the altitude is increased the temperature falls and the effects of the long wavelength tail become more important. At low altitudes, where the temperature is at its highest, the NASA 1997 data result in a J[O(^{1}D)] value 20% above NASA 1994, with the data of Talukdar *et al.* adding a further 5%. At 12 km, where the temperature has fallen to *ca.* 220 K, the NASA 1997 based value is 30% higher than that based on NASA 1994 and use of the data from Talukdar *et al.* adds a further 10%. The overall profile changes in shape as well, with the NASA 1994 data predicting a maximum J[O(^{1}D)] at 6 km, the data from NASA 1997 result in a much more shallow maximum at about 7 km, whilst the data of Talukdar *et al.* give an approximately constant value above 6 km (a very small maximum possibly being observed at 11 km). Hofzumahaus also noted that increasing the solar zenith angle had a pronounced affect on the J[O(^{1}D)] value calculated. At a solar zenith angle of 85°, where the J[O(^{1}D)] maximum is observed, inclusion of the long wavelength tail increases J[O(^{1}D)] by up to a factor of 5. The increase in J[O(^{1}D)] is explained by an increasing percentage of the solar flux being towards the red end of the UV spectrum as the solar zenith angle is increased, a result of the extra absorption of the shorter wavelengths due to the increased path length as the zenith angle increases.

Talukdar *et al.*[22] primarily presented his results in relation to the changing of the solar zenith angle. Table 3-5 shows the relationship between the J[O(^{1}D)] values calculated using his experimental data compared to three sets of data recommended for use in models. From Table 3-5 it can be seen that the inclusion of the vibrational channel, as in NASA 1997, leads to values that are close to those predicted using the data of Talukdar *et al.* for low zenith angles but at higher angles starts to deviate significantly. The model developed by Talukdar *et al.*, which allows for an O(^{1}D) quantum yield of 0.06 for wavelengths above 329 nm, an assumption that has been supported by the work of Bauer *et al.*,[28] shows an even greater yield of O(^{1}D) at very high zenith angles.

Zenith Angle ^{o}	NASA 1994	NASA 1997	Talukdar *et al.* Experimental Values	Talukdar *et al.* Model
40	75%	96%	100%	100%
50	68%	93%	100%	101%
60	60%	90%	100%	102%
70	42%	80%	100%	105%
80	20%	60%	100%	112%
85	20%	50%	100%	124%

Table 3-5 J(O(^{1}D)) value relative to that calculated using the experimental data of Talukdar *et al.*[22] The model developed by Talukdar *et al.* is a parametric fit of his data with ϕ(O(^{1}D))=0.06 for $\lambda \geq 329$ nm.

The rapidly falling cross section is countered by the high proportion of long wavelength radiation at high solar zenith angles until *ca.* 345 nm, above which the contribution of O(^{1}D) to the total J[O(^{1}D)] value becomes very small. As the production of O(^{1}D) is also dependent on the concentration of ozone, Talukdar *et al.* reported how the model : NASA 1997 ratio, by zenith angle, changed as the ozone column abundance was increased. It showed, for example, that at a zenith angle of 85° the ratio roughly doubled as the column abundance was doubled. Variation of J[O(^{1}D)] would make differences to models that take into account the hemisphere and season as the ozone column abundance in the northern hemisphere is typically double that of the southern, and the variation during the year can account for a further factor of two in its abundance.

In the very recent results of Smith *et al.*[45] the increase in the O(^{1}D) production rates with solar zenith angle exceeds that of other recent studies as a result of their greater spin-forbidden O(^{1}D) quantum yield. At high solar zenith angles (> 80°) their predicted rates are 1.2 times greater than those modelled using the NASA 2000 data and more than 1.5 times those of the NASA 1997 recommendation.

Whilst the studies of Hofzumahaus and Hancock, Smith *et al.* and Talukdar *et al.* concluded that the modelled changes in the production of O(^{1}D) caused by the changing data set could be significant, the effect is still not fully determined as the model of Michelsen *et al.*[9] is still in common use. One study has been reported,[46] which looked at the change that would be caused by switching from the model from Michelsen *et al.* to the data of Shetter *et al.*[42] The study aimed to investigate how the tropospheric photodissociation rate of various compounds

changed as the stratospheric ozone concentrations were altered. Ma and van Weele[46] concluded that whilst the increase in the $O(^1D)$ production rate went up by ~7% if the $O(^1D)$ quantum yield of Shetter *et al.* was used instead of that from the model of Michelsen *et al.* there was little effect (~1%) on how the $O(^1D)$ production rate would be changed once changes in the stratospheric ozone levels were allowed for. It should be noted though that while the model applies to a comparatively low solar zenith angle of 24.5°, it is for angles of double this figure that the effects of a long wavelength tail to the $O(^1D)$ quantum yield start to become pronounced.

A new $\phi(O(^1D))$ recommendation is clearly needed. Once the new recommendation has been made, the atmospheric modelling community will have an improved data set from which they will be able to calculate the production of $O(^1D)$ with more certainty. Knowing the rate of production of $O(^1D)$ more accurately than before will have an impact on the calculations made on the production of OH, and from there much of the chemistry of the troposphere, because of the importance of OH as an oxidant. The impact will be most noticeably seen for high solar zenith angles but its influence on the mid latitudes will still be significant as even small changes in the OH production rates could make a difference to the cleaning of the polluted atmosphere that tends to exist at these latitudes. A better statement of the temperature dependence will also aid the knowledge of the altitude profile of $O(^1D)$ production in the troposphere where the temperature falls from *ca.* 290 K to 220 K as the altitude is increased from ground level to the tropopause.

3.11 Conclusions

It has now been shown that above 310 nm, the expected thermodynamic limit, $O(^1D)$ is still produced from ozone photolysis and its production has been observed conclusively to 326 nm; using a technique that directly monitored the $O(^1D)$ produced. The dependence of the yield on temperature has been determined. At the lowest temperature investigated, 227 K, the yield settles to *ca.* 0.1 just above 310 nm and is observed at this level up to 328 nm. As the temperature is increased the yield in the 310 nm to 320 nm range increases, until at 298 K, the yield is *ca.* 0.2 in this range, whilst above the range a downward step is observed, so that above 324 nm the yield matches that at 227 K. The nature of the yield is such that there is strong evidence for the production of $O(^1D)$ *via* the spin-allowed pathway with additional energy provided by vibrational energy in the parent ozone as well as production *via* the spin-forbidden pathway. These figures are in-line with other measurements reported during the course of the

research presented in this thesis; though the indirect measurements are to the low end of the expected range.

As a result of the consensus in the results between the various groups that have been working on the problem of determining an accurate quantum yield for O(^{1}D), a new recommendation to replace the NASA 1997 values is currently being formulated.[47] The data stated in NASA 2000 have been derived from a subset of the data being included in the new formulation, but the data were not reanalysed. Data from this work are being included in the formulation process. The revised formulation, when applied to atmospheric models, has the potential to have a significant impact on the estimated oxidation capacity of the troposphere when compared to the estimates based upon the NASA 1997 data set.

Further work on determining an accurate O(^{1}D) quantum yield would be beneficial and should include the following. First, the recommendation is critically dependent on an accurate knowledge of the quantum yield at 308 nm as this is used as the calibration point for most studies. It would be beneficial to investigate the value of the quantum yield at 308 nm further and in particular its temperature dependence. Second, in many of the studies there is evidence that there is a temperature dependence and possible structure in the quantum yield between 300 nm and 308 nm and this should be examined further as it is currently assumed to be roughly constant. Thirdly, effort should be made to determine if there are any problems relating to the use of LIF based indirect methods for O(^{1}D) detection; if there are errors then any simple mean of the current data sets would result in an incorrect recommendation. Finally, whilst it is not expected to make a significant difference to atmospheric models, data with improved wavelength resolution should be obtained as improving this resolution may provide further insights to the mechanisms involved in the photodissociation of ozone.

References:

1 R.P. Wayne, *Chemistry of Atmospheres*, Oxford University Press, Oxford UK (2000).

2 G.P. Brasseur, J.J. Orlando and G.S. Tyndall, *Atmospheric Chemistry and Global Change*, Oxford University Press, New York USA (1999).

3 R.P. Wayne, *Handbook of Environmental Chemistry Vol.2 Part E - Reactions and Processes*, O. Hutzinger (ed.), Springer Verlag, Berlin (1989) 1.

4 W.B. DeMore, S.P. Sander, D.M. Golden, R.F. Hampson, M.J. Kurlo, C.J. Howard, A.R. Ravishankara, C.E. Kolb and M.J. Molina, *Chemical Kinetics and Photochemical Data for Use in Stratospheric Modeling Evaluation Number 12*, JPL 97-4, NASA Jet Propulsion Laboratory Publication (1997).

[5] R. Bacis, A.J. Bouvier, and J.M. Flaud, *Spectrochimica Acta Part A*, **54** (1998) 17.

[6] K. Takahashi, M. Kishigami, N. Taniguchi, Y. Matsumi and M. Kawasaki, *J. Chem. Phys.*, **106** (1997) 6390.

[7] S.M. Adler-Golden, E.L. Schweitzer and J. I. Steinfeld, *J. Chem. Phys.*, **76** (1982) 2201.

[8] M. Trolier and J.R. Weisenfeld, *J. Geophys. Res.*, **93** (1988) 7119.

[9] H.A. Michelsen, R.J. Salawitch, P.O. Wennberg and J.G. Anderson, *Geophys. Res. Lett.* **21** (1994) 2227.

[10] W. Denzer, G. Hancock, J.C. Pinot de Moira and P.L. Tyley, *Chem. Phys. Lett.*, **280** (1997) 496.

[11] W. Denzer, G. Hancock, J.C. Pinot de Moira and P.L. Tyley, *Chem. Phys.*, **231** (1998) 109.

[12] I.C. McDade and W.D. McGrath, *Chem. Phys. Lett.*, **73** (1980) 413.

[13] P.F. Zittel and D.D. Little, *J. Chem. Phys.*, **72** (1980) 5900.

[14] S.M. Ball, Studies of Laser Photolysis, D.Phil Thesis Oxford University 1995.

[15] J.C. Pinot de Moira, Laser Studies of Atmospheric Chemistry, D.Phil Thesis, Oxford University, 1998.

[16] K. Takahashi, N. Taniguchi, Y. Matsumi, M. Kawasaki and M.N.R. Ashfold, *J. Chem. Phys.*, **108** (1998) 7161.

[17] K. Takahashi, Y. Matsumi and M. Kawasaki, *J. Phys. Chem.*, **100** (1996) 4084.

[18] R.J. Wilson, J.A. Mueller and P.L. Houston, *J. Phys. Chem. A*, **101** (1997) 7593.

[19] J. Malicet, D. Daumont, J. Charbonnier, C. Parisse, A. Chakir and J. Brion, *J. Atmos. Chem.*, **21** (1995) 263.

[20] G.D. Greenblatt and J.R. Wiesenfeld, *J. Chem. Phys.*, **78** (1983) 4924.

[21] R.K. Talukdar, M.K. Gilles, F. Battin-Leclerc and A.R. Ravishankara, *Geophys. Res. Lett.*, **24** (1997) 1091.

[22] R.K. Talukdar, C.A. Longfellow, M.K. Gilles and A.R. Ravishankara, *Geophys. Res. Lett.*, **25** (1998) 143.

[23] S.M. Ball, G. Hancock, S.E. Martin and J.C. Pinot de Moira, *Chem. Phys. Lett.*, **264** (1997) 531.

[24] W. Armerding, F.J. Comes and B. Schülke, *J. Phys. Chem.*, **99** (1995) 3137.

[25] W.B. DeMore, S.P. Sander, D.M. Golden, R.F. Hampson, M.J. Kurlo, C.J. Howard, A.R. Ravishankara, C.E. Kolb and M.J. Molina, *Chemical Kinetics and Photochemical Data for Use in Stratospheric Modeling Evaluation Number 11*, JPL 94-26, NASA Jet Propulsion Laboratory Publication (1994).

[26] W.B. DeMore, R.R. Friedl, S.P. Sander, D.M. Golden, R.F. Hampson, M.J. Kurlo, R.E. Huie, G.K. Moortgat, A.R. Ravishankara, C.E. Kolb and M.J. Molina, *Chemical Kinetics and Photochemical Data for Use in Stratospheric Modeling Evaluation Number 13*, JPL 00-3, NASA Jet Propulsion Laboratory Publication (2000).

[27] N. Taniguchi, K. Takahashi, Y. Matsumi, *J. Chem. Phys.* **111** (1999) 6350.

[28] D. Bauer, L. D'Ottone and A. Hynes, *Phys. Chem. Chem. Phys.*, **2** (2000) 1421.

[29] W.B. DeMore and O.F. Raper, *J. Chem. Phys.*, **44** (1966) 1780.

[30] I.T.N. Jones and R.P. Wayne, *J. Chem. Phys.*, **51** (1969) 3617.

[31] C.L. Lin and W.B. Demore, *J. Photochemistry,* **2** (1973/74) 161.

[32] G.K. Moortgat and P. Warnek, *Z. Naturforsch.* **30a** (1975) 835.

[33] S.M. Ball, G. Hancock, J.C. Pinot de Moira, C.M. Sadowski and F. Winterbottom, *Chem. Phys. Lett.*, **245** (1995) 1.

[34] J.C. Brock and R.T. Watson, *Chem. Phys.*, **46** (1980) 477.

35 K. Takahashi, M. Kishigami, Y. Matsumi and M. Kawasaki, *J. Chem. Phys.*, **105** (1996) 5290.

36 S.M. Ball, G. Hancock and F. Winterbottom, *Faraday Discuss.*, **100** (1995) 215.

37 L.T. Molina and M.J. Molina, *J. Geophys. Res.*, **91** (1986) 14501.

38 A.M. Bass and R.J. Paur, *Proc. Quadriennial Ozone Symp.* Chalkidiki Greece, eds. C. Zefros and A. Ghazi. Reidel. Dordrecht, (1984) 606p.

39 J.P. Burrows, A. Richter, A. Dehn, B. Deters, S. Himmelmann, S. Voigt and J. Orphal, *J. Quant. Spectrosc. Radiat. Transfer.*, **61** (1999) 509.

40 R.G. Derwent, Gas Kinetic Discussion Group, Royal Society of Chemistry, Laboratory Studies of Atmospheric Chemistry (1997).

41 M. Muller, A. Kraus and A. Hofzumahaus, *Geophys. Res. Lett.*, **22** (1995) 679.

42 R. Shetter, C.A. Cantrell, K.O. Lantz, S.J. Flocke, J.J. Orlando, G.S. Tyndall, T.M. Gilpin, C.A. Fischer, S. Madronich, J.G. Calvert and W. Junkermann, *J. Geophys. Res.*, **101** (1996) 14631.

43 C. Blindauer, V. Rozanov and J.P. Burrows, *J. Atmos. Chem.*, **24** (1996) 1.

44 A. Hofzumahaus and G. Hancock, Final Report Contract No. ENV4-CT95-0158.

45 G.D. Smith, L.T. Molina and M.J. Molina, *J. Phys. Chem. A*, **104** (2000) 8916.

46 J. Ma and M. van Weele, *Chemosphere: Global Change Science,* **2** (2000) 23.

47 Y. Matsumi, F.J. Comes, G. Hancock, A. Hofzumahaus, A.J. Hynes, M. Kawasaki and A.R. Ravishankara, *J. Geophys. Res.*, to be submitted.

Chapter 4

Time-of-flight Studies on the O(^{1}D) Atomic Fragment

4.1 Introduction to REMPI

The advent of high power, tunable, sources of radiation has allowed the field of multiphoton ionisation (MPI) spectroscopy to develop. This technique relies on the atoms or molecules being studied absorbing more than one photon simultaneously. This process, whilst possible, is highly improbable and it is only when intense, and usually strongly focused, laser beams are employed that a sufficient number of the target species will be ionised for the method to be of use. It was observed that the ion yield spectra obtained were structured, and at certain wavelengths (species dependent) the probability for the MPI process increased by orders of magnitude. This structure results from the presence of an intermediate energy state between the initial state and final ionised state, which becomes resonant with the absorption of one or more photons. To become resonant the total energy of the photons must match the energy gap between the initial and intermediate states. The second transition, from the intermediate to ionised state, is generally without structure as the ejection of the electron is very rapid, < 0.1 fs, and the Heisenberg uncertainty principle requires that the uncertainty in the energy of the transition must be large, resulting in a large frequency width. This ionisation step enables the use of intermediate states that have very short lifetimes (e.g. resulting from predissociation), which is a major advantage of the technique compared to LIF, where the lifetime of the upper state must be long enough to have a measurable fluorescence yield (typically more than a few nanoseconds). A further benefit is that it is possible to collect the ions formed from the REMPI process with a very high efficiency, with some experiments monitoring both the ions and electrons formed during the ionisation process, so the technique is very sensitive.

REMPI transitions are usually described by the number of photons required for each step; a transition denoted as an $m + n$ REMPI transition requires the absorption of m photons to reach the intermediate state followed by the absorption of a further n photons to reach the ionised state. For the vast majority of REMPI schemes that have been used $m > n$, a common set of values being $m = 2$ and $n = 1$. These values are chosen mainly because of the experimental ease

of generating the wavelengths required and an increase in the number of accessible states. These reasons will be discussed further below. Cases of $n > m$ are known, such as the 1+3 scheme for NH_2 at 416.4 nm. Schemes with n>m are of use as the low energy of the intermediate state means that it is unlikely that this state will autoionise; however, they suffer from a high probability that the first step will be significantly saturated. Two useful review articles that cover many of the salient points of REMPI, and provide many examples, are by Hudgens[1] and Pratt.[2]

The wavelengths required for the REMPI process depend on a number of factors, such as the species under investigation, the nature of the intermediate state and the number of photons required in each step. The species and intermediate energy level dictates the energy that the photons have to supply to reach the resonant intermediate, and also the energy then required to achieve ionisation. For example some of the REMPI transitions for O(^{1}D) are *via* the 3s ^{1}D, 3p ^{1}P, 3p ^{1}F and 3p ^{1}D intermediate states, which lie 86790 cm^{-1}, 97338 cm^{-1}, 98131cm^{-1} and 100944 cm^{-1} respectively above the O(^{1}D) level. The number of photons required for each step is then often determined by experimental considerations. The ability to add the multiple photons' energy together means that transitions where the required wavelengths could be experimentally difficult to generate can still be probed, by summing the energy of longer wavelength photons, which are often easier to form. For example, for the above transitions single photons of 115.22 nm, 102.735 nm, 101.905 nm and 99.065 nm respectively would be required to achieve the intermediate energy level, whereas if two photons are used the wavelengths needed are 230.44 nm, 205.84 nm, 203.81 nm and 198.13 nm. However, only the 3s ^{1}D state can be accessed in a single photon absorption, the others requiring two-photon absorption. All of the first set of wavelengths lie in the vacuum ultra violet, a region of the electromagnetic spectrum that is difficult to generate and manipulate. The second set of wavelengths, whilst lying in the deep UV, can be generated by frequency doubling or mixing, require no evacuation of the beam path and can be handled using comparatively standard optical materials such as fused silica. It should be noted that whilst most studies use a single wavelength for all of the photons required for ionisation, this is not a strict requirement and it is not unknown for two wavelengths to be used. The use of more than one colour of photon is most common in pulsed field ionisation studies, e.g. on NO_2,[3] where the final photon is tuned so that the system just fails to ionise, the electron being raised to a high Rydberg state* that can

---

* The principle quantum number is usually in the region of 100.

then be ionised by applying an external electric field. Other examples of multi colour schemes are 1 + 1' for NO,[4] (1 + 1') + *n* for Cl_2 [5] and (1 + 1') + 1 for $O_2(b^1\Sigma^+_g)$.[6]

The use of more than one photon to reach the intermediate state has a further benefit, namely that the selection rules for a two-photon transition differ from those for a one-photon transition. As a result, transitions which are forbidden under the single photon selection rules may become allowed under the two-photon rules. A comparison of the selection rules for one- and two-photon absorption is given in Table 4-1.

Quantum Number / Property	Two Photons	One Photon
Total Parity	$+\leftrightarrow +$, $-\leftrightarrow -$	$+\leftrightarrow -$
Inversion Symmetry	$u\leftrightarrow u$, $g\leftrightarrow g$	$u\leftrightarrow g$
Electron Spin	$\Delta S = 0$	$\Delta S = 0$
Orbital Angular momentum for atoms	$\Delta l = \pm 2, 0$	$\Delta l = \pm 1$
Axial projection of electronic orbital angular momentum (for diatomics)	$\Delta\Lambda = \pm 2, \pm 1, 0$	$\Delta\Lambda = \pm 1, 0$
Total angular momentum	$\Delta J = \pm 2, \pm 1, 0$ $J = 0 \leftrightarrow\!\!\!\!\times\!\!\!\!\rightarrow 1$	$\Delta J = \pm 1, 0$ $J = 0 \leftrightarrow\!\!\!\!\times\!\!\!\!\rightarrow 0$

Table 4-1 A comparison of the main selection rules for one- and two-photon absorption in light atoms.

4.2 REMPI of O(^{1}D)

Figure 4-1 shows the atomic levels of interest in determining the intermediate state that should be used to detect O(^{1}D). The lowest energy levels of O^+ which can be reached by spin-allowed photon absorption steps from O(^{1}D) are the $^2D_{3/2}$ and $^2D_{5/2}$ states which lie 136,661 cm^{-1} and 136,645 cm^{-1} above the O($^3P_2$) ground state of oxygen. As the O(^{1}D) state lies 15,868 cm^{-1} above the ground state, the O(^{1}D) atom requires a minimum of 120,777 cm^{-1} of energy to be provided for the it to ionise. The lowest energy state of O^+, $^4S_{3/2}$, is not available for the REMPI of O(^{1}D) as it would require a spin-forbidden transition to take place.

Figure 4-1 shows that three intermediates lie at an energy where autoionisation to the $^4S_{3/2}$ ground state ion could occur. This autoionisation has been observed for the ^{1}P and ^{1}F states by Pratt *et al.*[7,8] even though it requires LS coupling rules to be broken by spin-orbit and spin-spin interactions. Pratt *et al.* also showed that, whilst autoionisation was observed, its rate was very low; therefore the ^{1}P and ^{1}F intermediates should have lifetimes which are sufficiently long that further photon absorption could occur.

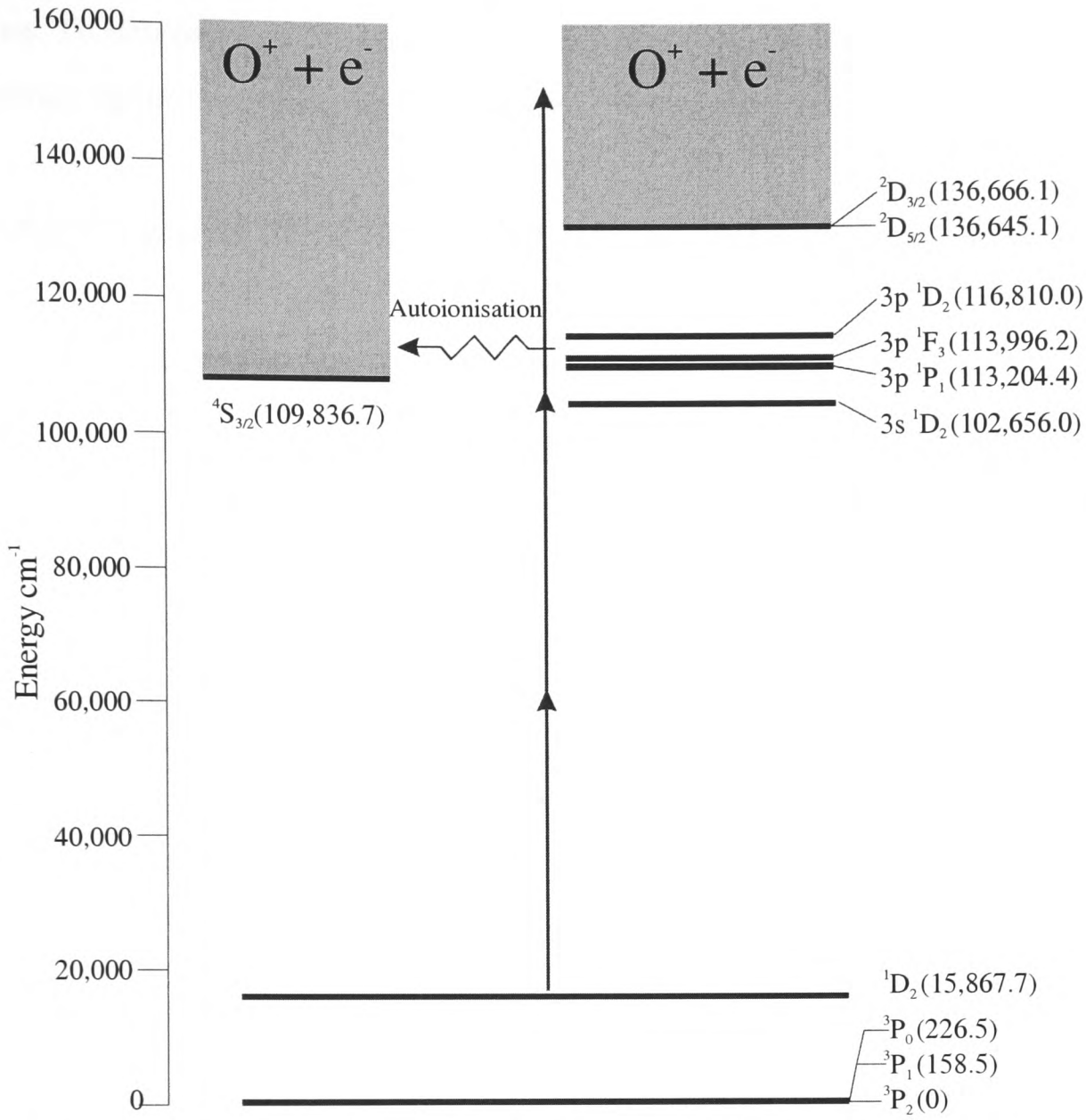

Figure 4-1 The REMPI scheme for O(^{1}D): the term energies in the brackets are taken from Moore[9] other than those for the $^1P_1$ and $^1F_3$ states which are from Eriksson and Isberg.[10]

If, for experimental reasons, we have to restrict the photons to $\lambda > 190$ nm, and to be of a single colour, the restriction mean that a minimum of three photons are required to ionise O(^{1}D). Assuming a 2 + 1 REMPI scheme, the intermediate state must lie at least 80,518 cm^{-1} above the O(^{1}D) level and the energetically accessible intermediate states are the 3s ^{1}D, 3p ^{1}P, 3p ^{1}F and 3p ^{1}D at 86,790 cm^{-1} (230.44 nm), 97,338 cm^{-1} (205.47 nm), 98,131 cm^{-1} (203.81 nm) and 100,944 cm^{-1} (198.13 nm) respectively above the O(^{1}D) level (the figure in brackets gives the two-photon wavelength required). The 3s ^{1}D level was not used as the absorption cross section of ozone at 230.44 nm is approximately fourteen times greater than for the other transitions (4.63×10^{-18} cm^2 molecule^{-1} vs. 3.35×10^{-19} cm^2 molecule^{-1} for 203.81 nm) and at least thirty times greater than in the Huggins band and would result in a significant background signal, even allowing for the low beam fluences that would be used for the REMPI process. The 3p ^{1}D level at 198.13 nm was discarded for the experimental reason that high reflectivity optics were already available for use around 204 nm to 205 nm. On the basis of previous work carried out by Pinot[11] it was decided to use the $^1F_3$ state as the intermediate for the quantum

yield studies. To determine if the choice of intermediate would have a significant effect on the results obtained further experiments were carried out and are reported in Section 4.3.

4.3 Observation of orbital alignment in O(^{1}D) REMPI

4.3.1 Time-of-flight investigation of $^1P_1$ and $^1F_3$ intermediate states

This section reports a comparison of the time-of-flight profiles observed when the $^1P_1$ and $^1F_3$ intermediate states were used to probe the O(^{1}D) produced from the photolysis of ozone. Figure 4-2 shows a scan that was carried out over the REMPI transitions and clearly shows the effect of hitting a resonant intermediate state. In this experiment a single laser was used to photolyse ozone and ionise the O(^{1}D) fragments that were produced. The ions were then detected in the bulb apparatus. It is clear in Figure 4-2 that the transitions are narrow and without structure.

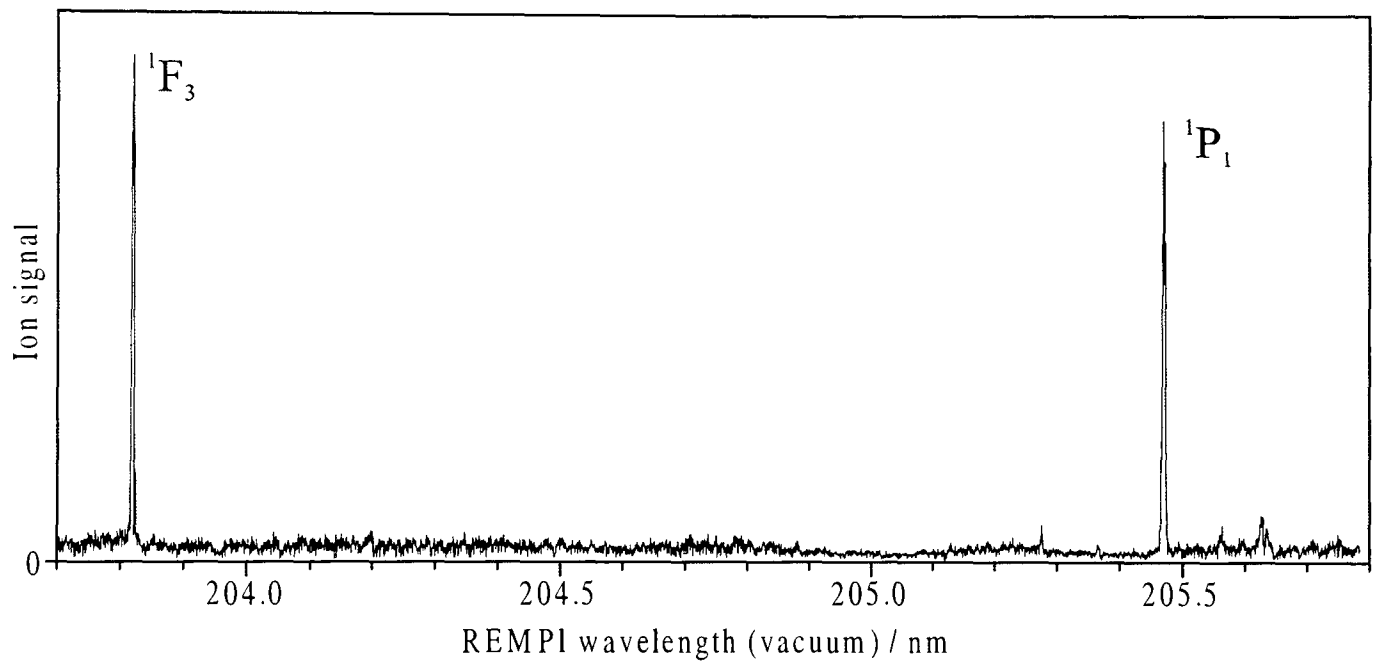

Figure 4-2 REMPI spectrum of O(^{1}D) between 203.7 nm and 205.8 nm.

To investigate any effect that the intermediate state might have on the time-of-flight profiles, a number of profiles were taken using both the $^1P_1$ and $^1F_3$ intermediates. The O(^{1}D) was generated by photolysing ozone at 301 nm; and the polarisation of both the photolysis and REMPI lasers was varied to investigate the anisotropy of the dissociation and any effects resulting from orbital alignment. These orbital alignment effects can be observed because of the preferred interaction of a photon with an atom whose transition dipole is parallel to the photon's polarisation. If, in the process of photodissociation, the emitted atom's electronic angular momentum is aligned in some manner to an external coordinate frame, then the transition moments (which must be parallel or perpendicular to the angular momentum) for photon absorption are also fixed to the coordinate frame. Therefore, unless this alignment is

lost before a further photon interacts, the strength of interaction of this photon will depend upon the alignment of the transition moments. The dependence between the strength of interaction and the transition moment alignment for further photon absorption means that there is a link between the detection efficiency, the type of transition and the detection photon's polarisation in the detection process.

The alignment of the atomic fragment occurs if the projection of **J** onto the atomic z-axis, M_J, is not distributed equally between all of the available states. Figure 4-3 shows the M_J populations for a J = 2 system which result in isotropic, oriented and aligned products. The difference between orientation and alignment is that the two ends of an oriented system can be distinguished from one another, whilst in an aligned system, there is a difference between end on and side on but not between the two ends.

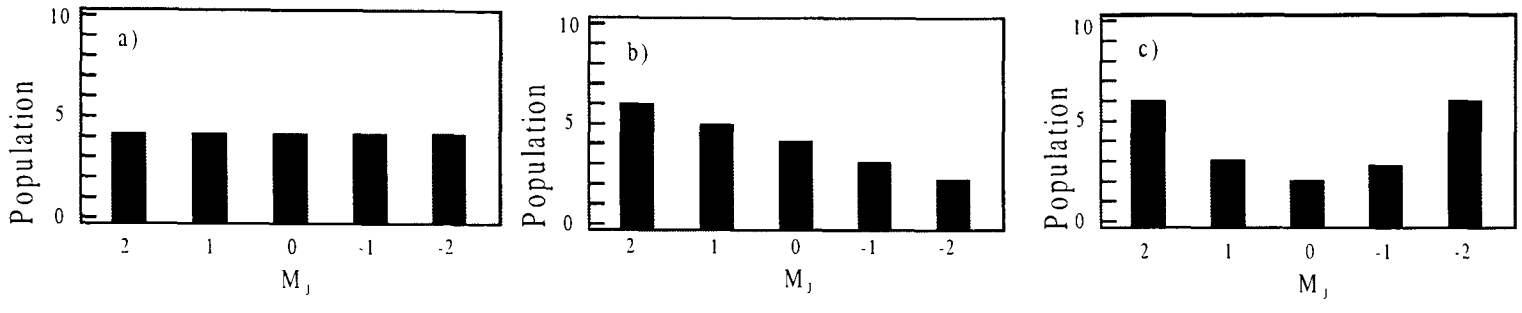

Figure 4-3 Comparison of M_J populations for an isotropic sample (a), oriented sample (b) or aligned sample (c).

These alignment effects are of great interest as a number of groups[12,13,14] have recently reported clear evidence that the O(^{1}D) produced from the photolysis of N_2O is orbitally aligned. A major feature of their observations of the angular distribution of the O(^{1}D) was that it changed significantly with the choice of intermediate state for O(^{1}D) 2+1 REMPI. Such a change in the apparent angular distribution can be seen in the β values of Ahmed *et al.*[12] who found the apparent value of β = 0.39 when probing *via* the $^1F_3$ state and β = 0.64 when using the $^1P_1$ state.

Figure 4-4 shows the profiles obtained when the REMPI laser was set to the magic angle, so as to try to minimise any orbital alignment effects, and the photolysis laser was switched between horizontal and vertical polarisation. It is immediately clear that there is a significant difference between the profiles obtained using the two different intermediates. Whilst the profiles taken with the photolysis laser vertical* are similar, the dip in the centre of the horizontal† profiles is much more pronounced for the $^1P_1$ than for $^1F_3$.

---

* This is for polarisation perpendicular to the time-of-flight axis (y axis in Figure 2-1).
† This is for polarisation in the time-of-flight axis (z in Figure 2-1).

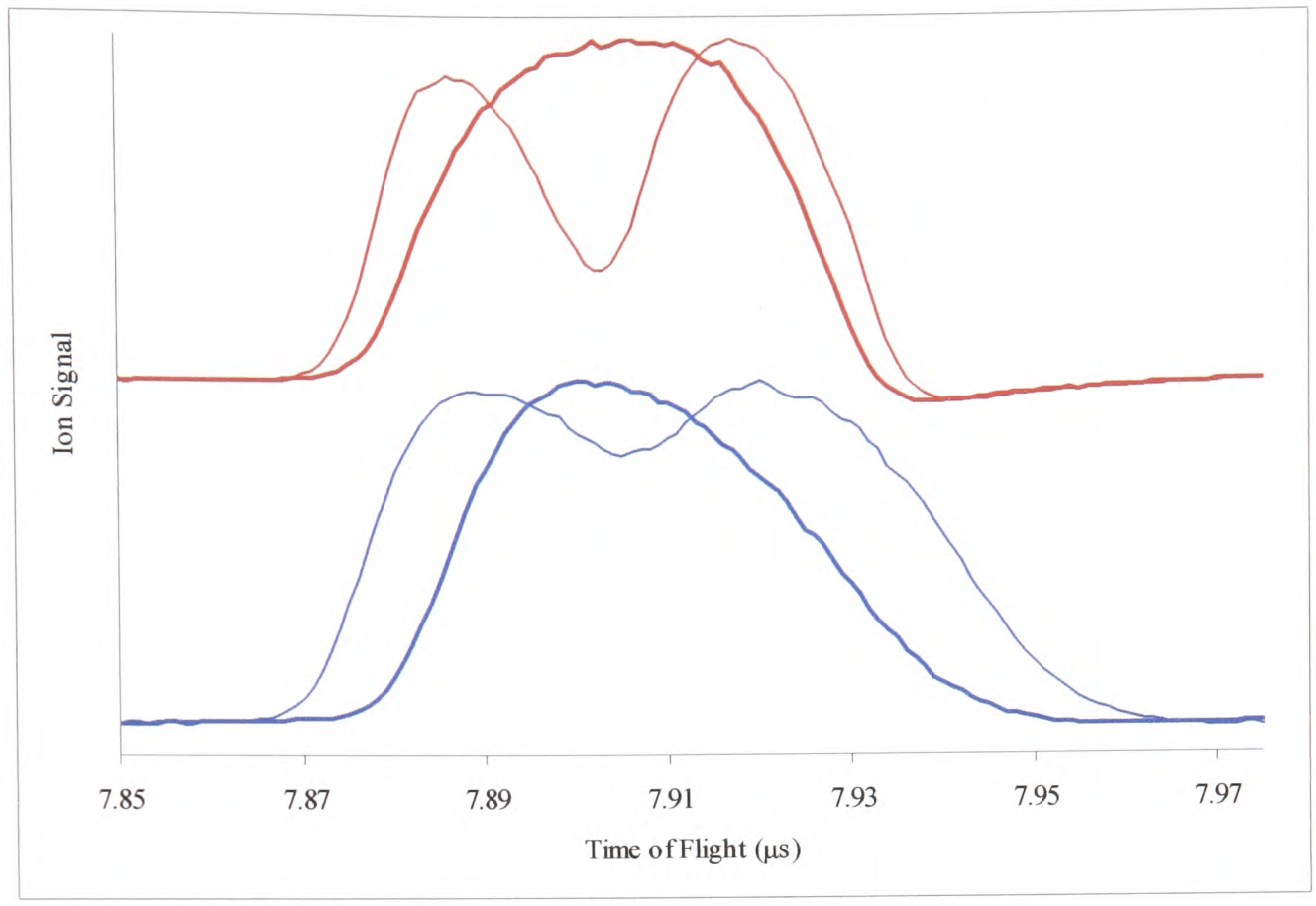

Figure 4-4 O(^{1}D) time-of-flight profiles obtained with the REMPI laser at the magic angle and the photolysis laser horizontal (thin) and vertical (thick). The upper red traces are REMPI *via* the $^1P_1$ state and the lower (blue) traces from the $^1F_3$.

The difference in the profiles recorded would severely affect measurements of the photofragment angular anisotropy, with the value of β measured *via* the $^1P_1$ state being larger than that measured *via* the $^1F_3$. Unfortunately it has not proved possible to extract exact values of β from these profiles as a result of core extraction problems which have prevented the extraction of the O(^{1}D) speed distribution. A distribution exists as the O_2 co-fragment formed has a range of rotational energies, and the distribution is needed as the value of β has been observed to be speed dependent. However, rough simulations, using a single β value and a single O(^{1}D) kinetic energy, have shown that the apparent β for the $^1F_3$ state is small and positive (*ca.* 0.1) and the value for the $^1P_1$ substantially larger (*ca.* 1).

Using the description governing the form of an ion image given by Neyer *et al.*,[13] in addition to the photodissociation anisotropy there is an angular dependent detection function. The inclusion of s detection function means that the model of ion distribution, as described in Section 2.6.2 no longer suffices and the observed ion distribution should now be modelled by:

$$I_{profile} \propto I_{recoil} \times I_{detection} \qquad \textbf{(4-1)}$$

where $I_{profile}$ is the measured signal, I_{recoil} is the ion's distribution due to the photodissociation:

$$I_{recoil} \propto 1 + \beta P_2(\cos(\theta)) \qquad \textbf{(4-2)}$$

and $I_{detection}$ is a detection efficiency function which is also dependent on θ, the angle between the laser polarisation axis and the recoil velocity. If a suitable form for $I_{detection}$ can be found it should be possible to model the profiles that would be obtained for different REMPI transitions. Neyer *et al.*[13] showed that the function required the scalar, dipolar and quadrupolar components of the spherical angular momentum tensors, along with Legendre polynomials of the same rank (P_k), to be included when linearly polarised radiation was being employed (should circular polarisation be used then odd ranks would have to be included). Once various normalisation factors had been allowed for Neyer *et al.* reported that the detection efficiency depended on the initial and final values of *J*, as well as θ, and took the form:

$$I_{detection} = 1 + a_2 A_0^{(2)} P_2(\cos(\theta)) + a_4 A_0^{(4)} P_4(\cos(\theta)) \qquad \textbf{(4-3)}$$

in which a_k (which allows for angular momentum and geometric factors) and $A_0^{(k)}$ (which accounts for alignment parameters) are *J* dependent functions. Like Ahmed *et al.*,[12] when the values of a_4 were calculated for transitions *via* the $^1P_1$ and $^1F_3$ intermediates Neyer *et al.* found that the value of the quadrupolar component, a_4, was approximately ten times larger for the $^1P_1$ state (-6.857) then the $^1F_3$ (-0.7347). The a_2 values were calculated as roughly equal in magnitude but opposite in sign (0.8163 for $^1F_3$ and -0.7143 for $^1P_1$). These values have great significance if the REMPI laser is at 54.7°, the angle at which $P_2(\cos(\theta))$ is zero, where only the a_4 term is active. Here the $^1F_3$ state's detection function will now be significantly less than that of $^1P_1$ and so profiles obtained at this angle will be closer to their true angular anisotropy. It should be noted that $P_4(\cos(\theta))$ also has angles at which it goes to zero (at 30.6° and 70.1°), and measurements made at these angles can help in confirming the values of a_2.

In addition to the studies on N_2O already mentioned, studies on ozone have observed marked orbital alignment of the O(^{1}D) produced. Whilst Taniguchi *et al.*[15] and Blunt and Suits[16] did not investigate both REMPI transitions, the ion images of both groups, taken *via* the $^1P_1$ state, show a marked anisotropy, which clearly appears to be strongly positive.

Figure 4-5 to Figure 4-7 show that irrespective of the photolysis laser's polarisation the profiles recorded *via* the $^1P_1$ intermediate state always show a more marked angular anisotropy. A further observation is that the profiles obtained *via* the $^1F_3$ state are **always** wider than those obtained *via* the $^1P_1$ state. These observations would suggest that REMPI *via* the $^1F_3$ state is probing a different speed distribution to that *via* the $^1P_1$ state. Once again it is possible that the

N_2O[13,14] studies might be able to help explain how apparently different speed distributions could exist. These studies found that the detectivity depends on the $|m_j|$ magnetic sublevel of the $^1D_2$ initial state, and that the sublevel population can depend on the rotational level of the N_2 co-fragment. The extent to which the sublevel can affect the detection function is shown in Figure 4-8 and in Figure 4-9 which are plots derived from the formulae and values of Neyer *et al.*[13] In these it can be seen that the value of the detection function, (4-3), for the $^1F_3$ transition has a value of zero for the $m_j = 0$ sublevel when the probe laser is set at zero degrees, whilst the detection function for the $^1P_1$ transition is zero for both the $m_j = 0$ and $m_j = 2$ sublevels. Therefore, when the REMPI laser polarization is set at zero degrees to the detection axis, the $^1P_1$ transition can only probe the $m_j = 1$ sublevel whilst the $^1F_3$ transition detects both the $m_j = 1$ and $m_j = 2$ sublevels. The increased width of the profiles taken *via* the $^1F_3$ transition could be explained as fast O(^{1}D) produced in the $m_j = 2$ sublevel. As the speed distribution for the O(^{1}D) is unknown it is not possible to extend the observations to cover changes with the rotational excitation of the O_2 fragment as Neyer *et al.*[13] were able to. To investigate this observation of orbital alignment further the angular and speed distributions need to be decoupled.

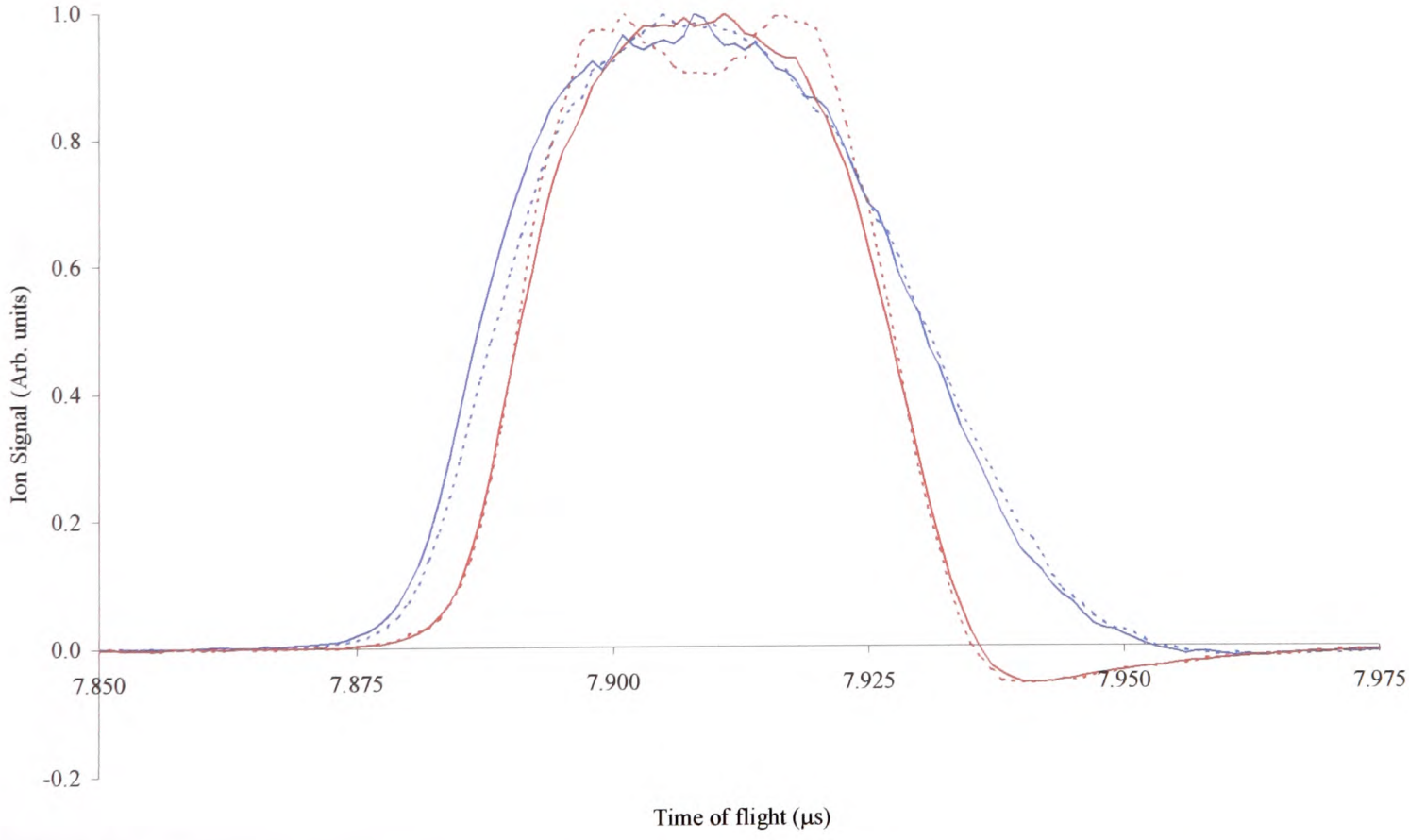

Figure 4-5 Profiles recorded with the photolysis laser at vertical polarisation. Solid lines are REMPI ($^1P_1$ red, $^1F_3$ blue) at vertical polarisation, dotted horizontal polarisation.

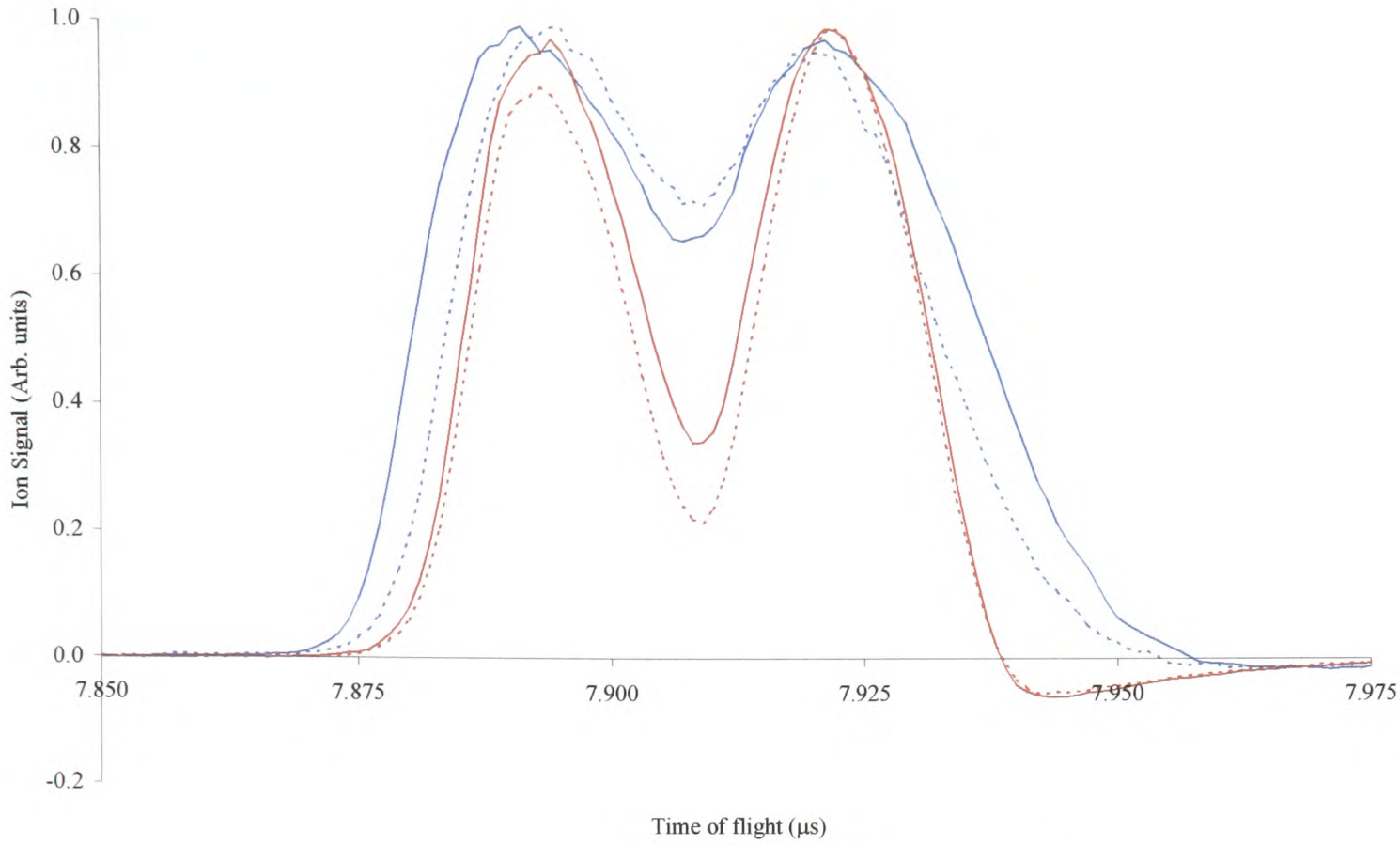

Figure 4-6 Profiles recorded with photolysis laser at horizontal polarisation.

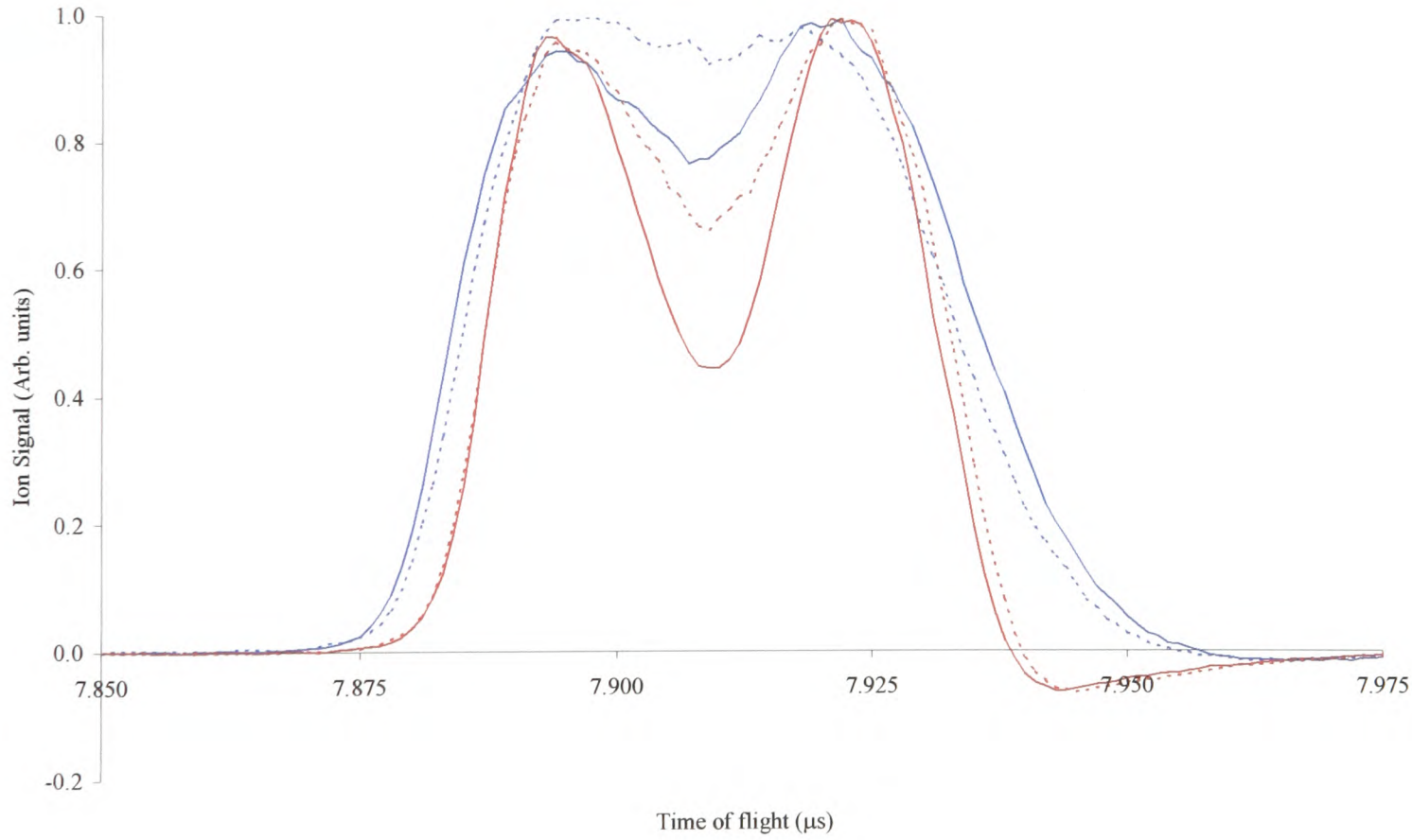

Figure 4-7 Profiles recorded with photolysis laser at magic angle polarisation.

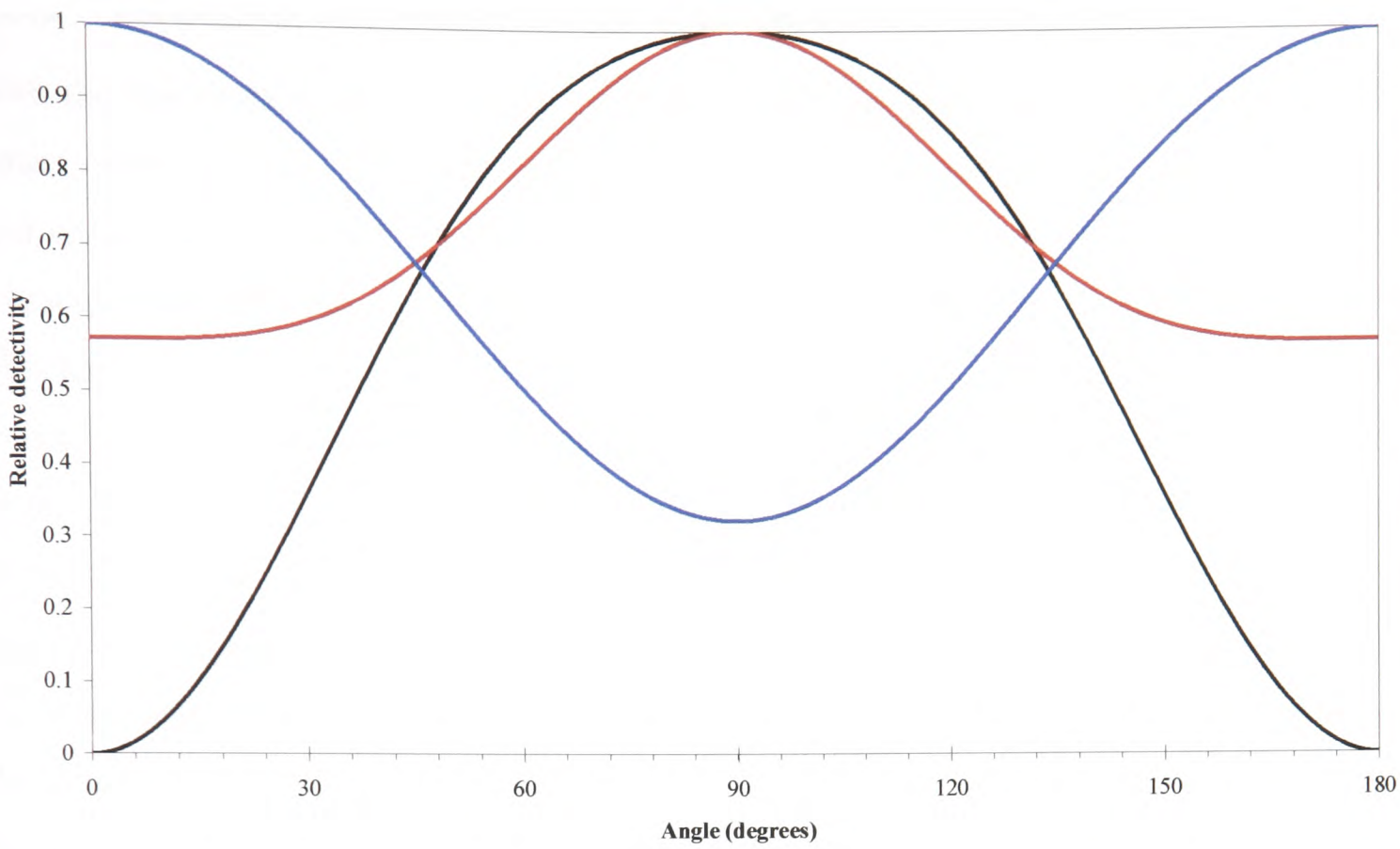

Figure 4-8 Relative detectivity plot for the $^1F_3$ intermediate. The m_j values are 0 (black), 1 (red) and 2 (blue). The curves have been renormalised to the maximum value for each m_j value. Values taken from Neyer *et al.*[13]

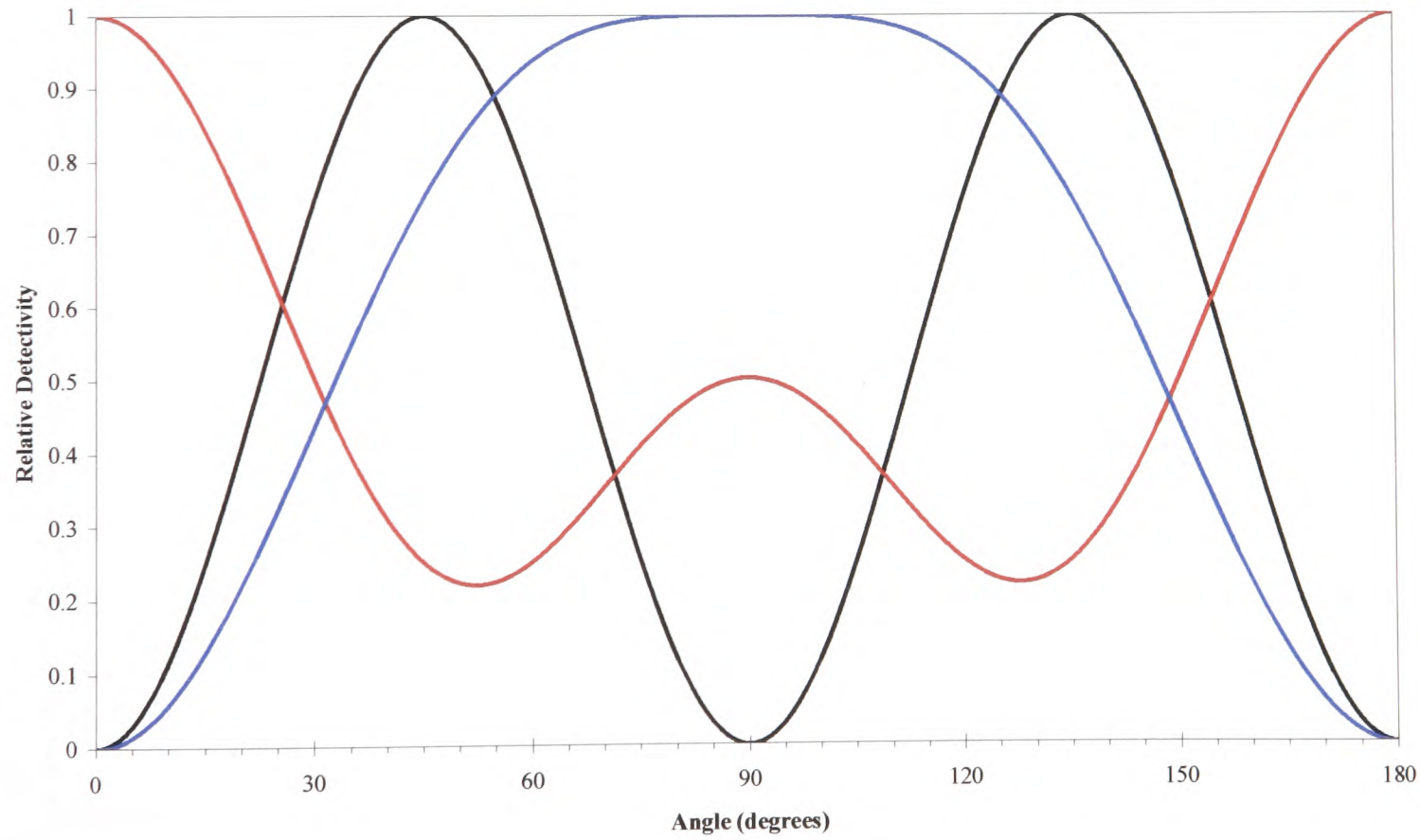

Figure 4-9 Relative detectivity plot for the $^1P_1$ intermediate. NB. the labels for m_j in Figure 5b of Neyer *et al.*[13] are incorrect, the above figure is correctly labelled.

4.3.2 Changing alignment factor with photolysis wavelength

With the observation that photolysis of ozone at 301 nm generates orbitally aligned O(^{1}D) the earlier choice of $^1F_3$ as the probe state for the quantum yield experiments was confirmed as the best option, as this state minimised the effects of orbital alignment. However, it was decided to investigate whether the degree of orbital alignment changed as a function of the photolysis wavelength which had not been explicitly examined before. If a change was observed it is possible that a correction to the calculated O(^{1}D) quantum yields would be required as a result of the detection efficiency varying for different pathways and / or surplus kinetic energy from the photolysis process. The investigation took the form of recording a number of profiles at photolysis wavelengths typical of each O(^{1}D) production pathway with the photolysis laser at the magic angle and switching the REMPI laser between horizontal and vertical polarisations. However, at the longer wavelengths the REMPI-only signal could form a significant fraction of the total signal therefore the photolysis laser was chopped during data acquisition so that an appropriate REMPI-only signal could be recorded and subtracted from the two-laser signal. After background subtraction, the profiles were then rescaled to have the same peak amplitude. The results are shown in Figure 4-10.

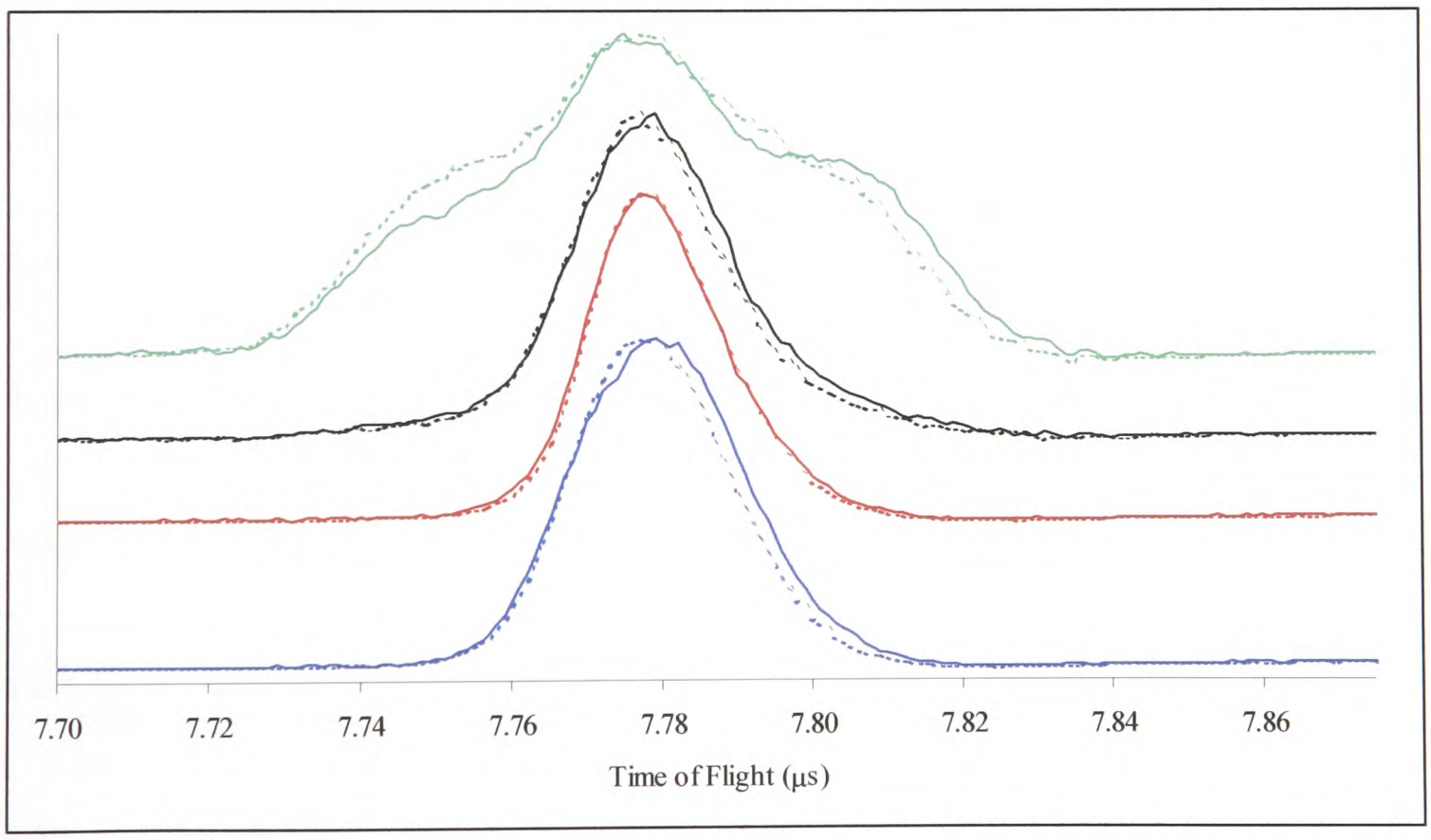

Figure 4-10 Comparison of the rescaled time-of-flight profiles taken with the photolysis laser (blue 305 nm, red 308 nm, black 315 nm, green 322 nm) at the magic angle and the REMPI laser switched between horizontal (solid line) and vertical (dotted line).

It can be seen from Figure 4-10 that there are no significant changes in the observed profile when the REMPI laser is rotated between the horizontal and vertical polarisations. The difference observed at 322 nm disappears if the profiles are made symmetrical about the centre point. The small differences that can be observed for the 305 nm and 315 nm profiles are at the edge of the experimental resolution and therefore are difficult to confirm as significant. Therefore, it would appear that under these conditions the experiments are insensitive to the effects of orbital alignment. The fact that orbital alignment was observed when photolysing at 301 nm but not at 305 nm does suggest that the degree of orbital alignment is speed dependent. Whilst the rotational levels populated in the work of Neyer *et al.*[13] were much higher than here, they did observe that the measured value of β became insensitive to the value of m_j at high rotational states. The small degree of alignment effects for the spin-forbidden channel can be seen by comparing the profiles in Figure 4-11 and Figure 4-12 which were taken with the photolysis wavelength at 321.9 nm, a peak in the absorption cross section. Figure 4-11 was taken with the REMPI laser's polarisation fixed at the magic angle and the photolysis laser's was varied; for Figure 4-12 the conditions were reversed.

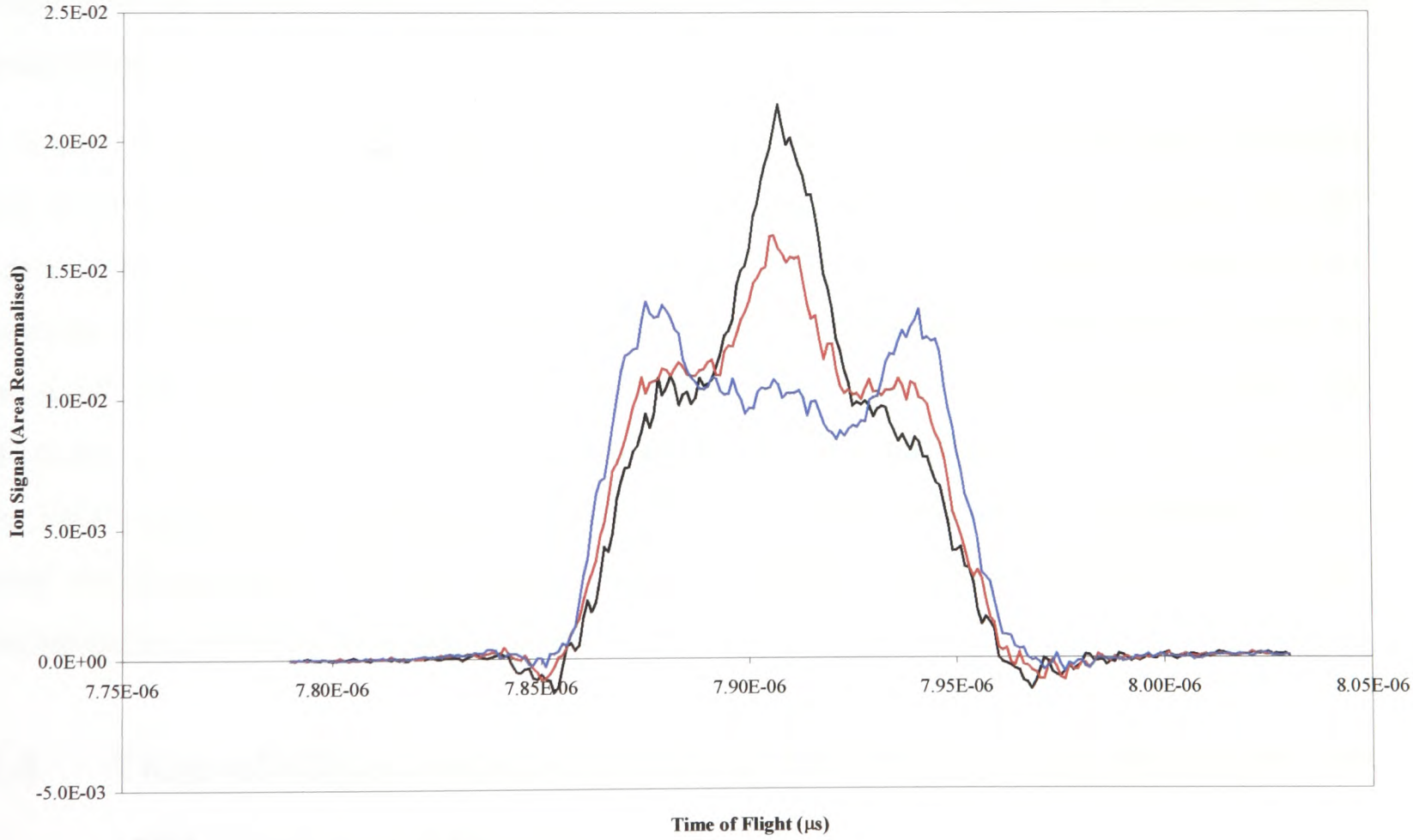

Figure 4-11 Time-of-flight profiles recorded with the REMPI laser at the 54.7° and the photolysis laser at vertical (black), magic angle (red) and horizontal (blue) polarisations.

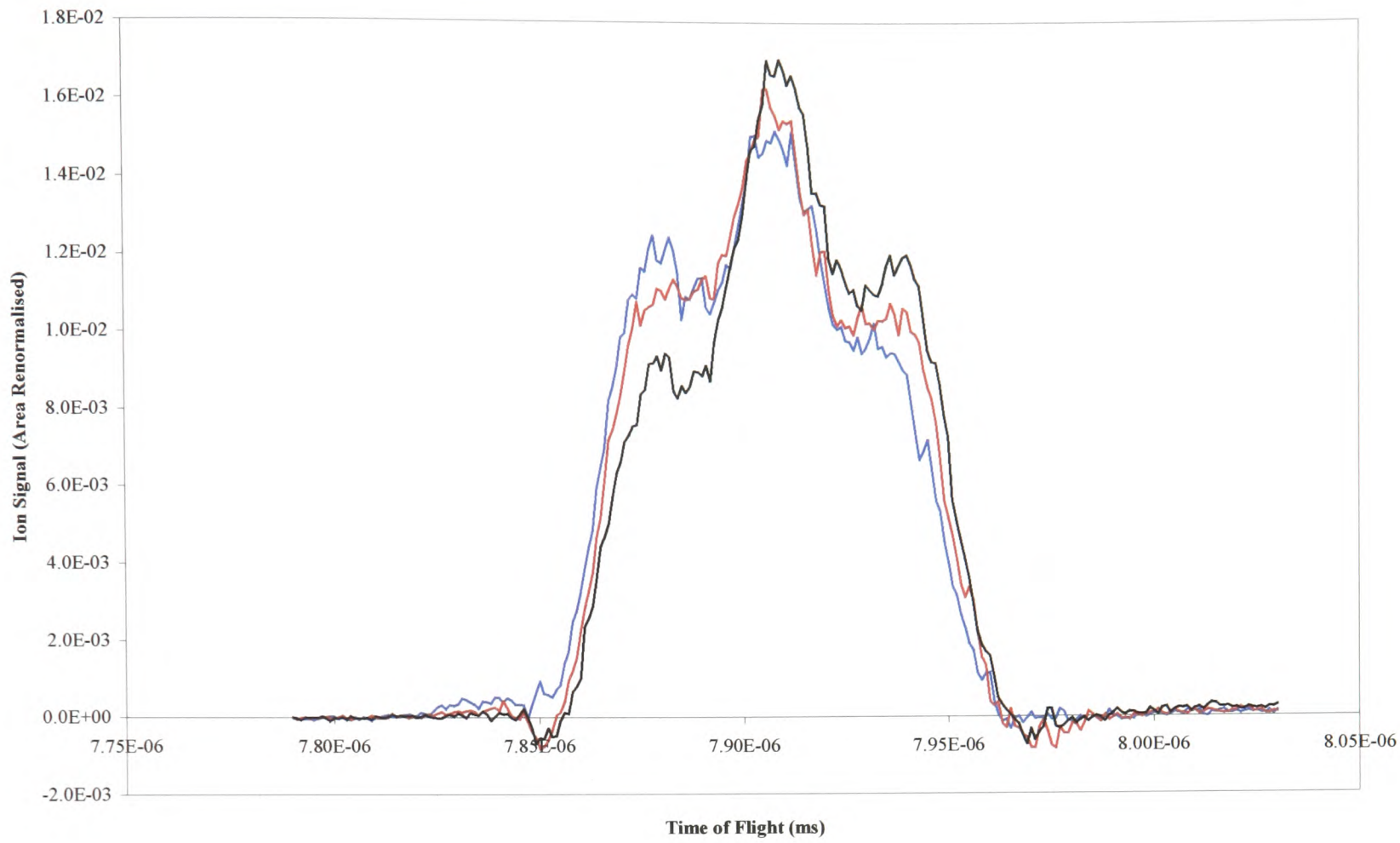

Figure 4-12 Time-of-flight profiles recorded with the photolysis laser fixed at the magic angle and the REMPI laser at vertical (black), magic angle (red) and horizontal (blue) polarisations.

It is clear in Figure 4-11 that the fragments are being produced in an anisotropic distribution and preferentially along the laser's polarisation. In Figure 4-12 there is little evidence that the signal is dependent on the polarisation of the REMPI laser. If the ion collection system used to generate the results in Chapter 3 could be affected by the polarisation of the lasers it would be expected that the polarisation of the photolysis laser would have the largest effect. As discussed in Section 3.2.6 no evidence was found for any variation of signal with changes in the laser's polarisation and therefore, unless orbital alignment can change significantly over a small wavelength range, the conclusion is that it is unlikely to produce a significant error in the determination of the O(^{1}D) quantum yield.

4.4 Time-of-flight measurements of O(^{1}D) from the photolysis of ozone (281 nm < λ < 329 nm)

In the work of Pinot[11] and Denzer *et al.*[17] short studies of the O(^{1}D) fragments formed from the photolysis of ozone above 310 nm were reported. The studies included the observation of fast O(^{1}D) fragments that originated from the spin-forbidden production of O(^{1}D). They also

reported a small increase in the energy of O(^{1}D) fragments formed just above the thermodynamic limit for the spin-allowed production of O(^{1}D). The latter was attributed to the excess energy available from vibrationally excited ozone being partitioned into fragment kinetic energy.

The present work looks in more detail at the changing time-of-flight profiles, covering a wider range of wavelengths, and shows profiles for the O(^{1}D) fragments formed when ozone is photolysed at wavelengths between 281 nm and 329 nm. The data will be presented according to the O(^{1}D) production pathway that is expected to dominate for the wavelength region.

4.4.1 Photolysis between 281 nm and 302 nm

In this region the O(^{1}D) comes exclusively from the spin-allowed pathway. It would be expected that as the wavelength decreases, and therefore the available energy increases, that the O(^{1}D) fragments would gain in energy and have a greater maximum speed. The increase in speed manifests itself in the time-of-flight profiles by a broadening of the profile and, if a positive β for the dissociation is assumed, the effect would appear as a pair of peaks moving apart for a photolysis beam polarised parallel to the detection axis. The observation can be seen clearly in Figure 4-13 where the black bands of the contour plot show the location of the peaks. What can also be seen is that at certain wavelengths the peaks suddenly rejoin, with only an apparently small signal continuing to broaden the profiles at the original rate. The peaks then start to move apart again as the wavelength is further reduced.

The change in profile would indicate that some process is removing a significant quantity of the energy available to partition between the fragments as kinetic energy. To ensure that the energy balance is met this energy must be going into internal energy of the O_2 fragment either as electronic or rovibrational energy. To determine the possible energy removal route, ΔE has to be evaluated, which can be achieved by calculating the energy difference between similar time-of-flight profiles. The most obvious choice of profiles being those where the fragments have very little translational energy i.e. where there is a single peak. The approximate locations of the profiles with similar appearance are 295.5 ± 0.5 nm and 283.0 ± 0.5 nm. The threshold of the spin-allowed O(^{1}D) channel has been determined by Taniguchi *et al.*[15] to be 309.45 nm for rovibrationally cold ozone and increases depending on the internal energy of the parent molecule. Evaluation of the average possible energy removed given these parameters is ΔE = 1505 ± 80 cm^{-1}.

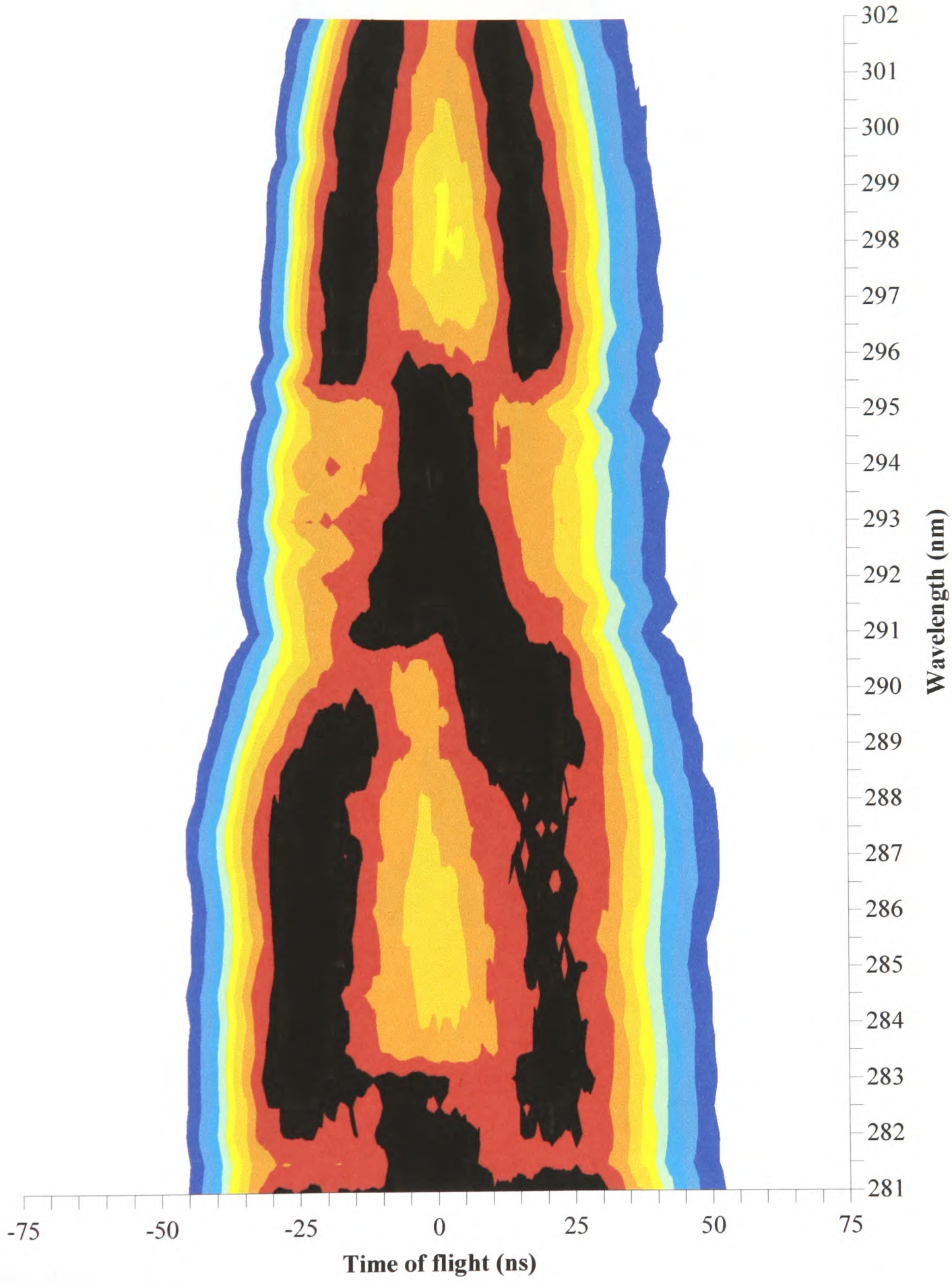

Figure 4-13 Time-of-flight profiles recorded for photolysis of ozone between 281 and 302 nm. The photolysis laser was at horizontal polarisation and the REMPI laser at the Magic angle. The profiles have been renormalised to their maximum value.

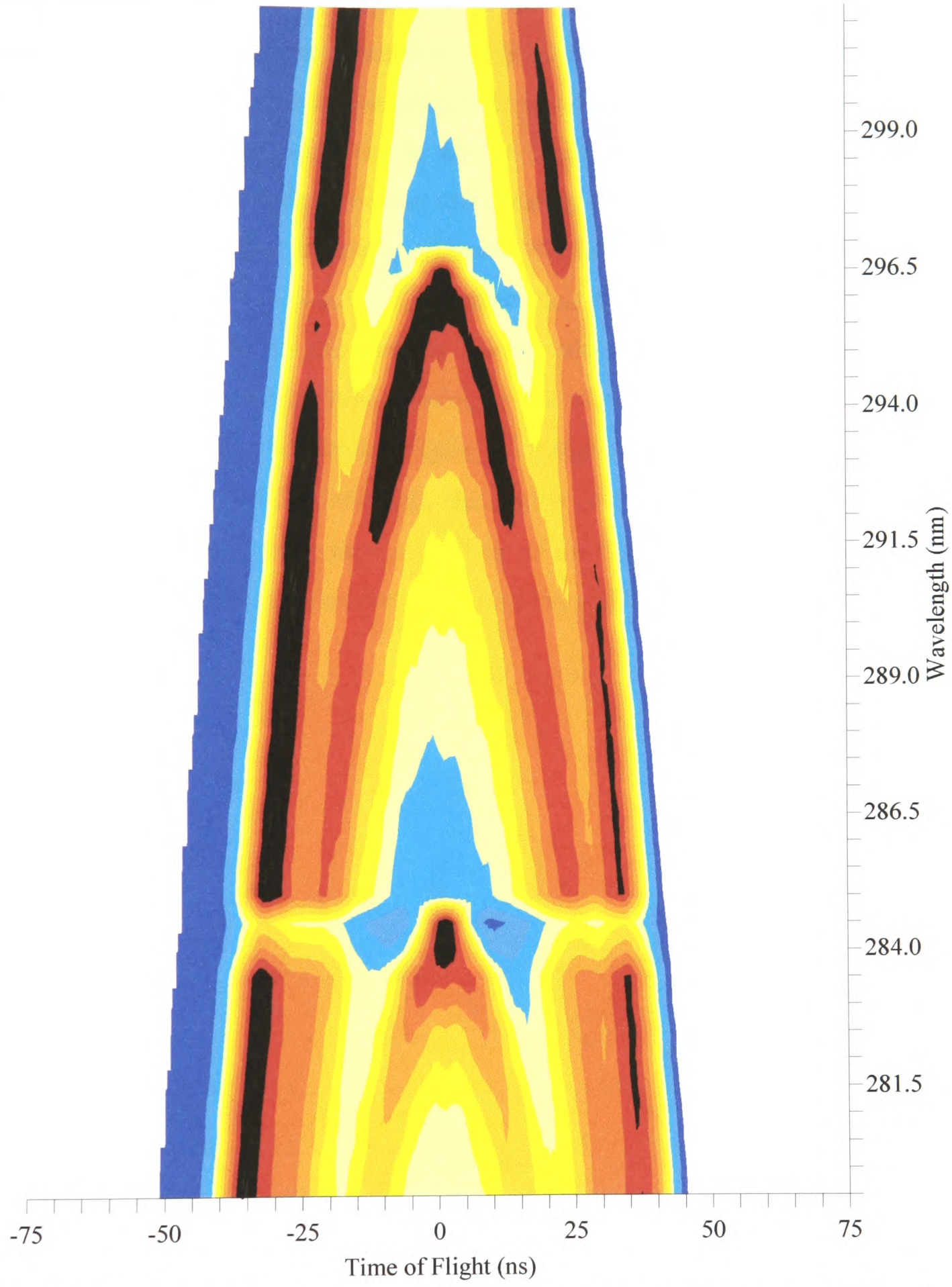

Figure 4-14 Composite of simulations of the time-of-flight profiles expected for photolysis wavelengths between 281 nm and 302 nm. The population of vibrational excitation was modelled using the vibrational populations of Valentini *et al.*[19]

The most obvious candidate for extraction of this energy is vibrational excitation of the $O_2(a^1\Delta_g)$ co-fragment, a quantum of which has 1483.5 cm^{-1} of energy.[18] Time-of-flight profiles have been simulated for ozone with the vibrational population of Valentini's *et al.*[19] but with no rotational excitation and the results can be seen in Figure 4-14. A comparison of Figure 4-14 with Figure 4-13 shows a fairly good match indicating that vibrational excitation is likely to responsible for the reduction in energy available for translation. Whilst it appears that the vibrationally excited $O_2(a^1\Delta_g)$ population is greater than that of the non excited fragments, as the signal maximum occurs for this channel, the appearance is an artefact resulting from core extraction. The slow fragments corresponding to the vibrationally excited $O_2(a^1\Delta_g)$ are core extracted less than the fast fragments. Figure 4-15 shows how a profile consisting of 30% vibrationally excited and 70% ground state $O_2(a^1\Delta_g)$ is constructed to generate the full profile, and it is clear that, even though only a minority of the $O_2(a^1\Delta_g)$ is vibrationally excited, the O(^{1}D) signal corresponding to it determines the maximum of the overall time-of-flight profile.

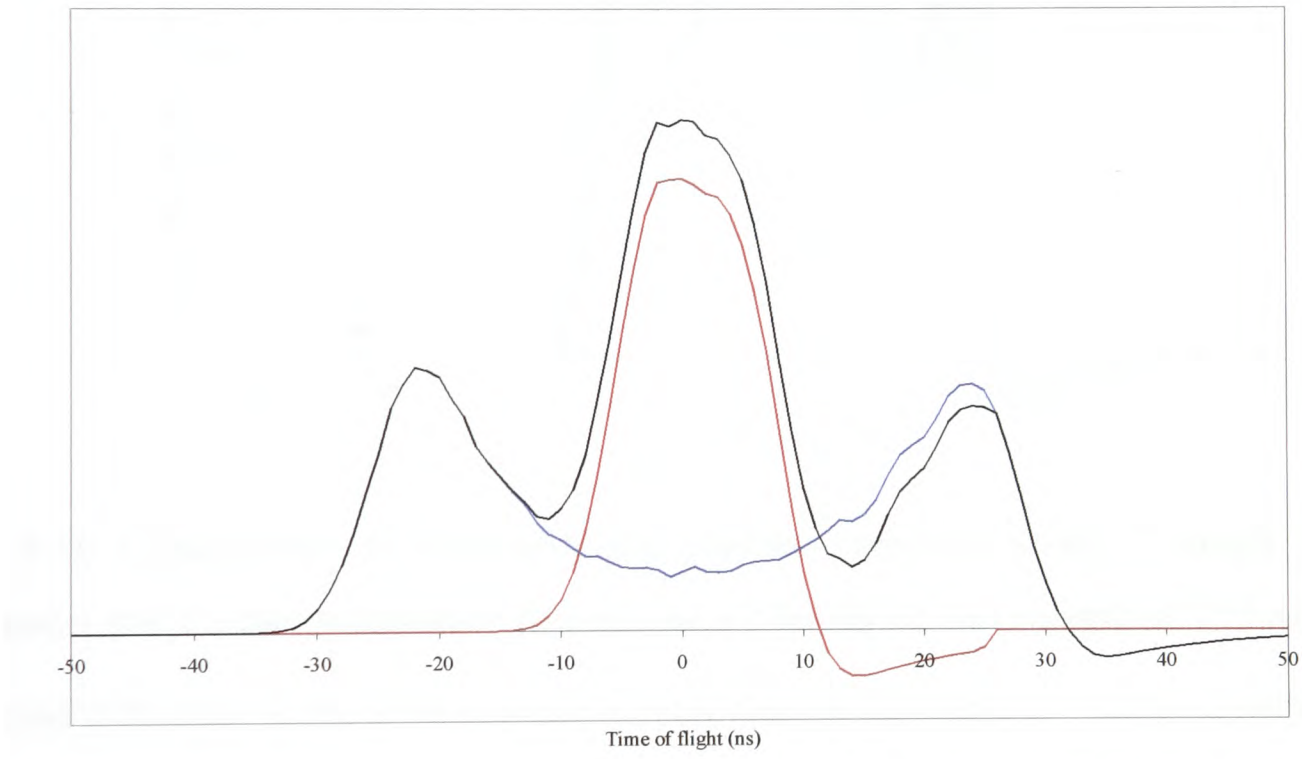

Figure 4-15 Time-of-flight simulations corresponding to the O(^{1}D) formed with ground state $O_2(a^1\Delta_g)$ (blue), vibrationally excited (red) and the total (black). The energies have been calculated based on photolysis at 296 nm.

The main discrepancy between Figure 4-13 and Figure 4-14 lies at the outer peaks particularly at wavelengths in the region of the opening of a new vibrational channel. In this region, whilst the simulation predicts that significant production of the v = 0 state should continue, it appears to be reduced with the fragments preferring to go into the v = 1 level. As the wavelength reduces further the measured data start to match the simulations once more. Figure 4-16 shows

a comparison of the simulation versus the data at 293 nm, a wavelength at which Valentini *et al.*[19] reported details of the vibrational and rotational populations. There are two main differences between the simulation and the measured profile. First, in the central region the simulation predicts two clear peaks whilst the recorded data show a broad single peak. This difference can be explained as the simulation does not allow for any rotational energy in the O_2 which would fill in the gaps between the vibrational levels. Valentini *et al.* found that the rotational population peaked at *ca.* $J = 14$, with a broad spread between $J = 6$ and $J = 18$. This rotational energy would lead to a reduction in the energy available to go into translation and therefore a pair of peaks would be expected for each rotational state the separation decreasing as the value of J increased and when these are summed a single broad peak would be expected, as observed in the black trace in Figure 4-16.

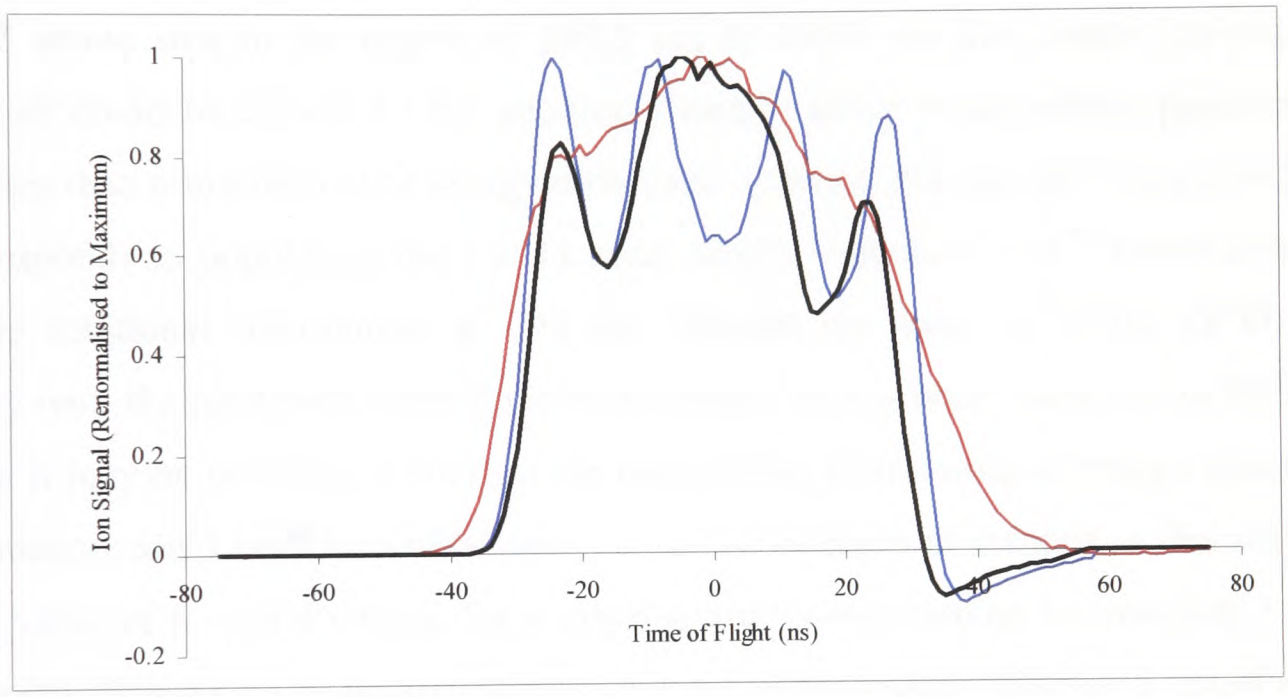

Figure 4-16 Comparison of time-of-flight profiles recorded (red), a rough simulation (blue) and a more exact simulation (black) for a photolysis wavelength of 293 nm.

The second difference is the 20% reduction in the fast O(^{1}D) peaks at ± 25 ns corresponding to production of O_2 (v = 0) between the recorded data and rough model. Once the rotational energy of the O_2 (v = 0) is taken into account this discrepancy is more or less removed, the main difference being the simulated dip between the two channels. The dip could be the result of either the populations used in the summation of the simulations being incorrect, possibly as a result of rotational energy available from the parent ozone molecule, or errors in the simulations themselves. The rotational populations for the v = 0 state reported by Valentini *et al.* were heavily biased to low J and substantially lower than predicted by a rotationally impulsive model. If the populations were greater for high J then, whilst the fast O(^{1}D) peak would be reduced in size, the dip would be filled in. The main feature within the simulations

that could be in error is the assumption of a single β value (+ 0.5) for all channels and speeds. From the work of Neyer *et al.*,[13] and others, it has been shown that the value of β for O(^{1}D) can vary markedly with the rotational population of the co-fragment.

Valentini *et al.*[19] argued that the low populations of the excited vibrational states were as a result of the following argument. The bond angle of the $^1B_2$ upper state of ozone has been calculated to be 108° which means, assuming dissociation occurs by a terminal oxygen being ejected, that most of the impulse felt by the O_2 fragment will be perpendicular to its bond rather than parallel to it. Impulse perpendicular to the bond would suggest that the excitation of the vibrational mode of oxygen would be comparatively weak when compared to rotational excitation. Thelen *et al.*[20] argued that this model was an over simplification of the true mechanism and that complex dynamics were in fact involved.

Figure 4-13 shows that in the region of 295.5 nm to 293.0 nm the profiles do not change greatly, which could be caused by the additional energy being preferentially partitioned into rotation rather than translation. The energy difference between 296 and 293.5 nm is ≈ 280 cm^{-1} which corresponds to populating the J = 14 state, which Valentini *et al.*[19] found to be at the peak of the rotational distribution at 293 nm. Should the value of β for O(^{1}D) change significantly with the rotational state of the co-fragment, as has been observed for O(^{1}D) from N_2O,[13] then it may be possible to confirm the preferential partitioning of energy into rotation. The confirmation could be achieved because, as the wavelength is scanned in this wavelength region, the value of β would change for a given speed (corresponding to changing J value as the wavelength changes). The investigation into a speed dependent value of β could be easily carried out by repeating this experiment using an ion imaging detection system. Changes in the value of β are readily seen in experiments using this technique and, with suitable processing, a value of β for each fragment speed can be determined, which would allow a more accurate determination of the vibrational and rotational populations to be made.

An accurate knowledge of the vibrational population distribution as the wavelength is changed could be important, since the assumption that the v = 0 population stays approximately constant has been used by Ball *et al.*[21] in their determination of the relative quantum yields of $O_2(a^1\Delta_g)$ as a function of wavelength. Careful testing by Ball *et al.* suggested that the assumption was valid and that the high vibrational states populated by production of $O_2(a^1\Delta_g)$ by the spin-forbidden process either cascaded down to the v = 0 level and was detected, or some other removal process existed, in which case their spin-forbidden quantum yields were a lower limit to the true values. Unfortunately, Ball *et al.*,[22] when investigating the kinetic

energies of the $O_2(a^1\Delta_g)$ did not take profiles close to the region where the v = 1 level starts to be formed. As they probed the $O_2(a^1\Delta_g)$ v = 0 REMPI transition the signal obtained, when suitably corrected for power and absorption cross section, would be expected to fall as some of the population moves from the v = 0 to v = 1 states. However, in the quantum yield measurements,[17] carried out over a wide range of conditions so the degree of collisional relaxation changed from 25% to 65%, no reduction in the quantum yield was detected as the wavelength was decreased, which would have been the case if the assumption was invalid.

4.4.2 Photolysis between 306 nm and 322 nm

This wavelength region spans the vibrationally mediated spin-allowed and spin-forbidden pathways for the production of O(^{1}D) from the photolysis of ozone. Because of the rapid fall in the absorption cross section of ozone and the falling quantum yield it is not possible to view the entire range of raw profiles on a single plot, as the profiles taken at the longest wavelengths are much smaller in magnitude than those taken below 308 nm. The change in signal amplitude is illustrated for the range 306 nm to 311 nm in Figure 4-17, where it can be seen that the magnitude of the maximum ion signal falls by a factor of *ca.* 5 over this range.

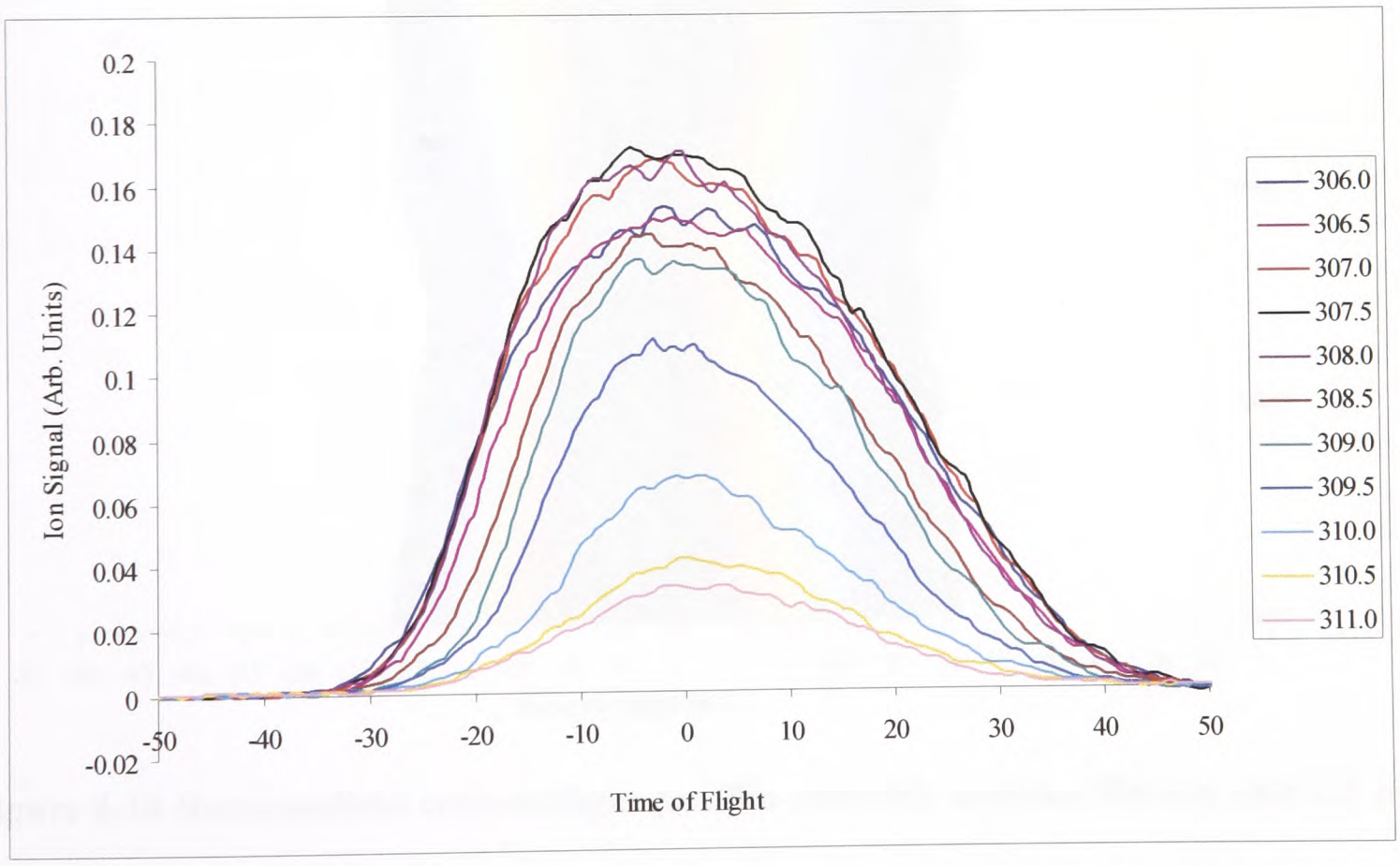

Figure 4-17 Comparison of time-of-flight profiles recorded between 306 nm and 311 nm. These have not been corrected for changing laser energy or absorption cross section.

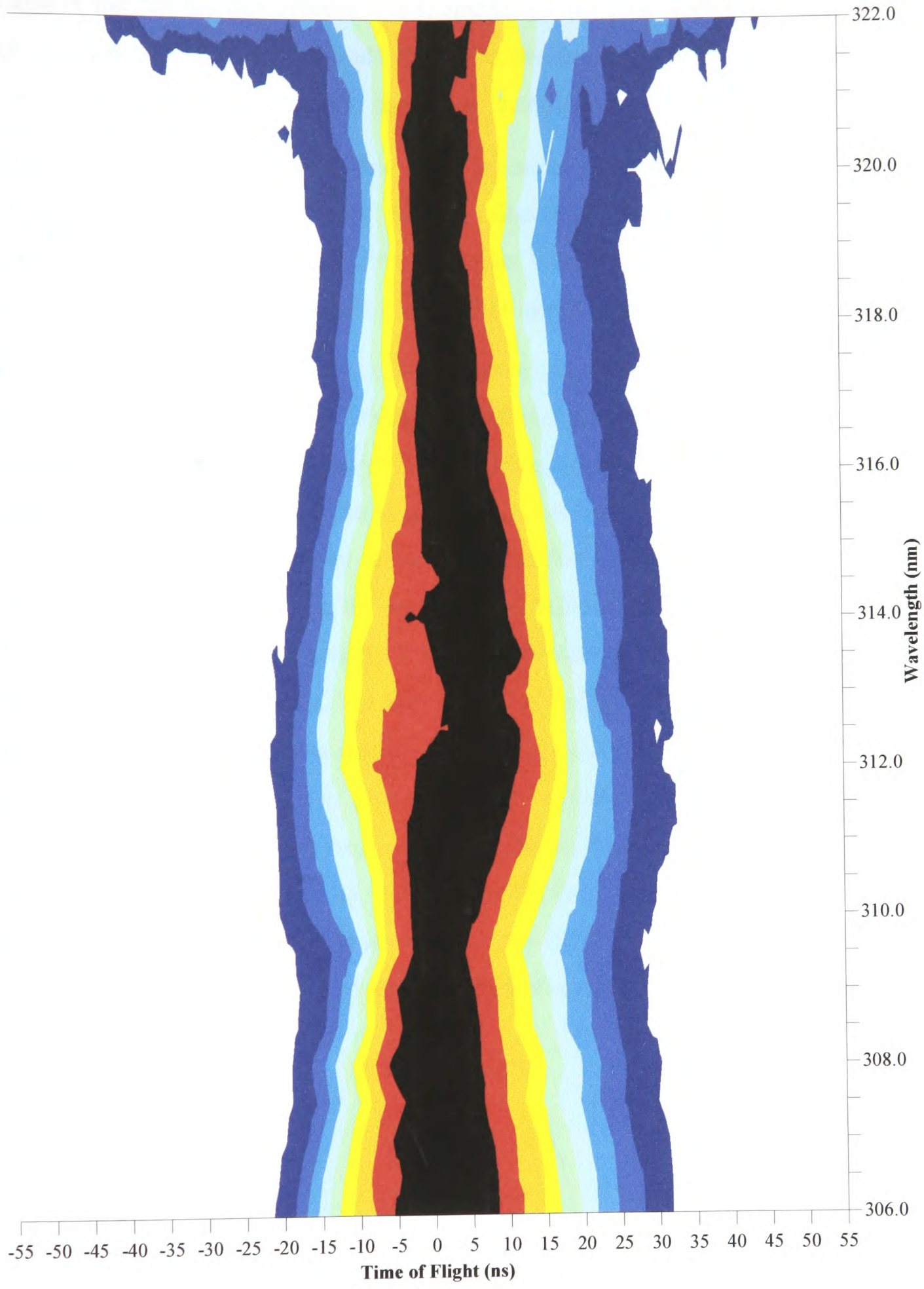

Figure 4-18 Renormalised time-of-flight profiles recorded between 306 nm and 322 nm.

Whilst in theory it should be possible to correct this picture so that the signal is directly related to the quantum yield, such a correction is not possible in practice because it is not possible to correct for fluctuations in the REMPI energy, on which the signal has a squared dependence. If individual profiles were recorded, they could be shot to shot normalised and then averaged at

the end of the run but this process was found to be very slow and was not followed. The most useful comparisons that can be made, therefore, are those in which it is the relative proportions of the ion signal arriving at specific times that is compared between wavelengths.

Figure 4-18 shows the profiles that were recorded between 306 nm and 322 nm, with a wavelength separation of 0.5 nm; these profiles have been renormalised to the maximum amplitude of the signal. There are two significant features to this figure. First, there is a waist at *ca.* 309.5 nm and second, the profiles above 321 nm become much wider than those below.

The waist can be easily explained when the thermodynamics of the spin-allowed pathway are considered. As the wavelength of the photolysis radiation is increased from 306 nm the energy available for fragment kinetic energy is decreasing, which means that the fragments will arrive closer to the time expected for fragments with no initial kinetic energy. As the ozone used in the time-of-flight machine is not vibrationally cooled and only rotationally cooled to a small extent, production of O(^{1}D) *via* the spin-allowed pathway can continue to longer wavelengths. The evidence for this vibrationally mediated channel is in the increased profile width just above the waist peaking at *ca.* 312 nm. The ν_3 vibration adds a further 1042 cm^{-1} to the total available energy, which means that the O(^{1}D) fragment can have up to 700 cm^{-1} of additional kinetic energy when ozone is photolysed just above the thermodynamic limit for O(^{1}D) production from ground state ozone. This additional kinetic energy would be expected to be seen as a separation of peaks, as was seen in Section 4.4.1. The profile at 312 nm has been extracted from Figure 4-18 and is shown in Figure 4-19, and it can be seen that a small splitting in the main peak occurs. This was also seen by Denzer *et al.*[17] at 313.5 nm.

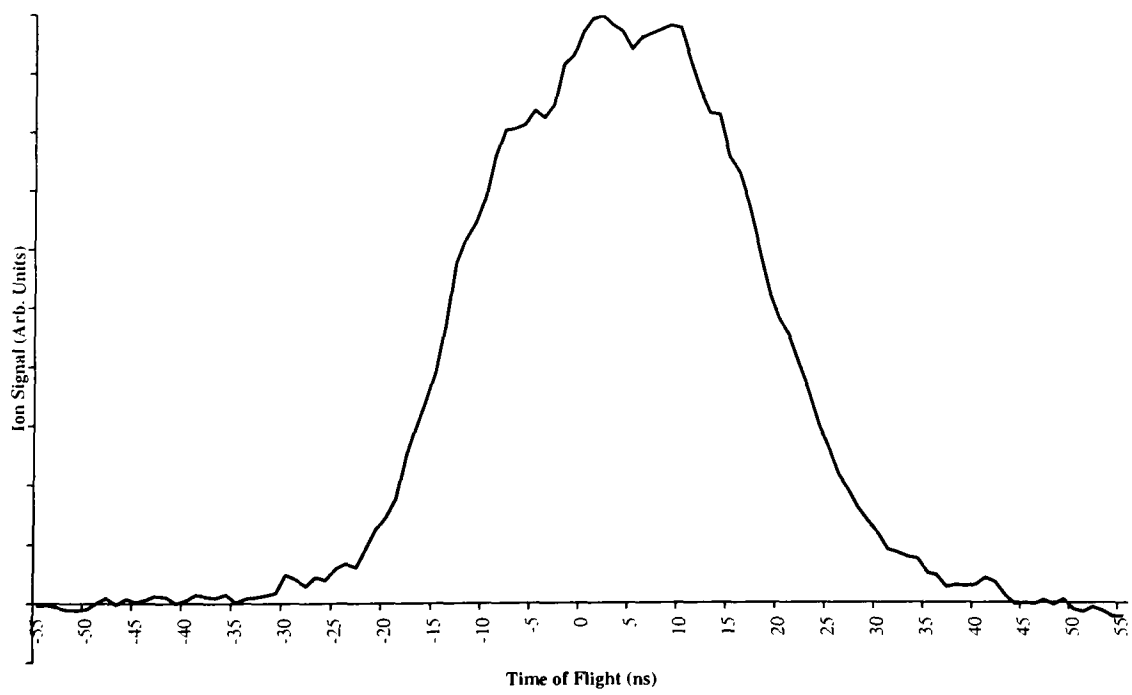

Figure 4-19 Time-of-flight profile taken at 312 nm.

The separation of the peaks is significantly smaller than that predicted if all of the available energy was put into translation, a simulation having shown that the peaks would be separated by *ca.* 30 ns. This observation is explicable if the energy is partitioned efficiently into rotation of the O_2 co-fragment. As the ozone is vibrationally excited for this production channel, enhancement of the higher rotational populations compared to O_2 formed from dissociation of ground vibrational state ozone could be reasonably expected.

The width of the time-of-flight profile obtained for photolysis above 321 nm will be discussed in the next section, but it is worth noting that the kinetic energy of the O(^{1}D) being detected in the wings of these profiles is much greater than could be expected if the production was from vibrationally excited ozone in either the $\nu_3 = 1$ or $\nu_3 = 2$ states; and therefore leaves the spin-forbidden pathway as the only possible source for O(^{1}D).

4.4.3 Photolysis between 321 nm and 329 nm

In this wavelength region it is expected that the majority of the O(^{1}D) produced is *via* the spin-forbidden pathway, as has been observed by Denzer *et al.*[17] and Takahashi *et al.*[23] The profiles obtained can be seen in Figure 4-20; the limits to the times of arrival for fragments formed by the spin-forbidden process partnered by O_2 with no internal energy are marked on the figure by the two vertical black lines. These data have been made symmetric about zero time as a result of minor misalignments over the several days during which the data were recorded. It is fairly clear that the ions forming the leading and trailing edges of the time-of-flight profiles match the expected arrival times well, which further confirms the probability that the spin-forbidden pathway is responsible for the production of O(^{1}D) at these wavelengths. What can also be seen is that the shape of the profile changes significantly within this region, and the changes occur on a local scale. Figure 4-21 shows a number of the profiles extracted from this plot.

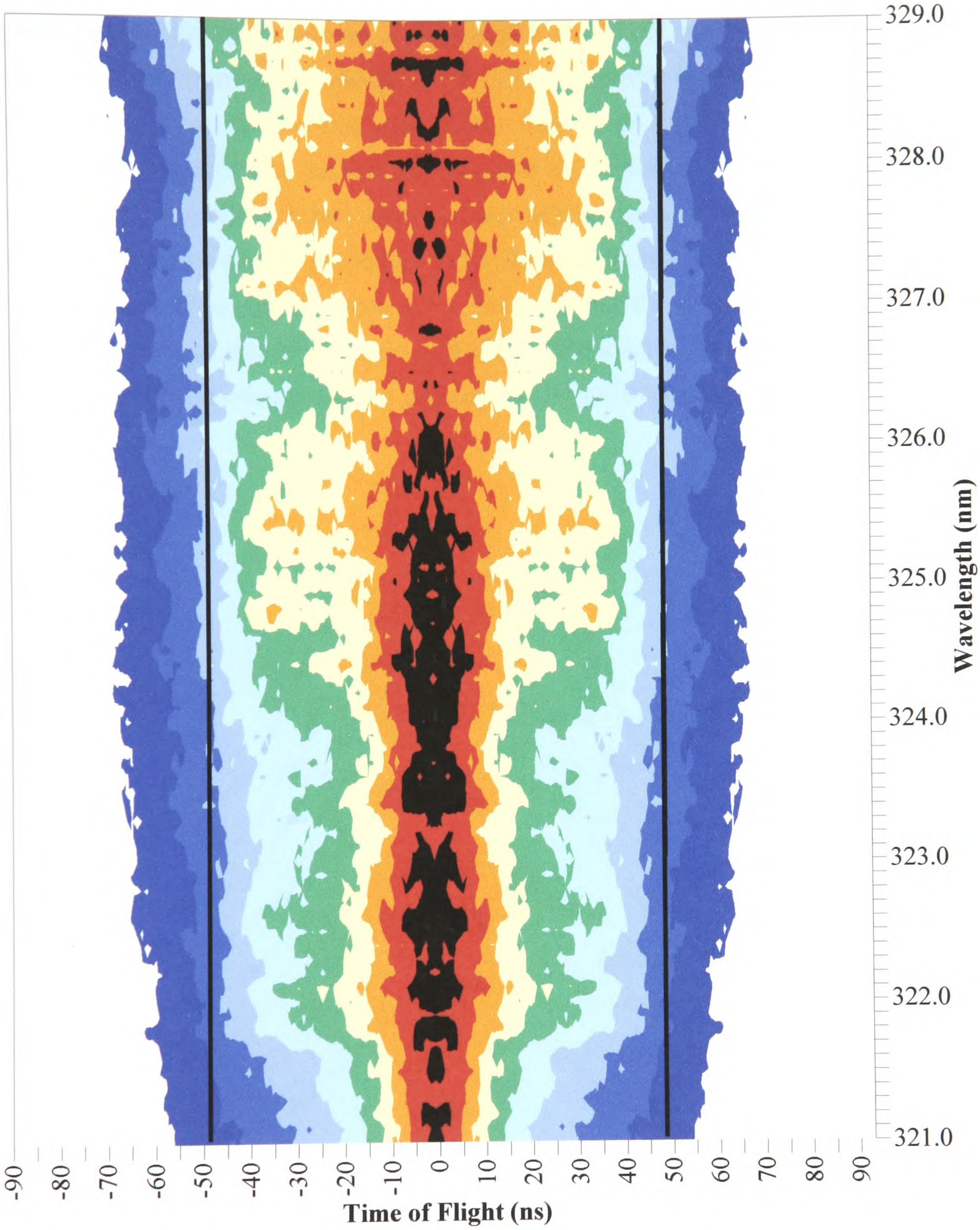

Figure 4-20 Renormalised time-of-flight profiles taken between 321 nm and 329 nm at a resolution of 0.1 nm. Features appearing on a scale smaller than this result from the surface fitting function.

The most obvious feature in the profiles is that as the wavelength of the photolysis radiation increases then so does the population of the faster O(^{1}D). At 321 nm the majority of O(^{1}D) is produced with little translational energy. At 321.9 nm the profile is broader with a significant contribution from fast O(^{1}D). This contribution dies down slightly as the wavelength is increased further to 323.9 nm, but then grows so that at 324.8 nm a clear pair of peaks can be observed and these widely separate peaks are approaching the same magnitude as the central slow atoms. By 325.5 nm the population of O(^{1}D) being formed at speeds between the fast peaks and central slow peak has increased to the point that the various peaks are no longer distinct. The slow peak then grows again until 326.5 nm where the slow peak is dominating the profile. Above this wavelength the fast populations increases again generating a single broad peak at 329 nm.

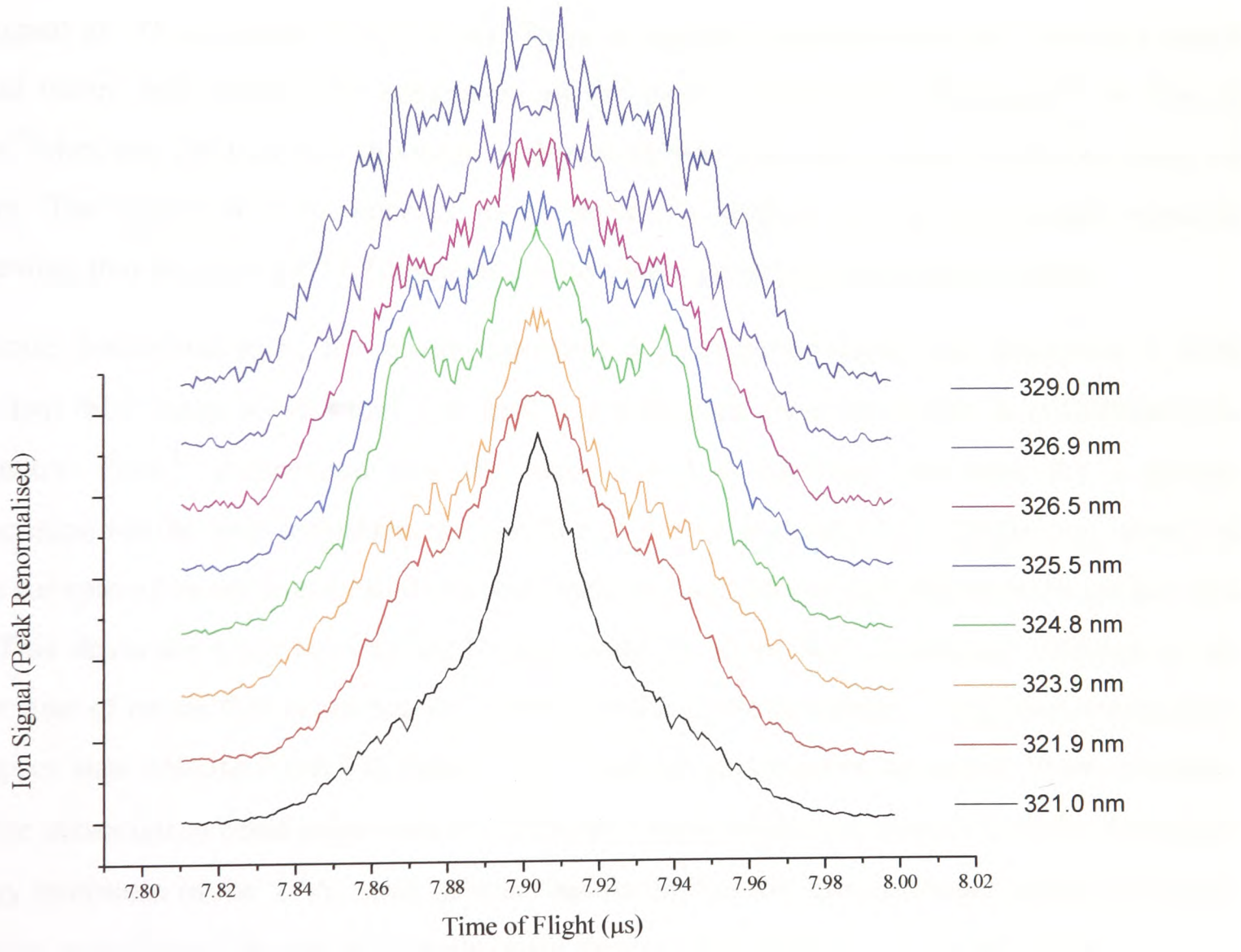

Figure 4-21 Selected time-of-flight profiles in the region 321 nm to 329 nm.

In the comparison of the profiles obtained it is instructive to also look at vertical slices from Figure 4-20, that is how the signal at a specific point in time on the time-of-flight profile changes with wavelength and these can be seen in Figure 4-22.

The times selected for the comparison relate to the centre of the profile (t = 0) where the fragments are slow, the fast fragment peak (t = -35 ns), on the side of the profile (t = -45 ns) and at the baseline (t = -85ns). Unsurprisingly the baseline signal does not change with wavelength. The signals at -45 ns and -20 ns follow each other quite well with a steady increase in the signal observed at these times as the wavelength increases. The signal at -45 ns is just inside the expected peak position for fast O(^{1}D) fragments produced with no internal energy in their partner O_2 product. The signal at -35 ns was selected for examination as this time corresponds to the clear outer peaks in the profile at 324.8 nm. Denzer *et al.*[17] and Takahashi *et al.*[23] have already established that the signal in the region of these fast O(^{1}D) peaks appears to be linked to the absorption cross section. If the trace is compared to the absorption cross section shown in the panel below there does appear to be a correlation between the two. The only peak in the absorption cross section that is not matched by a peak in the signal at -35 ns occurs at 324.2 nm. There is no clear evidence why the lack of a match should occur, and neither the assignment of the ozone spectrum by Katayama[24] or that by Joens[25] shed any light on why this peak in the absorption spectrum should be different from the others. The signal at 0 ns appears to be declining slightly as the wavelength increases suggesting that the slow O(^{1}D) fragments are no longer generating the largest signals.

Accurate determination of the speed dependent β parameters would help determine if there were two different processes and give further information about the upper state's lifetime and symmetry. Pinot[11] determined that the value for β is far from the limit for a parallel dissociation for the spin-forbidden channel (0.9 at 321.91 nm and 0.3 at 324.80 nm), whilst the value for spin-allowed dissociation has been measured at 230 nm and 266 nm to be greater than 1.1. This deviation from the expected value could be either due to different lifetimes of the upper state of ozone that is reached or a change in the ozone geometry. Using measurements on the upper state lifetime from Takahashi *et al.*[26] and the anisotropies measured, Pinot calculated that the dissociation bond angle was 84° close to a bond angle that would occur for a potential energy minimum in the 2 $^1A_1$ state. It was speculated that the spin-forbidden pathway resulted from the crossing to a dissociative triplet state through this potential energy minimum.

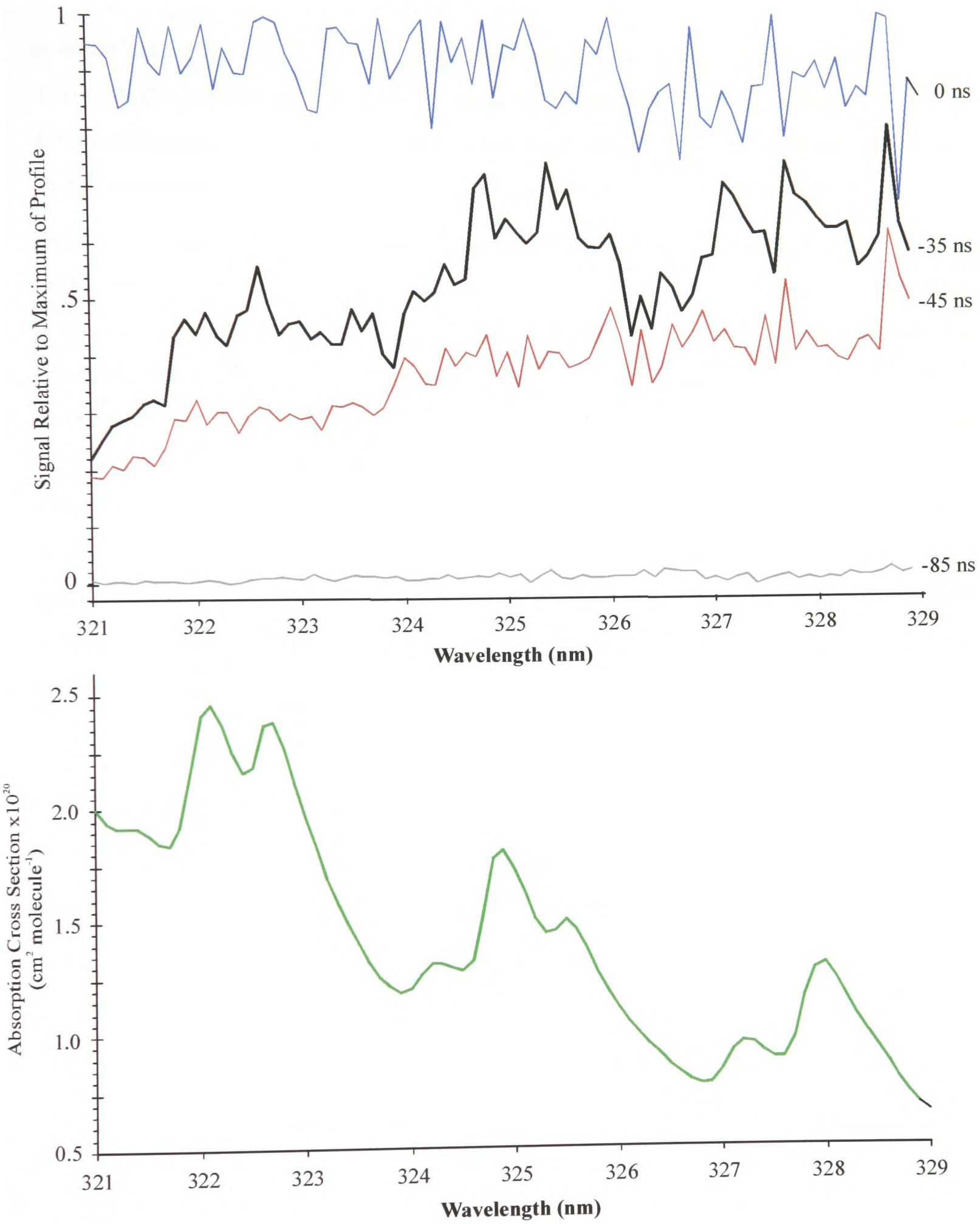

Figure 4-22 Comparison of signal at set times vs. wavelength (top panel) and ozone absorption cross section (bottom panel).

4.4.4 Higher Resolution Study of O(^{1}D) formed over a peak in the absorption cross section of ozone

In addition to the previous work presented in Section 4.4 a more in-depth investigation into the time-of-flight profiles generated over a peak in the absorption cross section was carried out. The investigation was done as evidence has been seen for an anti-correlation between the O(^{1}D) quantum yield and the absorption cross section, as reported in Section 3.9.

Figure 4-23 shows the profiles obtained, as detailed previously. A small decrease in the width of the central peak is seen as the wavelength increases as would be expected for the reduction in kinetic energy available. Above 319 nm the first signs of the spin-forbidden channel can be observed. More information is available in Figure 4-24 in which the raw profiles have been corrected for changes in photolysis power and the changing absorption cross section. In Figure 4-24 it would appear that there is a peak in the renormalised signals between 318.5 and 319.0 nm. This peak is of interest as this wavelength region is the same as that in which an anti-correlation was observed in the quantum yield (the integral of the profile should match the quantum yield if there is no change in the detection efficiency according to the time of arrival). A plot of the signal at time zero, which was found to match that of the integrals of the profiles, compared to the absorption cross section can be seen in Figure 4-25.

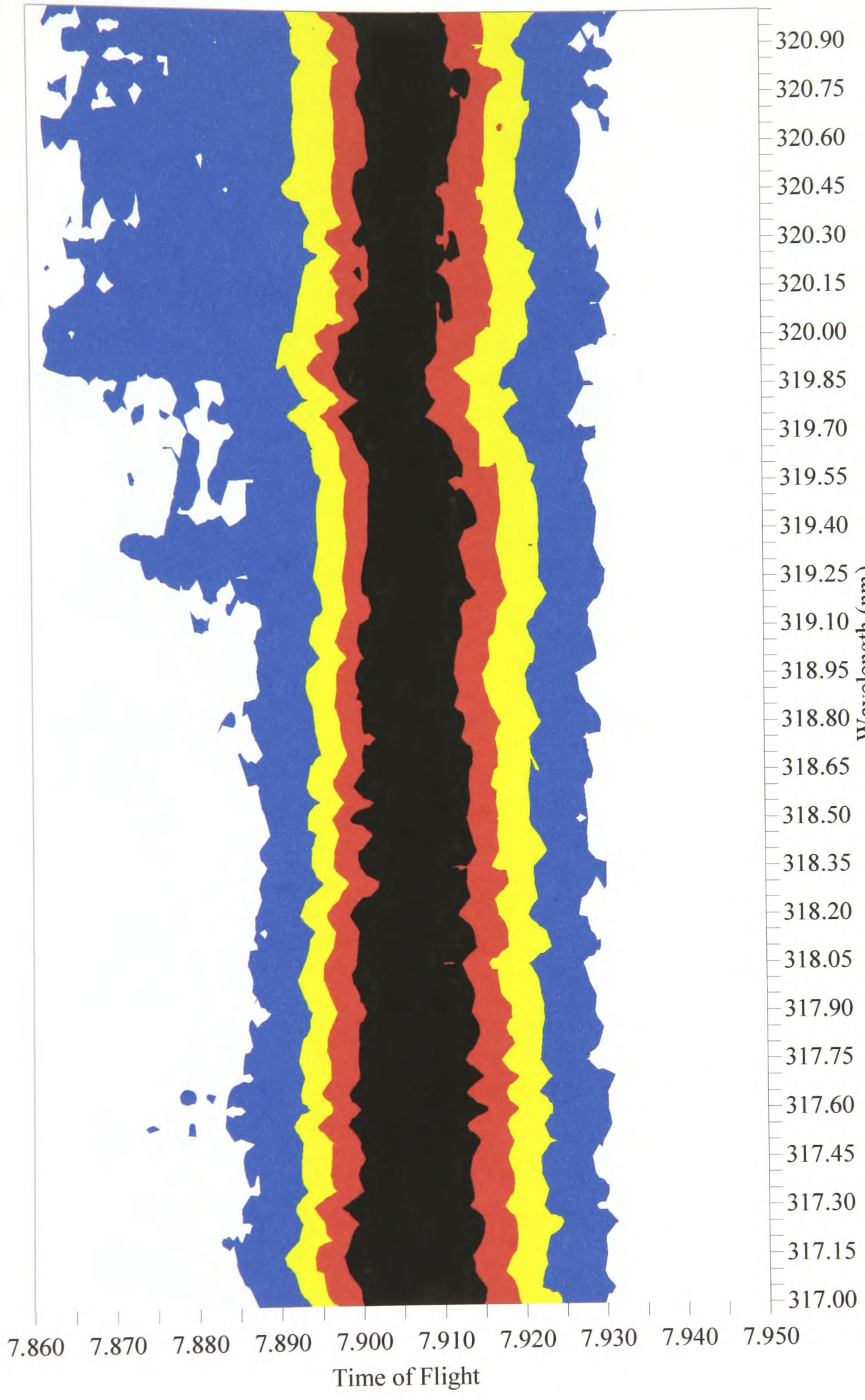

Figure 4-23 Time-of-flight profiles recorded between 317 nm and 321 nm at a resolution of 0.05 nm. Profiles have been renormalised to maximum signal.

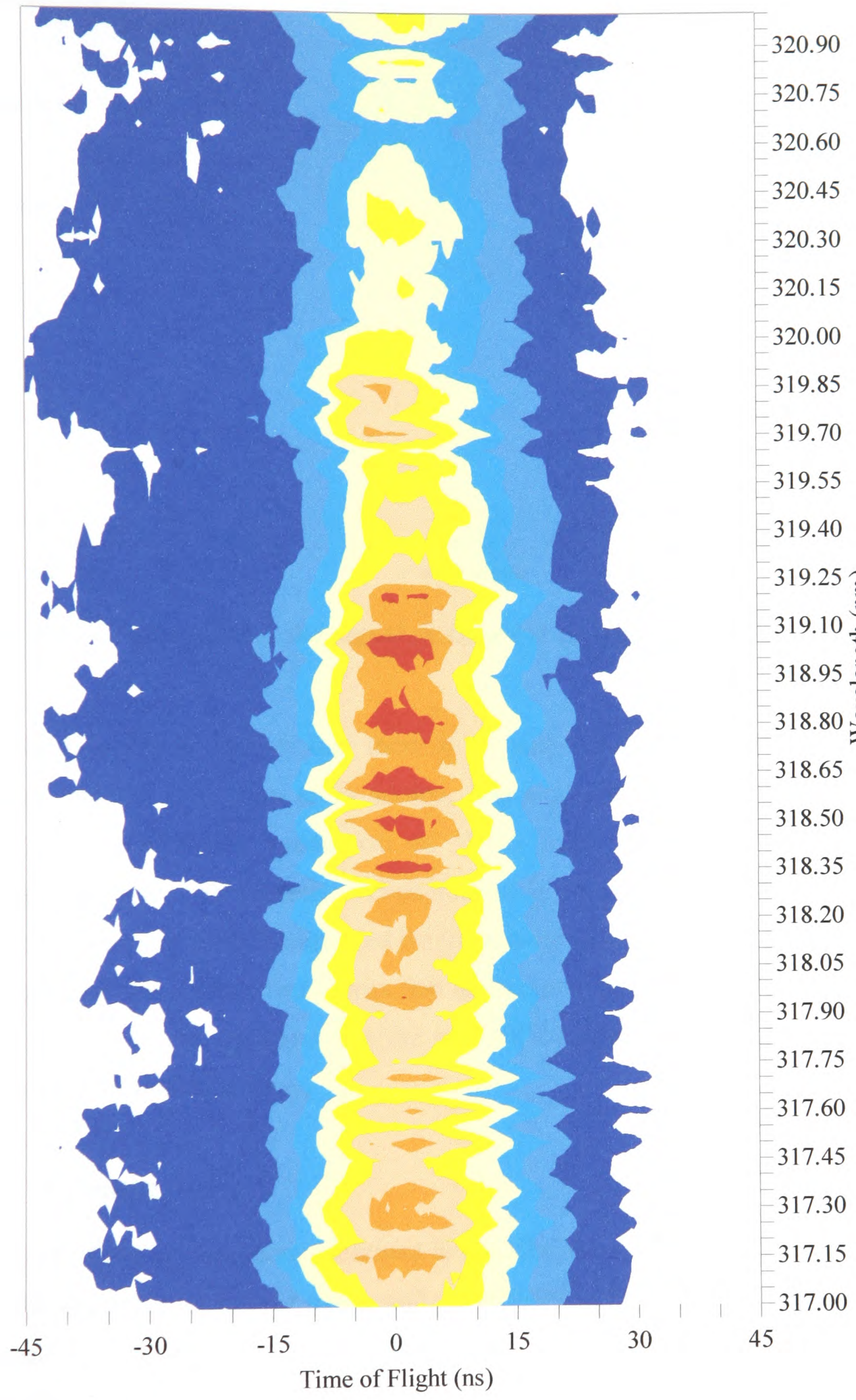

Figure 4-24 Time-of-flight profiles recorded between 317 nm and 321 nm at a resolution of 0.05 nm. The profiles have been renormalised to power and absorption cross section.

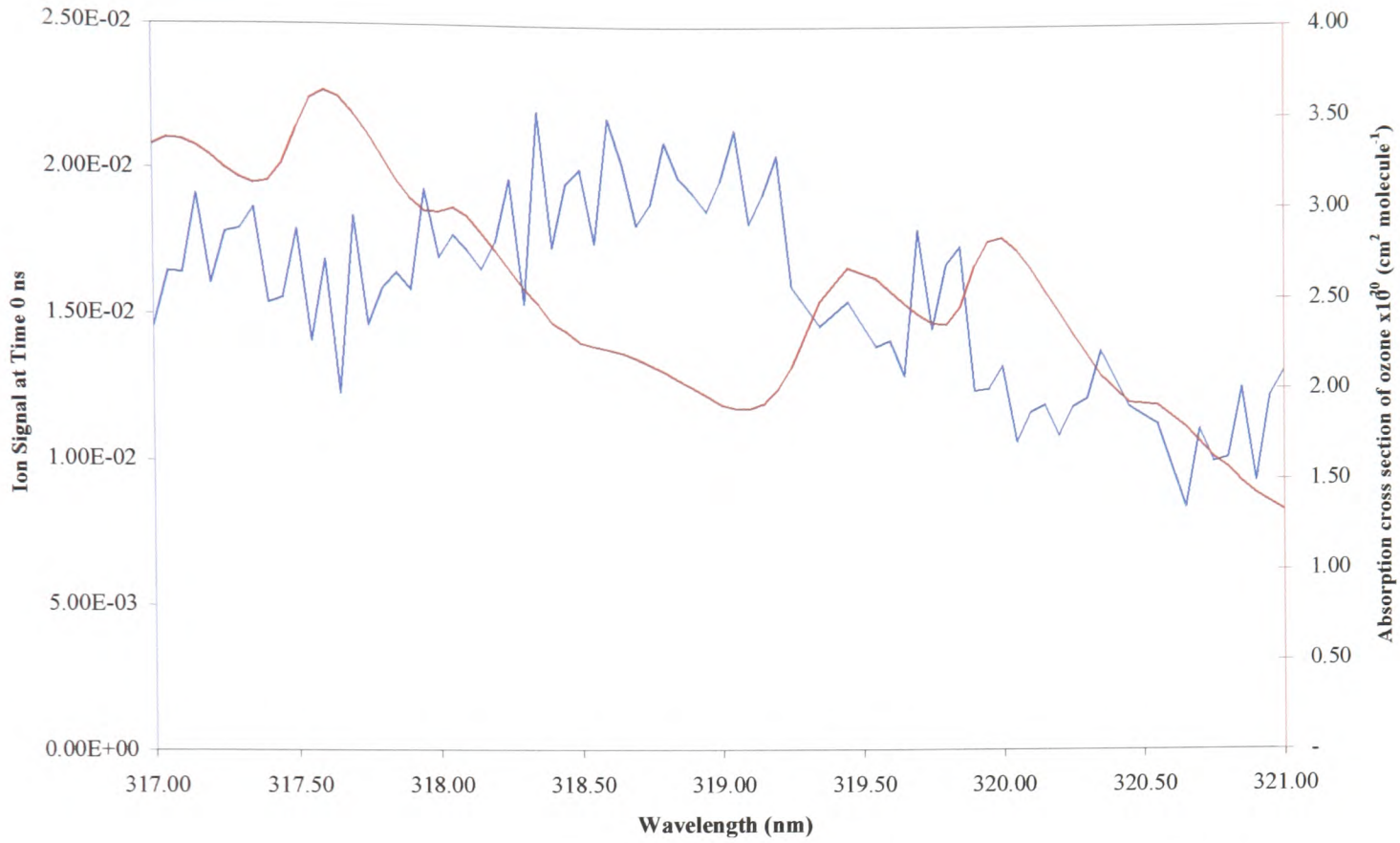

Figure 4-25 Comparison of the signal at time t=0 ns with the absorption cross section of ozone.

As in Section 3.9 it appears that there is an anti-correlation between the yield of O(^{1}D) produced and the absorption cross section. The explanation for this anti-correlation is that, whilst the spin-forbidden production of O(^{1}D) maps the absorption cross section, the production from the vibrationally excited channel is constant and therefore produces an anti-correlation when the signal is corrected for the absorption cross section. Given that it is not just the integral of the profiles that shows this anti-correlation, but also the central peak, further weight is given to the argument that the slow O(^{1}D) detected is formed *via* the vibrationally enhanced spin-allowed pathway.

4.5 Conclusions

As a result of the investigations presented in this Chapter a number of conclusions can be made about the photodissociation of ozone and the REMPI of O(^{1}D). First, and in many ways most important, is the observation that the choice of REMPI process for O(^{1}D) detection can have a major effect on the observed time-of-flight profile. It appears that the intermediate state chosen for the majority of the studies presented in this thesis, $^1F_3$, has been a good choice as it the experimental evidence is that the $^1F_3$ state is significantly less affected by orbital alignment than the $^1P_1$ intermediate.

The time-of-flight profiles taken between 281 nm and 329 nm have shown a number of interesting features. Below 300 nm the onset of the production of vibrationally excited $O_2(a^1\Delta_g)$ can clearly be seen, and the time-of-flight evidence suggests that the surplus energy from the photodissociation is channelled preferentially into rotation, than into translation. Between 300 nm and 329 nm the O(^{1}D) can be seen to have translational energies that correspond to the three production channels outlined in Chapter 3 and that the production pathways are structured.

References:

1 J.W. Hudgens, *Progress in Resonance Enhanced Multiphoton Ionisation Spectroscopy of Transient Free Radicals,* in *Advances in Multiphoton Processes and Spectroscopy* S.H. Lin (ed), World Scientific (1987).

2 S.T. Pratt, *Rep. Prog. Phys.*, **58** (1995) 821.

3 O.L.A. Monti, H. Dickenson, S.R. Mackenzie and T.P. Softley, *J. Chem. Phys.*, **112** (2000) 3699.

4 M. Hippler and J. Pfab, *Chem. Phys. Lett.* , **243** (1995) 500.

5 M.N. Al-Kahali, R.J. Donovan, K.P. Lawley, Z. Min and T. Ridley, *Chem. Phys.*, **208** (1996) 165.

6 P. O'Keeffe, T. Ridley, S. Wang, K. Lawley, R.J. Donovan, *Chem. Phys. Lett.*, **298** (1998) 368

7 S.T. Pratt, P.M. Dehmer and J.L Dehmer, *Phys. Rev. A*, **43** (1991) 282.

8 S.T. Pratt, P.M. Dehmer and J.L Dehmer, *Phys. Rev. A*, **43** (1991) 4702.

9 C.E. Moore, *Atomic energy Levels*, National Standard Reference Data Series, National Bureau of Standards, Circ. No. 35, Vol. 1, U.S. G.P.O. Washington D.C. (1971).

10 K.B.S. Eriksson and H.B.S. Isberg, *Arkiv for Fysik*, **37** (1968) 221.

11 J.C. Pinot de Moira, Laser Studies of Atmospheric Chemistry, D.Phil Thesis, Oxford University, 1998.

12 M. Ahmed, E.R. Wouters, D.S. Peterka, O.S. Vasyutinskii and A.G. Suits, *Faraday Discuss.*, **113** (1999) 425.

13 D.W. Neyer, A.J.R. Heck, D.W. Chandler, J.M. Teule and M.H.M. Janssen, *J. Phys. Chem.*, **103** (1999) 10388.

14 J.M. Teule, G.C. Groenenboom, D.W. Neyer, D.W. Chandler and M.H.M. Janssen, *Chem. Phys. Lett.*, **320** (2000) 177.

15 N. Taniguchi, K. Takahashi,Y. Matsumi, S.M. Dylewski, J.D. Geiser and Houston PL, *J. Chem. Phys.*, **111** (1999) 6350.

16 D.A. Blunt and A.G. Suits, *Am. Chem. Soc. Symposium Series*, **678** (1997) 99.

17 W. Denzer, G. Hancock, J.C. Pinot de Moira and P.L. Tyley, *Chem. Phys.*, **231** (1998) 109.

18 K.P. Huber and G. Herzberg, *Molecular Spectra and Molecular Structure IV Constants of Diatomic Molecules*, Van Nostrand Reinhold 1979.

19 J.J. Valentini, D.P. Gerrity, D.L. Phillips, J-C Nieh and K.D. Tabor, *J. Chem. Phys.*, **86** (1987) 6745.

20 M.A. Thelen, T. Gejo, J.A. Harrison and J.R. Huber, *J. Chem. Phys.*, **103** (1995) 7946.

[21] S.M. Ball, G. Hancock, I.J. Murphy and S.P. Rayner, *Geophys. Res. Lett.*, **20** (1993) 2063.

[22] S.M. Ball, G. Hancock, J.C. Pinot de Moira, C.M. Sadowski and F. Winterbottom, *Chem. Phys. Lett.*, **245** (1995) 1.

[23] K. Takahashi, M. Kishigami, Y. Matsumi, M. Kawasaki and A.J. Orr-Ewing, *J. Chem. Phys.*, **105** (1996) 5290.

[24] D.H. Katayama, *J. Chem. Phys.*, **71** (1979) 815.

[25] J.A. Joens, *J. Chem. Phys.*, **101** (1994) 5431.

[26] K. Takahashi, M. Kishigami, N. Taniguchi, Y. Matsumi and K. Kawasaki, *J. Chem. Phys.* **106** (1997) 5431.

Chapter 5

Time-of-flight Studies on the $O_2(a^1\Delta_g)$ Molecular Fragment

5.1 Introduction

This chapter presents results that were obtained by studying the $O_2(a^1\Delta_g)$ fragment produced by the spin-allowed photodissociation of ozone. The experiments directly probed $O_2(a^1\Delta_g)$ by 2+1 REMPI transitions that occur in the 310 nm, 320 nm and 330 nm regions. Unlike previous studies carried out by Ball[1] and Pinot,[2] the aim of this work was not to provide an assignment of the $O_2(a^1\Delta_g)$ REMPI transitions, but rather to investigate what evidence could be provided by kinetic energy and angular momentum polarisation studies of the fragments that might aid in the assignment process.

The band around 330 nm has been generally assigned to the $O_2(d^1\Pi_g, v' = 1) \leftarrow\leftarrow O_2(a^1\Delta_g, v'' = 0)$ transition but the exact rotational assignment of the spectrum has been complicated by perturbations due to the $1^1\Pi_g$ and $1^3\Pi_g$ valence states. Observations of the high J assignments ($J > 15$) are complicated as S branch lines can be overlapped by R branch lines of higher J ($J_R = J_S + 5$). It is believed that time-of-flight profiles obtained *via* the two branches would be different and through the differences it may be possible to determine the dominant J component of each line. The $O_2(a^1\Delta_g)$ product, from the photolysis of ozone, shows a strong angular momentum polarisation with **J** preferentially perpendicular to the velocity, **v**, as expected for the photodissociation of a triatomic molecule. This anisotropic distribution of **J** means that the transition dipole moments also have an anisotropic distribution. As transitions *via* the R and S branches sample the transition dipole moment differently, the branches are sensitive to the angular momentum polarisation. The differing transition probabilities for the R and S branches mean that the shape of the measured time-of-flight profiles will be different.

In the region of 320 nm the transition $O_2(d^1\Pi_g, v' = 2) \leftarrow\leftarrow O_2(a^1\Delta_g, v'' = 0)$ occurs. This band is heavily congested with rotational features which are perturbed by the $1^1\Pi_g$ valence state. The $O_2(d^1\Pi_g, v' = 3) \leftarrow\leftarrow O_2(a^1\Delta_g, v'' = 0)$ transition occurs in the region of 312 nm and is also perturbed, with O, P, Q, R and S branches all overlapping between 311.8 nm and 312.8 nm. A

good assignment for the rotational structure in all three of these bands has been established only during the course of this thesis by Lewis *et al.*[3] and it is this assignment, with modifications by Morrill,[4] that will be used as the reference assignment throughout the chapter.

5.2 General Information

The REMPI spectrum of $O_2(a^1\Delta_g)$ has been studied by several groups with Johnson *et al.*,[5] Ogorzalek-Loo *et al.*,[6] Park *et al.*,[7,8] Ball,[1] Pinot[2] and Morrill[4] having reported detailed observations of various bands. As an example of the complexity of the REMPI spectrum, Figure 5-1 presents data covering the wavelength range 317.0 nm to 331.5 nm in which the $O_2(a^1\Delta_g)$ was prepared by photolysis of ozone at 230 nm. $O_2(a^1\Delta_g)$ has two spin-allowed bands in this region near 320 nm and 330 nm, and a spin-forbidden band around 325 nm,[5] which given the high *J* rotational states populated by 230 nm photolysis may be the origin of the band seen at 324 nm.

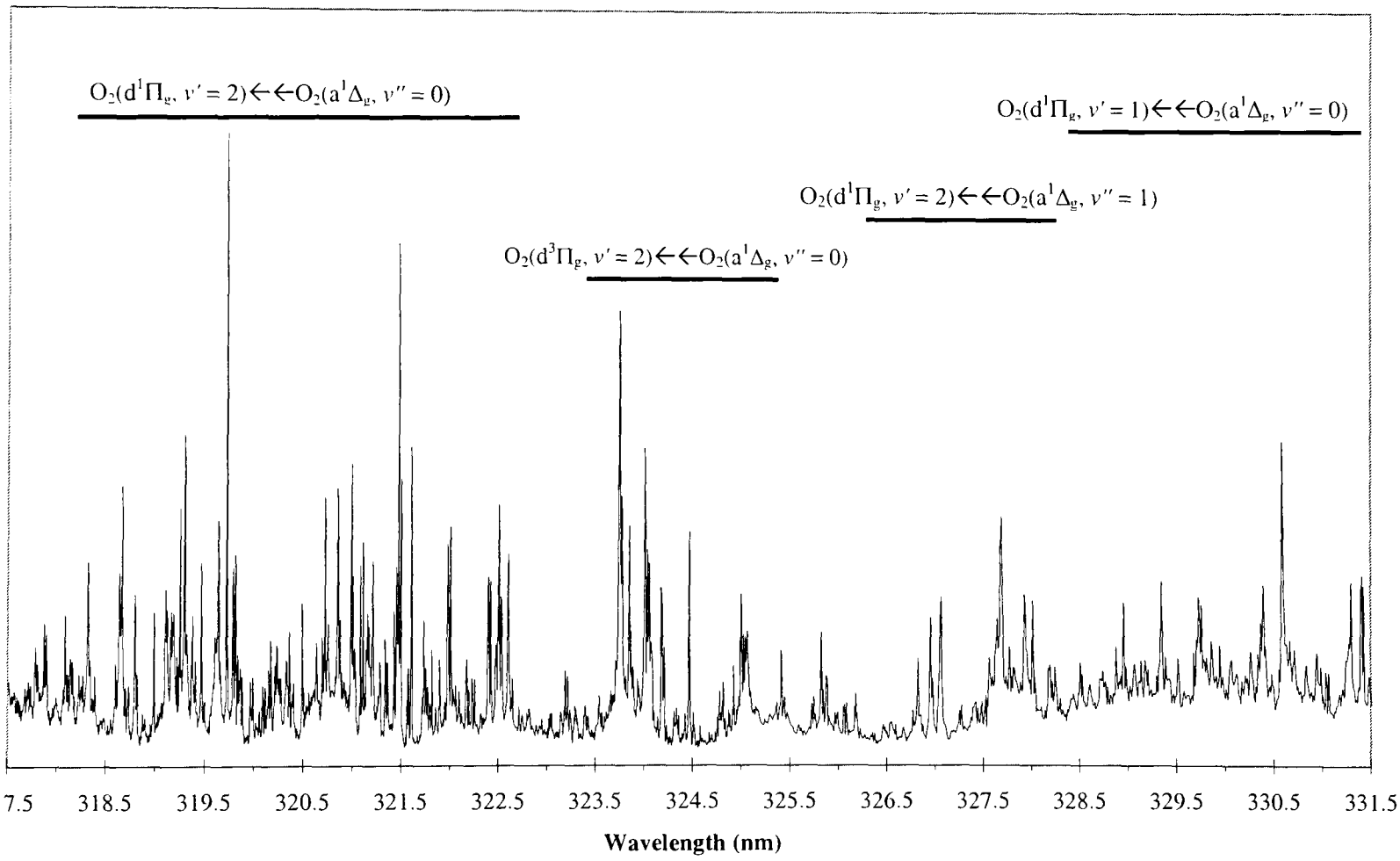

Figure 5-1 REMPI spectrum obtained when ozone is photolysed at 230 nm. This spectrum covers the (1,0) and (2,0) bands of the $O_2(d^1\Pi_g)\leftarrow\leftarrow O_2(a^1\Delta_g)$ transition.

To ionise an $O_2(a^1\Delta_g)$ molecule with no rovibrational energy in a 2+1 REMPI process the photons' wavelength must be shorter than 335.3 nm. The first transition that can be made by a

2+1 process uses the $O_2(3s\sigma_g\ d^1\Pi_g,\ v' = 1)$ Rydberg state as the resonant intermediate and occurs around 331.5 nm.

5.2.1 Experimental

The dye laser made by LAS was used to generate the REMPI wavelengths as it was capable of generating more power than the laser from Lambda Physik. This additional power was required as $O_2(a^1\Delta_g)$ was found to have a lower effective REMPI cross section than $O(^1D)$. Additionally, the autotracking unit for the LAS laser could be scanned over wide wavelength ranges whilst maintaining a fairly (± 5%) constant power. The use of a wedge as the beam energy sampling optic greatly reduced the apparent oscillation in power that had been previously observed when a quartz flat had been employed. The $O_2(a^1\Delta_g)$ was produced by the photolysis of ozone with the time-of-flight mass spectrometer used as the detection system. The $O_2(a^1\Delta_g)$ was generated either by a second laser beam, originating from the other dye laser (Lambda Physik), which operated at wavelengths where the spin-allowed production of $O_2(a^1\Delta_g)$ could occur, or by the probe beam itself. When two lasers were used, the time delay between their firing was *ca.* 20 ns, to ensure that the nascent rotational populations were probed.

5.2.2 Spin-forbidden production of $O_2(a^1\Delta_g)$

At wavelengths greater than 310 nm $O_2(a^1\Delta_g)$ can be produced by two routes: by photolysis of vibrationally excited ozone, as seen in Chapter 3, and by the spin-forbidden process (reported by Ball *et al.*[9,10]) whose threshold wavelength is at 611 nm. In the latter case it would be expected that the $O_2(a^1\Delta_g)$ would have significant translational energy (there is *ca.* 1.85 eV of available energy for photolysis at 320 nm). Whilst some of this surplus energy will be partitioned into internal energy of the $O_2(a^1\Delta_g)$, a significant quantity would be left for translation. For example populating the $J = 20$ level of $O_2(a^1\Delta_g,\ v = 0)$ would only take *ca.* 75 meV, or 4% of the surplus energy at 320 nm.

As the atomic fragment for each channel has its internal energy fixed by its electronic state the energy available to the molecular fragment in a given (v, J) state is fixed; therefore the time-of-flight profile is not complicated by having a spread in cofragment energies. The time-of-flight profile for relatively low J states would be expected to be broad, with the shape depending on the anisotropy of the dissociation, the polarisation of the photolysis laser relative to the time-of-flight drift tube and any anisotropy of the REMPI process itself. Pinot[2] found the value of β

in this region for the spin-forbidden path was *ca.* 1.2, similar to that found for the spin-allowed channel at shorter wavelengths in the Hartley band. Photolysis radiation polarised parallel to the time-of-flight axis would therefore be expected to generate a profile from the spin-forbidden channel that has two widely spaced peaks. Figure 5-2 shows an example of the profiles taken, one on a peak in the $O_2(a^1\Delta_g)$ REMPI spectrum and one off resonance. In addition to the fast peaks in the profiles a clear slow peak in the centre is observed. The central peak could be caused by signal coming from the vibrationally mediated spin-allowed channel which would have little surplus energy or by some other unknown multi-photon process. Observations made on this central signal have been inconclusive as to the signal's origin. As a result, the single-laser REMPI spectra shown in Figure 5-5 and Figure 5-21 were recorded by monitoring the area of the fast peak only which is known to correspond to $O_2(a^1\Delta_g)$.

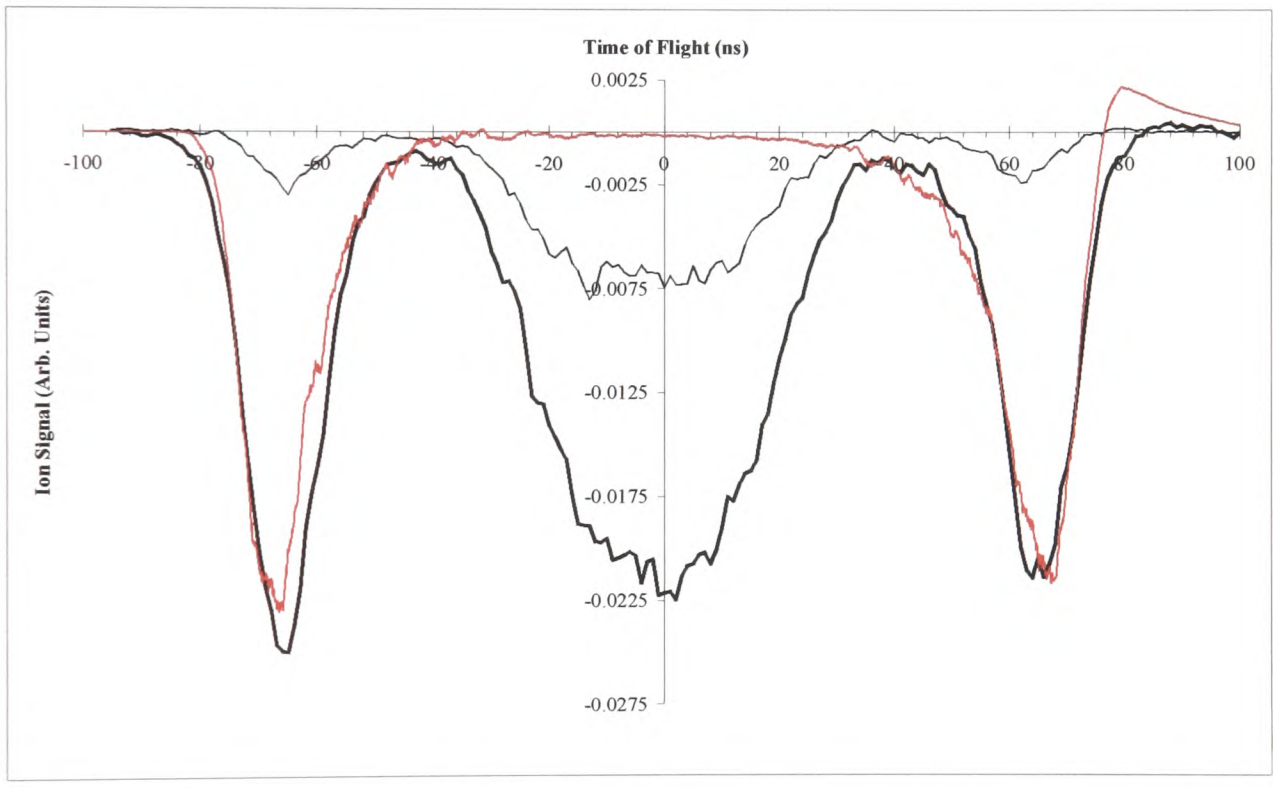

Figure 5-2 Example of $O_2(a^1\Delta_g)$ time-of-flight profiles. These were taken with the laser horizontally polarised on a peak in the $O_2(a^1\Delta_g)$ spectrum 321.775 nm (thick) and just off the peak at 321.767 nm (thin). The red profile is a simulation using the expected energy available for the spin-forbidden pathway and $\beta = 1.2$.

5.2.3 Background subtraction in two-laser experiments

The single-laser production of $O_2(a^1\Delta_g)$ discussed above could pose a significant problem for two-laser experiments if its magnitude is such that it forms a significant fraction of the total signal. This potential problem was countered in two ways. First, in the two-laser experiments the absorption cross section for ozone at the photolysis wavelength was always much greater than at the probe wavelengths; and the quantum yield for production of $O_2(a^1\Delta_g)$ is in the

region of 0.9. These two factors mean that significantly more $O_2(a^1\Delta_g)$ is produced (for laser pulses of similar energy) from the photolysis pulse than from the REMPI pulse; in fact, the enhancement was sufficient that it was possible to reduce the REMPI power considerably whilst still obtaining a reasonable signal. The second method of minimising any contamination from the REMPI laser was to chop the photolysis beam, when necessary, so a background signal could be subtracted from the two-laser signal obtained, leaving the desired signal.

5.2.4 Core extraction

As the photolysis wavelength decreases, the energy available for translational motion increases, which poses a problem if the velocity of the fragments becomes such that a significant percentage of them will miss the detector. The loss of ions which miss the detector as a result of their off-axis velocity components is known as core extraction.

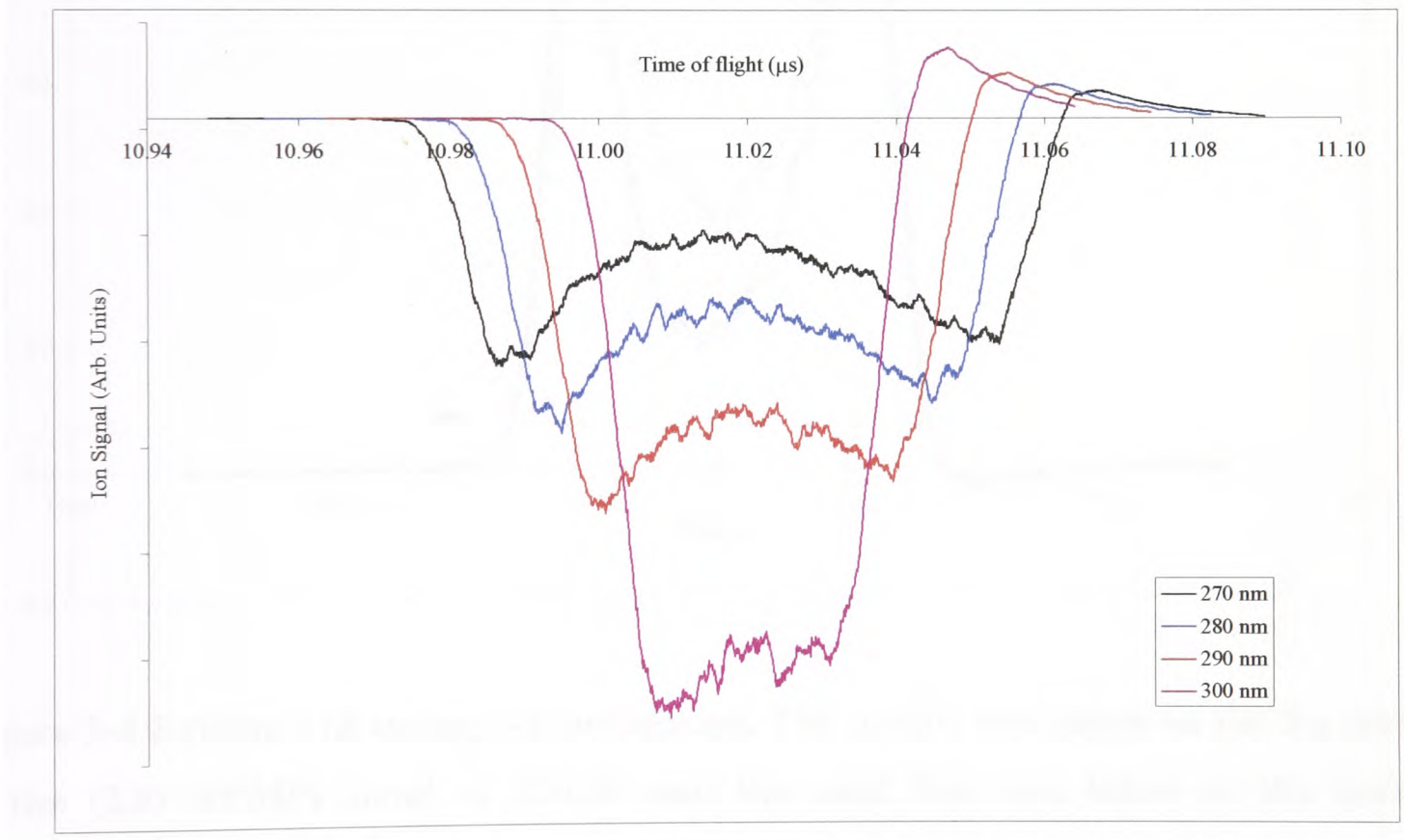

Figure 5-3 Simulations showing the effect of core extraction for ozone photolysis at various wavelengths at the magic angle.

The effect of core extraction on the expected profiles can be seen in Figure 5-3. Clear deviation from the expected "top hat" profiles is observed as the photolysis wavelength is reduced. Core extraction introduces the problem that there is a reduction in the sensitivity of the instrument to ions not travelling along the time-of-flight axis, and that this reduction is speed dependent.

5.2.5 Angular momentum polarisation, v-J correlation

In addition to the problems caused by core extraction, the shape of the time-of-flight profile is also affected by angular momentum polarisation in the product being probed. These concerns are similar to those described in Chapter 4, but now it is the rotational angular momentum that is aligned rather than the electronic. Suits *et al.*[11] reported ion images of $O_2(a^1\Delta_g)$, formed from ozone photolysis at 248 nm, probed *via* the 4-0 and 4-1 bands which clearly indicated the occurrence of a strong **v-J** correlation. Suits *et al.* also demonstrated that the sensitivity of the detection process was strongly dependent on the REMPI transition used, with O and S branches apparently showing a more anisotropic fragment distribution than the P or R branches.

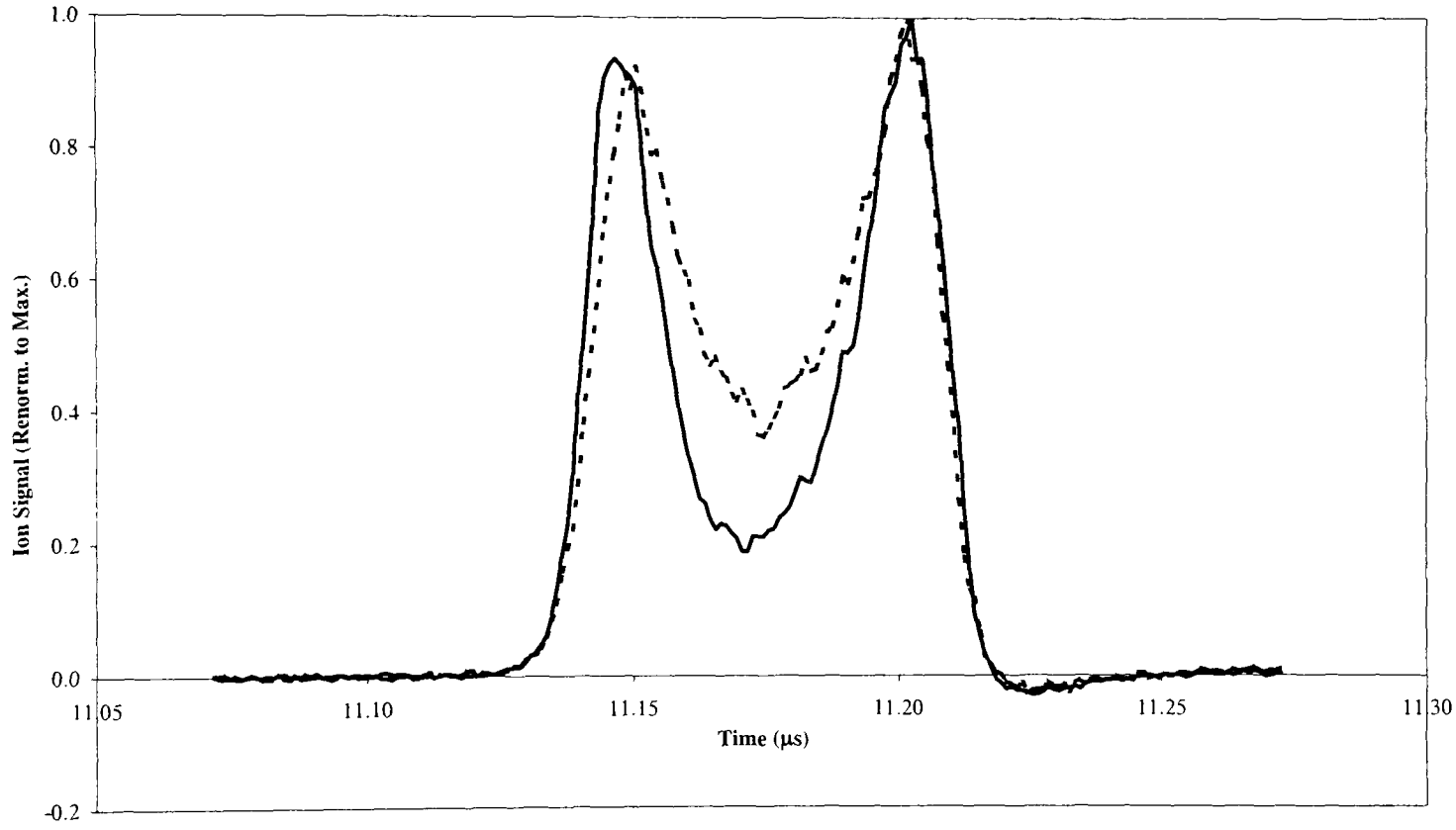

Figure 5-4 Evidence of strong v-J correlation. The profile was taken on the S_{20} transition of the (2,0) REMPI band at 320.50 nm; the solid line was taken at the horizontal polarisation and dotted at the vertical polarisation. The photolysis wavelength was 280 nm and the laser was polarised at the magic angle.

Pinot[2] reported that alignment was observed when $O_2(a^1\Delta_g)$ was probed at 331.52 nm (believed to be O branch from $J \approx 13$) after photolysis at 290 nm. Evidence of angular momentum alignment was therefore expected in these studies and can be seen in Figure 5-4.

The fact that different transition branches probe the angular momentum distribution differently leads to differences in the detectivity function for the transitions. As the detectivity function directly affects the time-of-flight profile observed, the result is that the profiles taken on identical

fragments but *via* different branches, or with different polarisations of the REMPI laser, looking dissimilar. It was decided to investigate the use of time-of-flight fingerprints, caused by the effects of angular momentum polarisation, as markers of individual branches (e.g. R / S) to help assign the congested REMPI spectra.

5.3 O_2 energy levels: important aspects

O_2 has a number of features in its spectroscopy that arise from the fact that the oxygen atom is a boson with nuclear spin I = 0. A fundamental property of a boson is that its wavefunction is totally symmetric; and therefore, there are restrictions on the wavefunctions that can be combined to form the total. Within the Born-Oppenheimer approximation the total wavefuntion can be separated into independent wavefunctions i.e.:

$$\Psi_{total} = \Psi_{ns}\Psi_{vib}\Psi_{rot}\Psi_{elec} \qquad \textbf{(5-1)}$$

where Ψ_i denote the nuclear spin, vibrational, rotational and electronic wavefunctions. Oxygen has no nuclear spin and so the nuclear spin wavefunction can only be symmetric; as is the vibrational wavefunction of a homonuclear diatomic (with respect to exchange of particles). Therefore, the product of the rotational and electronic wavefunctions must be symmetric. The rotational wavefunction's symmetry is specified by the value of J and is symmetric for even J and antisymmetric for odd J. For the ground state of oxygen, $O_2(X^3\Sigma_g^-)$, the electronic wavefunction is antisymmetric, which requires that the rotational wavefunction is also antisymmetric. The result of this symmetry requirement is that only odd values of J are permitted. A significant consequence of the restriction on the values of J will be discussed shortly.

$O_2(a^1\Delta_g)$, however, can have both a symmetric and an antisymmetric electronic wavefunction because of lambda doubling. Λ, the quantum number representing the projection of the orbital angular momentum onto the internuclear axis, is doubly degenerate for $\Lambda > 0$ (the two states differing by the sense of rotation about the axis) in the absence of molecular rotation. This degeneracy is lifted when the molecule rotates, resulting in two states split by a small energy gap that increases as J increases. One of these states is symmetric and the other antisymmetric with respect to reflection in the plane of rotation. Symmetry restrictions mean that each value of J can only have one lambda doublet associated with it; for even J $O_2(a^1\Delta_g)$ only the symmetric lambda doublet is permitted, whilst for odd J the antisymmetric doublet is the only permitted lambda doublet.

There are some interesting spectroscopic and dynamical consequences of the preceding statements. Valentini *et al.*[12,13] studied the $O_2(a^1\Delta_g)$ rovibrational distribution resulting from the photolysis of ozone by Coherent Anti-Stokes Raman Spectroscopy (CARS) and observed an alternation in the rotational populations with the odd J levels being depleted relative to the even J levels. It was observed that the degree of depletion depended on the photolysis wavelength (shorter wavelengths increasing the degree of depletion) and the vibrational state of the $O_2(a^1\Delta_g)$ (v = 0 showing the greatest degree of depletion). By carrying out the same experiments on O_2 which included ^{18}O isotopes they determined that the selective reduction resulted from dissociation to produce $O_2(X^3\Sigma_g^-)$ which is a channel that is only open to odd J levels. The removal of only the odd J levels can be explained as $O_2(X^3\Sigma_g^-)$ can only have odd J states and the symmetry of the rotational wavefunction must not change during the curve crossing. Therefore, the crossing is only open to $O_2(a^1\Delta_g)$ with odd J levels and depletion of the population of the odd J levels occurs.

O'Keeffe *et al.*[14] studied the photolysis of ozone at 254 nm and observed the $O_2(a^1\Delta_g)$ produced by REMPI; they also observed features that suggested significant depopulation of the odd J states occurred. By contrast, when they probed $O_2(b^1\Sigma_g^+)$ they found that the spectra showed no odd J states at all, as the symmetric nature of the electronic state requires only even J.

5.4 The $O_2(d^1\Pi_g$- $a^1\Delta_g)$ (2,0) band

5.4.1 REMPI Spectrum

The REMPI transition near 320 nm for $O_2(a^1\Delta_g)$ uses the $d^1\Pi_g(v=2)$ Rydberg state as its resonant intermediate. As can be seen in Figure 5-5, which compares a single-laser spectrum with a two-laser spectrum (photolysis at 230 nm), the wavelength range covers a highly complex spectral region with a number of rotational bands. The complexity of the spectrum results from a number of perturbations,[3] mainly the crossing of $d^1\Pi_g$ levels by several of the vibrational levels of the $1\ ^1\Pi_g$ valence state and predissociation of the low J rotational levels. Lewis *et al.*[3] found the major perturbations to be in the regions of $J \approx 5$, 24 and 32, with an additional weak perturbation at $J \approx 16$. To determine the location of the REMPI transitions, so they could be used later in time-of-flight studies, several spectra were recorded in which the $O_2(a^1\Delta_g)$ was formed from the photolysis of ozone at different wavelengths, to ensure that a

range of J would be covered. The spectra obtained are presented in Figure 5-6. The single-laser spectrum monitors the channel associated with the spin-forbidden production of $O_2(a^1\Delta_g)$.

There are four clear features that are common to the spectra recorded. These are the S branch below 320.78 nm, the R branch between 320.78 nm and 321.05 nm, the peak at 321.4 nm and the congested region above 321.7 nm. It should be noted that the spectra have been renormalised to the maximum value of the signal within each spectrum for ease of display. In the 270 nm photolysis spectrum this renormalisation has resulted in a reduction in the clarity of the R and S branch lines as the peak at 321.4 nm dominates the spectrum. The absolute positions of the assignments have been shifted from the quoted values as a result of a calibration error in the original data used to determine the assignments.[3] The shift was determined by fitting the O_b branch to the one-laser spectrum but for some of the transitions there appears to be a residual 0.01 nm error.

The S_b branch, which is seen in all of the spectra, appears to start with $J = 14$, a value that lies in the region of a perturbation (S_{12} to S_{14} also being predicted above 321.8 nm). For values of $J > 16$ there appears to be a slight alternation in intensity (as expected) which is most prominent in the 280 nm spectrum. An increase in the populations of the higher J levels is seen as the photolysis wavelength falls. The reduced intensity of the S_b branch in the 270 nm spectrum could be affected by a further perturbation which is predicted to occur for $J \approx 24$, with the next section (S_c) occurring at *ca.* 319.7 nm. Whilst not seen in any of the two-laser spectra, the single-laser spectrum shows evidence of the change in direction of the S branch. The single peak seen in the two-laser spectra at *ca.* 320.5 nm (S_{20}) becomes a broader double peak feature (adding S_{22}) in the single-laser spectrum.

The R_b branch between 320.78 and 321.05 nm is overlapped by low J S_b branch lines in the region, which makes the assignment of the lines more difficult. It is believed that the lines are predominantly from the R branch with the low J S_a branch lines observed at longer wavelengths. If the intensities of the low J R branch lines, between 320.96 nm and 321.05 nm, are typical then the low J S branch lines would be difficult to observe. The alternation in the intensity of the R branch lines is more obvious than for the S branch and can be seen in all of the two-laser spectra. Two comments can be made on the change in the intensity of the lines as the photolysis wavelength changes. First, as for the S_b branch, the low J lines decrease as the photolysis wavelength decreases. Second, for photolysis at 270 nm the peak heights decrease in intensity, apart from the line at 320.815 nm, which may have gained in intensity as a result of population moving to the $J = 23$ state whose transition energy overlaps the $J = 18$ transition.

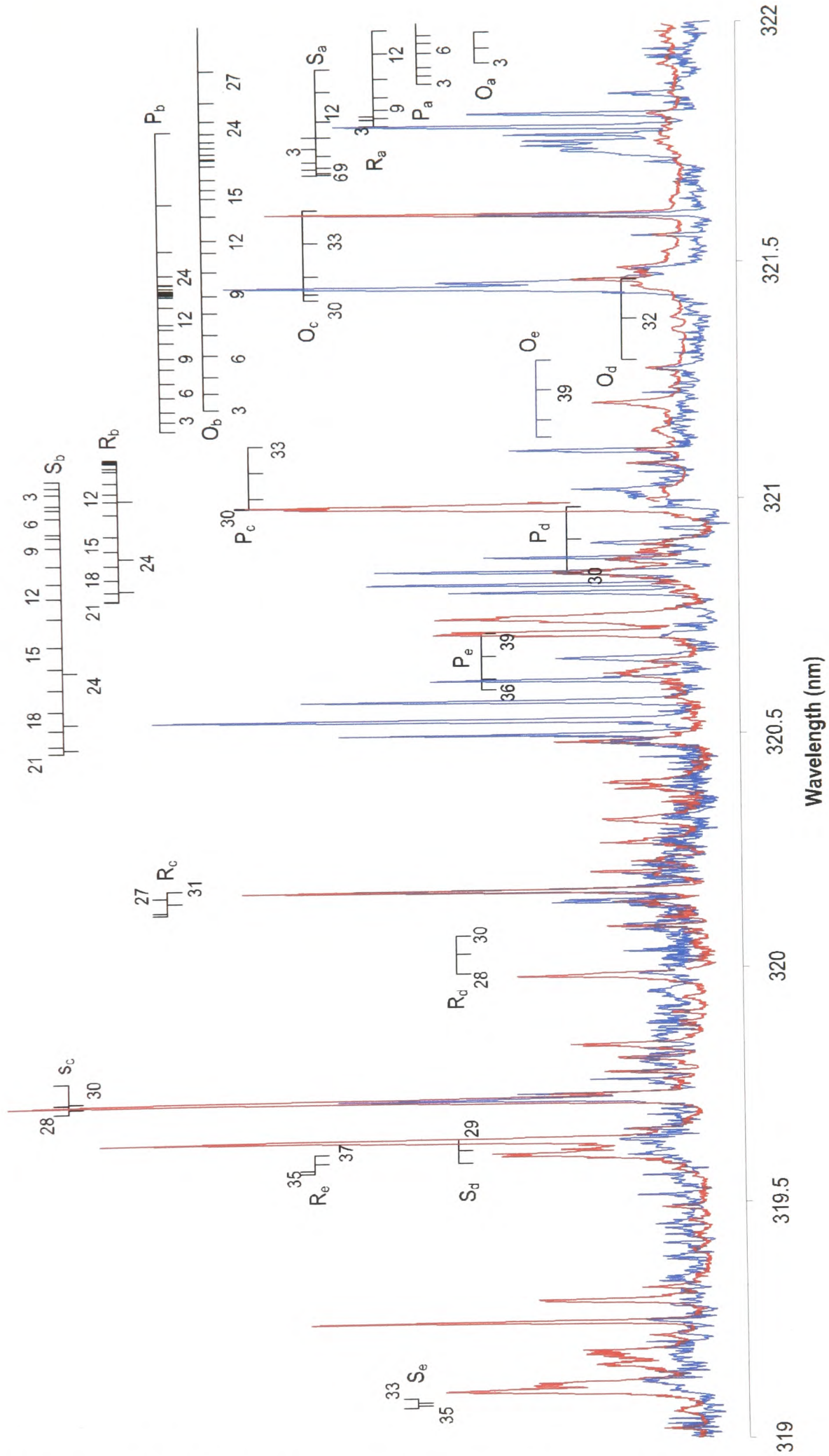

Figure 5-5 Rempi spectra of $O_2(a^1\Delta_g)$ around 320 nm. The blue spectrum is a single-laser spectrum and the red a spectrum taken when the $O_2(a^1\Delta_g)$ was prepared by photolysis at 230 nm. The spectra are from Johnson[15] and the assignment from Lewis *et al.*[3]

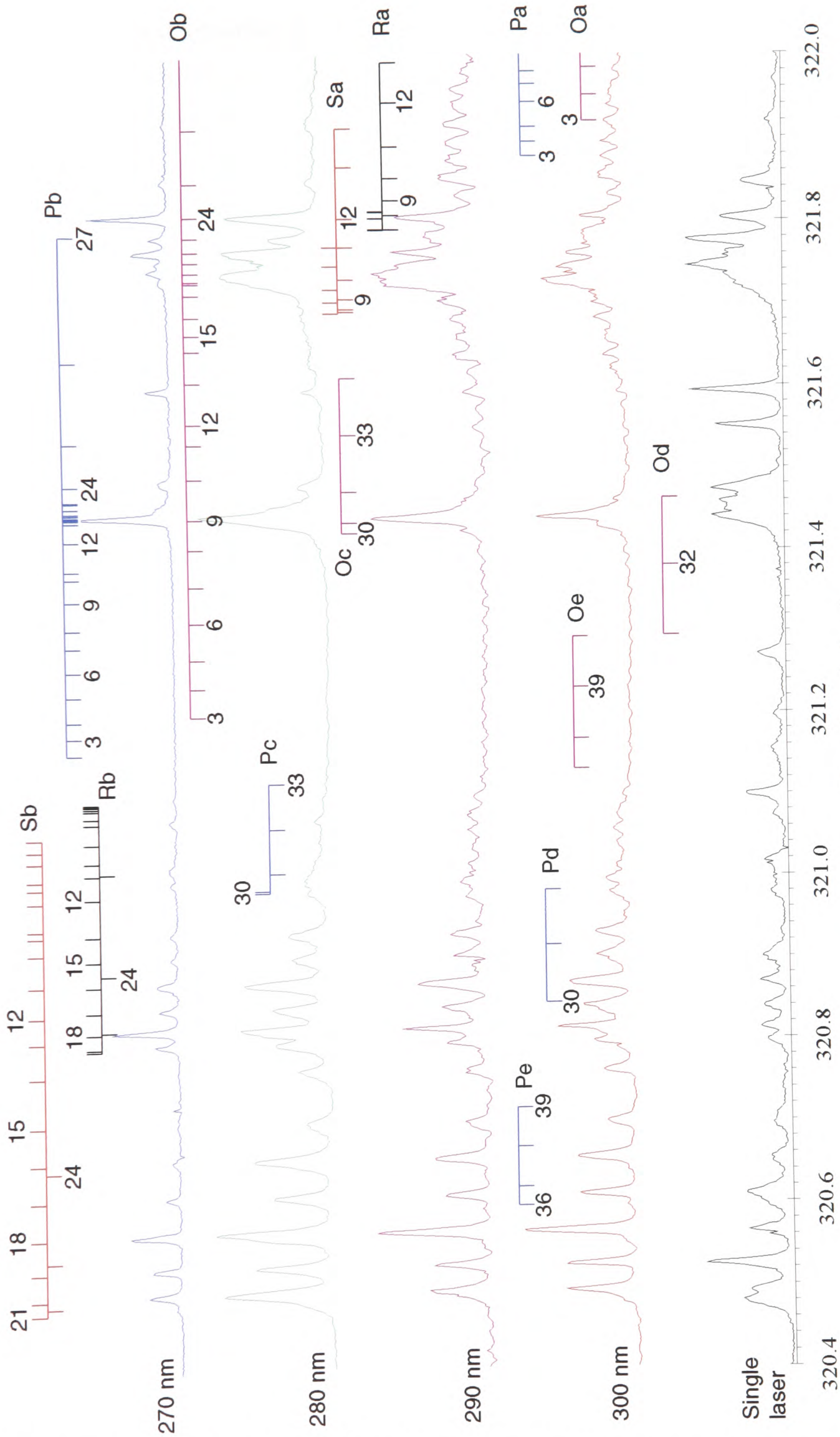

Figure 5-6 Rempi spectra obtained after photolysis at 270 nm (blue), 280 nm (green), 290 nm (purple), 300 nm (red) and single laser (black). The assignment lines are those of Lewis *et al.*[3] and are colour coded, O branch (purple), P branch (blue), R branch (black).

The substantial peak observed at 321.44 nm appears to belong to either a congested region in the P_b branch or possibly the $J = 9$ level of the O_b branch. There is no clear evidence for either assignment but the single-laser spectrum shows a broad structure with a number of peaks, which shows a better match for the P branch than the two peaks of the O branch available. There is evidence for a P line ($J \approx 13$) just to the blue of the main peak, which decreases in intensity as the photolysis wavelength is reduced. The reduction in intensity is in keeping with the rotational population moving towards higher J as the wavelength reduced. There is also a peak to the red (at 321.48 nm) which matches the P_{24} transition, which, as expected, grows as the wavelength falls.

Between the peak at 321.48 nm and the final region starting at 321.7 nm, there are two peaks in the single-laser spectrum, one of which starts to be observed as the photolysis wavelength is reduced. It would appear that these lines match well to the O_{12} and O_{13} transitions. This assignment must be queried though as there is no evidence of the O_{12} line in the two-laser spectra, whilst the O_{13} does occur despite the fact that a depletion of the odd J states is expected. The peak at 321.55 nm in the one-laser spectrum, which is missing from the two-laser spectra, may be the O_{33} line that is predicted to lie here, a value for J which is quite possible in the spin-forbidden production of $O_2(a^1\Delta_g)$ but unlikely at the wavelengths employed in the two-laser spectra. One unusual observation is that there is no O_{11} line apparent in any of the spectra recorded, which may be due to efficient predissociation in the $d^1\Pi_g$ $v = 2$ state.

Finally, there are the series of lines that can be observed above 321.70 nm. This is a region in which some lines can be assigned quite well, but others less so. The problems with assignment are because the low J lines of all of the branches and the first perturbed O branch (O_b), which covers a wide range of J, all overlap in this region. The dominant lines appear to belong to the perturbed O_b branch with lines to the blue of them belonging to the S_a branch. Above 321.85 nm the spectra from 290 nm and 300 nm photolysis show lines that match the expected progressions of the O_a and P_a branches. There is no clear evidence of any intensity alternation within this band.

If the rotational populations are considered for the photolysis wavelengths used it would appear that the populations detected here are at higher J than Valentini *et al.*[13] observed at 293 nm. At 293 nm Valentini *et al.* found that the rotational populations were heavily biased towards low J, although values of J up to 20 were observed. In the spectra at 300 nm and 290 nm there are low J lines above 321.8 nm, but they are not very intense, and it appears that majority of the population is in J levels between 10 and 20. It should be noted that these results do not imply

that the populations of Valentini *et al.* are wrong. The spectra have not been corrected for the REMPI cross section or the detection efficiency of the transition and so the spectra give the location and expected relative signal strength rather than any measure of population.

The rotational populations observed in the one-laser spectrum do not follow those expected given the excess energy available (320 nm photolysis *via* the spin-forbidden channel releases the same energy as 213 nm photolysis *via* the spin-allowed channel). It is clear from Figure 5-5 that photolysis at 230 nm produces population in rotational states with much higher values of J than seen in the single-laser experiment and that values of J below *ca.* 30 are hardly detected in the two-laser experiment. The difference in J level populations suggests that the spin-forbidden mechanism prefers to partition energy into translation rather than rotation for $O_2(a^1\Delta_g, v = 0)$. The preferential partitioning of energy could be explained by a consideration of the potential surfaces involved, shown in Figure 1-1.

The spin-allowed dissociation takes place *via* the $^1B_2$ surface which is sharply repulsive at low internuclear separation and only has a small maximum further out. Therefore, the departing atom accelerates away from the O_2 fragment whilst generating a large torque on the O_2, which could be capable of producing high J rotational states. The spin-forbidden dissociation could be the result of a spin-allowed absorption followed by a crossing to a triplet surface or direct spin-forbidden absorption to a triplet surface. The likely states leading to dissociation for these are the $2\ ^1A_1$ and $2\ ^3B_2$ states respectively, both of which have an initial potential gradient which is smaller than that for the $^1B_2$ state, have a local maximum at *ca.* 1.7 Å and then have a sharp negative gradient leading to the dissociation products. The fact that the maximum acceleration of the fragments occurs at a greater internuclear separation than for the spin-allowed dissociation, and the resulting torque on the O_2 fragment is lower, could reduce the probability of forming high J states. The measured β parameter for $O_2(a^1\Delta_g)$ produced in the spin-forbidden process suggests that it is the excited singlet state that is optically prepared. Pinot[2] determined that the spin-allowed absorption was the probable path.

An interesting future experiment would be to photolyse a sample of ozone at 213 nm (giving the same energy available to the fragments in a spin-allowed step as for spin-forbidden dissociation at 320 nm) and observe the REMPI spectrum. The REMPI spectrum recorded is not expected to match that obtained from the spin-forbidden channel as a result of the possibly different upper states, but could provide insights into the form of the excited state potential energy surface(s).

5.4.2 Time-of-flight studies

Having already seen evidence for a strong **v-J** correlation in the $O_2(a^1\Delta_g)$ fragment the first aim was to try to confirm that different branches exhibit different detectivities, and therefore produce different time-of-flight profiles, resulting from angular momentum alignment. Therefore profiles were taken with ozone undergoing photolysis at 270 nm and 280 nm and, with the photolysis beam polarised at the magic angle and the REMPI laser switched between horizontal and vertical polarisation. The REMPI lines chosen consisted of the strong R and S branch lines, the peak at 321.44 nm and a number of points in a congested region *ca.* 321.7 nm. It was found that the profiles could be separated into four groups with the character of a profile being defined as follows: **H** characterises a profile whose central intensity is less for the horizontal polarisation than the vertical, **V** for *vice versa* and **S** when it was decided that they were the same. A further character **I** was needed as in a number of cases it was not possible to determine the nature of the profiles. Examples of the renormalised profiles, used to determine the characters are shown in Figure 5-7 to Figure 5-10. To enable the results to be discussed more easily the 270 nm and 280 nm REMPI spectra and the assignments of Lewis *et al.*[3] from Figure 5-6 are expanded in Figure 5-11 and the character of the time-of-flight profiles taken marked onto the spectra.

From the profile character assignments, as given in Figure 5-11, for the R and S branches it is immediately obvious that there is a pattern linking the character of a profile to the branch probed. The pattern can be seen more clearly for the profiles obtained at 280 nm photolysis, as the 270 nm profiles occasionally suffered from a small asymmetry in the profiles making it difficult to assign the character unambiguously. Therefore the profiles presented in the following figures, 5-7 to 5-10, were from the 280 nm photolysis of ozone, but the same trends were also observed for the 270 nm photolysis profiles.

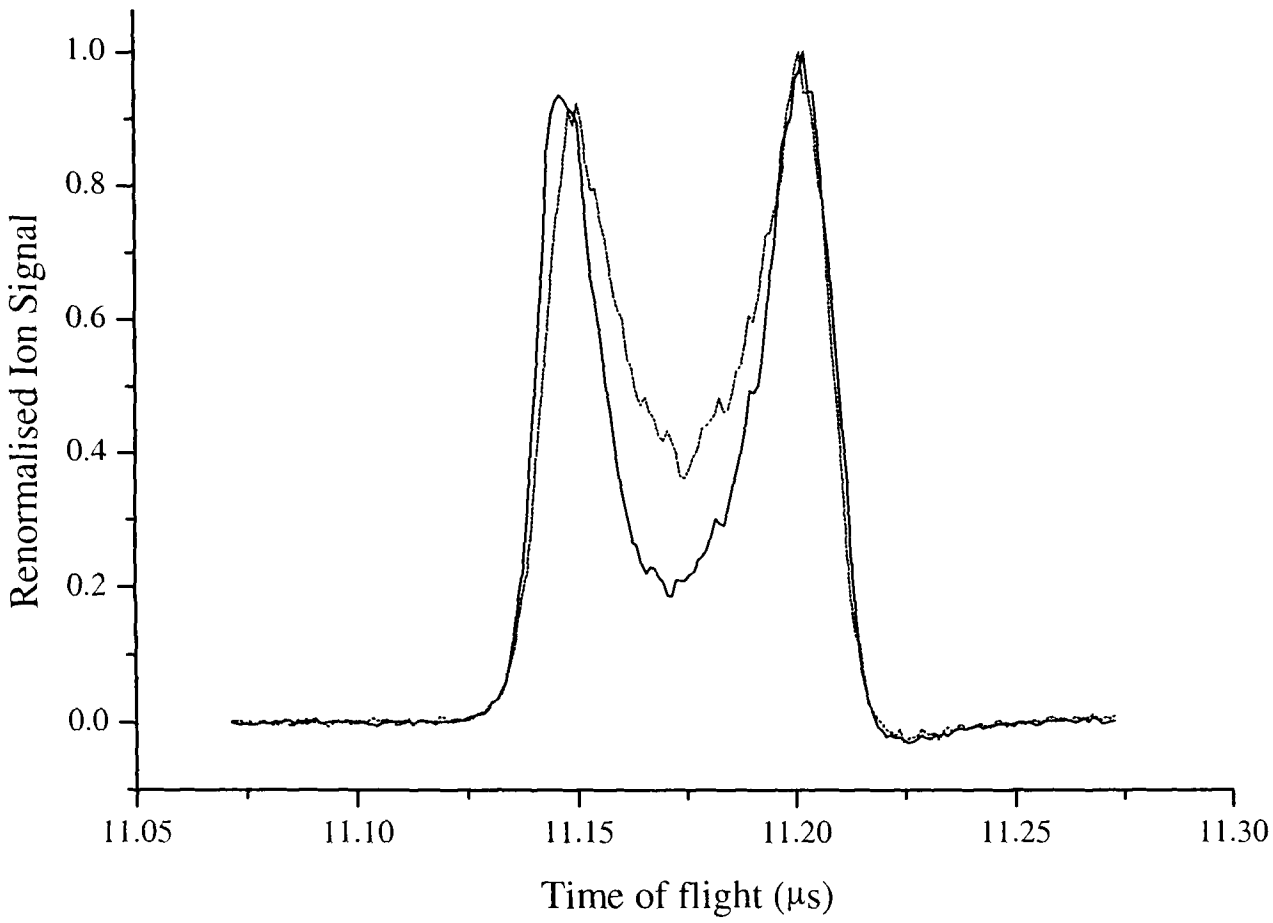

Figure 5-7 Time-of-flight profiles taken with the photolysis laser at 280 nm and polarised at the magic angle. The REMPI laser was switched between horizontal (solid) and vertical (dotted) polarisations at 320.489 nm (S_{22} or S_{20}).

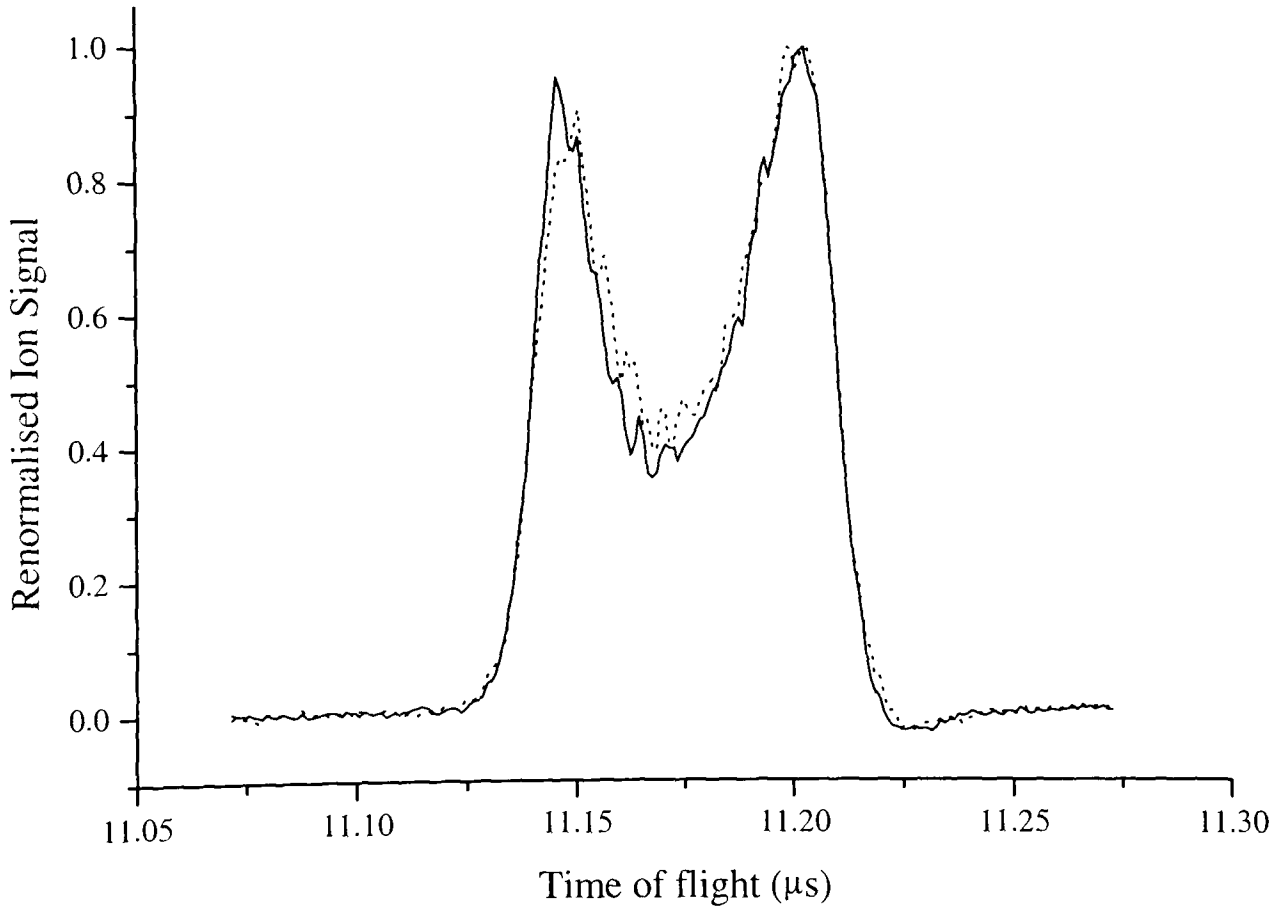

Figure 5-8 Time-of-flight profiles taken with the photolysis laser at 280 nm and polarised at the magic angle. The REMPI laser was switched between horizontal (solid) and vertical (dotted) polarisations at 320.529 nm (S_{19}).

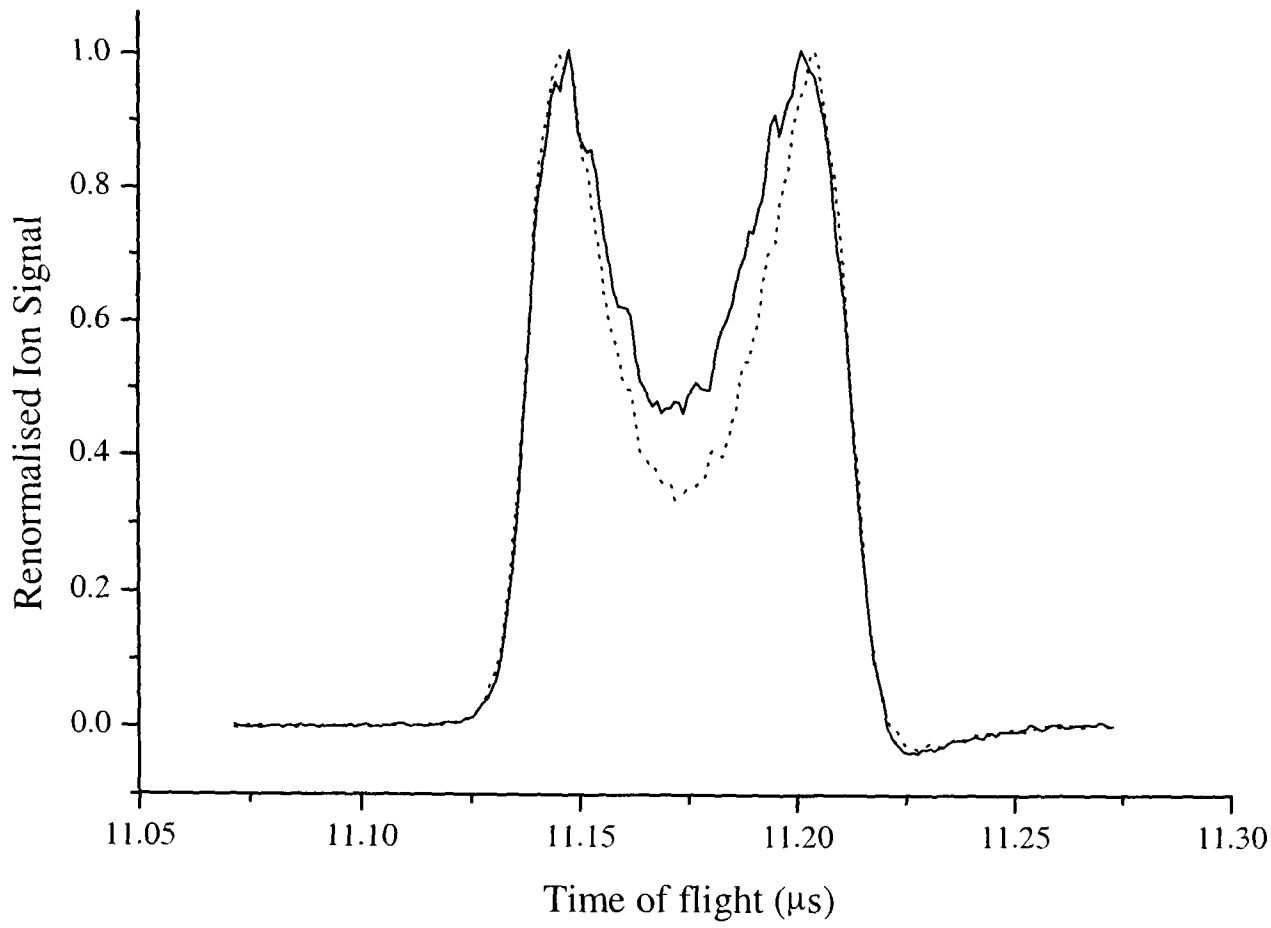

Figure 5-9 Time-of-flight profiles taken with the photolysis laser at 280 nm and polarised at the magic angle. The REMPI laser was switched between horizontal (solid) and vertical (dotted) polarisations at 320.815 nm (R_{18} or R_{23}).

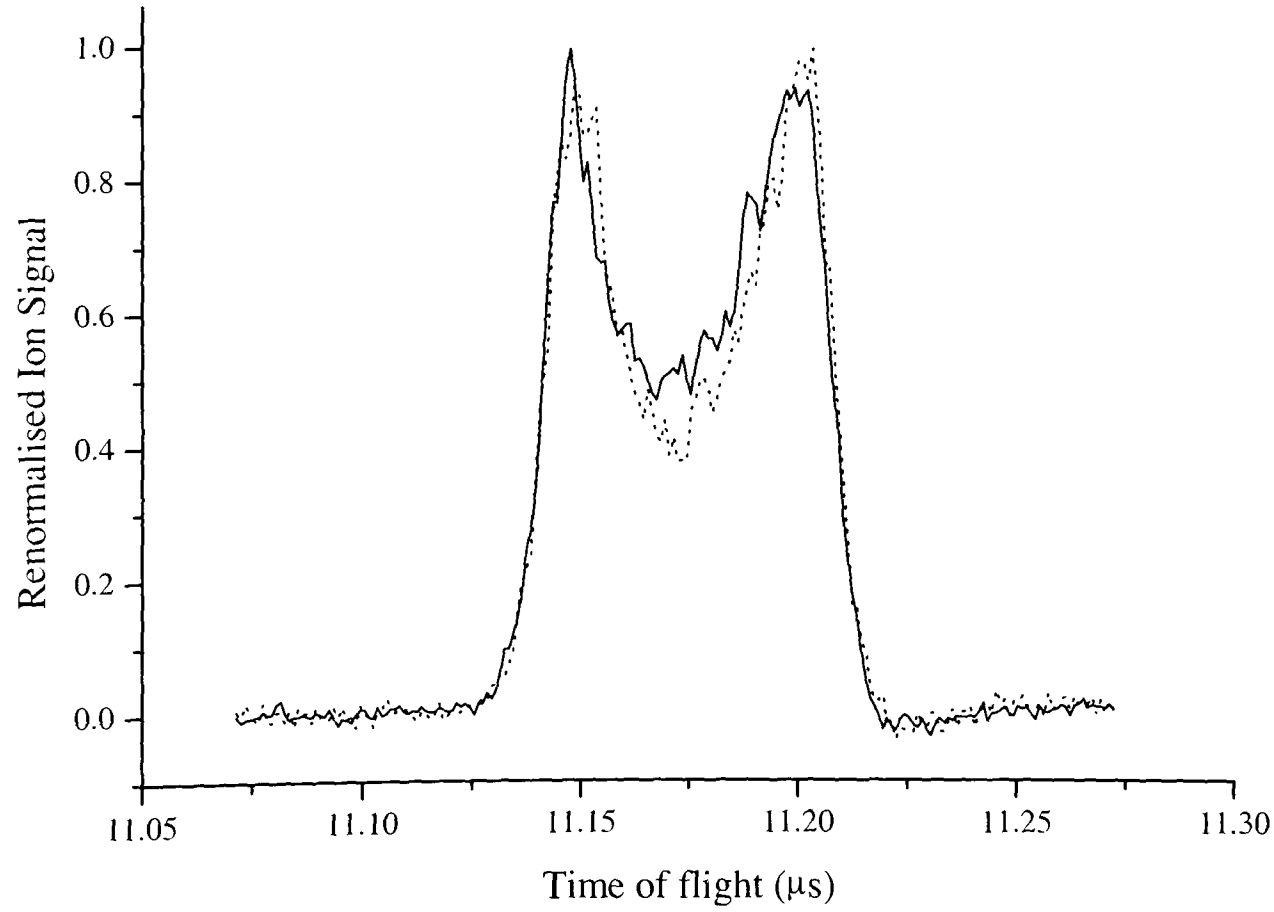

Figure 5-10 Time-of-flight profiles taken with the photolysis laser at 280 nm and polarised at the magic angle. The REMPI laser was switched between horizontal (solid) and vertical (dotted) polarisations at 320.839 nm (R_{17}).

The S branch profiles show that for lines assigned to even values of J the horizontal profile always dips below that of the vertical profile. For odd values of J the traces appear to be very similar and no clear alignment effects can be seen. The odd J values for the R branch follow the same pattern as those in the S branch: i.e. there is no clear difference between the two polarisations. The even J R branch lines show the opposite trend to the S branch, with the even J horizontal profiles now showing a reduced central dip. These observations lead to the following apparent rules:

Horizontal Dip	**Even J, S branch**	**(5-2)**
Horizontal Rise	**Even J, R branch**	**(5-3)**
Similar Profiles	**Odd J, R and S branch**	**(5-4)**

This is a very significant result in that it allows observations of angular momentum polarisation to be used in elucidating spectral assignments. These rules should be generally applicable with the P branch behaving like the R and the O branch like the S.

The S branch exhibits a greater detectivity for fast fragments, which can be explained as follows. For a triatomic molecule, which is not subject to out of plane rotation, fast dissociation leads to the velocity of the fragments being aligned in the laboratory frame and perpendicular to the rotational angular momentum. The profiles show that in the horizontal REMPI polarisation experiments the fragments whose velocity is parallel to the time flight axis are preferentially detected. Thus, the transition dipole moment must be aligned horizontally and is therefore also perpendicular to **J**. This alignement is expected since an S branch transition is equivalent to two single photon absorptions with $\Delta J = 1$, each of which has its transition dipole moment perpendicular to J.

The R branch, which has one $\Delta J = 1$ absorption and one $\Delta J = 0$, does not require that the transition moment is perpendicular to **J** for both transitions. Given its mixed R / Q nature a different time-of-flight profile is expected and observed. In this case the effect is a relative enhancement in the detection of slow fragments, suggesting that the Q transition makes the dominant contribution to the detection sensitivity.

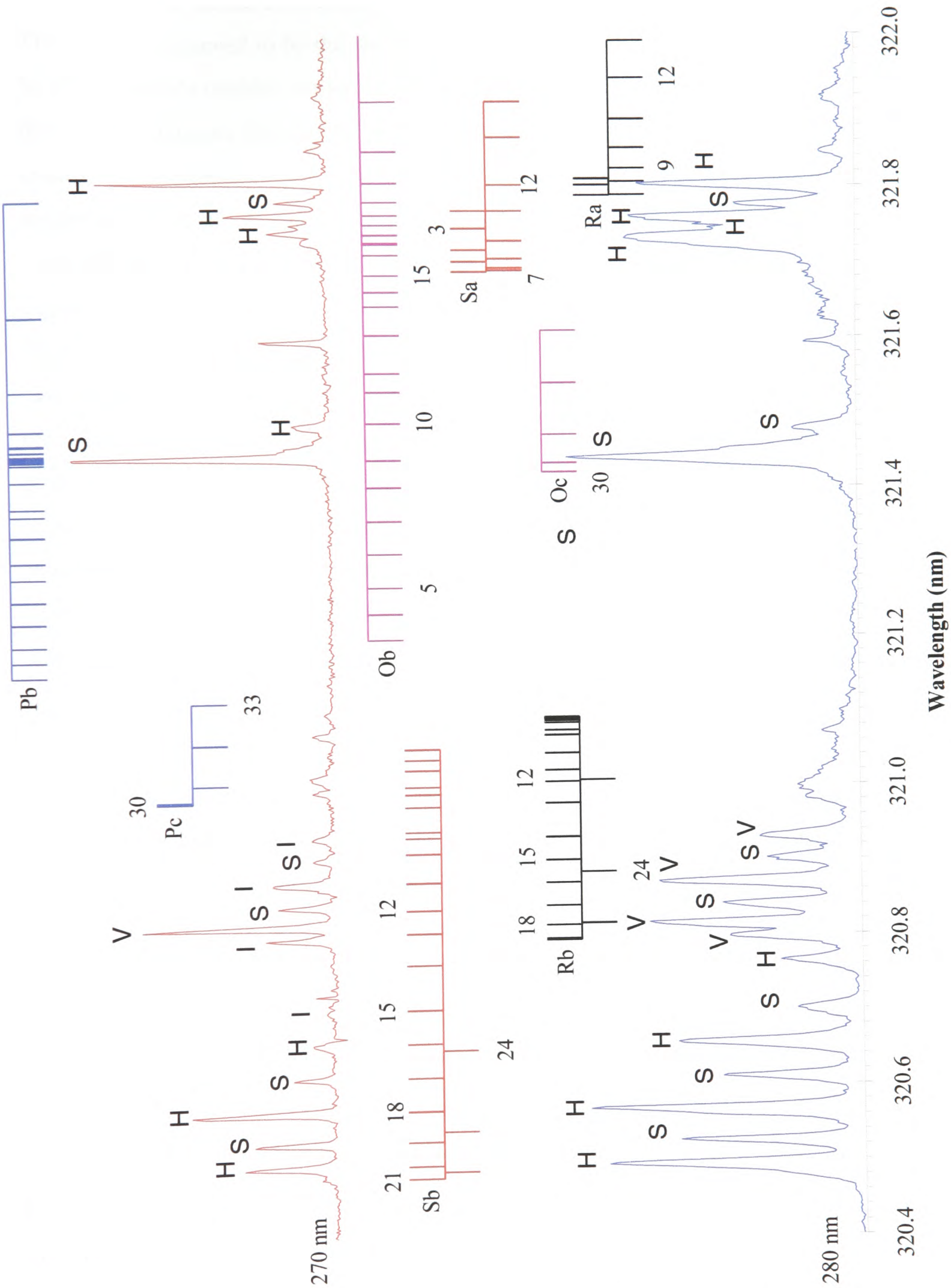

Figure 5-11 Comparison of spectra taken with 270 nm and 280 nm photolysis. Marked on the chart is the assignment of Lewis et al.[3] and the character of the time of flight profiles as shown in Figure 5-7 to Figure 5-10.

The observed difference in the time-of-flight profiles of odd and even *J* states, probed on the same branch, is caused by different detectivities as a result of angular momentum polarisation. This effect is believed to be due to the permitted lambda doublet states. The even *J* states must be the A' lambda doublet whilst the odd *J* states must be the A" lambda doublet. The nature of the profiles suggests that the A" lambda doublet is strongly depolarised whilst the A' doublet retains its polarisation. Production of the A' lambda doublet is expected as the dissociation of ozone occurs on an A' surface. Population of the A" doublet could be the result of Coriolis coupling between the $^1B_2$ A' surface and the A" surface, or from inelastic scattering in the exit channel. Different angular momentum polarisations for the two lambda doublets have been observed in reactive scattering studies of Brouard *et al.*[16] and Hall *et al.*[17] In these studies the two lambda doublets of the OH product showed the same angular scattering but only one of them had a strong rotational polarisation. The observed difference in angular momentum polarisation was attributed to exit channel effects. The A" doublet is formed by inelastic scattering of the strongly polarised A' lambda doublet within the exit channel. The collisions responsible for this population transfer scramble the angular momentum polarisation. Inelastic scattering in the exit channel has also been observed in the photodissociation of CH_3ONO[18] where it is manifest as a non-equilibrium spin-orbit distribution in the NO fragment.

If these rules are now applied to the other profiles that were taken, the following conclusions are made. In the congested region the majority of the profiles show a greater dip in the horizontal profiles than the vertical, suggesting that the lines are predominantly even *J*, as shown in Figure 5-12 for 321.735 nm. The first peak probed coincides with the wavelength expected for O_{20}, the second coincides with O_{22} and S_{11}, with the profile character suggesting that it is the O_{22}. The profile taken between these two also indicates even *J*, even though it coincides with the O_{21} assignment, which is an apparent mismatch. However, since the width of the surrounding even *J* lines and the low intensity of the O_{23} line make it possible that the observed even character is due to the signal from the odd *J* line being swamped by the large even *J* lines on either side. The next line has odd *J* character, as shown in Figure 5-13, and matches the location expected for O_{23} and the last line shows even *J*, which matches the expected wavelength for both the O_{24} and S_{12} transitions.

The profiles taken on the peak at 321.44 nm appear to be the same and therefore this peak seems to be an odd *J* line of unknown branch. However, because of the congestion in the P series at this wavelength the observation may be the result of simultaneously probing a number of *J* value transitions.

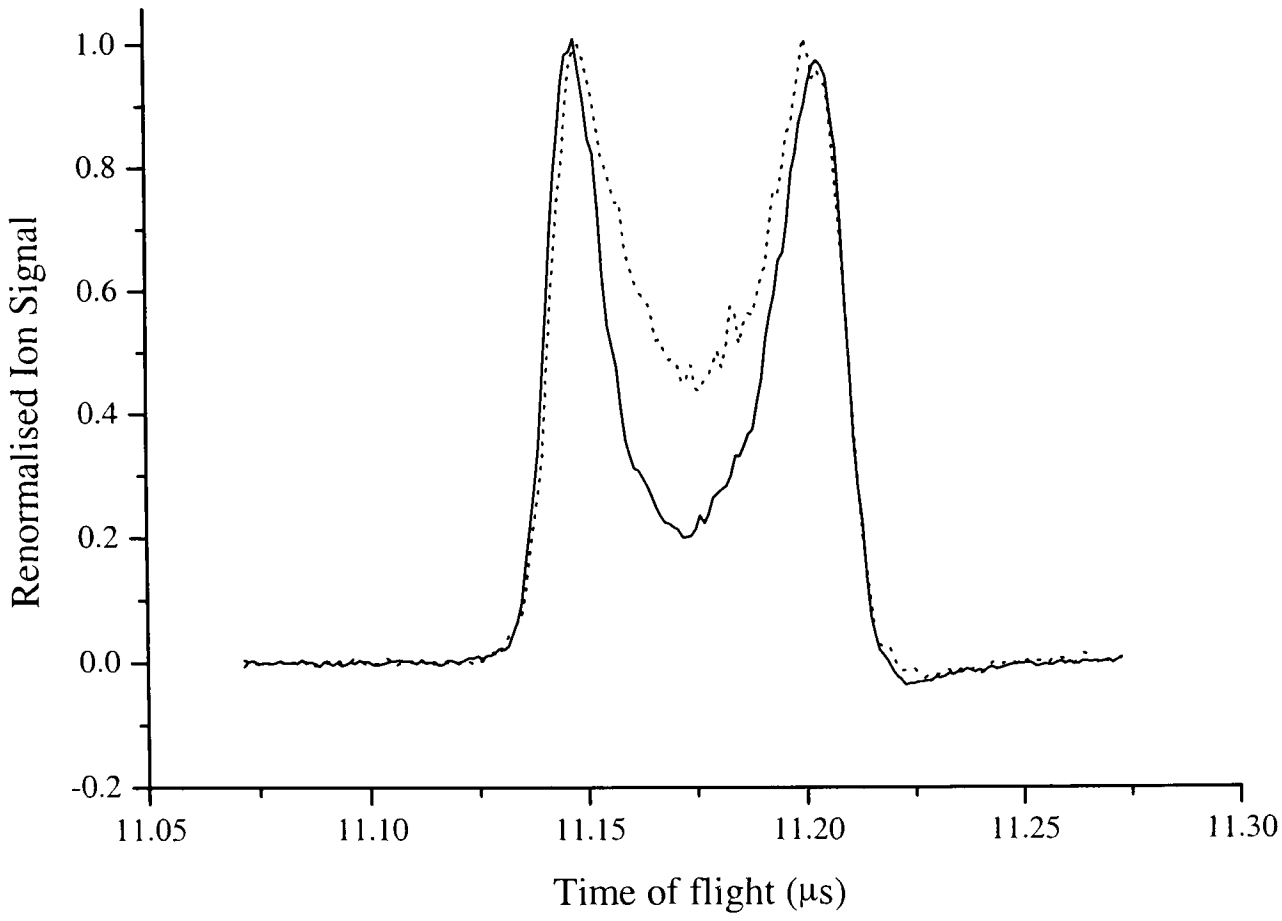

Figure 5-12 Profiles taken at 321.735 nm showing a dip in the horizontal profile suggesting even *J* O / S branch.

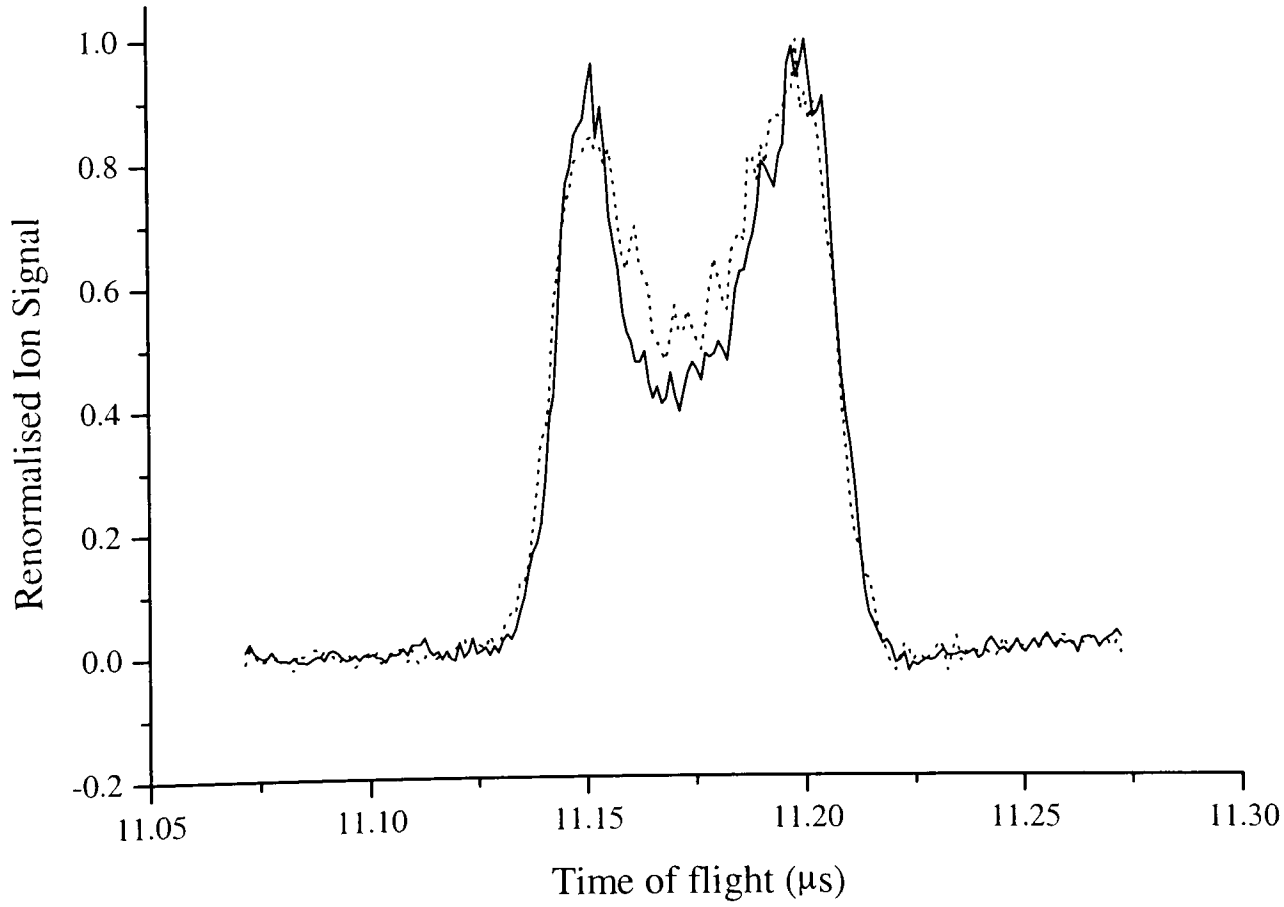

Figure 5-13 Profiles taken at 321.776 nm. The profiles are very similar suggesting an odd value of *J*.

5.5 The $O_2(d^1\Pi_g - a^1\Delta_g)$ (1,0) band

5.5.1 REMPI spectrum

Figure 5-14 presents the REMPI spectra in the $d^1\Pi_g - O_2(a^1\Delta_g)$ (1,0) band that were obtained for photolysis between 300 nm and 270 nm. Each spectrum has been renormalised to the maximum signal within it. For photolysis at 300 nm and 293 nm, the spectra at wavelengths below 331.35 nm have had their magnitudes magnified by a factor of five to make them easier to view. In general a trend to higher J as the photolysis wavelength is decreased can be seen from the assignments in the R and S branches. In all of the spectra there is a region between 330.70 nm and 331.00 nm which appears to be devoid of any clear structure. This gap is caused by a perturbation of the energy levels by nearby valence states. The perturbation has been ascribed by Lewis *et al.*[3] to the crossing of the $d^1\Pi_g$ rotational levels near $J = 12$ by the $v = 5$ rotational term series of the valence state. This valence state is dissociative on a short enough timescale that makes absorption of a third photon is unlikely to take place, so the REMPI process can not occur. Van der Zande *et al.*[19] determined, from the relative yields of $O(^1D)$ and $O(^3P)$ products, that the $d^1\Pi_g(v = 1)$ Rydberg state predissociates predominantly (77%) *via* the $1^3\Pi_g$ valence state, with the rest *via* the $1^1\Pi_g$ valence state. The competition between the REMPI and predissociation pathways was found by Ball[1] to be strong even at wavelengths away from this region, with the REMPI power dependence at 331.45 nm being 2.48 ± 0.13 (the expected value is 2).

A further section of the spectra appears to be heavily perturbed, that between 330.30 and 330.40 nm. Whilst there is evidence of structure in this region, corresponding to the $J = 21$ and 22 lines of the R branch, the structure is not as clean as the peaks that are observed either side of it. The lack of clarity is likely to be caused by perturbations by the valence states but no assignment has been made of the perturbating state(s).

The lines at shorter wavelengths are of interest as these show evidence of an intensity alternation. The alternation has been previously observed by Pinot[2] for the photolysis of ozone at 266 nm and after comparison with the results of Valentini *et al.*,[13] which have already been discussed, it was considered that the odd J branch lines were being depleted, but as R and S branch lines overlap ($J_R = J_S + 5$) and they have opposite rotational parity, structure was still observed at the odd J wavelengths.

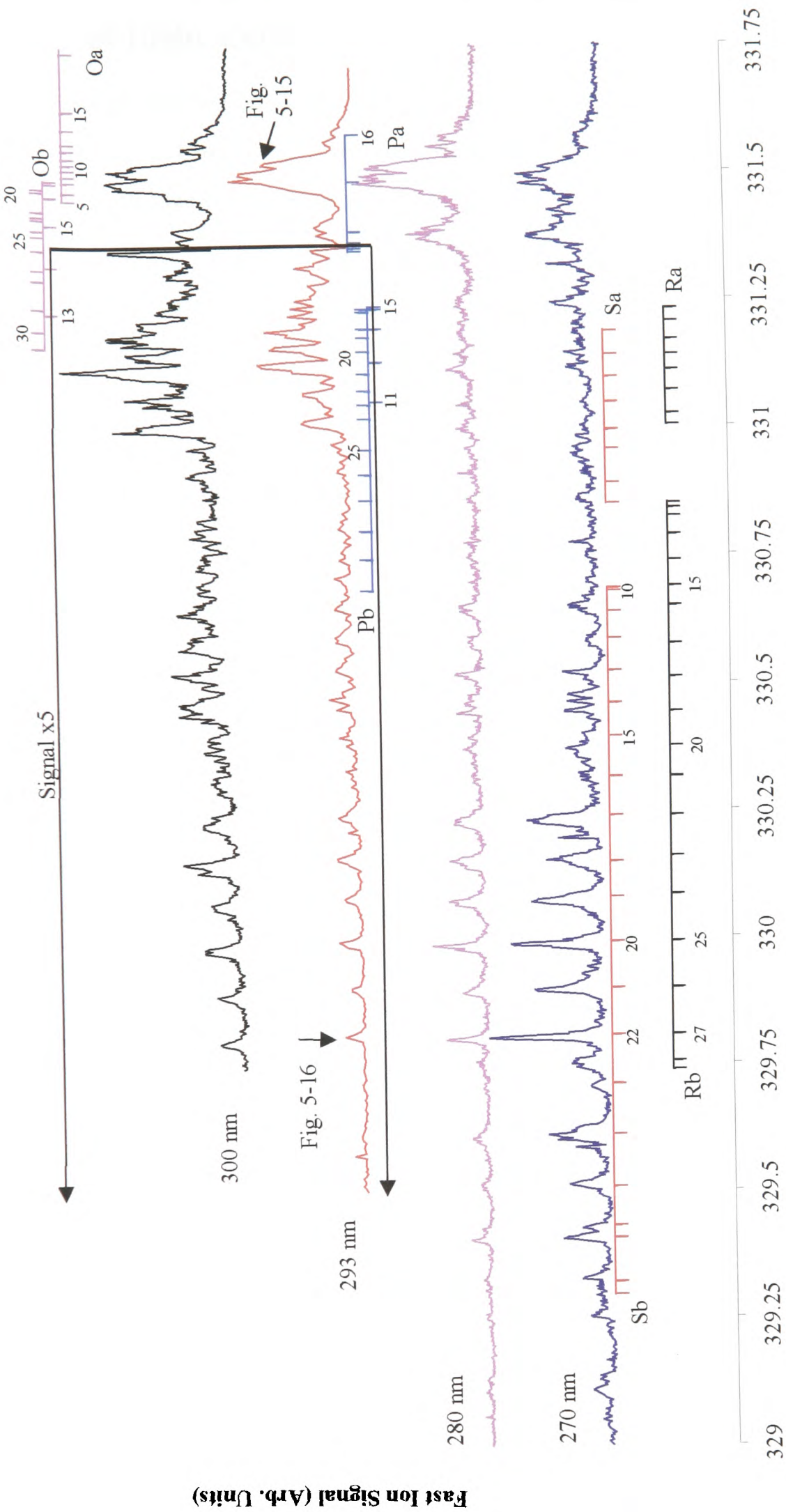

Figure 5-14 Two-laser REMPI spectrum for photolysis at 300 nm (black), 293 nm (red), 280 nm (purple) and 270 nm (blue). The signals have been renormalised to the maximum value in the spectrum.

5.5.2 Time-of-flight studies

As a result of some of the signal oscillations seen in the spectra and the fact that the R and S branch lines overlap for high J ($J > 15$), the time-of-flight profiles of the states probed at this wavelength were examined to try to assign the observed transitions. The comparison was carried out in a similar way to that discussed in Section 5.4.2, with ozone being photolysed at the magic angle and a number of wavelengths to form $O_2(a^1\Delta_g)$. Profiles were then recorded, with the REMPI polarisation switched between horizontal and vertical, for a number of the main peaks in the REMPI spectra shown in Figure 5-14.

5.5.2.1 Angular momentum alignment

Examples of the results obtained when the REMPI polarisation was switched can be seen in Figure 5-15 and in Figure 5-16 for which ozone was photolysed at 293 nm. At this wavelength, where the translational energy of the $O_2(a^1\Delta_g)$ is low, a signal that is broadly "top hat" with a small central dip resulting from core extraction would be expected, as seen in Figure 5-15. Also, as the value of J increases for the line being probed, it would be expected that the time-of-flight profile would become narrower as energy that was available for translation is taken up by rotation of the $O_2(a^1\Delta_g)$ fragment. This effect can be seen by comparing the widths of the profiles in Figure 5-15 and Figure 5-16. As was seen for the (2,0) band there is significant evidence in these figures for the occurrence of a strong **v-J** correlation in the probed fragment with the profile's form changing depending upon the transition (the horizontal polarisation shows a marked dip at 329.81 nm but not at 331.517 nm). To enable a comprehensive study to be carried out and to cover a wide range of J values, multiple photolysis wavelengths were used. Examples of the profiles that were obtained for photolysis at 290 nm, 280 nm and 270 nm are shown in Figure 5-17 to Figure 5-19 respectively.

The clearest observed effect is that as the photolysis wavelength is reduced the degree of core extraction increases. Again as the probe transition changes it is found that the character of the profiles changes as well. It was also observed that, for a number of the profiles, the character of the profiles changed as a function of photolysis wavelengths. A full list of the characters of the lines is presented in Table 5-1. Unfortunately, as many of the R and S branch lines between 329.8 nm and 330.8 nm overlap, the type of analysis done on the profiles in the (2,0) band cannot be done here. However, the character of the profiles for a given branch must be the same as observed in the (2,0) band, which allows confirmation of the spectral assignments. The results of the application of the rules, (5-2) to (5-4), are presented in the next section.

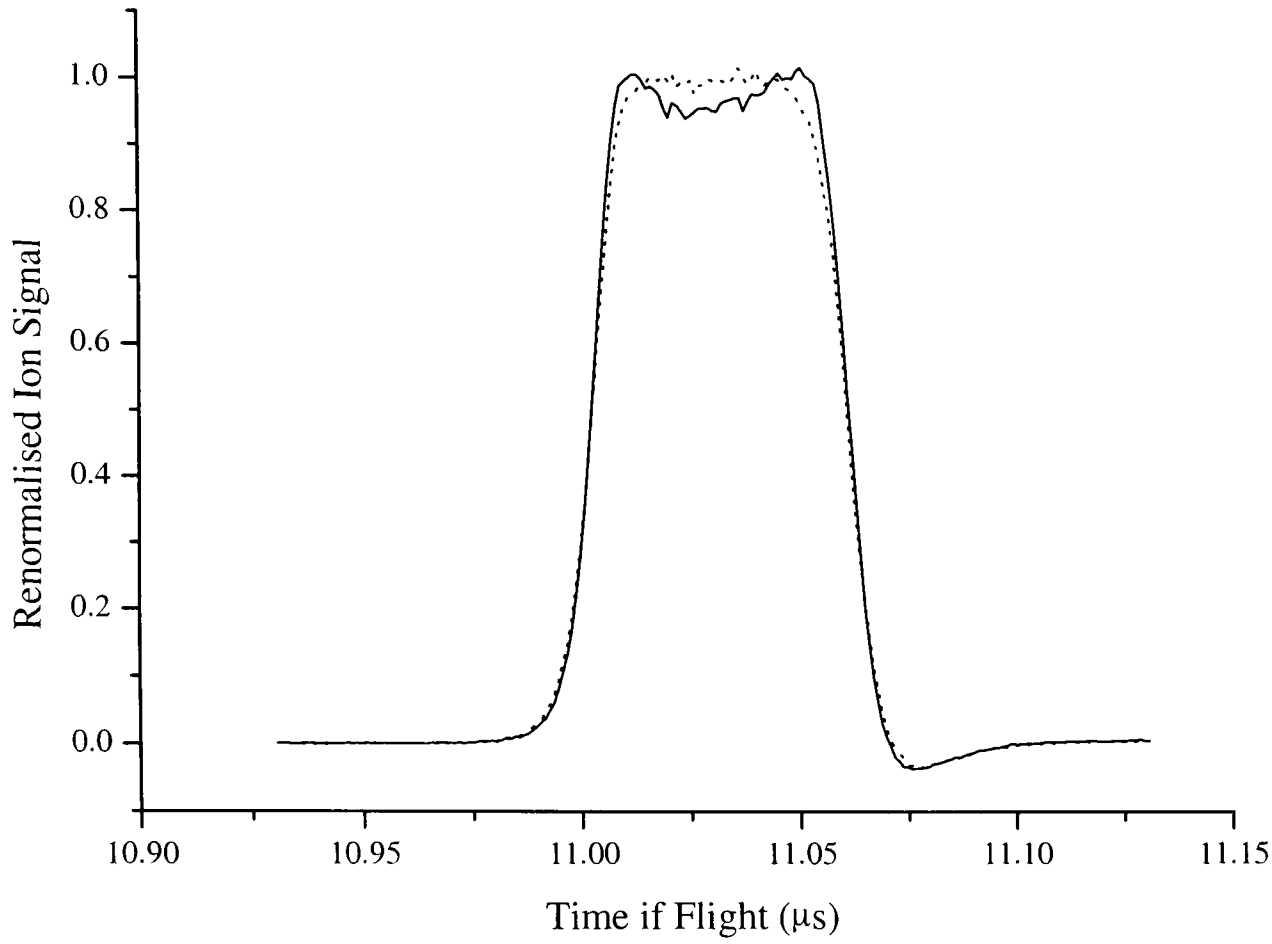

Figure 5-15 Time-of-flight profiles recorded at 331.517 nm ($O_{\approx 9}$). The 293 nm photolysis laser was at the magic angle and the REMPI laser was switched between vertical (dotted) and horizontal (solid).

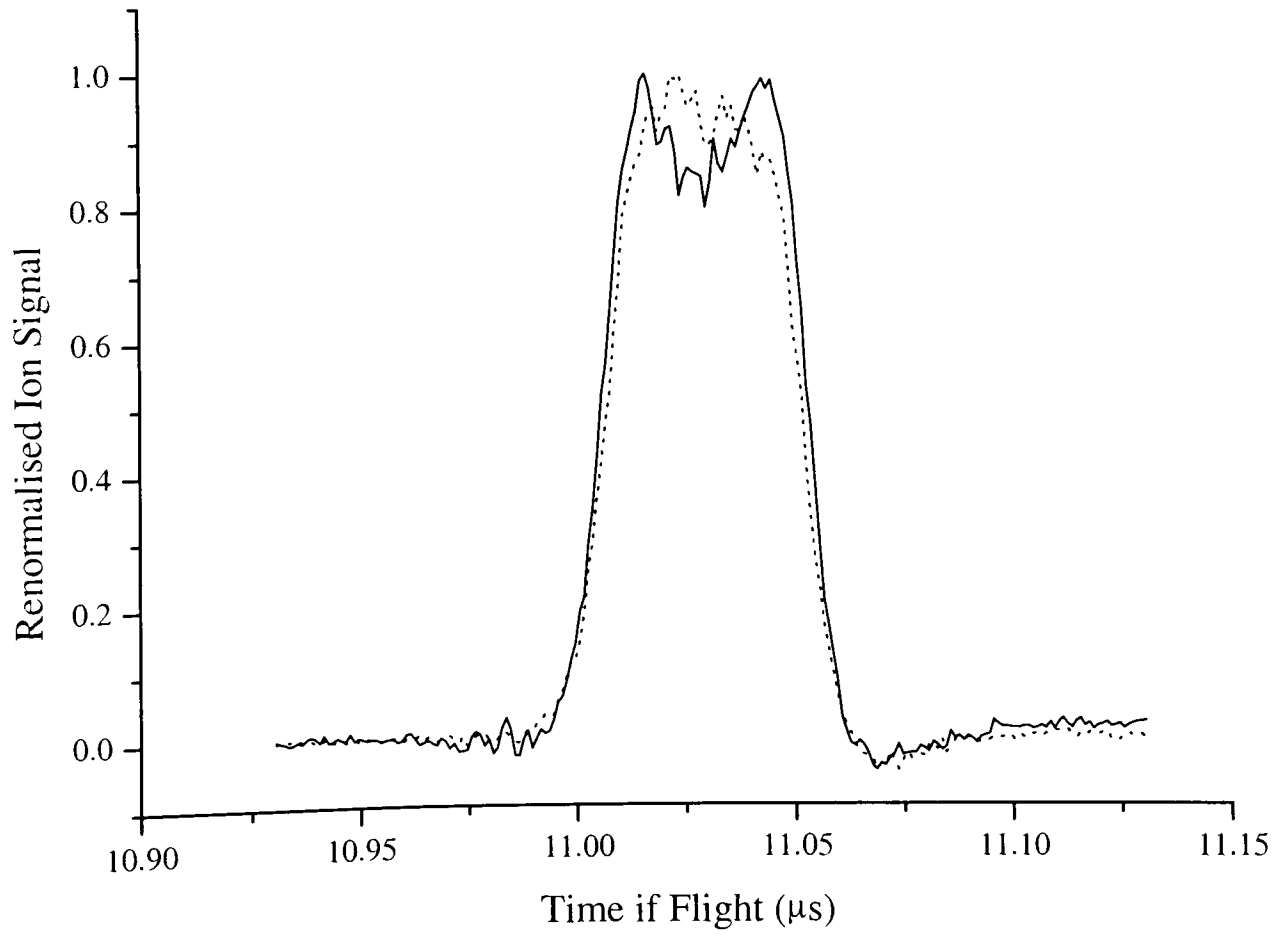

Figure 5-16 Time-of-flight profiles recorded at 329.81 nm (S_{22} or R_{27}). Laser conditions as for 5-15. The form of the profile suggests that it is S_{22}.

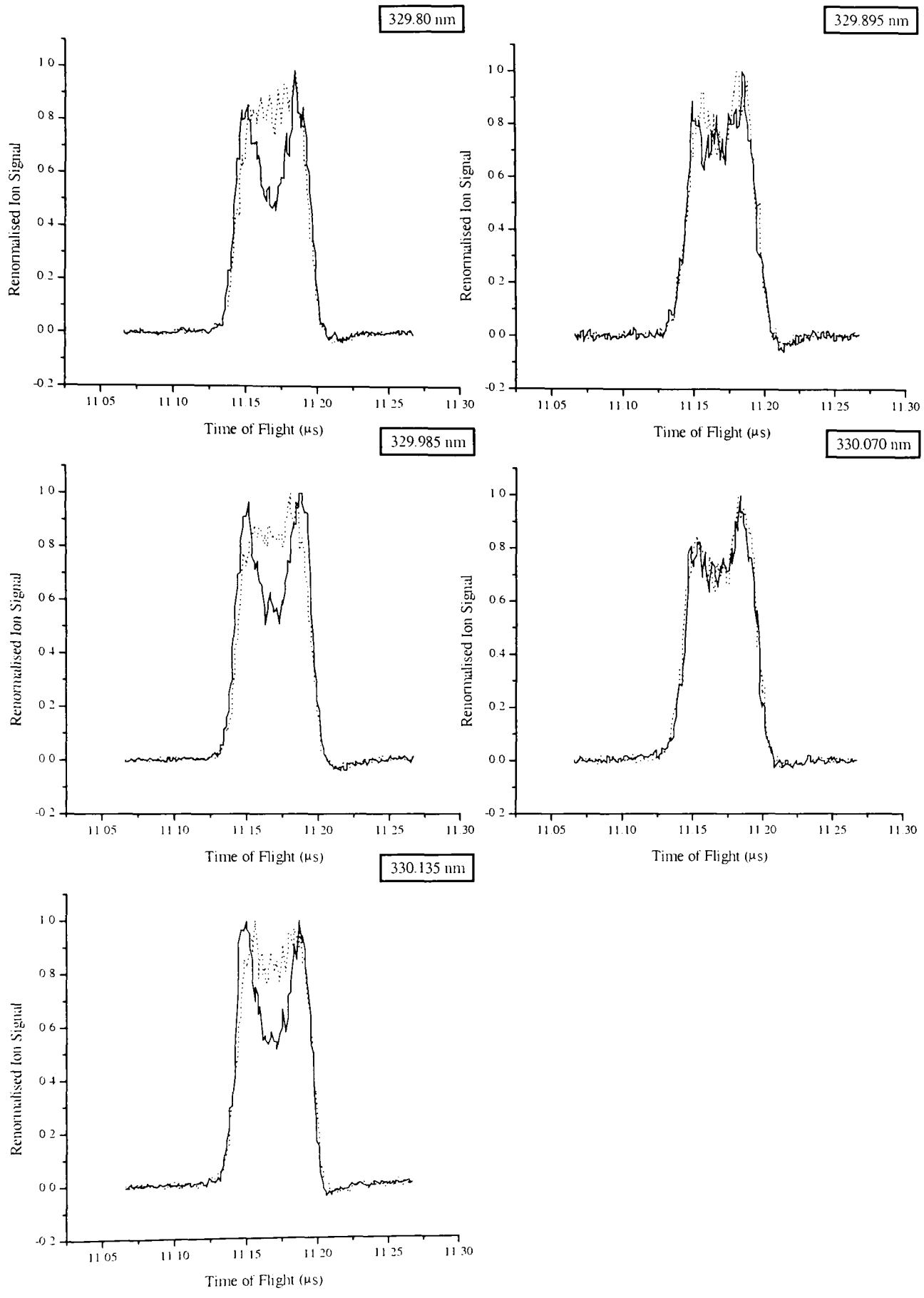

Figure 5-17 Examples of time-of-flight profiles taken with the photolysis laser at 290 nm. The boxed figure is the wavelength of the transition being probed.

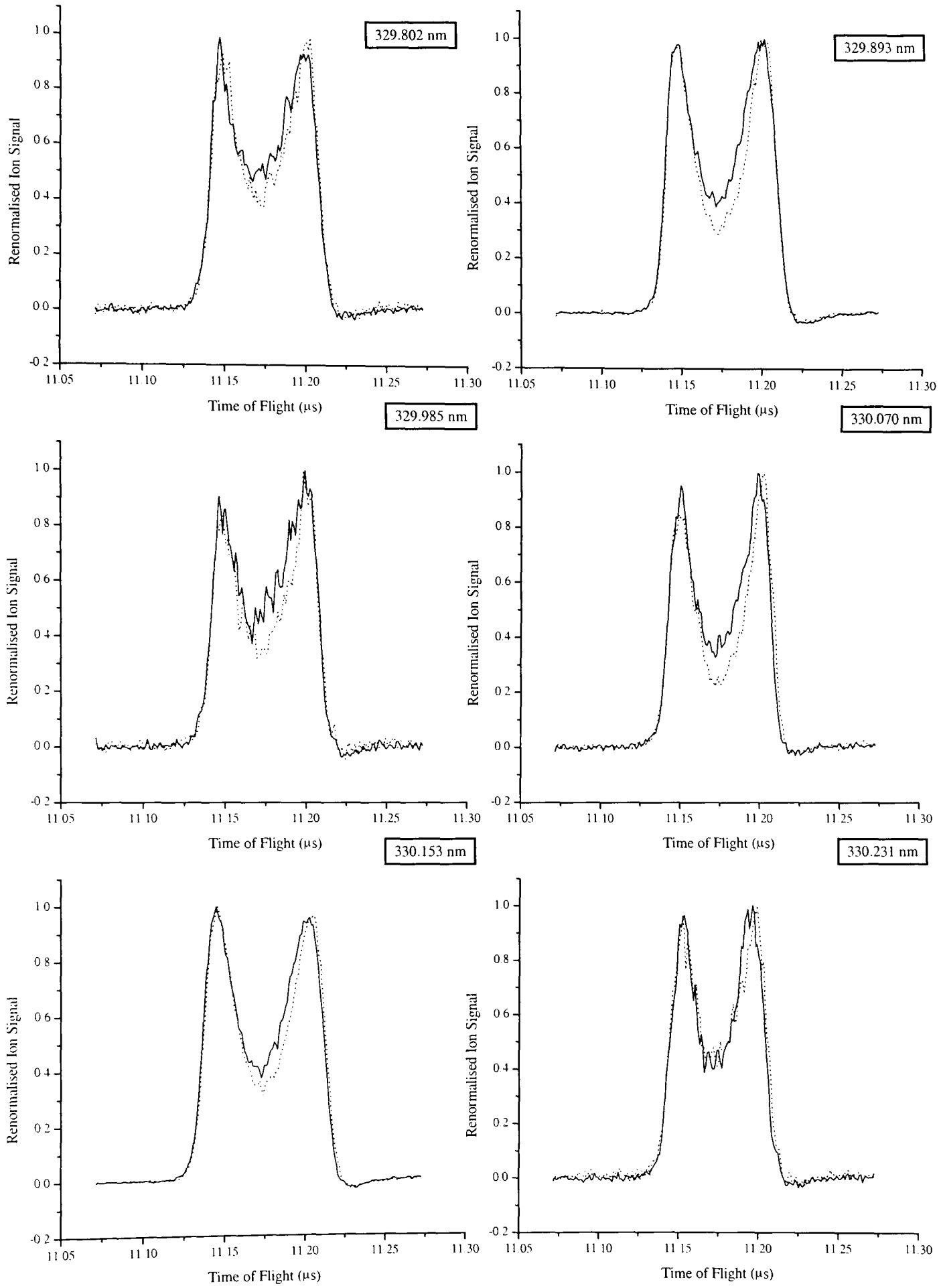

Figure 5-18 Examples of the time-of-flight profiles taken at 280 nm.

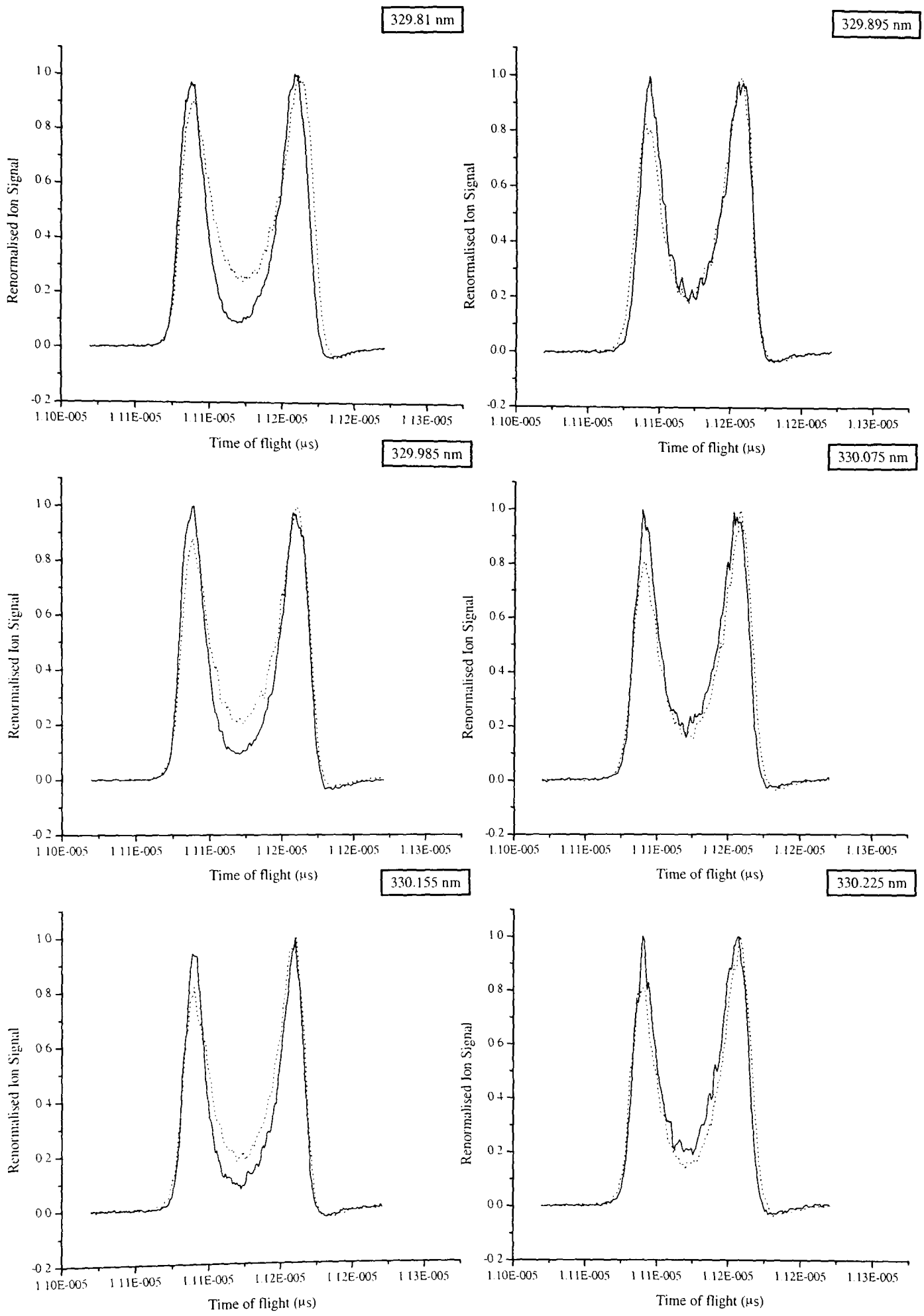

Figure 5-19 Examples of the time-of-flight profiles taken at 270 nm.

5.5.3 Extension of rules from (2,0) to the (1,0) band

Having had good success predicting the line assignments based on the time-of-flight profiles in the (2,0) band, the polarisation based rules were then applied to the profiles shown in Section 5.5.2 to determine if the REMPI transitions could be more confidently assigned. Table 5-1 shows the character of the transitions probed, a statement as to the apparent transition type according to the rules from the (2,0) band and the assignment given by Morrill[4] to compare against the prediction. The comparison between the predicted *J* values and the assigned values seems to be a good one, with most lines character matching their assignment. Interestingly, the changing rotational population makes an observable contribution to the time-of-flight profiles. This is shown in the 329.8 nm to 330.8 nm wavelength region where the character of the lines changes as a function of photolysis wavelengths. The changing character is believed to be the result of the changing rotational population, as higher *J* R branch lines overlap S branch lines, and can be explained with reference to Figure 5-20.

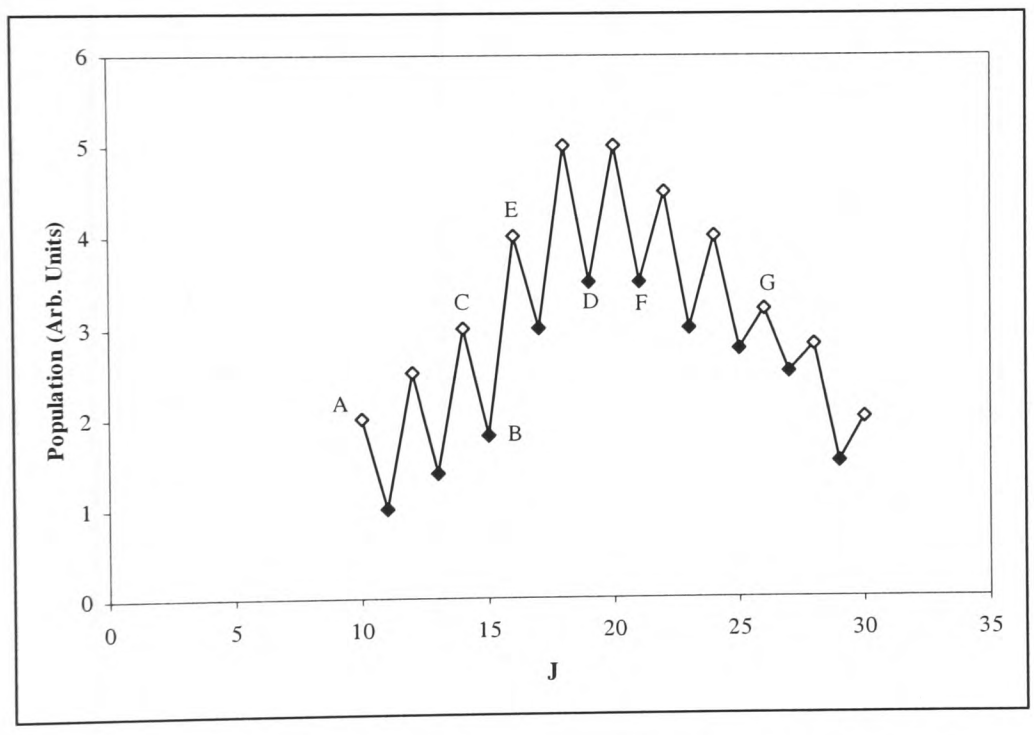

Figure 5-20 Example of how the changing rotational populations could affect the character of a time-of-flight profile. This figure is illustrative only.

Knowing that the S branch probes a lower *J* than the overlapping R branch the following statements can be made. Initially at the longer wavelengths only low *J* states are populated and the even *J* lines population exceeds that of the higher odd *J* (A > B) and therefore dominates. As the wavelength is reduced a point is reached where the even *J* population is less than the odd (C < D), where the character would be expected to change. Reducing the wavelength still further causes the original situation to resume as the population peaks in odd *J*, but the even *J* probed by the S branch are still growing (E > F). Finally as the shortest wavelengths are

reached the odd J S branch lines will dominate the higher even J lines (F > G, this case was not observed). The description just given is only a qualitative explanation as the rotational state distributions of $O_2(a^1\Delta_g, v = 0)$ produced by photolysis at 270 nm and 280 nm have not been published.

Transition	293 nm	290 nm	280 nm	270 nm	According to type	Assignment
331.592	H				Even S	O14
331.573	S				Odd	O13
331.555	H				Even S	O12?
331.517	H?				Even S?	O9
331.485	S				Odd	O7
331.389		B			Odd	P?
331.380	S?				Odd?	P?
331.369		B			Odd	P?
331.110	S				Odd	R7
331.000	B				Odd	R9, R10
330.646			H		Even S	R16
330.582	H		S		Odd	R17, S12
330.519			H		Even S	R18
330.477			H		Even S	?
330.460	H				Even S	S14
330.440	H		H		Even S	R19
330.225	B		S	V	Odd / Even R	R22, S17
330.155	H	H	S	H	Odd / Even S	R23, S18
330.075	B	B	V	S	Even R / Odd	R24, S19
329.985	H	H	S/V?	H	(Odd / Even?) R / Even S	R25, S20
329.895	S	B	V	S	Even R / Odd	R26, S21
329.800	H	H	S	H	Even S	R27, S22
329.743			V	S	Even R / Odd	R28, R29
329.708			V	H	Even R / Even S	S23
329.610			H	H	Even S	S24
329.514			S	S	Odd	S25
329.427			H	H	Even S	S30?
329.405			H	H	Even S	S26
329.326			H	S	Even S / Odd	S28?, S27
329.250			S	S	Odd	?
329.105			H	H	Even S	?

Table 5-1 Comparison of time-of-flight profile character, predicted *J* parity and branch and line assignments. Profiles taken on transitions within 0.02 nm of each other between different photolysis wavelengths have been grouped together (the exact wavelengths used for each photolysis wavelength were based on the spectra in Figure 5-14 and varied by a small amount). The character B denotes both profiles dipping at a photolysis wavelength where top hat profiles should be observed and is thought to equate to S character.

5.6 The $O_2(d^1\Pi_g - a^1\Delta_g)$ (3,0) band

5.6.1 Spectrum

The transition *via* the Rydberg intermediate, $O_2(3s\sigma_g\ d^1\Pi_g,\ v' = 3)$, is predicted to result in a REMPI spectrum between 311.0 nm and 313.0 nm. Figure 5-21 shows a portion of this spectrum in the region of the main spectral features.

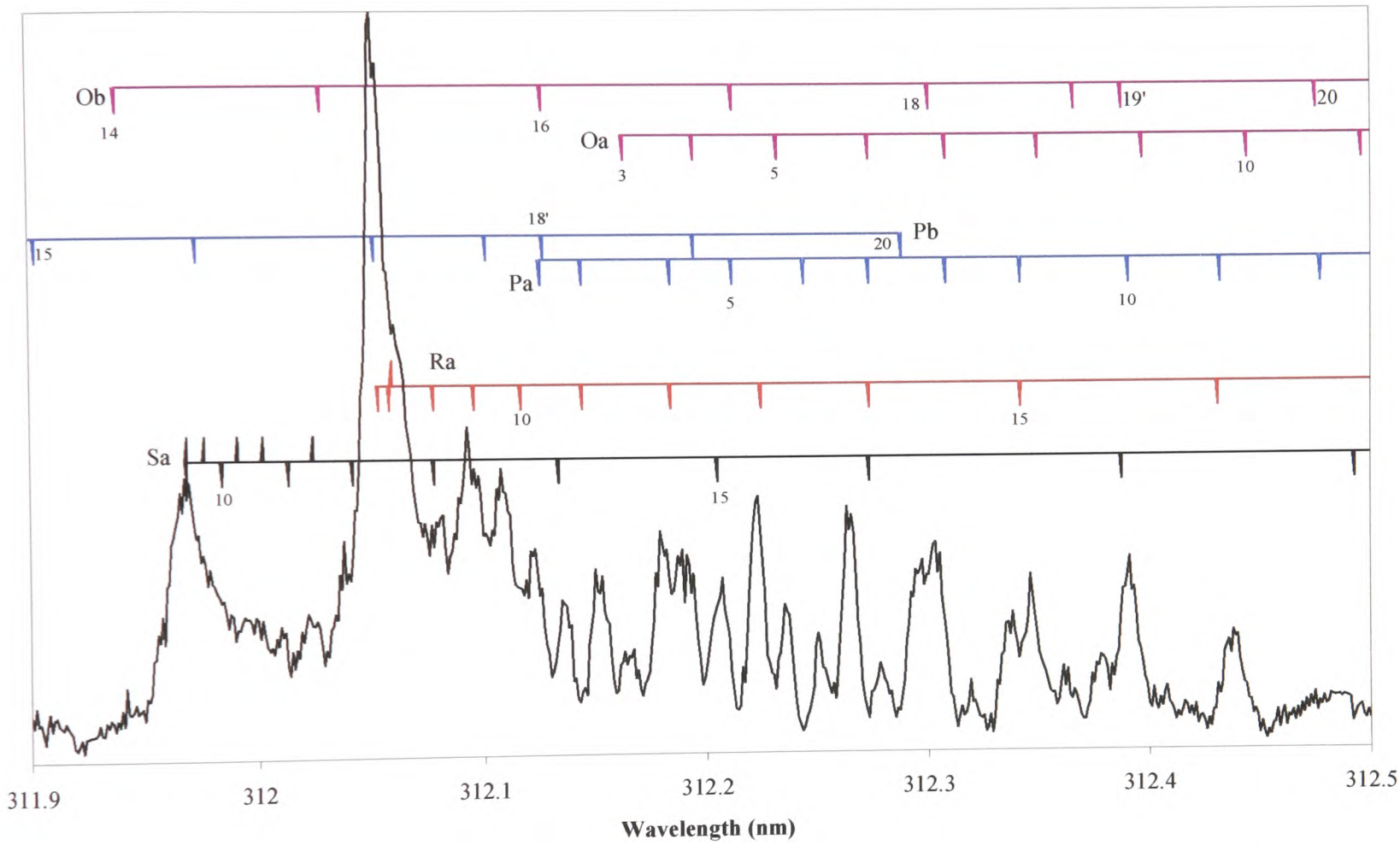

Figure 5-21 Single-laser REMPI spectrum taken between 311.9 nm and 312.5 nm.

Once again the spectroscopy of the region is complicated by valence interactions, with major perturbations occurring at *ca.* $J = 14$ and $J = 20$. The perturbations are sufficiently large that there is significant overlap between many of the branches and sub branches.

5.6.2 Time-of-flight profiles

To determine whether the same form of analysis that was carried out in the (1,0) band could be used in the (3,0) band, a number of time-of-flight profiles were recorded. The $O_2(a^1\Delta_g)$ was prepared by ozone photolysis at 293 nm at the magic angle, and profiles were recorded on many of the peaks in the spectrum. Examples of the results are shown in Figure 5-22.

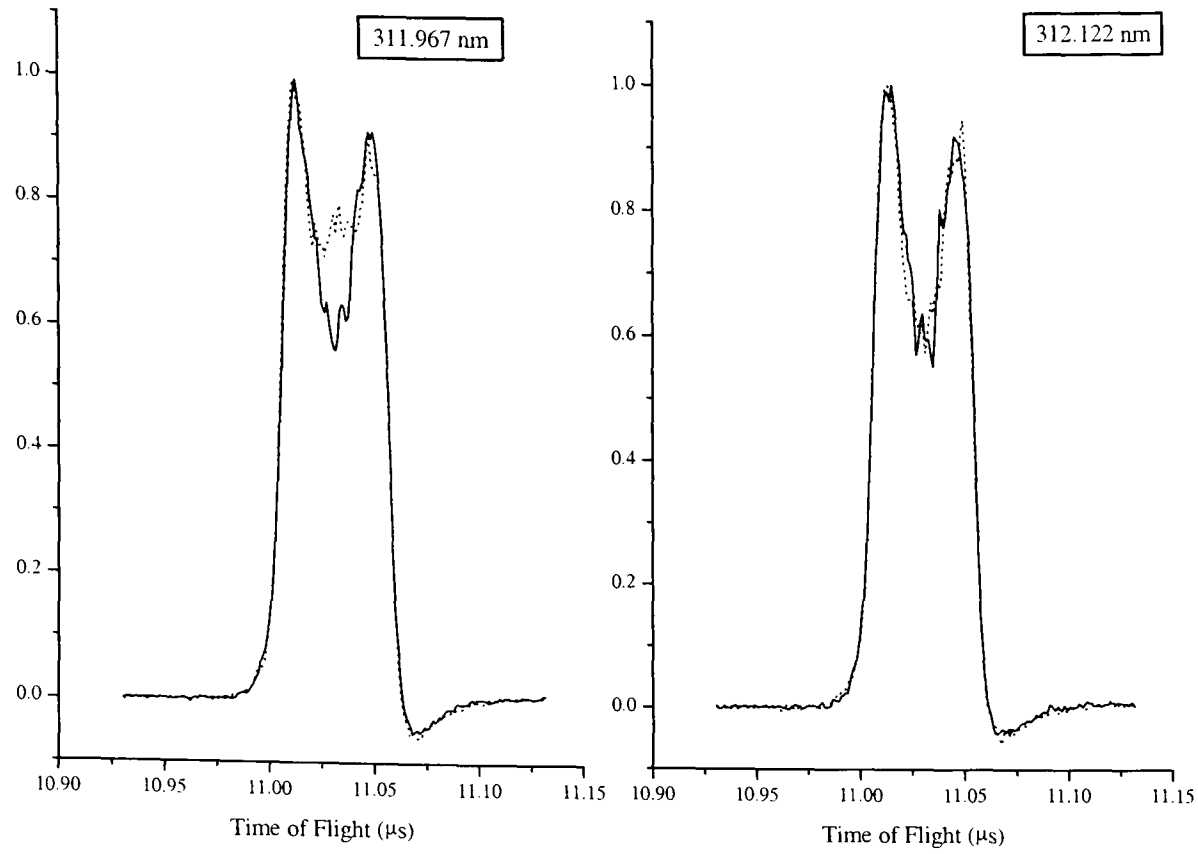

Figure 5-22 Examples of the time-of-flight profiles of $O_2(a^1\Delta_g)$ prepared by photolysis at 293 nm at the magic angle and detected by REMPI *via* the (3,0) band.

The time-of-flight profiles do show differences for the different REMPI polarisations, but the comparison of how the changes in profile relate to the assignment is not as clear as for the other REMPI bands. At the shorter wavelengths the horizontal profiles show a dip, changing in the mid wavelength region to profiles similar to each other, and then at the longer wavelengths a small central peak can be seen. Also, it appears that the vertical profiles change in shape showing dips and troughs but in no obvious pattern. Evidence from the 320 nm band would

suggest that the changing profiles indicates a change in the transition branch between the short wavelength and long wavelength, whilst the intermediate wavelengths are of odd *J* character. Given the complexity of the spectrum it is felt that a more detailed examination of the time-of-flight profiles characteristics is needed. The detail required could be achieved by recording profiles at 0.005 or 0.0025 nm steps across the spectrum rather than just on the peaks and investigating any correlation between them and the assigned spectrum. Additional photolysis wavelengths could also prove useful, as the core extraction at shorter photolysis wavelengths appears to simplify the observation of any angular momentum polarisation effects.

5.7 Conclusions

The aim of the work detailed in this chapter was to investigate the possibility that measurements made on the time-of-flight profiles resulting from the REMPI of $O_2(a^1\Delta_g)$ could generate useful information to aid in the assignment of heavily perturbed spectra. The usefulness of details within the time-of-flight profiles has been successfully demonstrated by using the changing shapes of the time-of-flight profiles as a fingerprint to identify both the spectral branch, and the parity, of the rotational state being probed. The differences in time-of-flight profiles for different spectral branches are due to angular momentum polarisation and it has been shown that odd *J* levels show negligible angular momentum polarisation while even *J* levels are strongly polarised with **v** perpendicular to **J**.

References:

1 S.M. Ball, *Studies of Laser Photolysis*, Ph.D. Thesis, Oxford University, 1995.

2 J.C. Pinot de Moira, *Laser Studies of Atmospheric Chemistry*, Ph.D. Thesis, Oxford University, 1998.

3 B.R. Lewis, S.T. Gibson, J.S. Morrill and M.L. Ginter, *J. Chem. Phys.*, **111** (1999) 186.

4 J.S. Morrill, *TheElectronic Structure of Molecular Oxygen and the Rotational Structure of the $d^1\Pi_g$ Rydberg State,* Ph.D. Thesis, University of Maryland, 1999.

5 R.D. Johnson, G.R. Long and J.W. Hudgens, *J. Chem. Phys.*, **87** (1987) 1977.

6 R. Ogorzalek-Loo, J. Marinelli, P.L. Houston, S. Arepalli, J.R. Wiesenfeld and R.W. Field, *J. Chem. Phys.*, **91** (1989) 5185.

7 H. Park, L. Li and W.A. Chupka, *Chem. Phys. Lett.*, **162** (1989) 317.

8 H. Park, L. Li and W.A. Chupka, *J. Chem. Phys.*, **92** (1990) 61.

9 S.M. Ball, G. Hancock, I.J. Murphy and S.P. Rayner, *Geophys. Res. Lett.*, **20** (1993) 2063.

10 S.M. Ball, G. Hancock, J.C. Pinot de Moira, C.M. Sadowski and F. Winterbottom, *Chem. Phys. Lett.*, **245** (1995) 1.

11 A.G. Suits, R.L. Miller, L.S. Bontuyan and P.L. Houston, *J. Chem. Soc. Faraday Trans.*, **89** (1993) 1443.

12 J.J. Valentini, *Chem. Phys. Lett.*, **96** (1983) 395.

13 J.J. Valentini, D.P. Gerrity, D.L. Phillips, J.C. Nieh and K.D. Tabor, *J. Chem. Phys.*, **86** (1987) 6745.

14 P. O'Keeffe, T. Ridley, S. Wang, K.P. Lawley and R.J. Donovan, *Chem. Phys. Lett.*, **298** (1998) 368.

15 R.D.J. Johnson, Part II Thesis, Oxford University (1999).

16 M. Brouard, H.M. Lambert, J. Short and J.P. Simons, *J. Phys. Chem.*, **99** (1995) 403.

17 H.L. Kim, M.A. Wickaaratchi, X. Zheng and G.E. Hall, *J. Chem. Phys.*, **101** (1994) 2033.

18 F. Lahmani, C. Lardeux and D. Olgadi, *Chem. Phys. Lett.*, **102** (1983) 523.

19 W.J. van der Zande, J.R. Peterson, W. Koot and J. Los, *Chem. Phys. Lett.*, **140** (1987) 175.